



MONASH University

**The Complex Magmatic Evolution and
Crustal Processes of Asteroid 4
Vesta**

Jennifer Tallis Mitchell

MGeol

A thesis submitted for the degree of Doctor of Philosophy at

Monash University in 2020

Department of Earth, Atmosphere and Environment

Copyright notice

© Jennifer T. Mitchell (2020).

I certify that I have made all reasonable efforts to secure copyright permissions for third-party content included in this thesis and have not knowingly added copyright content to my work without the owner's permission.

ABSTRACT

Asteroid 4 Vesta is the likely parent body of the howardite-eucrite-diogenite (HED) meteorite suite and presents a unique window into the evolution and behaviour of magmatism in the early Solar System. Eucrites are typically olivine-absent basalts and gabbros. Diogenites are orthopyroxene-dunite cumulates thought to represent either magma ocean cumulates or multiple crustal intrusions. Howardites are mechanical breccias of these lithologies.

pMELTS modelling of 11 bulk Vesta compositions was carried out to determine if diogenites can be formed from a crystallising magma ocean, and the results compared to 200 natural diogenite meteorites. Natural diogenites have a wide range of orthopyroxene compositions (En_{53-82}), whereas olivine-bearing diogenites are less diverse (En_{71-76}). Olivine-bearing diogenites are therefore not the most magnesian samples, contradicting expected crystallisation trends expected from a homogeneous magma ocean source. pMELTS modelling of recently suggested Vestan $f\text{O}_2$ conditions produce pyroxenes that are too magnesian compared to natural samples. Modelling shows that small changes in $f\text{O}_2$ produce large changes in orthopyroxene composition. The model finds that melting of primitive mantle compositions with $f\text{O}_2$ of ΔIW -1.6 to -1.2 produce magmas that crystallise orthopyroxenes that most closely match those found in natural diogenites. Variations in $f\text{O}_2$ can be explained by sulfidation reactions in the diogenite source. Further pMELTS modelling addresses the Ca-depletion observed in natural diogenite orthopyroxene relative to the modelled compositions, finding that the removal of <20 % of a mean eucrite component from the source satisfactorily reduces the Ca-content of the crystallising pyroxenes. Therefore, eucrite magmatism must have begun prior to diogenite magmatism. THERMOCALC modelling of a primitive Vestan mantle and an evolved mantle reflecting this initial eucrite removal constrains the temperatures at which each melt and the proportion of melt produced as a function of temperature and pressure. Eucrites require primitive mantle temperatures <1240 °C whereas dunitic diogenites were likely produced at temperatures >1340 °C during a second stage of melting. Thermal models were developed using these

compositional and temperature constraints to examine the thermal evolution of Vesta as a function of different accretion times. These models suggest that Vesta must have accreted 1.5-1.75 Myr after CAI formation. Earlier accretion ages would produce very high temperatures and thus komatiite-like lithologies, which are not observed in the meteorite collection. Models for later accretion ages do not reach high enough temperatures to create diogenite lithologies. The extraction of an initial eucrite melt extracts much of the ^{26}Al from the primitive mantle to the asteroid's crust to form a shallow magma ocean and hot lid upon convective lockup, allowing Vesta's interior to heat until diogenite magmatism can begin and causing the thermal metamorphism observed in eucrites. Diogenite material was later emplaced to the crust through dykes as a series of intrusions, which underwent gravitational mineral settling and fractional crystallisation.

Petrographic and petrofabrics analysis of ureilites – mantle residue samples from a disrupted asteroid – offer insights into what might be expected from Vesta's hidden mantle. Neutron scattering analysis of ureilites NWA 3140 and Watson 018 finds a strong lineation likely generated through high-temperature solid-state deformation mechanisms such as pencil-glide. This is an update to previous views of the observed lineation with reference to modern interpretations of ureilite petrogenesis. Additional EBSD analysis of poikilitic harzburgitic diogenite NWA 5480 finds no crystallographic orientation, suggesting that this meteorite formed from a large impact melt sheet as opposed to the Vestan mantle as has been suggested.

PUBLICATIONS DURING ENROLMENT

Mitchell, J.T., Tomkins, A.G. (2019), On the source of diogenites and olivine diogenites: compositional diversity from variable fO_2 , *Geochimica et Cosmochimica Acta*, **258**, 37-49

Mitchell, J.T., Tomkins, A.G., Newton, C., Johnson, T.E. (*in review*), A model for evolving crust on 4 Vesta through combined compositional and thermal modelling, *Accepted in Earth and Planetary Science Letters*

COVID-19 DISCLOSURE

The Covid-19 Pandemic interrupted data collection for Chapter 4 due to the closure of internal and external collaborating facilities, both domestic and international. Whilst the majority of analysis was able to be completed, certain samples were not able to be studied prior to the submission of this thesis. I aim to finish data collection once facility access returns to normal in order to complete the research presented in Chapter 4. The other research chapters were not affected by the pandemic.

ACKNOWLEDGEMENTS

This PhD has taught me many things, but most importantly it has taught me my own worth. I leave Monash University a braver, bolder, and stronger person, fully aware of my skills and capabilities both current and future.

Without the support of my friends and family, I would never have made it this far. For that, I thank you all. To Cathie and Howard Mitchell, my wonderful parents, thank you for letting me explore this chapter of my life even if I was away from home for so long. To Cathryn and Nicholas Mitchell, thank you for inspiring and supporting me from such a young age. To Natasha Stephen, thank you for setting me on this journey and your unwavering faith in me. To Anne Whitworth, Amrei Ladwig, Andrew Langendam, Alice Roberts, and Helen Brand – I am so lucky to have known you all, and I will forever treasure our time together. Friendships like this last a lifetime.

I would also like to thank the staff of the Department of Earth, Atmosphere & Environment for their ongoing support and expertise. Their help has been invaluable to me. In particular, I would like to thank Melanie Finch for inspiring me to reach higher and to forge my path with kindness and confidence.

Finally, to Andy Tomkins, my supervisor – thank you for everything you have done for me and all the support and trust you have shown me. I look forwards to working with you again in the future, making grand claims about rocks billions of years old and sharing stories over a Nullarbor fire.

This research was supported by an Australian Government Research Training Program (RTP) Scholarship.

Onward to the next adventure...

"This is the discipline that deals with the universe's divine revolutions, the stars' motions, sizes, distances, risings and settings... for what is more beautiful than heaven?"

Nicolaus Copernicus

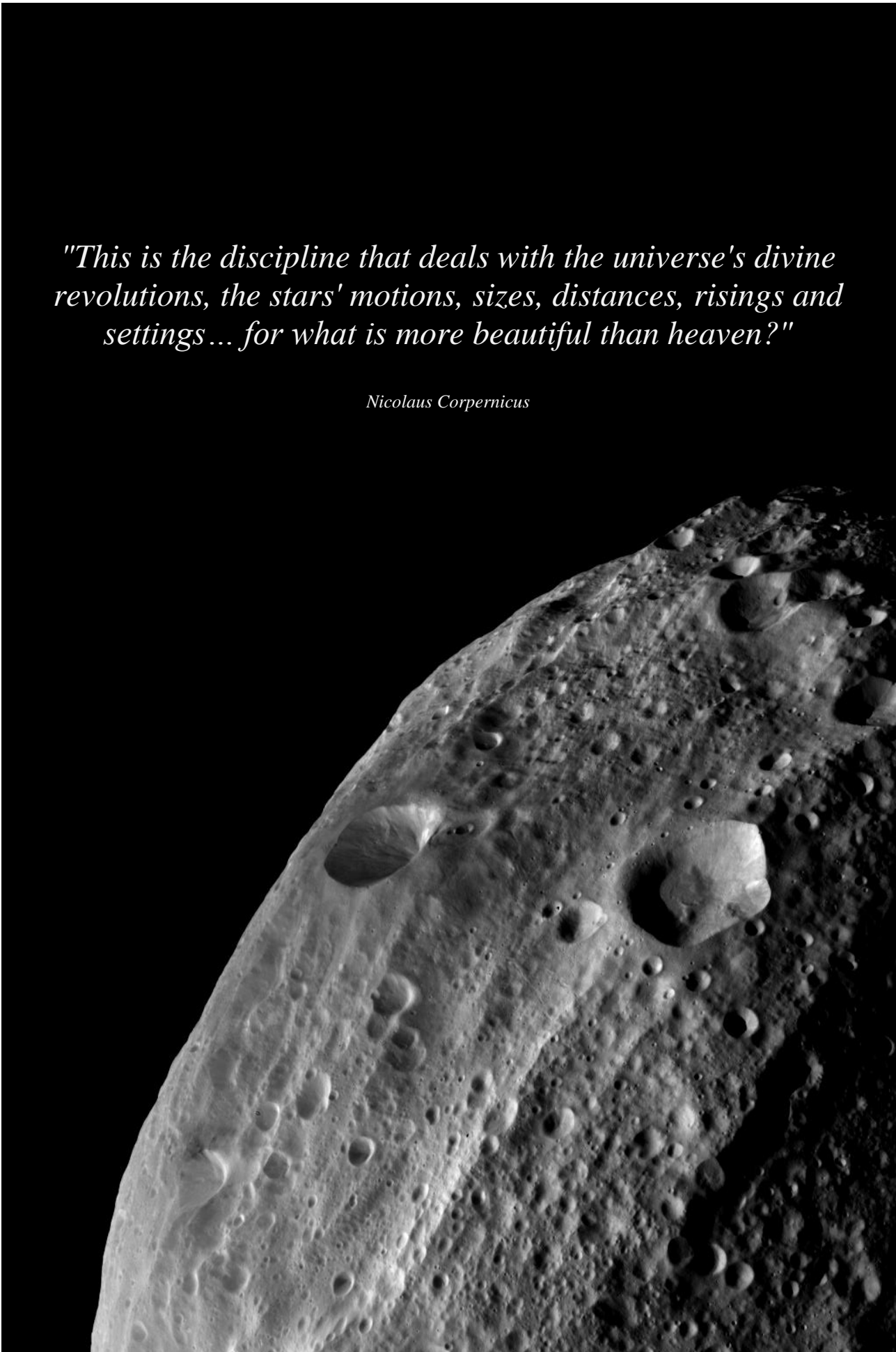


TABLE OF CONTENTS

CHAPTER 1: INTRODUCTION	1
1.1. The Study of Meteorites & Planetary	2
1.2. The HED Clan of Meteorites	3
1.3. Asteroid 4 Vesta & The Dawn Mission	7
1.4. Project Aims & Overview	11
1.5. Chapter References	13
CHAPTER 2: ON THE SOURCE OF DIOGENITES AND OLIVINE DIOGENITES: COMPOSITIONAL DIVERSITY FROM VARIABLE fO_2	29
Abstract	30
2.1. Introduction	31
2.2. Methods	33
2.3. Results	35
2.3.1. <i>Variable Degrees of Initial Partial Melting</i>	36
2.3.2. <i>Effects of Variable Oxygen Fugacity</i>	38
2.4. Discussion	42
2.4.1. <i>Comparison with Oxygen Isotope Data</i>	42
2.4.2. <i>fO_2 Diversity during Diogenite Formation</i>	43
2.4.3. <i>Note on the Scarcity of Olivine-Bearing Diogenites in the Meteorite Collection</i> .	47
2.4.4. <i>Implications of Heterogeneity in Vestan Mantle fO_2</i>	48
2.5. Conclusions	49
2.6. Acknowledgements & Author Contributions	50
2.7. Chapter References	50

**CHAPTER 3: A MODEL FOR EVOLVING CRUST ON 4 VESTA THROUGH
COMBINED COMPOSITIONAL AND THERMAL MODELLING..... 61**

Abstract	62
3.1. Introduction	63
3.2. Methods.....	65
3.2.1. <i>New pMELTS Modelling</i>	65
3.2.2. <i>THERMOCALC Modelling</i>	67
3.2.3. <i>Thermal Evolution Modelling</i>	68
3.3. Results	71
3.2.1. <i>pMELTS Modelling</i>	71
3.2.2. <i>THERMOCALC Modelling</i>	73
3.2.3. <i>Thermal Evolution Modelling</i>	74
3.4. Discussion	76
3.5. Conclusions.....	84
3.6. Acknowledgements & Author Contributions.....	85
3.7. Chapter References	85

**CHAPTER 4: A COMPARISON OF PETROFABRICS IN UREILITES AND
DIOGENITES: IMPLICATIONS FOR DISTINGUISHING BETWEEN MANTLE
RESIDUE, MAGMA CUMULATE, AND IMPACT MELT ORIGINS 95**

Abstract	96
4.1. Introduction	97
4.2. Samples & Methods	98
4.2.1. <i>Optical Microscopy</i>	99
4.2.2. <i>Imaging & Medical Beamline</i>	99
4.2.3. <i>Neutron Scattering Techniques; Dingo Neutron Tomography and Kowari Strain Scanner</i>	100

4.2.3. Electron Backscatter Diffraction	102
4.3. Results	103
4.3.1. <i>Optical Microscopy</i>	103
4.3.2. <i>Imaging & Medical Beamline</i>	106
4.3.3. <i>Neutron Scattering Techniques; Dingo Neutron Tomography and Kowari Strain Scanner</i>	108
4.3.3. <i>Electron Backscatter Diffraction</i>	109
4.4. Discussion	112
4.4.1. <i>Mineral Alignment in Asteroidal Mantles</i>	112
4.4.2. <i>Mineral Alignment in Asteroidal Magma Chambers</i>	114
4.4.3. <i>An Impact Melt Sheet Origin for NWA 5480</i>	118
4.5. Conclusions	122
4.6. Acknowledgements & Author Contributions.....	123
4.7. Chapter References	123
CHAPTER 5: THE COMPLEX MAGMATIC EVOLUTION AND CRUSTAL PROCESSES OF ASTEROID 4 VESTA, A SUMMARY	140
5.1. Timing of Accretion for Vesta	141
5.2. Vesta's Magmatic Evolution & Crustal Processes.....	142
5.3. Expectations for Vesta's Hidden Mantle	146
5.4. Future Work	146
5.5. Concluding Remarks	147
5.6. Chapter References	148
APPENDIX	153

LIST OF FIGURES

1.1. Cross-polarised light images of thin sections of eucrites, diogenites, and howardites, demonstrating textural and compositional differences between the different classes	4
1.2. Pyroxene compositions of diogenites, cumulate eucrites, and basaltic eucrites	6
1.3. Maps generated during NASA's Dawn mission.....	9
2.1. Pyroxene compositions of diogenites from the Meteoritical Bulletin	36
2.2. Modal abundance of olivine and orthopyroxene for each starting composition as generated by pMELTS modelling.....	37
2.3. The range of orthopyroxene compositions produced by each starting composition as a function of varying degrees of initial partial melting	38
2.4. Modal abundances of olivine and orthopyroxene for each starting composition under different fO_2 conditions.....	39
2.5. Pyroxene compositions produced by each starting composition under various fO_2 ΔIW conditions with 40 ± 0.1 % initial starting melt.....	42
2.6. High-Mg orthopyroxenes plotted against the global meteorite collection and pyroxenes generated by each of the starting compositions used in this study at fO_2 ΔIW -2.05	46
3.1. Orthopyroxene compositions generated through pMELTS modelling of each silicate starting bulk composition and the adjustments of each composition to reflect 5-20 % eucrite removal from the diogenite source.....	72
3.2. THERMOCALC pseudosections of (A) the undepleted, initial bulk silicate R-HED-CI composition and (B) the depleted R-HED-CI -15 composition.....	74
3.3. Thermal models of Vesta at various accretion ages, showing the variations in heat production and temperature caused by the ^{26}Al and ^{60}Fe through time relative to CAI formation.....	75
3.4. Simplified schematic of Vesta's evolution as established from modelling presented in this study	79
4.1. Photomicrographs of NWA 5480	103
4.2. Photomicrographs of Watson 018.....	104
4.3. Photomicrographs of NWA 3140	105

4.4. X-Ray computed tomography images from IMBL of diogenites Dhofar 700, NWA 7977 and 8265.....	107
4.5. Dingo data of diogenites Dhofar 700, NWA 7977 and NWA 8265.....	108
4.6. Dingo and Kowari strains scanner data for ureilites Watson 018 and NWA 3140	109
4.7. Pyroxene compositions of NWA 5480 compared to natural diogenite compositions	110
4.8. EBSD phase maps indexed for olivine, enstatite (orthopyroxene) and chromite	111
4.9. Differences in crystal orientation between random orientation, foliation, lineation	112
5.1. A simplified schematic of Vesta's evolution	144

LIST OF TABLES

2.1. Bulk compositions used in this study (wt%).....	35
2.2. Mg# ranges in orthopyroxene generated by each starting composition at varying degrees of initial partial melt.....	37
2.3. Mg# ranges for pyroxenes generated for each starting composition at various fO_2 ΔIW conditions at 40 ± 0.1 % partial melt	40
2.4. Temperatures ($^{\circ}C$) required to reach 40 ± 0.1 % partial melt.....	41
3.1. Compositions used in THERMOCALC modelling	67
3.2. Symbols, definitions, and values used in the thermal evolution modelling.....	69
3.3. ^{26}Al and ^{60}Fe abundances at each model stage for selected accretion times	71
4.1. Pyroxene and olivine compositions of NWA 5480	110
A.1. Pyroxene compositions of olivine diogenites, diogenites, cumulate eucrites and basaltic eucrites (Meteoritical Society Bulletin Database)	154
A.2. Pyroxene compositions generated through pMELTS modelling when the degree of initial partial melt is changed	161
A.3. Pyroxene compositions generated from each starting composition under varying oxygen fugacity conditions.....	164
A.4. Compositions adapted from literature through the removal of eucrite used to generate pMELTS models.....	168
A.5. Pyroxene compositions generated through pMELTS modelling of each starting composition at various degrees of eucrite removal.....	170

*“Dawn has done an amazing job showing that
asteroids aren’t just hunks of rock.*

They’re worlds.”

Carrie Nugent



Chapter 1

An Introduction to HED Meteorites and Asteroid 4 Vesta

Jennifer T. Mitchell¹

¹School of Earth, Atmosphere and Environment, Monash University, Australia

1.1. THE STUDY OF METEORITES & PLANETARY GEOLOGY

The study of meteorites provides us with unique insights into the formation of planetary bodies in the early Solar System, billions of years ago. These pieces of rock and metal represent a sparse sampling of a vast number of asteroids, planetesimals, moons and planets, and record an assortment of processes that would otherwise be unknown. There are upwards of 45 types of meteorite, though they are largely grouped into the following major categories; chondrite, primitive achondrite, evolved achondrite, stony-iron, and iron.

Chondrites are the most abundant group in the global meteorite collection and are composed of spherical amalgamations of largely olivine and orthopyroxene known as chondrules which have undergone various degrees of thermal metamorphism. Although the formation mechanisms of chondrules are poorly understood, it is thought that they formed within the first few million years of initial condensation of the solar nebula through the solidification of free-floating melt droplets, which then went on to gravitationally aggregate into chondritic bodies (Hewins, 1997; Alexander et al., 2001; Alexander et al., 2008). Importantly, a subset of chondrites – carbonaceous chondrites, rich in carbon with evidence of aqueous alteration (Takir et al., 2013) – contain some of the oldest material in the Solar System. These early condensates are referred to as calcium-aluminium-inclusions (CAIs) and have been dated to 4568.2 Ma (Bouvier & Wadhwa, 2010), which is widely considered to represent the beginning of solar nebula condensation (T_0).

Achondrites are meteorites that have undergone partial melting, which caused destruction of their chondrules. The transition from chondrite to achondrite is sometimes preserved in highly metamorphosed chondrites and primitive achondrites (Tomkins et al., 2020). Primitive achondrites represent the first stages of partial melting 1-5 Myr after the formation of CAIs (Schulz et al., 2010), and have compositions comparable to their chondrite precursors (Palme

et al., 1981; Nehru et al., 1983; Przylibski et al., 2005). In rare cases, relict chondrules are preserved (Schrader et al., 2017). Petrological analysis of these meteorites has revealed silicate melt networks and pockets, which formed in response to high temperatures within the parent body (Takeda et al., 1984; Tait et al., 2014; Tomkins et al., 2020) largely due to the decay of ^{26}Al , a short-lived radioisotope that was abundant in the early Solar System (Jura et al., 2013).

Evolved achondrites have undergone extensive melt fractionation, commonly during the primary differentiation of the parent body. This category includes Martian and Lunar meteorites, as well as those from asteroid 4 Vesta. A vast array of igneous and metamorphic textures and processes are recorded in these meteorites including mineral foliation during magma emplacement (Daly et al., 2019), sulfidation reactions in ejecta blankets (Zhang et al., 2013), and extensive thermal and shock metamorphism (Yamaguchi et al., 1997; 2009).

This project is focused on the howardite-eucrite-diogenite (HED) clan of meteorites and the evolution of their parent body, asteroid 4 Vesta.

1.2. THE HED CLAN OF METEORITES

The howardite-eucrite-diogenite (HED) clan of meteorites are a group of ultramafic-mafic achondrites associated with the asteroid 4 Vesta (McCord et al., 1970; Binzel & Xu, 1993; De Sanctis et al., 2013; McSween et al., 2013a) and are one of the few meteorite groups that have a clear parent body association. With over 2,300 classified HED meteorites (Meteoritical Society Bulletin Database), these are the most abundant and diverse achondrites in the global collection, recording a vast range of processes that occurred during the magmatic evolution and crustal development of Vesta. As such, individual HEDs can be roughly divided into three broad types, regardless of mineralogy; those that represent igneous fractionation, thermal metamorphism, and impact processes (Mittlefehldt, 2015). Almost all HEDs are brecciated,

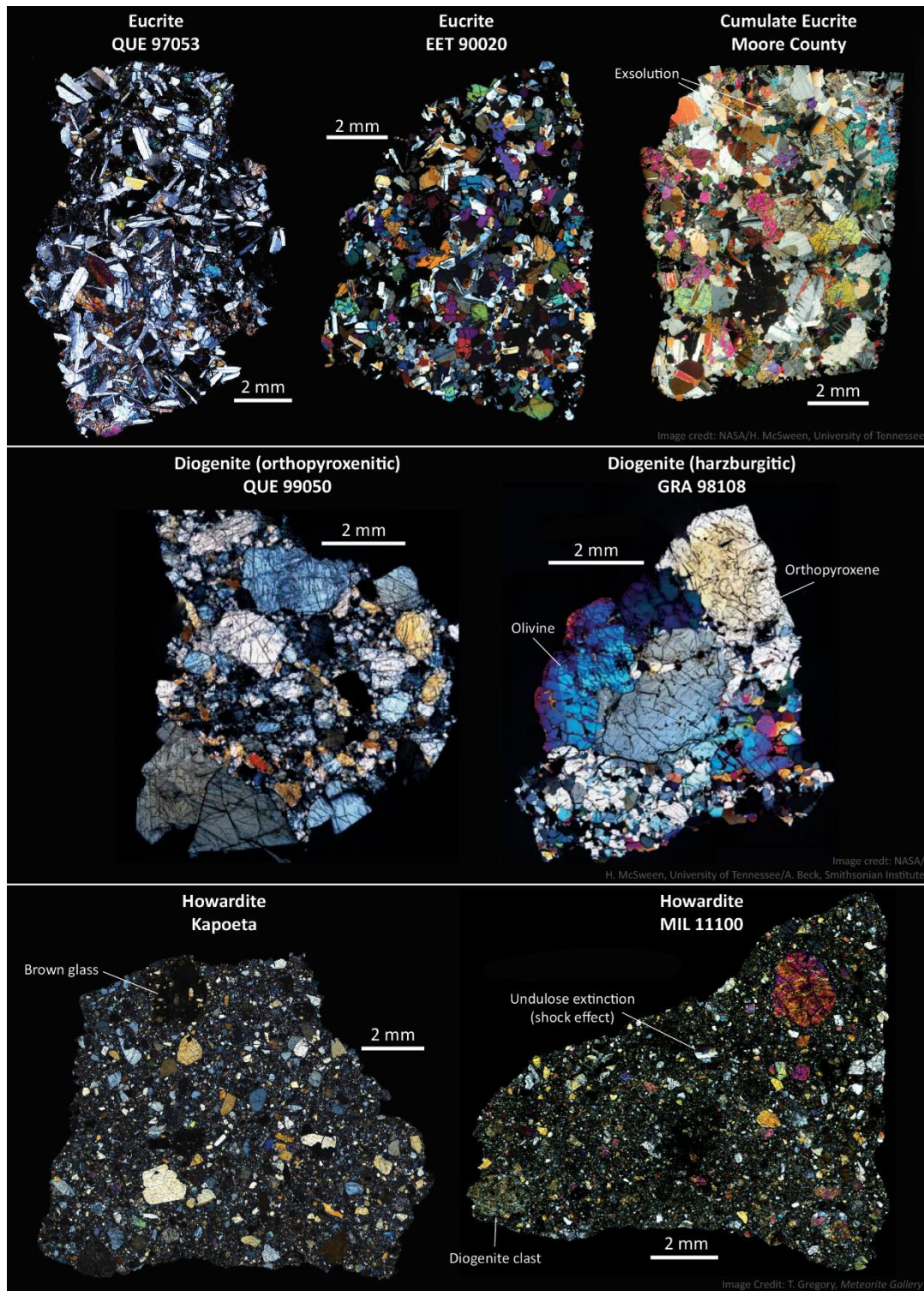


Figure 1.1. Cross-polarised light images of thin sections of eucrites, diogenites, and howardites, demonstrating textural and compositional differences between the different classes. Basaltic eucrites QUE 97053 and EET 90020 show common textures – plagioclase laths and more equant grains respectively – whilst cumulate eucrite Moore County is significantly coarser-grained. Exsolution in pigeonite (pyroxene) can be observed, as well as twinning in plagioclase. Orthopyroxenitic diogenite QUE 99050 and harzburgitic diogenite GRA 98108 are similar in texture and compositionally/texturally distinct from eucrites. Howardites Kapoeta and MIL 11100 display angular mineral fragments in a fine-grained matrix, with assorted brown glasses and shock effects. Image credit: Eucrites: NASA/ H. McSween, University of Tennessee, www.jpl.nasa.gov/spaceimages; Diogenites: NASA/ H. McSween, University of Tennessee, A. Beck, Smithsonian Institute, photojournal.jpl.nasa.gov; Howardites: T. Gregory, www.tim-gregory.co.uk/gallery

but rare unbrecciated samples do exist in the global meteorite collection (Mayne et al., 2009; Barrat et al., 2010).

Eucrites – the most common of the HED suite – are basalts and gabbros that are referred to as basaltic eucrites and cumulate eucrites respectively, composed of high- and low-Ca pyroxenes (Fig. 1.1, 1.2) and calcic plagioclase (Duke & Silver, 1967), with accessory phases including chromite, ilmenite, troilite, Fe-Ni metals, silica polymorphs, apatite, and zircon (Misawa et al., 2005; Mayne et al., 2009; Sarafian et al., 2013; Haba et al., 2014; Miyahara et al., 2014). They typically retain their primary igneous textures and compositions, as well as secondary features caused by crustal thermal metamorphism (Yamaguchi et al., 1996, 1997) and impact events. Most eucrites have undergone some degree of thermal metamorphism through prolonged magmatism (Takeda & Graham, 1991; Yamaguchi et al., 1997), with some samples showing granoblastic textures indicative of high degrees of metamorphism in Vesta's crust (Mayne et al., 2009; Yamaguchi et al., 2009). Exsolution of pigeonite to augite as a result of crustal metamorphism, is common, and typically appears as fine lamellae on (001) (Miyamoto & Takeda, 1977; Takeda, 1997; Miyamoto et al., 2001).

Basaltic eucrites are fine- to medium-grained, subophitic to ophitic rocks (Fig. 1.1), and are further categorised into two broad groups based on chemical differences. Main Group-Nuevo Laredo trend eucrites represent the majority of eucrite samples, and typically show high FeO/MgO ratios and decreasing Mg# with increasing incompatible element concentrations (Warren & Jerde, 1987; Barrat et al., 2007; Mayne et al., 2009). Stannern trend eucrites are significantly enriched in Ti as well as incompatible trace elements but have lower, more consistent FeO/MgO ratios (Mayne et al., 2009). Stannern trend eucrites are thought to be the result of contamination of Main Group eucrite magmas by crustal partial melts (Barrat et al., 2007). Cumulate eucrites are genetically related to, and formed contemporaneously with, basaltic eucrites (Barrat et al., 2000; Barrat, 2004; Hublet et al., 2017), representing Vesta's

lower crust (Takeda, 1997; Mandler & Elkins-Tanton, 2013; Hublet et al., 2017). These are typically equigranular, medium to coarse-grained gabbros with relatively homogeneous compositions (Hsu & Crozaz, 1997), and contain more Mg-rich pyroxenes than those in basaltic eucrites (Consolmagno & Drake, 1977; Stolper, 1977).

Diogenites are coarse-grained orthopyroxenite cumulates (Fig. 1.1), with rare examples of harzburgite and dunite compositions (Beck & McSween, 2010; Beck et al., 2011) that are classically referred to as olivine diogenites. The majority of diogenite orthopyroxene compositions are approximately $\text{En}_{80-65}\text{Fs}_{20-35}\text{Wo}_{1-3}$ (Fig. 1.2; Mitchell & Tomkins, 2019). Accessory phases include olivine in orthopyroxenitic diogenites, plagioclase, chromite, troilite, Fe-Ni metals, and silica (Berkley & Boynton, 1992; Domanik et al., 2004). Diogenites are considered to represent either: a) cumulates formed through mineral settling in a global magma ocean (Righter & Drake, 1997; Ruzicka et al., 1997) with olivine-bearing diogenites being part of Vesta's mantle (Sack et al., 1991; Tkalcic et al., 2013; Kared et al., 2019), or b) multiple discrete crustal magma chambers that evolved through fractional crystallisation (Berkley & Boynton, 1992; Grove & Bartels, 1992; Yamaguchi et al., 2011).

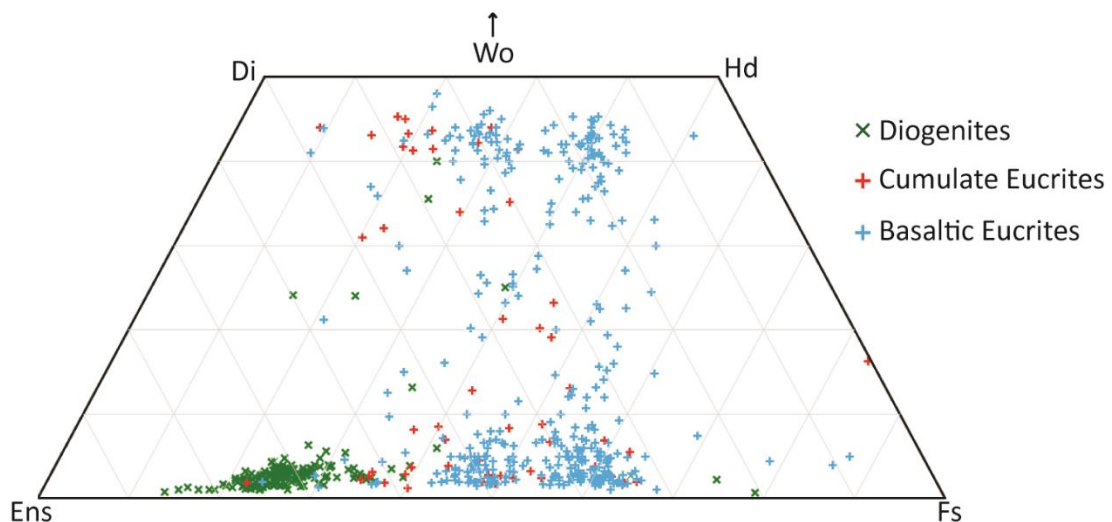


Figure 1.2. Pyroxene compositions of diogenites, cumulate eucrites, and basaltic eucrites (data from Meteoritical Society Bulletin Database and compiled in the appendix, Table A1).

Howardites are mechanical breccias formed through impact gardening, composed of multiple types of eucrite and diogenite clasts and associated mineral fragments in a fine-grained matrix (Fig. 1.1), sampling Vesta's regolith and recording a range of igneous processes prior to lithification (Duke & Silver, 1967; Lunning et al., 2016; Mayne et al., 2016). Howardites are distinguished from polymict eucrites by the amount primary orthopyroxene (diogenite lithologies) entrained, where polymict eucrites contain <10% primary orthopyroxene (diogenite) and polymict diogenites contain <10% eucrite component. Howardites, therefore, are polymict breccias containing >10% diogenite and >10% eucrite material (Delaney et al., 1983). In some cases, howardites also preserve evidence of the impactor and/or material exogenous to Vesta. For instance, chondritic clasts have been identified in a number of Vestan breccias (Wilkening, 1973; Gounelle et al., 2003), as well as primitive achondrite and potential stony-iron material (Lorenz et al., 2007; Beck et al., 2012).

1.3. ASTEROID 4 VESTA & THE DAWN MISSION

Asteroid 4 Vesta was discovered in 1807 by German astronomer Heinrich Wilhelm Olbers and named by mathematician Carl Friedrich Gauss. Vesta orbits at approximately 2.5 AU and is the second largest body in the main asteroid belt with a mean diameter of 525 km (Russell et al., 2012). Spectroscopic analysis (McCord et al., 1970; Binzel & Zu, 1993; Gaffey, 1997) and Hubble Space Telescope imaging (Binzel et al., 1997; Li et al., 2010) suggested that Vesta was similar in composition to the HED meteorite clan and mapped compositional variations across the asteroid's surface (Li et al., 2010), as well as a large impact crater over 460 km in diameter near Vesta's south pole (Thomas et al., 1997). The link between HEDs and Vesta and the presence of the southern impact crater was confirmed by NASA's Dawn mission.

Launched in September 2007, the Dawn mission arrived at Vesta in July 2011 and orbited the asteroid until September 2012 before moving on to the primary target of the mission, the dwarf

planet Ceres. Dawn imaged around 80% of Vesta's surface during three survey phases at various altitudes (Jaumann et al., 2012) using the Framing Camera (FC, visible light), the Visual and Infrared Imaging Spectrometer (VIR), and the Gamma Ray and Neutron Detector (GRaND) instruments. Gravity data (Konopliv et al., 2011, 2014) were collected alongside the images and spectra.

Dawn found that Vesta has a complex topography (Fig. 1.3A) of HED lithologies (Ammannito et al. 2013a; De Sanctis et al., 2013; Thangjam et al., 2013; Buczkowski et al., 2014) that is dominated by cratering and associated mass-wasting features (Krohn et al., 2014). The large crater detected by the Hubble Space Telescope was resolved as two overlapping impact basins by Dawn (Fig. 1.3B) – Veneneia (~400 km diameter) and the younger Rheasilvia (~500 km diameter) impact basins (Jaumann et al., 2012; Marchi et al., 2012; Schenk et al., 2012) – and the ejecta of which has been identified in Vesta's northern hemisphere (Ruesch et al., 2014; Schäfer et al., 2014; Combe et al., 2015). Large impact events such as those that formed Veneneia and Rheasilvia were ubiquitous early in the Solar System's history, but this does not seem to be the case for Vesta. The morphology, intact rim topographies, and lack of later cratering within both impact basins (Marchi et al., 2012; Schenk et al., 2012), $^{40}\text{Ar}/^{39}\text{Ar}$ dating of howardites (Lindsay et al., 2015) and chronological modelling based on asteroid flux (Williams et al., 2014) suggest that Veneneia and Rheasilvia are potentially as young as 2 Ga and 1 Ga respectively. Although strikingly recent, these ages are in keeping with estimates of the formation of the Vesta dynamic family of asteroids (Marzari et al., 1996; Asphaug, 1997; Nesvorný et al., 2008).

One of the key discoveries from the Dawn mission is that, unexpectedly, Rheasilvia did not expose the olivine-rich mantle (Ammannito et al., 2013b). Although there are challenges in identifying olivine due to the overlapping orthopyroxene spectra (Beck et al., 2013; McSween et al., 2013b), olivine-rich harzburgitic (>40% olivine) and dunitic lithologies can be detected

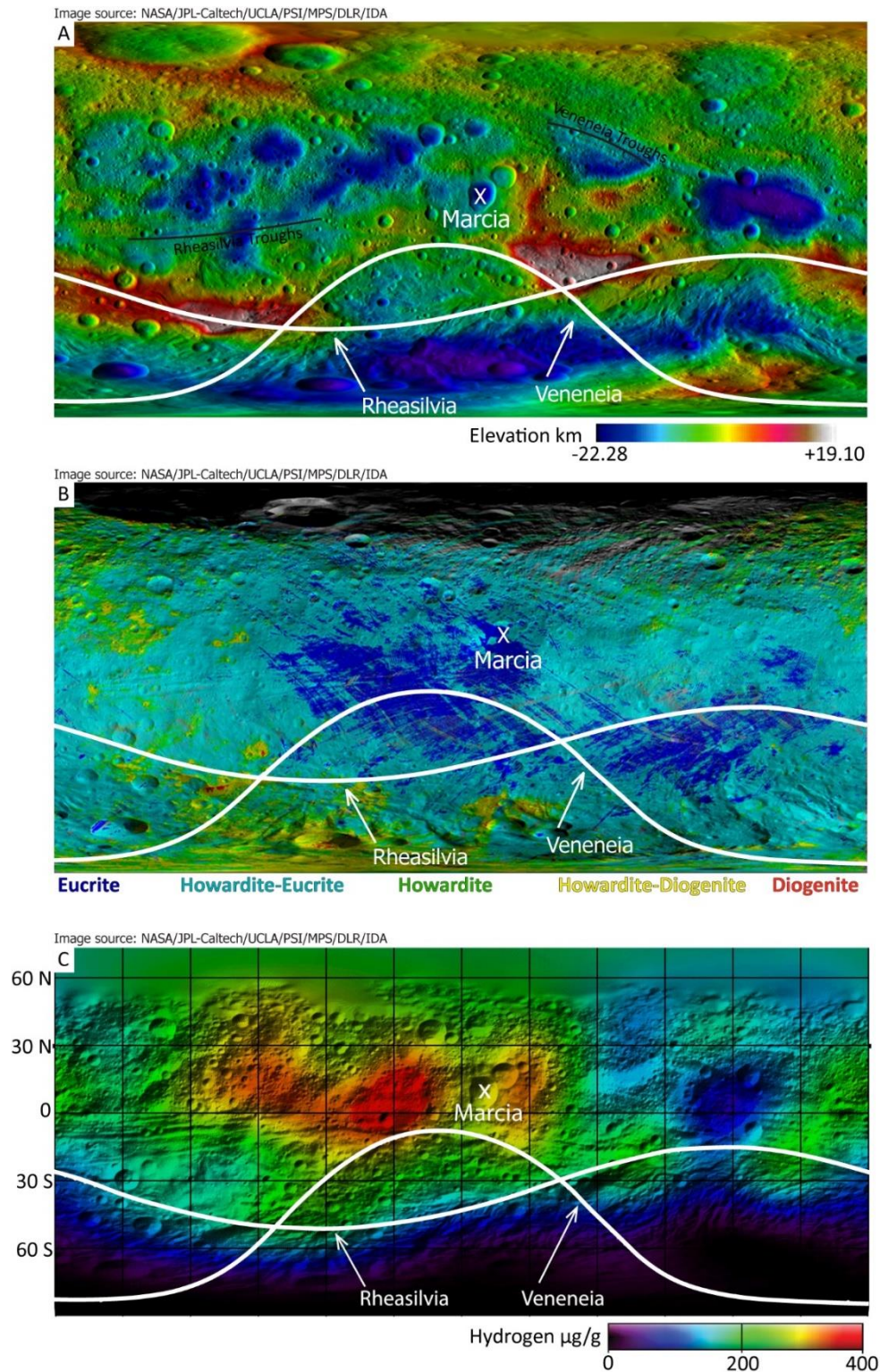


Figure 1.3. Maps generated during NASA’s Dawn mission. A) Topographic map of Vesta with Rheasilvia and Veneneia impact basins and associated troughs outlined. Highest elevations correlate to southern impact basin crater rims and Rheasilvia central uplift; B) Visual and infrared map of HED lithologies, showing heterogeneous distribution of rock types across the asteroid; C) Hydrogen map of Vesta. Highest hydrogen concentrations are associated with ejecta units from the Veneneia impact (Reddy et al., 2012). Rheasilvia and Veneneia troughs are clearly visible in this image (Image credits: NASA/JPL-Caltech, UCLA/PSI/MPS/DLR/IDA).

(25% olivine is the detection limit). For instance, olivine is observed in the northern hemisphere and is unrelated to ejecta from the southern impact basins (Ammanito et al., 2013b; Thangjam et al., 2014; Palomba et al., 2015). Instead, Rheasilvia is floored by diverse orthopyroxene-rich diogenite-howardite lithologies (Ammanito et al., 2013a, 2015; McSween et al., 2013b). Post-Dawn models for Vesta's structure now suggest that the crust-mantle boundary is significantly deeper than originally expected – over 80 km deep (Clenet et al., 2014) – and is not exposed at the surface.

The southern impact basins are also thought to be associated with the unusual large-scale troughs that roughly ring the equator (Fig. 1.3A). The morphology of these troughs is distinct from the fractures observed on small, undifferentiated bodies and instead are more similar to graben structures on terrestrial worlds (Buczkowski et al., 2012). The equatorial troughs accommodate several km of vertical displacement over tens to hundreds of km length and appear to be linked to the formation of the Rheasilvia impact basin (Buczkowski et al., 2012; Jaumann et al., 2012; Yingst et al., 2014), whereas a second set observed in the northern hemisphere seem to be related to Veneneia (Scully et al., 2014). It is thought that during the southern impact basin events, Vesta underwent both brittle and ductile deformation due to its differentiated structure (Buczkowski et al., 2012), effectively causing the asteroid to buckle.

Dawn also detected localised occurrences of hydrated minerals (Fig. 1.3C) and dark materials across Vesta's surface that are not associated with an HED lithology. Typically associated with craters, this dark material has been ascribed to infall of carbonaceous chondrites and subsequent impact mixing with the Vestan regolith (McCord et al., 2012; Reddy et al., 2012; Nathues et al., 2014; Palomba et al., 2014; Turrini et al., 2014), supported by the identification of clasts and fragments of carbonaceous chondrites – most commonly CM2 (Reddy et al., 2012) – in a number of howardite samples (Wilkening et al., 1973; Buchanan et al., 1993). It has been suggested that this carbon-rich material was delivered during the Veneneia impact event due

to the concentration of this dark material around Veneneia's rim (Reddy et al., 2012; Nathues et al., 2014). As such, it is likely that Veneneia was formed through the low velocity impact of a large carbonaceous chondrite bolide (Reddy et al., 2012) in contrast to the basaltic impactor that produced Rheasilvia (Ivanov & Melosh, 2013).

1.4. PROJECT AIMS & OVERVIEW

Although Dawn has provided a wealth of information about Vesta, there are still many unanswered questions. For instance, what is the genetic and chronological relationship between diogenites and eucrites? Why is olivine so uncommon in HED meteorites? Do olivine-bearing diogenites represent samples of the Vestan mantle as many have suggested? What should be expected of Vesta's mantle in terms of composition and evolution? And, most pivotally, did Vesta evolve through a magma ocean or through a more complex magmatic differentiation history?

This project aims to address the genesis of orthopyroxenite and olivine-bearing diogenites, their relation to eucrites, and the behaviour of magmatism in the early Solar System. In *Chapter 2: "On the Source of Diogenites and Olivine Diogenites: Compositional Diversity from Variable fO_2 "*, which has been published in Mitchell & Tomkins (2019; *Geochimica et Cosmochimica Acta* 258:37-49), we explore how small changes in oxygen fugacity in the source magma affect the compositions of the crystallising minerals using pMELTS (Ghiorso et al., 2002) modelling. This chapter also establishes that a magma ocean scenario cannot produce compositions comparable to those observed in natural diogenites and, instead, finds that diogenites most likely represent multiple discrete crustal magma chambers with varying source compositions.

In *Chapter 3: "A Model for Evolving Crust on 4 Vesta through Combined Compositional and Thermal Modelling"* (Mitchell et al.; currently accepted in *Earth and Planetary Science*

Letters) we continue the work of previous chapter, investigating the Ca-depletion observed in diogenites by considering their relationship with eucrites. Here, we remove a eucrite component from the diogenite source to reduce the Ca content and combine pMELTS, THERMOCALC (Powell & Holland, 1988) and thermal modelling based on the decay of short-lived radioisotopes ^{26}Al and ^{60}Fe (Moskovitz & Gaidos, 2011; Mare et al., 2014) to produce a simplified magmatic-thermal evolution of Vesta. We find that initial eucrite magma extraction forms a shallow magma ocean and subsequent hot lid, satisfactorily depleting the diogenite source in Ca, whilst insulating the interior of the body to reach the temperatures required for diogenite magmatism. Thus, we conclude that diogenites post-date the onset of eucrite magmatism, further strengthening the view that they represent late-stage crustal intrusions (Barrat et al., 2010; Yamaguchi et al., 2011). This chapter also finds that the timing of Vesta's accretion played a vital role in determining the lithologies produced and the development of the asteroid's internal structure, supporting an early accretion age for Vesta.

Chapter 4: "A Comparison of Petrofabrics in Ureilites and Diogenites: Implications for Distinguishing Between Mantle Residue, Magma Cumulate, and Impact Melt Origins" utilises novel neutron scattering (Dingo Neutron Tomography and Kowari Strain Scanner, ANSTO, Australia) and synchrotron-source X-Ray (Imaging & Medical Beamline, Australian Synchrotron) techniques that allow for the study of whole 3D samples alongside electron backscatter diffraction (EBSD) to investigate variations in mineral alignment across different magmatic settings on asteroids, as well as determining a provenance for the enigmatic Northwest Africa 5480 meteorite (an atypical diogenite). I have found a clear mineral lineation in both ureilites studied and suggest potential mechanisms that may have caused this, updating those presented in Berkley et al., (1976, 1980) to reflect the modern interpretation of ureilite genesis. I have also found that there is a random crystal orientation throughout NWA 5480. As such, it is likely that NWA 5480 represents a sample of a solidified impact melt that

incorporated pre-existing harzburgitic lithologies from Vesta's crust, as opposed to sampling Vesta's mantle.

1.5. CHAPTER REFERENCES

Alexander, C.M.O'D., Boss, A.P., Carlson, R.W. (2001), The early evolution of the inner solar system: a meteoritic perspective, *Science*, **293**, 64-68

Alexander, C.M.O'D., Grossman, J.N., Ebel, D.S., Ciesla, F.J. (2008), The formation conditions of chondrules and chondrites, *Science*, **380**, 1617-1619

Ammanito, E., De Sanctis, M.C., Combe, J.-Ph., Frigeri, A., Jaumann, R., Longobardo, A., McSween, H.Y., Palomba, E., Tosi, F., Raymond, C.A., Russell, C.T., the Dawn Science Team (2015), Compositional variations in the Vestan Rheasilvia basin, *Icarus*, **259**, 194-202

Ammannito, E., De Sanctis, M.C., Capaccioni, F., Capria, M.T., Carraro, F., Combe, J.-P., Fonte, S., Frigeri, A., Joy, S.P., Longobardo, A. Magni, G., Marchi, S., McCord, T.B., McFadden, L.A., McSween, H.Y., Palomba, E., Pieters, C.M., Polanskey, C.A., Raymond, C.A., Sunshine, J.M., Tosi, F., Zambon, F., Russell, C.T. (2013a), Vestan lithologies mapped by the visual and infrared spectrometer on Dawn, *Meteoritics & Planetary Science*, **48**, 2185-2198

Ammannito, E., De Sanctis, M.C., Palomba, E., Longobardo, A., Mittlefehldt, D.W., McSween, H.Y., Marchi, S., Capria, M.Y., Capaccioni, F., Frigeri, A., Pieters, C.M., Ruesch, O., Tosi, F., Zambon, F., Carraro, F., Fonte, S., Hiesinger, H., Magni, G., McFadden, L.A., Raymond, C.A., Russell, C.T., Sunshine, J.M. (2013b), Olivine in an unexpected location on Vesta's surface, *Nature*, **504**, 122-125

- Asphaug, E. (1997), Impact origin of the Vesta family, *Meteoritics & Planetary Science*, **32**, 965-980
- Barrat, J.-A. (2004), Determination of parental magmas of HED cumulates: the effects of interstitial melts, *Meteoritics & Planetary Science*, **39**, 1767-1779
- Barrat, J.-A., Bilchert-Toft, J., Gillet, Ph., Keller, F. (2000), The differentiation of eucrites: the role of in situ crystallization, *Meteoritics & Planetary Science*, **35**, 1087-1100
- Barrat, J.-A., Yamaguchi, A., Greenwood, R.C., Bohn, M., Cotton, J., Benoit, M., Franchi, I.A. (2007), The Stannern trend eucrites: contamination of main group eucritic magmas by crustal partial melts, *Geochimica et Cosmochimica Acta*, **71**, 4108-4124
- Barrat, J.-A., Yamaguchi, A., Zanda, B., Bollinger, C., Bohn, M. (2010), Relative chronology of crust formation on asteroid Vesta: insights from the geochemistry of diogenites, *Geochimica et Cosmochimica Acta*, **74**, 6218-6231
- Beck, A.W., McCoy, T.J., Sunshine, J.M., Viviano, C.E., Corrigan, C.M., Hiroi, T., Mayne, R.G. (2013), Challenges in detecting olivine on the surface of 4 Vesta, *Meteoritics & Planetary Science*, **48**, 2155-2165
- Beck, A.W., McSween, H.Y. (2010), Diogenites as polymict breccias composed of orthopyroxenite and harzburgite, *Meteoritics & Planetary Science*, **45**, 850-872
- Beck, A.W., Mittlefehldt, D.W., McSween, H.Y., Rumble III, D., Lee, C.-T.A., Bodnar, R.J. (2011), MIL 03443, a dunite from asteroid 4 Vesta: evidence for its classification and cumulate origin, *Meteoritics & Planetary Science*, **46**, 1133-1151
- Beck, A.W., Welten, K.C., McSween, H.Y., Viviano, C.E., Caffee, M.W. (2012), Petrologic and textural diversity among the PCA 02 howardite group, one of the largest pieces of the Vestan surface, *Meteoritics & Planetary Science*, **47**, 947-969

- Berkley, J.L., Boynton, N.J. (1992), Minor/major element variation within and among diogenite and howardite orthopyroxenite groups, *Meteoritics*, **27**, 387-394
- Berkley, J.L., Gassaway Brown, H., Keil, K., Carter, N.L., Mercier, J.-C.C. (1976), The Kenna ureilite: an ultramafic rock with evidence for igneous, metamorphic, and shock origin, *Geochimica et Cosmochimica Acta*, **40**, 1429-1437
- Berkley, J.L., Taylor, G.J., Keil, K., Harlow, G., Prinz, M. (1980), The nature and origin of ureilites, *Geochimica et Cosmochimica Acta*, **44**, 1579-1597
- Binzel, R.P., Gaffey, M.J., Thomas, P.C., Zellner, B.H., Storrs, A.S. Wells, E.N. (1997), Geologic mapping of Vesta from 1994 Hubble Space Telescope images, *Icarus*, **128**, 95-103
- Binzel, R.P., Xu, S. (1993), Chips off of Asteroid 4 Vesta: evidence for the parent body of basaltic achondrite meteorites, *Science*, **260**, 186-191
- Bouvier, A., Wadhwa, M. (2010), The age of the Solar System redefined by the oldest Pb-Pb age of a meteoritic inclusion, *Nature Geoscience*, **3**, 637-641
- Buchanan, P.C., Zolensky, M.E., Reid, A.M. (1993), Carbonaceous chondrite clasts in the howardites Bholghati and EET87513, *Meteoritics*, **28**, 659-682
- Buczkowski, D.L., Wyrick, D.Y., Iyer, K.A., Kahn, E.G., Scully, J.E.C., Nathues, A., Gaskell, R.W., Roatsch, T., Preusker, F., Schenk, P.M., Le Corre, L., Reddy, V., Yingst, R.A., Nest, S., Williams, D.A., Garry, W.B., Barnouin, O.S., Jaumann, R., Raymond, C.A., Russell, C.T. (2012), Large-scale troughs on Vesta: a signature of planetary tectonics, *Geophysical Research Letters*, **39**, L18205
- Buczkowski, D.L., Wyrick, D.Y., Toplis, M., Yingst, R.A., Williams, D.A., Garry, W.B., Mest, S., Kneissl, T., Scully, J.E.C., Nathues, A., De Sanctis, M.C., LeCorre, L., Reddy, V.,

- Hoffmann, M., Ammannito, E., Frigeri, A., Tosi, F., Preusker, F., Roatsch, T., Raymond, C.A., Jaumann, R., Pieters, C.M., Russell, C.T. (2014), The unique geomorphology and physical properties of the Vestalia Terra plateau, *Icarus*, **244**, 89-103
- Clenet, H., Barrat, J.-A., Asphaug, E.I., Benz, W.I., Gillet, P. (2014), A deep crust-mantle boundary in the asteroid 4 Vesta, *Nature*, **511**, 303-306
- Combe, J.-P., McCord, T.B., McFadden, L.A., Ieva, S., Tosi, F., Longobardo, A., Frigeri, A., De Sanctis, M.C., Ammannito, E., Ruesch, O., Palomba, E., Fulchignoni, M., Raymond, C.A., Russell, C.T. (2015), Composition of northern regions of Vesta analyzed by the Dawn mission, *Icarus*, **259**, 53-71
- Consolmagno, G.J., Drake, M.J. (1977), Compositions and evolution of the eucrite parent body: evidence from rare earth elements, *Geochimica et Cosmochimica Acta*, **41**, 1271-1282
- Daly, L., Piazzolo, S., Lee, M.R., Griddin, S., Chung, P., Campanale, F., Cohen, B.E., Hallis, L.J., Trimby, P.W., Baumgartner, R., Forman, L.V., Benedix, G.K. (2019), Understanding the emplacement of Martian volcanic rocks using petrofabrics of the nakhlite meteorites, *Earth and Planetary Science Letters*, **520**, 220-230
- De Sanctis, M.C., Ammannito, E., Capria, M.T., Capaccioni, F., Combe, J.-P., Frigeri, A., Longobardo, A., Magni, G., Marchi, S., McCord, T.B., Palomba, E., Tosi, F., Zambon, F., Carraro, F., Fonte, S., Li, Y.J., McFadden, L.A., Mittlefehldt, D.W., Pieters, C.M., Jaumann, R., Stephan, K., Raymond, C.A., Russell, C.T. (2013), Vesta's mineralogical composition as revealed by the visible and infrared spectrometer on Dawn, *Meteoritics & Planetary Science*, **48**, 2166-2184

- Delaney, J.S., Takeda, H., Prinz, M., Nehru, C.E., Harlow, G.E. (1983), The nomenclature of polymict basaltic achondrites, *Meteoritics*, **18**, 103-111
- Domanik, K., Kolar, S., Musselwhite, D., Drake, M.J. (2004), Accessory silicate mineral assemblages in the Bilanga diogenite: a petrographic study, *Meteoritics & Planetary Science*, **39**, 567-579
- Duke, M.B., Silver, L.T. (1967), Petrology of eucrites, howardites and mesosiderites, *Geochimica et Cosmochimica Acta*, **31**, 1637-1665
- Gaffey, M.J. (1997), Surface lithologic heterogeneity of asteroids 4 Vesta, *Icarus*, **127**, 130-157
- Ghiorso, M.S., Hirschmann, M.M., Reiners, P.W., Kress, III, V.C. (2002), The pMELTS: A revision of MELTS aimed at improving calculation of phase relations and major elements partitioning involved in partial melting of the mantle at pressures up to 3 GPa, *Geochemistry, Geophysics, Geosystems*, **3**, 1-35
- Gounelle, M., Zolensky, M.E., Liou, J.-C., Bland, P.A., Alard, O. (2003), Mineralogy of carbonaceous chondritic microclasts in howardites: identification of C2 fossil micrometeorites, *Geochimica et Cosmochimica Acta*, **67**, 507-527
- Grove, T.L., Bartels, K.S. (1992), The relation between diogenite cumulates and eucrite magmas, *Proceedings of Lunar and Planetary Science*, **22**, 437-445
- Haba, M.K., Yamaguchi, A., Horie, K., Hidaka, H. (2014), Major and trace elements of zircons from basaltic eucrites: implications for the formation of zircons on the eucrite parent body, *Earth and Planetary Science Letters*, **387**, 10-21
- Hewins, R.H. (1997), Chondrites, *Annual Reviews of Earth and Planetary Science*, **25**, 61-83

- Hsu, W., Crozaz, G. (1997), Mineral chemistry and petrogenesis of eucrites: II cumulate eucrites, *Geochimica et Cosmochimica Acta*, **61**, 1293-1302
- Hublet, G., Debaille, V., Wimpenny, J., Yin, Q.-Z. (2017), Differentiation and magmatic activity in Vesta evidenced by ^{26}Al - ^{26}Mg dating in eucrites and diogenites, *Geochimica et Cosmochimica Acta*, **218**, 73-97
- Ivanov, B.A., Melosh, H.J. (2013), Two-dimensional numerical modeling of the Rheasilvia impact formation, *Journal of Geophysical Research Letters: Planets*, **118**, 1545-1557
- Jaumann, R., Williams, D.A., Buczkowski, D.L., Yingst, R.A., Preusker, F., Hiesinger, H., Schmedemann, N., Kneissl, T., Vincent, J.B., Blewett, D.T., Buratti, B.J., Carsenty, U., Denevi, B.W., De Sanctis, M.C., Garry, W.B., Keller, H.Y., Kersten, E. Krohn, K., Li, J.-Y., Marchi, S., Matz, K.D., McCord, T.B., McSween, H.Y., Mest, S.C., Mittlefehldt, D.W., Mottola, S., Nathues, A., Neukum, G., O'Brien, D.P., Pieters, C.M., Prettyman, T.H., Raymond, C.A., Roatsch, T., Russell, C.T., Schenk, P. Schmidt, B.E., Scholten, F., Stephan, K., Sykes, M.V., Tricarico, P., Wagner, R., Zuber, M.T., Sierks, H. (2012), Vesta's shape and morphology, *Science*, **336**, 687-690
- Jura, M., Xu, S., Young, E.D. (2013), ^{26}Al in the early solar system: not so unusual after all, *The Astrophysical Journal Letters*, **775**, L41
- Kared, R., Moine, B.N., Seddiki, A., Yves Cottin, J., Greenwood, R.C., Franchi, I.A. (2019), Petrology, mineralogy, and geochemistry of the olivine diogenite NWA 4255: new insights into the magmatic evolution of asteroid 4 Vesta, *Arabian Journal of Geosciences*, **12**, 442

- Konopliv, A.S., Asmar, S.W., Bills, B.G., Mastrodemos, N., Park, R.S., Raymond, C.A., Smith, D.E., Zuber, M.T. (2011), The Dawn gravity investigation at Vesta and Ceres, *Space Science Reviews*, **163**, 461-486
- Konopliv, A.S., Asmar, S.W., Park, R.S., Bills, B.G., Centinello, F., Chamberlin, A.B., Ermakov, A., Gaskell, R.W., Rambaux, N., Raymond, C.A., Russell, C.T., Smith, D.E., Tricarico, P., Zuber, M.T. (2014), The Vesta gravity field, spin pole and rotation period, landmark positions, and ephemeris from the Dawn tracking and optical data, *Icarus*, **240**, 103-117
- Krohn, K., Jaumann, R., Otto, K., Hoogenboom, T., Wagner, R., Buczkowski, D.L., Gary, B., Williams, D.A., Yingst, R.A., Scully, J., De Sanctis, M.C., Kneissl, T., Schmedemann, N., Kersten, E., Stephan, K., Matz, K.-D., Pieters, C.M., Preusker, F., Roatsch, T., Schenk, P., Russell, C.T., Raymond, C.A. (2014), Mass movement on Vesta at steep scarps and crater rims, *Icarus*, **244**, 120-132
- Li, J.-Y., McFadden, L.A., Thomas, P.C., Mutchler, M.J., Parker, J.Wm., Young, E.F., Russell, C.T., Sykes, M.V., Schmidt, B.E. (2010), Photometric mapping of asteroid (4) Vesta's southern hemisphere with Hubble Space Telescope, *Icarus*, **208**, 238-251
- Lindsay, F.N., Delaney, J.S., Herzog, G.F., Turrin, B.D., Park, J., Swisher III, C.C. (2015), Rheasilvia provenance of the Kapoeta howardite inferred from $\sim 1 \text{ Ga } ^{40}\text{Ar}/^{39}\text{Ar}$ feldspar ages, *Earth and Planetary Science Letters*, **413**, 208-213
- Lorenz, K.A., Nazarov, M.A., Kurat, G., Brandstaetter, F., Ntaflos, Th. (2007), Foreign meteoritic material of howardites and polymict eucrites, *Petrology*, **15**, 109-125

- Lunning, N.G., Welten, K.C., McSween, H.Y., Caffee, M.W., Beck, A.W. (2016), Grosvenor Mountains 95 howardite pairing group: insights into the surface regolith of asteroid 4 Vesta, *Meteoritics & Planetary Science*, **51**, 167-194
- Mandler, B.E., Elkins-Tanton, L.T. (2013), The origin of eucrites, diogenites, and olivine diogenites: magma ocean crystallization and shallow magma chamber processes on Vesta, *Meteoritics & Planetary Science*, **48**, 2333-2349
- Marchi, S., McSween, H.Y., O'Brien, D.P., Schenk, P., De Sanctis, M.C., Gaskell, R., Jaumann, R., Mottola, S., Preusker, F., Raymond, C.A., Roatsch, T., Russell, C.T. (2012), The violent collisional history of asteroid 4 Vesta, *Science*, **336**, 690-694
- Mare, E.R., Tomkins, A.G., Godel, B.M. (2014), Restriction of parent body heating by metal-troilite melting: Thermal models for the ordinary chondrites, *Meteoritics & Planetary Science*, **49**, 636-651
- Marzari, F., Cellino, A., Davis, D.R., Farinella, P., Zappalà, V., Vanzai, V. (1996), Origin and evolution of the Vesta asteroid family, *Astronomy and Astrophysics*, **316**, 248-262
- Mayne, R.G., McSween, H.Y., McCoy, T.J., Gale, A. (2009), Petrology of the unbrecciated eucrites, *Geochimica et Cosmochimica Acta*, **73**, 794-819
- Mayne, R.G., Smith, S.E., Corrigan, C.M. (2016), Hiding in the howardites: unequilibrated eucrite clasts as a guide to the formation of Vesta's crust, *Meteoritics & Planetary Science*, **51**, 2387-2402
- McCord, T.B., Adams, J.B., Johnson, T.V. (1970), Asteroid Vesta: spectral reflectivity and compositional implications, *Science*, **168**, 1445-1447
- McCord, T.B., Li, J.-Y., Combe, J.-P., McSween, H.Y., Jaumann, R., Reddy, V., Tosi, F., Williams, D.A., Blewett, D.T., Turrini, D., Palomba, E., Pieters, C.M., De Sanctis,

- M.C., Ammannito, E., Capria, M.T., Le Corre, L., Longobardo, A., Nathues, A., Mittlefehldt, D.W., Schröder, S.E., Hiesinger, H., Beck, A.W., Capaccioni, F., Carsenty, U., Keller, H.U., Denevi, B.W., Sunshine, J.M., Raymond, C.A., Russell, C.T. (2012), Dark material on Vesta from the infall of carbonaceous volatile-rich material, *Nature*, **491**, 83-86
- McSween, H.Y., Ammannito, E., Reddy, V., Prettyman, T.H., Beck, A.W., De Sanctis, M.C., Nathues, A., Le Corre, L., O'Brien, D.P., Yamashita, N., McCoy, T.J., Mittlefehldt, D.W., Toplis, M.J., Schenk, P., Palomba, E., Turrini, D., Tosi, F., Zambon, F., Longobardo, A., Capaccioni, F., Raymond, C.A., Russell, C.T. (2013b), Composition of the Rheasilvia basin, a window into Vesta's interior, *Journal of Geophysical Research: Planets*, **118**, 335-346
- McSween, H.Y., Binzel, R.P., De Sanctis, M.C., Ammannito, E., Prettyman, T.H., Beck, A.W., Reddy, V., Le Corre, L., Gaffey, M.J., McCord, T.B., Raymond, C.A., Russell, C.T., the Dawn Science Team (2013a), Dawn; the Vesta-HED connection; and the geologic context for eucrites, diogenites, and howardites, *Meteoritics & Planetary Science*, **48**, 2090-2104
- Misawa, K., Yamaguchi, A., Kaiden, H. (2005), U-Pb and ²⁰⁷Pb-²⁰⁶Pb ages of zircons from basaltic eucrites: implications for early basaltic volcanism on the eucrite parent body, *Geochimica et Cosmochimica Acta*, **69**, 5847-5861
- Mitchell, J.T., Tomkins, A.G. (2019), On the source of diogenites and olivine diogenites: compositional diversity from variable *f*O₂, *Geochimica et Cosmochimica Acta*, **258**, 37-49

- Mittlefehldt, D.W. (2015), Asteroid (4) Vesta: 1. The howardite-eucrite-diogenite (HED) clan of meteorites, *Chemie der Erde*, **75**, 155-183
- Miyahara, M., Ohtani, E., Yamaguchi, A., Ozawa, S., Sakai, T., Hirao, N. (2014), Discovery of coestite and stishovite in eucrite, *PNAS*, **111**, 10939-10942
- Miyamoto, M., Mikouchi, T., Kaneda, K. (2001), Thermal history of the Ibitira noncumulate eucrite as inferred from pyroxene exsolution lamella: evidence for reheating and rapid cooling, *Meteoritics & Planetary Science*, **36**, 231-237
- Miyamoto, M., Takeda, H. (1977), Evaluation of a crust model of eucrites from the width of exsolved pyroxene, *Geochemical Journal*, **11**, 161-169
- Moskovitz, N., Gaidos, E. (2011), Differentiation of planetesimals and the thermal consequences of melt migration, *Meteoritics & Planetary Science*, **46**, 903-918
- Nathues, A., Hoffmann, M., Cloutis, E.A., Schäfer, M., Reddy, V., Christensen, U., Sierks, H., Thangjam, G.S., Le Corre, L., Megel, K., Vincent, J.-B., Russell, C.T., Prettyman, T., Schmedemann, N., Kneissl, T., Raymond, C., Gutierrez-Marques, P., Hall, I., Büttner, I. (2014), Detection of serpentine in exogenic carbonaceous chondrite material on Vesta from Dawn FC data, *Icarus*, **239**, 222-237
- Nehru, C.E., Prinz, M., Delaney, J.S. (1983), Brachina: a new type of meteorite, not a Chassignite, *Journal of Geophysical Research*, **88**, B237-B244
- Nesvorný, D., Roig, F., Gladman, B., Lazzaro, D., Carruba, V., Mothé-Diniz, T. (2008), Fugitives from the Vesta family, *Icarus*, **193**, 85-95

- Palme, H., Schultz, L., Spettel, B., Weber, H.W., Wäke, H. (1981), The Acapulco meteorite: chemistry, mineralogy and irradiation effects, *Geochimica et Cosmochimica Acta*, **45**, 727-752
- Palomba, E., Longobardo, A. De Sanctis, M.C., Zinzi, A., Ammannito, E., Marachi, S., Tosi, F., Zambon, F., Capria, M.T., Russell, C.T., Raymond, C.A., Cloutis, E.A. (2015), Detection of new olivine-rich locations on Vesta, *Icarus*, **258**, 120-134
- Palomba, E., Longobardo, A., De Sanctis, M.C., Zambon, F., Tosi, F., Ammannito, E., Capaccioni, F., Frigeri, A., Capria, M.T., Cloutis, E.A., Jaumann, R., Combe, J.-P., Raymond, C.A., Russell, C.T. (2014), Composition and mineralogy of dark material units on Vesta, *Icarus*, **240**, 58-72
- Powell, R., Holland, T. (1988), An internally consistent dataset with uncertainties and correlations: 3. Applications to geobarometry, worked examples and a computer program. *Journal of Metamorphic Geology*, **6**, 173-204
- Przylibski, T.A., Zagożdżon, P.P., Kryza, R., Pilski, A.S. (2005), The Zakłodzie enstatite meteorite: mineralogy, petrology, origin and classification, *Meteoritics & Planetary Science*, **40**, A185-A200
- Reddy, V., Le Corre, L., O'Brien, D.P. Nathues, A., Cloutis, E.A., Durda, D.D., Bottke, W.F., Bhatt, M.U., Nesvorný, D., Buczkowski, D., Scully, J.E.C., Palmer, E.M., Sierks, H., Mann, P.J., Becker, K.J., Beck, A.W., Mittlefehldt, D., Li, J.-Y., Gaskell, R., Russell, C.T., Gaffey, M.J., McSween, H.Y., McCord, T.B., Combe, J.-P., Blewett, D. (2012), Delivery of dark material to Vesta via carbonaceous chondritic impacts, *Icarus*, **221**, 544-559
- Righter, K., Drake, M.J. (1997), A magma ocean on Vesta: core formation and petrogenesis of eucrites and diogenites, *Meteoritics & Planetary Science*, **32**, 929-944

- Ruesch, O., Hiesinger, H., Blewett, D.T., Williams, D.A., Buczkowski, D., Scully, J., Yingst, R.A., Roatsch, F., Jaumann, R., Russell, C.T., Raymond, C.A. (2014), Geologic map of the northern hemisphere of Vesta based on Dawn Framing Camera (FC) images, *Icarus*, **244**, 41-59
- Russell, C.T., Raymond, C.A., Coradini, A., McSween, H.Y., Zuber, M.T., Nathues, A., De Sanctis, M.C., Jaumann, R., Konopliv, A.S., Preusker, F., Asmar, S.W., Park, R.S., Toplis, M.J., Christensen, U.R., Feldman, W.C., Lawrence, D.J., McCoy, T.J., Prettyman, T.H., Reedy, R.C., Sykes, M.E., Titus, T.N. (2012), Dawn at Vesta: testing the protoplanetary paradigm, *Science*, **336**, 684-686
- Ruzicka, A., Snyder, G.A., Taylor, L.A. (1997), Vesta as the howardite, eucrite and diogenite parent body: implications for the size of a core and for large-scale differentiation, *Meteoritics & Planetary Science*, **32**, 825-840
- Sack, R.O., Azeredo, W.J., Lipschutz, M.E. (1991), Olivine diogenites: the mantle of the eucrite parent body, *Geochimica et Cosmochimica Acta*, **55**, 1111-1120
- Sarafian, A.R., Roden, M.F., Patinño-Douce, A.E. (2013), The volatile content of Vesta: clues from apatite in eucrites, *Meteoritics & Planetary Science*, **48**, 2135-2154
- Schäfer, M., Nathues, A., Williams, D.A., Mittlefehldt, D.W., Le Corre, L., Buczkowski, D.L., Kneissl, T., Thangjam, G.S., Hoffmann, M., Smedemann, N., Schäfer, T., Scully, J.E.C., Li, J.-Y., Reddy, V., Garry, W.B., Krohn, K., Yingst, R.A., Gaskell, R.W., Russell, C.T. (2014), Imprint of the Rheasilvia impact on Vesta – geologic mapping of quadrangles Gegania and Lucaria, *Icarus*, **244**, 60-73
- Schenk, P., O'Brien, D.P., Marchi, S., Gaskell, R., Preusker, F., Roatsch, T., Jaumann, R., Buczkowski, D., McCord, T.B., McSween, H.Y., Williams, D., Yingst, A., Raymond,

- C.A., Russell, C.T. (2012), The geologically recent giant impact basins at Vesta's south pole, *Science*, **336**, 694-697
- Schrader, D.L., McCoy, T.J., Gardner-Vandy, K. (2017), Relict chondrules in primitive achondrites: remnants from their precursor bodies, *Geochimica et Cosmochimica Acta*, **205**, 295-312
- Schulz, T., Münker, C., Mezger, K., Palme, H. (2010), Hf-W chronometry of primitive achondrites, *Geochimica et Cosmochimica Acta*, **74**, 1706-1718
- Stolper, E. (1977), Experimental petrology of eucritic meteorites, *Geochimica et Cosmochimica Acta*, **41**, 587-911
- Takeda, H. (1997), Mineralogical records of early planetary processes on the howardite, eucrite, diogenite parent body with reference to Vesta, *Meteoritics & Planetary Science*, **32**, 841-853
- Takeda, H., Graham, A.L. (1991), Degree of equilibration of eucritic pyroxenes and thermal metamorphism of the earliest planetary crust, *Meteoritics*, **26**, 129-134
- Takeda, H., Huston, T.J., Lipschutz, M.E. (1984), On the chondrite-achondrite transition: mineralogy and chemistry of Yamato 74160 (LL7), *Earth and Planetary Science Letters*, **71**, 329-339
- Takir, D., Emery, J.P., McSween, H.Y., Hibbitts, C.A., Clark, R.N., Pearson, N., Wang, A. (2013), Nature and degree of aqueous alteration in CM and CI carbonaceous chondrites, *Meteoritics & Planetary Science*, **48**, 1618-1637
- Thangjam, G., Nathues, A., Mengel, K., Hoffmann, M., Schäfer, M., Reddy, V., Cloutis, E.A., Christensen, U., Sierks, H., Le Corre, L., Vincent, J.-B., Russell, C.T. (2014), Olivine-

- rich exposures at Bellicia and Arruntia craters on (4) Vesta from Dawn FC, *Meteoritics & Planetary Science*, **49**, 1831-1850
- Thomas, P.C., Binzel, R.P., Gaffey, M.J., Storrs, A.D., Wells, E.N., Zellnert, B.H. (1997), Impact excavation on asteroid 4 Vesta: Hubble Space Telescope results, *Science*, **277**, 1492-1494
- Tkalcec, B.J., Golabek, G.J., Brenker, F.E. (2013), Solid-state plastic deformation in the dynamic interior of a differentiated asteroid, *Nature Geoscience*, **6**, 93-97
- Tomkins, A.G., Johnson, T.E., Mitchell, J.T. (2020), A review of the chondrite-achondrite transition, and a metamorphic facies series of equilibrated primitive stony meteorites, *Meteoritics & Planetary Science*, **54**, 1462-1477
- Turrini, D., Combe, J.-P., McCord, T.B., Ockay, N., Vincent, J.-B., Prettyman, T.H. McSeen, H.Y., Consolmagno, G.J., De Sanctis, M.C., Le Corre, L., Longobardo, A., Palomba, E., Russell, C.T. (2014), The contamination of the surface of Vesta by impacts and the delivery of the dark material, *Icarus*, **240**, 86-102
- Warren, P.H., Jerde, E.A. (1987), Composition and origin of Nuevo Laredo trend eucrites, *Geochimica et Cosmochimica Acta*, **51**, 713-725
- Wilkening, L.L. (1973), Foreign inclusions in stony meteorites – I. carbonaceous chondritic xenoliths in the Kapoeta howardite, *Geochimica et Cosmochimica Acta*, **37**, 1985-1989
- Williams, D.A., Jaumann, R., McSween, H.Y., Marchi, S., Schmedemann, N., Raymond, C.A., Russell, C.T. (2014), The chronostratigraphy of protoplanet Vesta, *Icarus*, **244**, 158-165
- Yamaguchi, A., Barrat, J.-A., Greenwood, R.C., Shirai, N., Okamoto, C., Setoyanagi, T., Ebihara, M., Franchi, I.A., Bohn, M. (2009), Crustal partial melting on Vesta: evidence

from highly metamorphosed eucrites, *Geochimica et Cosmochimica Acta*, **73**, 7162-7182

Yamaguchi, A., Barrat, J.-A., Ito, M., Bohn, M. (2011), Posteuclitic magmatism on Vesta: evidence from the petrology and thermal history of diogenites, *Journal of Geophysical Research*, **116**, E08009

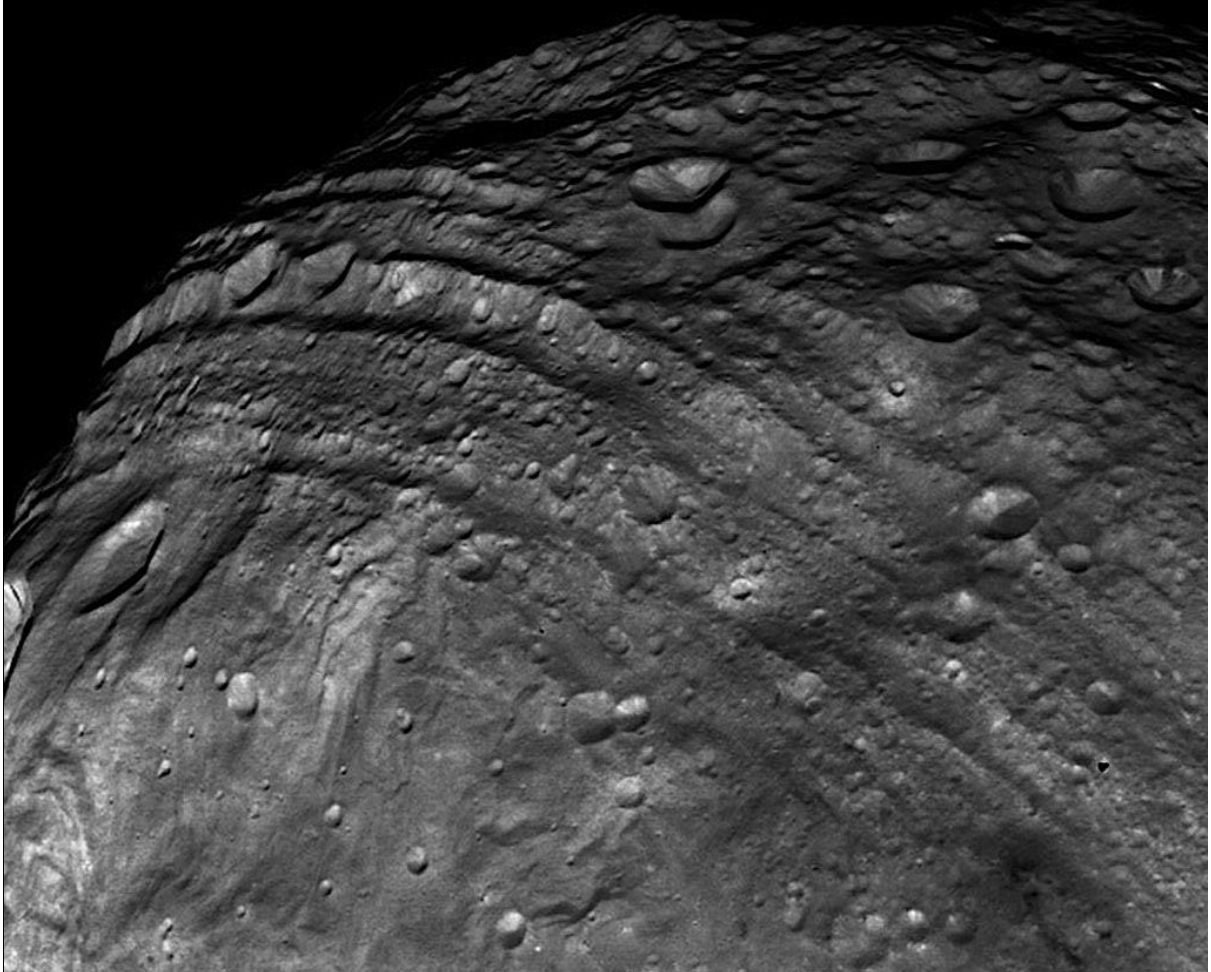
Yamaguchi, A., Taylor, G.J., Keil, K. (1996), Global crustal metamorphism of the eucrite parent body, *Icarus*, **124**, 97-112

Yamaguchi, A., Taylor, G.J., Keil, K. (1997), Shock and thermal history of equilibrated eucrites from Antarctica, *Antarctic Meteorite Research*, **10**, 415-436

Zhang, A.-C., Wang, R.-C., Hsu, W.-B., Bartoschewitz, R. (2013), Record of S-rich vapors on asteroid 4 Vesta: sulfurization in the Northwest Africa 2339 eucrite, *Geochimica et Cosmochimica Acta*, **109**, 1-13

"When you look at the stars and the galaxy, you feel that you are not just from any particular piece of land, but from the Solar System."

Kalpana Chawla



Chapter 2

On the Source of Diogenites and Olivine Diogenites: Compositional Diversity from Variable fO_2 [†]

Jennifer T. Mitchell¹ & Andrew G. Tomkins¹

¹School of Earth, Atmosphere and Environment, Monash University, Australia

[†]Published: Mitchell, J.T., Tomkins, A.G. (2019), On the source of diogenites and olivine diogenites: compositional diversity from variable fO_2 , *Geochimica et Cosmochimica Acta*,

258, 37-49

ABSTRACT

The genesis of diogenites and olivine-bearing diogenites has been debated for decades, with current models favouring formation via either mineral settling in a homogeneous magma ocean, or as late stage intrusions into the crust of asteroid 4 Vesta. Using pMELTS, both equilibrium and fractional crystallisation modelling was conducted on a large range of melt compositions generated by varied extent of batch melt extraction from 11 bulk Vesta starting compositions at a range of fO_2 conditions to simulate the magma ocean concept. The resulting mineral compositions were compared with those of 200 diogenite meteorites in an attempt to resolve this debate. Models that involve < 20% initial partial melt cannot produce orthopyroxenites. Orthopyroxenitic diogenites have compositional ranges from En₅₃-En₈₂, whereas ‘olivine diogenites’ show less compositional diversity with orthopyroxenes ranging from En₇₁-En₇₆. Olivine-bearing diogenites are therefore not the most magnesian samples, which contradicts expected crystallisation trends expected from a single homogeneous source. The orthopyroxene compositions produced by models that use fO_2 previously suggested for Vesta of ΔIW -2.05 are too magnesian, and the extent of source partial melting used in the models has negligible effect on this result. Modelling using different initial oxygen fugacity conditions produces a large range of pyroxene compositions that better match the range seen in diogenites, with models ranging from ΔIW fO_2 -1.6 to -1.2 producing the best fit. These results thus imply that the diogenites crystallised from a variety of magmas sourced from a region of heterogeneous oxygen fugacity. This variation can be explained by metasomatism of a homogenous source region by fO_2 -modifying sulfidation reactions. The model orthopyroxene compositions are displaced with regards to Wo from natural diogenites; this can be explained by a delayed genesis model whereby a Ca-poor diogenite source developed in response to the melt extraction necessary for formation of a eucritic crust. Our models suggest that diogenites were derived from a series of magma chambers in the Vestan crust.

2.1. INTRODUCTION

The howardite-eucrite-diogenite (HED) clan of meteorites is a series of ultramafic to mafic rocks ranging from coarse-grained cumulates to surface lavas and impact-associated breccias. Groundbased spectral data have been used to suggest that the HEDs were derived from the differentiated asteroid 4 Vesta (McCord et al., 1970). This link was validated by NASA's Dawn mission, which orbited Vesta from 2011 to 2012, revealing large regions dominated by eucrite and howardite-like material, with smaller outcroppings of diogenite and exogenic material (Ammanito et al., 2013a; Rayman & Mase, 2014; McCord & Scully, 2015).

Diogenites are predominately orthopyroxenites, with less common samples also containing olivine. The term "olivine diogenites" has been variably used to refer to orthopyroxenites with a range of olivine contents. The various suggestions include olivine contents: (1) greater than an accessory phase (Sack et al., 1991) or of 1-5% (Shearer et al., 2010), (2) > 10% (Mandler & Elkins-Tanton, 2013), or (3) >40% (McSween et al., 2013). Beck & McSween (2010) presented a revised taxonomy in which diogenites are given the terrestrial prefixes orthopyroxenitic, harzburgitic, and dunitic to distinguish between samples with > 90% orthopyroxene, between 40 and 90% olivine, and > 90% olivine respectively. This scheme is, perhaps, the most useful as it highlights the natural variation in composition and facilitates comparison with terrestrial petrological and geochemical principles. However, it does not include the term "olivine orthopyroxenite", as is used in terrestrial samples, referring to an orthopyroxene dominated rock with 10-40% olivine. As such, diogenites in this paper will be referred to using updated terrestrial prefixes; dunitic (> 90% olivine), harzburgitic (40-90% olivine), olivine orthopyroxenitic (10-40% olivine), and orthopyroxenitic (<10% olivine).

There are two main schools of thought regarding diogenite genesis. Firstly, it has been proposed that they formed as a result of mineral settling from a global magma ocean (Righter

& Drake, 1997; Ruzicka et al., 1997; Takeda, 1997; Warren, 1997; Kawabata & Nagahara, 2017) based largely on isotopic and geochemical evidence. Magma oceans are a generally accepted stage of planetary evolution and can account for the ancient ages of some of these igneous meteorites (Righter & Drake, 1997; Schiller et al., 2017). It is thought that the short-lived decay of ^{26}Al (half-life of $\sim 717,000$ years; Thomas et al., 1984) in particular was responsible for heating early planetesimals to achieve widespread partial melting required to generate a magma ocean, which also led to the homogenisation of oxygen isotopes that is a characteristic feature of the HED meteorites (Greenwood et al., 2005, 2014).

Alternatively, diogenites have been argued to have formed in magma chambers within the Vestan crust through fractional crystallisation (Grove & Bartels, 1992; Domanik et al., 2004; Shearer et al., 2010; Mandler & Elkins-Tanton, 2013; Clenet et al., 2014; Yamaguchi et al., 2015). A number of authors – including Mittlefehdt (1994), Fowler et al. (1995), Barrat (2004) and Barrat et al. (2008) – have proposed that diverse magma compositions could account for the chemical variations observed in the meteorite collection. Similarly, Yamaguchi et al. (2011), Jutzi et al. (2013), and Clenet et al. (2014) added to the crustal intrusion model by proposing that the crust was thickened by diogenite plutons, and that the diversity of lithologies in howardites may reflect this, as well as the lack of mantle exposure on Vesta itself.

The distinction between the magma ocean model and intracrustal magma chambers model is important as it has implications for both the behaviour of magmatism on small bodies in the early solar system and the structure of Vesta. For example, Clenet et al., (2014) presented models of Vesta's interior structure that vary greatly depending on the style of magmatism. A magma ocean produces a thin eucritic crust overlaying a layer of pyroxene-rich cumulates, with an olivine-rich mantle beneath. In contrast, intracrustal diogenitic magma chambers significantly thicken the crust and perhaps more than double the depth of the crust-mantle boundary. As such, a thicker crust may explain the lack of a clear mantle exposure on the

asteroid. It is therefore prudent to consider whether or not an early magma ocean is necessary to explain all the observations of Vesta and the HED meteorites.

Here, we investigate the plausible mechanisms that could produce the observed compositional trends in diogenites using the thermodynamic software pMELTS (Ghiorso & Sack, 1995) to model crystallisation paths over a range of conditions and variables. Ashcroft & Wood (2015) used both MELTS and experimental modelling to investigate magma crystallisation on Vesta, and determined that the software is largely accurate. Their study produced both eucrites and diogenites through sequential partial melting from a mantle of Mg# ~70 at fO_2 ΔIW +1.8. However, Righter & Drake (1997) suggested that the oxidation state on Vesta is below the IW buffer, and such values have been used in a number of other studies; fO_2 at ΔIW -4 (Pringle et al., 2013), fO_2 at ΔIW -2.5 (Peslier et al., 2015), fO_2 at ΔIW -2.05 (Steenstra et al., 2016), fO_2 = IW (Toplis et al., 2013). Hoff et al., (2014) used an oxygen fugacity at the IW buffer to produce a magma ocean model that aimed to relate eucrites and diogenites. However, the experimental modelling did not produce the expected results, and they were unable to draw clear conclusions regarding the relationship between the two groups of meteorites. This study therefore focuses on the effects of variable oxygen fugacity on producing the range of orthopyroxene compositions observed in the global meteorite collection of diogenites and the implications this has for understanding the relationship between the dunitic, harzburgitic, olivine-orthopyroxenitic and orthopyroxenitic diogenites.

2.2. METHODS

Paired ortho- and clinopyroxene compositions for 200 diogenites (including 11 olivine diogenites as officially classified) were collected from the Meteoritical Bulletin Database and plotted on the pyroxene quadrilateral diagram to investigate compositional trends. Although errors may be contained within the data reported by the Meteoritical Bulletin, it does provide

access to a large number of samples that do not appear in literature; clearly incorrect values were not included in this study. Use of this large dataset also helps to minimise the impact that brecciation has in disguising the primary igneous mineralogy of diogenites. When needed, the EnFsWo composition of the pyroxenes were calculated from elemental abundances provided. These compositions were then compared with the data generated through the pMELTS calculations.

Modelling of batch melt extraction and subsequent fractional crystallisation was carried out using pMELTS v5.6.1 software (Ghiorso et al., 2002; melt compositions produced by the software verified for accuracy by Ashcroft & Wood 2015), using starting bulk compositions from literature as summarised in Table 1, an initial oxygen fugacity of $\Delta IW = -2.05$ (Steenstra et al., 2016), and pressure of 86.59 MPa, corresponding to 100 km in depth. These models effectively simulate a range of magma ocean scenarios and a resulting onion-skin model of Vesta.

Fractional crystallisation was modelled for each of the 11 starting composition in Table 2.1, divided into a range of batch extraction models reflecting 50 %, 40 %, 30 %, and 20 % initial partial melting. These 44 models involved a range of initial temperatures (as required to reach the desired extent of partial melting) and cooling in 20 °C steps until the melt crystallised clinopyroxene, which is not observed in diogenites as a major component. In later additional models, the degree of initial partial melt was kept constant (40 ± 0.1 % liquid) and, for each of the 11 starting compositions, the effects of varying oxygen fugacity were varied from $\Delta IW - 2.50$ to -1.00 in steps of -2.50 , -2.05 (see Steenstra et al., 2016), -1.8 , -1.6 , -1.4 , -1.2 and -1.0 .

Table 2.1. Bulk compositions used in this study (wt%).

		Righter & Drake (1997)				Ruzicka et al., (1997)				Dreibus & Wänke (1980)	Boesenberg & Delaney (1997)
		RD CV-H	RD CV-L	RD CM-H	RD CM-L	R HED-CI	R HED-CM	R HED-L	R HED-EH		
SiO₂	42.59	40.3	46.1	43.5	49.4	45.34	45.74	46.96	49.06	46.2	44.64
TiO₂	0.1	0.13	0.15	0.13	0.15	0.18	0.18	0.21	0.26	0.16	0.16
Al₂O₃	2.7	2.75	3.12	2.89	3.25	3.29	3.25	3.71	4.63	3.27	2.81
Cr₂O₃		0.61	0.67	0.66	0.73	0.85	0.88	0.92	0.98	0.87	0.67
FeO	24.42	27.4	18.21	21.73	12.2	14.34	14.48	15.11	16.25	14.8	19.1
MnO		0.36	0.38	0.37	0.39	0.4	0.41	0.44	0.49	0.42	0.35
MgO	27.92	26.6	29.31	28.8	31.72	32.67	32.16	29.3	24.15	31.5	29.06
CaO	2.2	2.24	2.49	2.34	2.59	2.78	2.76	3.17	3.97	2.57	2.31
Na₂O	0.07	1.01	1.06	1.03	1.07	0.12	0.12	0.14	0.17	0.11	0.84
K₂O		0.11	0.11	0.11	0.11	0.01	0.01	0.01	0.01	0.0092	
P₂O₅						0.02	0.02	0.03	0.04		
Mg#	67	63	74	70	82	80	79	76	72	79	73

2.3. RESULTS

The pyroxene compositions of diogenites reveal two key patterns. Firstly, orthopyroxenes in diogenites have a wide range of compositions from ~En85 to En60 (Wo0-6), with some rare exceptions (Fig.2.1). This entire range is not found in any one diogenite, and individual non-brecciated meteorites have narrow ranges of orthopyroxene compositions of typically a few percent enstatite. Secondly, dunitic to olivine-orthopyroxenitic diogenites have orthopyroxene compositions that plot within the main cluster, in the range En71.1 to En76.6; several orthopyroxenitic diogenites with $\Delta^{17}\text{O}$ consistent with other diogenites (Lunning et al., 2015) have more enstatitic orthopyroxene compositions. Diogenite compositions in any given sample are typically reported as being homogeneous (although this could plausibly be due to their large crystal size and small sample surface in which to study). As a result, collating a large number of diogenite compositions helps to provide a more realistic picture of the compositional range within the class.

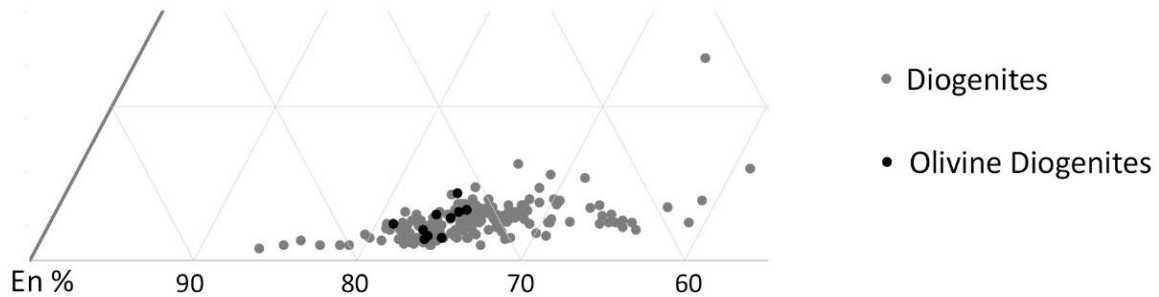


Figure 2.1. Pyroxene compositions of diogenites from the Meteoritical Bulletin. The term “olivine diogenite” is used here as this is how samples are classified in the Meteoritical Bulletin. A full list of diogenite pyroxene compositions is compiled in the appendix (Table A1).

2.3.1. Variable Degrees of Initial Partial Melting

Models of variation in mineral modal abundance of each starting composition tend to show very similar patterns despite changing the degree of initial partial melting. The change from olivine-only crystallisation (which would form cumulate dunites) to orthopyroxene-only (i.e., cumulate orthopyroxenites) is abrupt, occurring over a range of approximately 20 °C. All models, save for R HED-EH, crystallise dunitic compositions before moving into orthopyroxenites at between 50-30 % initial partial melt (Fig. 2.2). The R HED-EH starting composition produces a harzburgite primarily under these conditions, followed by an orthopyroxenite. As the degree of initial partial melt decreases, so too does the initial temperature, so the extent of olivine crystallisation becomes increasingly limited for all starting compositions at lower degrees of initial partial melt. This is particularly apparent at 20 % initial partial melt, where the Toplis, Ruzicka HED-CI, HED-CM, Driebus & Wänke, and Boesenberg & Delaney compositions produce harzburgitic diogenites instead of dunitic diogenites during the first stages of crystallisation. In contrast, all Righter & Drake starting compositions do not crystallise orthopyroxenites at 20% initial partial melt, nor does the Ruzicka HED-EH composition. The degree of initial partial melt has very little effect on the compositions of orthopyroxenes produced during crystallisation across all starting compositions, with only

minor variations in Mg# (Table 2.2) and enstatite-ferrosilite-wollastonite components (Fig. 2.3).

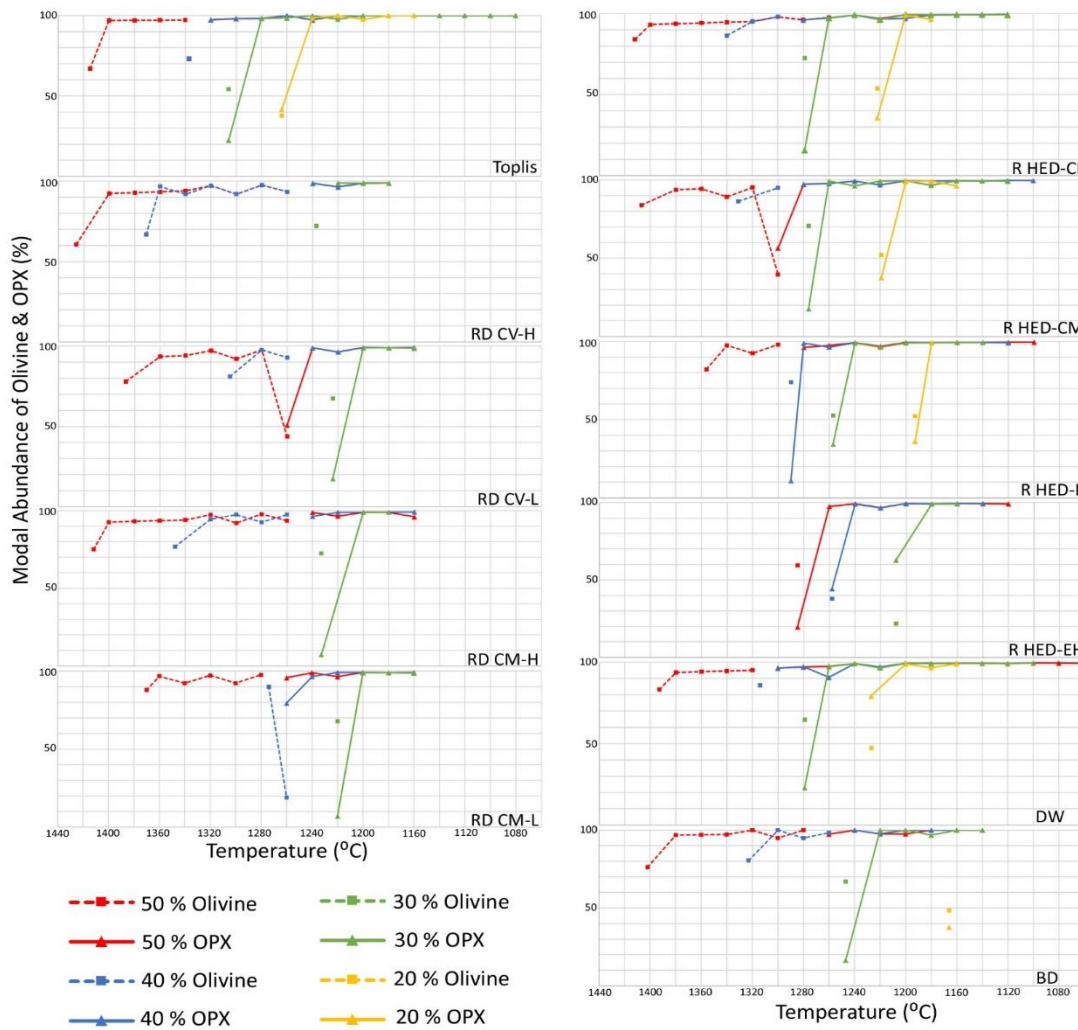


Figure 2.2. Modal abundance of olivine and orthopyroxene for each starting composition as generated by pMELTS modelling, over a range of initial partial melt percentages (e.g., in the legend, the contour for 50% Olivine indicates the change in olivine mode as a function of temperature in the model for batch extraction from 50% initial melting). pMELTS models include an additional alloy phase that is crystallising concurrently, which is not shown on these graphs.

Table 2.2. Mg# ranges in orthopyroxene generated by each starting composition at varying degrees of initial partial melt

% Melt	Toplis et al., 2013	Righter & Drake (1997)				Ruzicka et al., (1997)				Dreibus & Wänke (1980)	Boesenberg & Delaney (1997)
		RD CV-H	RD CV-L	RD CM-H	RD CM-L	R HED-CI	R HED-CM	R HED-L	R HED-EH		
50%	88-74	86-83	87-81	85-82	87-81	87-78	87-76	86-76	87-78	87-74	86-80
40%	88-74	86-82	86-82	86-82	86-81	87-78	87-79	87-79	86-80	87-76	86-80
30%	88-75	85-83	86-82	86-83	86-83	87-79	87-79	86-80	85-82	87-77	86-81
20%	87-81					76-84	86-83	85-84		86-83	85

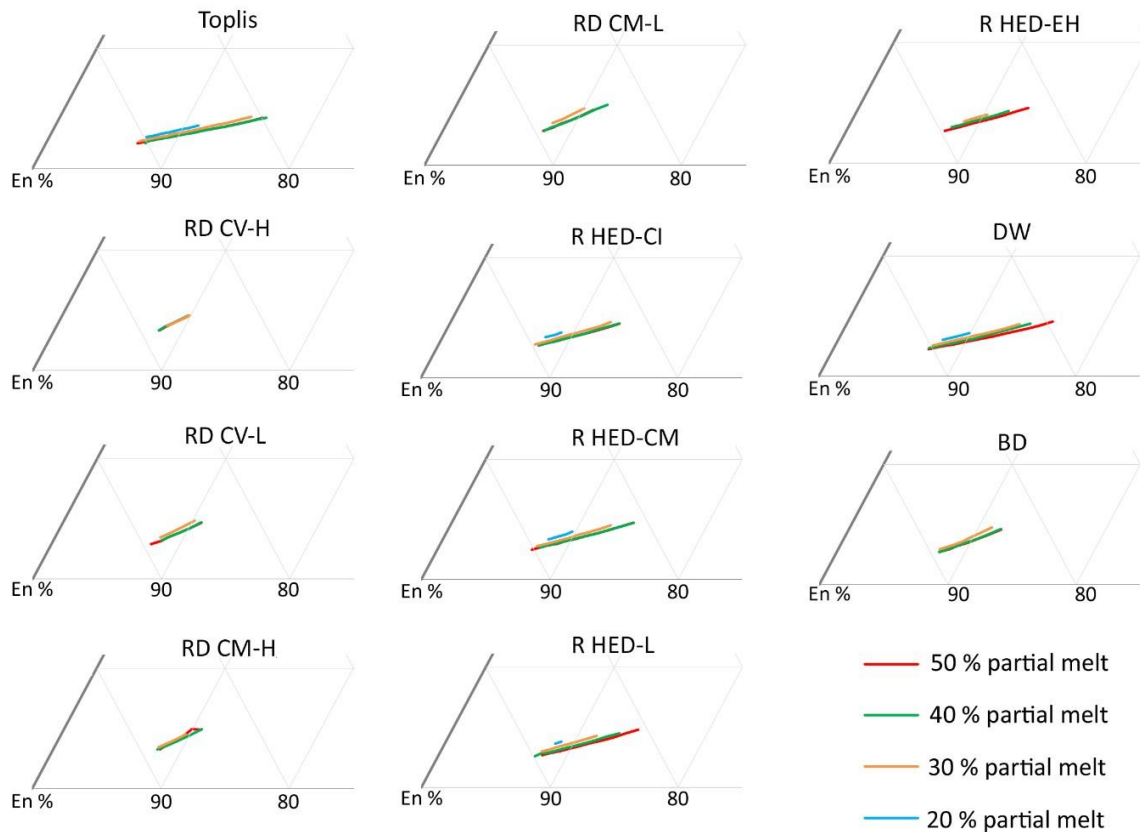


Figure 2.3. The range in orthopyroxene compositions produced by each starting composition as a function of varying degrees of initial partial melting. Compositions are compiled in the appendix, Table A2.

As such, variable degrees of 159 initial partial melt have been discounted as a viable mechanism to explain the range of diogenite 160 pyroxene compositions.

2.3.2. Effects of Variable Oxygen Fugacity

In initial modelling it was noted that changes in pressure, and therefore depth, have minimal effect on the melt compositions and mineral/melt abundances generated. Similarly, the degree of partial melt has negligible effect on pyroxene compositions. In the subsequent models investigating the effects of changing oxygen fugacity (ΔIW -2.5 to -1.0 applied to the 40% partial melt models) the modal abundances of olivine and orthopyroxene once again show that the transition from dunitic to orthopyroxenitic is rapid, and that orthopyroxene is the dominant crystallising phase in most models (Fig. 4). The Righter & Drake CV-H, CV-L and CM-H

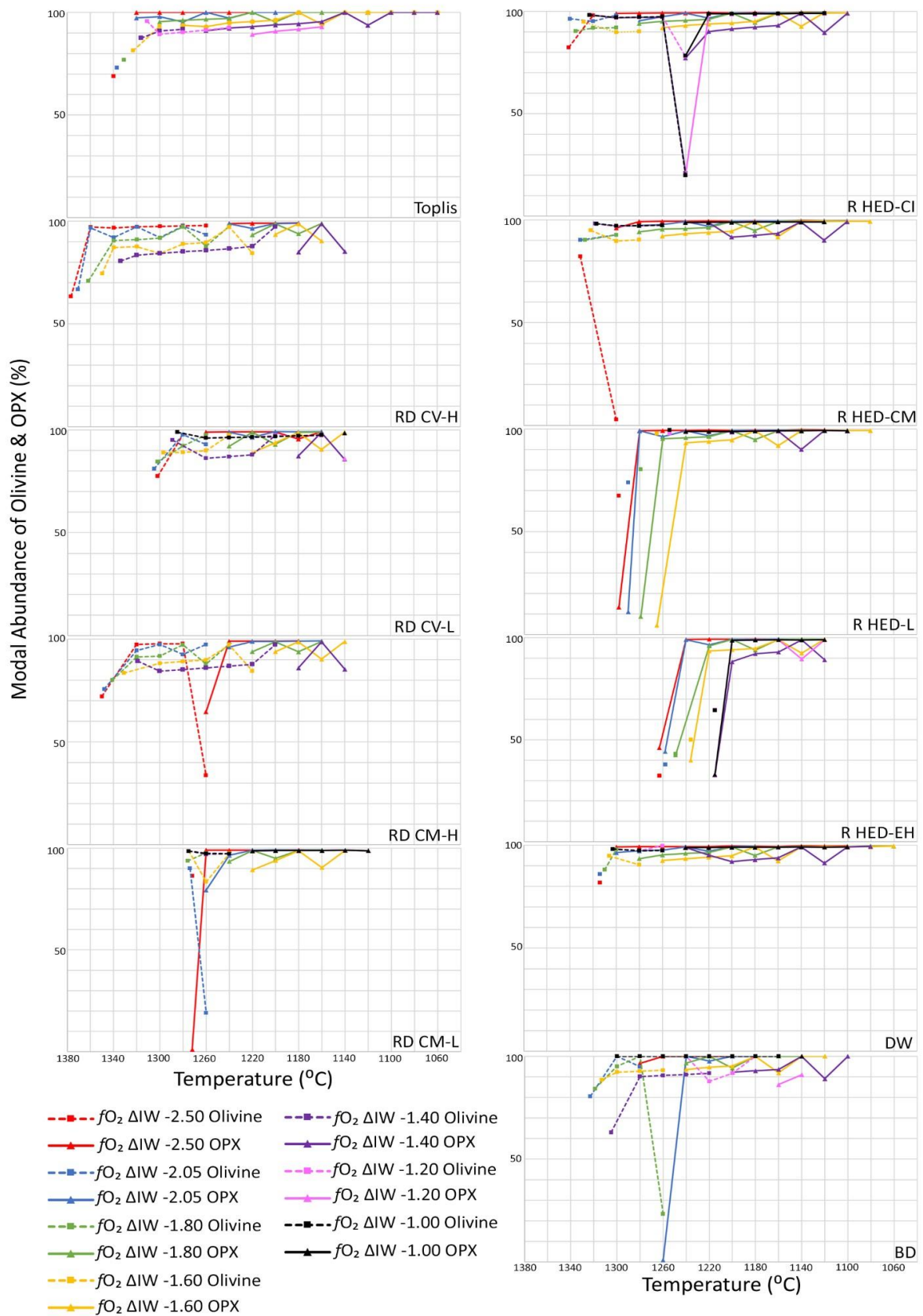


Figure 2.4. Modal abundances of olivine and orthopyroxene for each starting composition under different fO_2 conditions. pMELTS models include an additional alloy phase that is crystallising concurrently, which is not shown on these graphs.

crystallise olivine over a notably wider range of temperatures than the other starting compositions, suggesting that these are not the best match for a diogenite starting composition, given the rarity of olivine diogenites.

The results of this second phase of modelling reveal that orthopyroxene compositions become less magnesian as fO_2 nears the IW buffer (Table 2.3; Fig. 2.4). We find that for all starting compositions fO_2 values of ΔIW -2.05 and lower are too reduced to produce the observed diogenite orthopyroxene compositions, whereas fO_2 values of ΔIW -1.8 and upwards fit the observed compositional range of orthopyroxenes in the most magnesian diogenites well.

Table 2.3. Mg# ranges for pyroxenes generated for each starting composition at various fO_2 ΔIW conditions at $40 \pm 0.1\%$ partial melt.

fO_2 ΔIW	Toplis et al., 2013	Righter & Drake (1997)				Ruzicka et al., (1997)				Dreibus & Wänke (1980)	Boesenberg & Delaney (1997)
		RD CV- H	RD CV-L	RD CM- H	RD CM- L	R HED -CI	R HED -CM	R HED -L	R HED -EH		
-2.50	93-88	92-91	92-90	92-91	92-90	92-89	92-88	92-89	82-89	92-88	92-91
-2.05	88-74	86-82	86-82	86-82	86-81	87-78	86-76	87-78	86-80	87-76	86-80
-1.80	83-63	81-76	81-76	80-76	81-74	77-63	82-69	82-69	81-72	82-65	82-71
-1.60	77-55	75-72	76-69	74-69	76-69	70-56	77-60	77-59	76-66	77-56	77-66
-1.40	71-46	68-64	66-63	68-64	74-61	70-53	70-55	72-54	68-59	71-51	68-57
-1.20	61-53		56		74-61	70-53	70-55	72-53	68-55	70-50	57-55
-1.00			55		87-61	70-53	70-55	72-53	68-54	70-50	52

However, the Righter & Drake CV-H and CM-H compositions fail to produce orthopyroxene at fO_2 $\Delta IW > -1.2$, and the Toplis composition fails at $fO_2 > \Delta IW -1.0$. Similarly, the Righter & Drake CV-L and Boesenberg & Delaney compositions only crystallise orthopyroxene over a narrow temperature interval at these conditions. Changing fO_2 conditions also effects the temperature required to reach a given degree of partial melting by up to approximately 77 °C (Table 2.4).

Table 2.4. Temperatures (°C) required to reach 40 ±0.1 % partial melt, to the nearest whole degree.

fO_2 ΔIW	Toplis et al., 2013	Righter & Drake (1997)				Ruzicka et al., (1997)				Dreibus & Wänke (1980)	Boesenberg & Delaney (1997)
		RD CV- H	RD CV- L	RD CM- H	RD CM- L	R HED -CI	R HED -CM	R HED -L	R HED -EH		
-2.50	1340	1377	1302	1350	1272	1341	1331	1298	1263	1314	1323
-2.05	1337	1371	1305	1348	1274	1340	1331	1290	1258	1314	1323
-1.80	1331	1362	1302	1341	1276	1335	1327	1279	1249	1310	1319
-1.60	1323	1350	1297	1331	1275	1328	1322	1265	1236	1306	1313
-1.40	1316	1334	1289	1319	1275	1323	1318	1254	1215	1303	1305
-1.20	1311	1317	1285	1305	1275	1323	1317	1254	1215	1303	1300
-1.00	1310	1300	1285	1302	1275	1323	1317	1254	1215	1303	1300
ΔT	30	77	17	48	3	18	14	44	48	11	23

As can be seen in Figure 2.5, the orthopyroxene compositions produced by the fO_2 -focused models are typically higher in Ca/wollastonite content than the diogenites of the global meteorite collection. This may be because the models use starting compositions for bulk Vesta assuming that there has been no removal of a eucritic crust, which is a requirement of the magma ocean model. Eucrites contain a large volume of clinopyroxene and plagioclase, both of which are rich in calcium, so subtraction of voluminous eucrite from bulk Vesta significantly modifies the Ca abundance in the residue (implications discussed below). It is not the purpose of this study to determine the exact starting compositions for diogenites for anything other than a magma ocean scenario, but to establish the effects of variable oxygen fugacity on the compositions produced. As such, it is the relative enstatite/ferrosilite content of the orthopyroxenes that is of import.

The models of fractional crystallisation from batch melt extraction generate dunites and orthopyroxenites over large temperature ranges, implying that these would be abundant products of Vestan magmas, provided that the temperatures were sufficient to generate dunites. Apparently less common would be harzburgites and olivine orthopyroxenites, the latter of which form in a narrow temperature window of typically only 10-20 °C. Orthopyroxene is the

most dominant mineral in the fractional crystallisation models, particularly those involving lower degrees of partial melting, which is also true of the global diogenite collection.

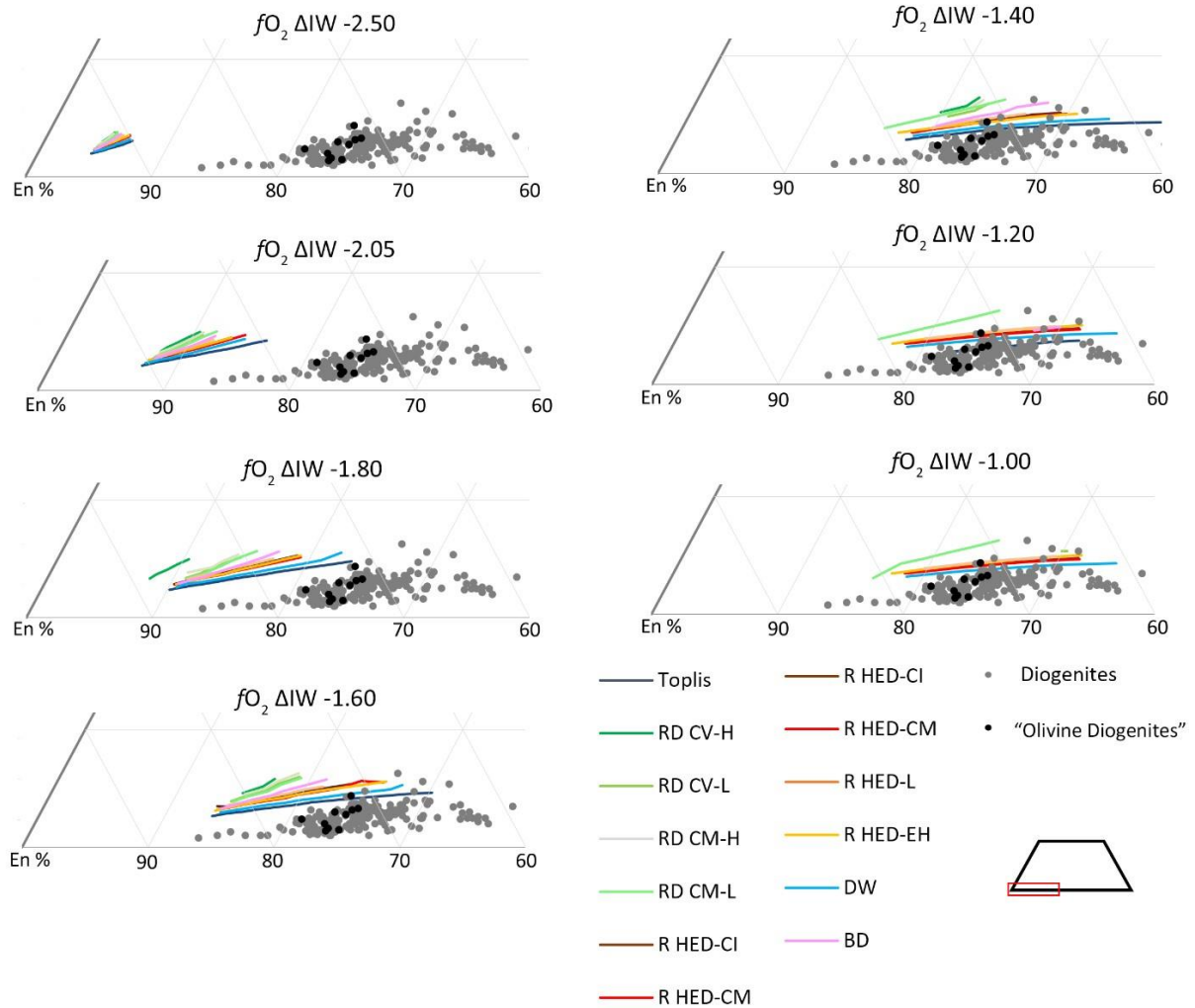


Figure 2.5. Pyroxene compositions produced by each starting composition under various $fO_2 \Delta IW$ conditions with 40 ± 0.1 % initial starting melt. Compositions are compiled in the appendix, Table A3.

2.4. DISCUSSION

2.4.1. Comparison with Oxygen Isotope Data

As well as ascribing HED meteorites to Vesta, oxygen isotope homogeneity is often called upon to support a magma ocean model, as all diogenites and eucrites (excluding a few rare cases) display the same restricted range of oxygen isotopes (Wiechert et al., 2004; Greenwood et al., 2014). This concept is consistent with the significantly wider range in $\Delta^{17}O$ seen in

primitive achondrites and equilibrated chondritic materials (Greenwood et al., 2017), which likely came from bodies that did not form magma oceans. However, Barrat et al. (2010) and Yamaguchi et al. (2011) showed that the trace element geochemistry of diogenites suggest that they formed after formation of at least some eucritic crust. This result implies that Vesta and the diogenite source region(s) were already homogenised with regards to oxygen isotopes at the time of diogenite emplacement (Greenwood et al., 2014). If so, the oxygen isotope data suggest that a magma ocean stage predated diogenite formation, and thus it is best to use geochemical and petrological evidence to explore diogenite genesis.

2.4.2. fO_2 Diversity During Diogenite Formation

Our pMELTS modelling showing that the range of diogenite orthopyroxene compositions requires an inhomogeneous source region is a modification of previous geochemical studies of diogenites, which suggested that a diverse range of melt compositions generated crustal cumulates (Mittlefehldt, 1994; Fowler et al., 1995; Barrat, 2004; Barrat et al., 2008; Shearer et al., 2010; Beck et al., 2011; Mittlefehldt et al., 2012). Instead of compositional diversity, we can explain the range of diogenite orthopyroxene compositions simply by varying fO_2 ; compositional diversity in the source region has less effect. Our models show that orthopyroxene should become progressively less magnesian progressing from dunitic to harzburgitic to olivine-orthopyroxenitic to orthopyroxenitic diogenites, but those in the global meteorite collection do not fit this trend. If dunitic to harzburgitic diogenites are mantle rocks, they should be more primitive than the orthopyroxenitic diogenites that are supposedly derived from them (Zuber et al., 2011). Instead, their orthopyroxene compositions plot within the main cluster. This result cannot be reproduced by fractional crystallisation of a magma derived from a globally homogenous source, no matter the degree of partial melting – inconsistent with the magma ocean model of diogenite formation.

The modelling has also shown that orthopyroxene compositions derived from a magma ocean are too Ca-rich compared to the global diogenite collection. This can be explained by the extraction of Ca-rich eucritic melt, possibly in a magma ocean scenario, prior to a later stage or stages of melting of the residue to produce the diogenites. This late stage model is supported by the distinct negative Eu anomalies of diogenites, which are consistent with extraction of the (Ca-rich) plagioclase (enriched in Eu) needed to form a eucritic crust (Barrat et al., 2010). Thus, the magma ocean-based onion-skin model of Vesta in which a eucrite crust sits above a diogenite layer and then an olivinerich mantle is not appropriate. Instead, our findings support the notion that diogenites formed in magma chambers, derived from a source heterogeneous in both bulk chemistry and fO_2 conditions.

Wilson & Keil (2012) showed that removal of silicate melt from zones of partial melting in asteroidal mantles is a very efficient process, meaning that magma oceans consisting of high degrees of partial melt amongst residual crystals are unlikely. Instead, melt is thought to be extracted progressively to form sills at the base of the lithosphere and magma chambers within the crust. This concept is supported by gravity data from NASA's Dawn mission to Vesta, which show discrete areas of high density that are thought to be diogenitic intrusions in the crust (Ermakov et al., 2014; Raymond et al., 2016). A potential example of this is Brumalia Tholus, observed by Dawn and interpreted to represent a dyke-fed diogenitic laccolith (Buckowski et al., 2014; De Sanctis et al., 2014).

On Earth, dunites and harzburgites typify the depleted mantle, where they are residues of melt extraction. They can also form through fractional crystallisation of ultramafic magmas within the crust. Although asteroidal gravity is significantly less than Earth's, experimental studies focused on understanding cumulate eucrites have shown that intercumulus liquid can be expelled from crystal mushes under lower gravity to produce cumulate rocks (Walker et al., 1998), much the same as in terrestrial intrusions (Tharp et al., 1988). Thus, it is possible to

generate dunitic cumulates in an asteroidal magma chamber, and the presence of olivine does not require a residual genesis within a mantle setting.

Although there is disagreement as to whether or not dunitic and harzburgitic diogenites are related to the orthopyroxenitic diogenites, Beck et al., (2011) and Shearer et al., (2010) found a continuous trend in minor and trace element characteristics between the two groups. As such, the dunitic, harzburgitic, and olivine-orthopyroxenitic diogenites should be considered as part of the diogenite suite. Both the pMELTS models presented here, and the mineralogy of the diogenite collection itself, suggest that orthopyroxene is the most common phase to crystallise from plausible parent melt compositions. The modelling indicates that orthopyroxene crystallises over the broadest range of temperatures and thus the longest period of time. It is therefore reasonable to infer that the orthopyroxene-dominated zones of fractionated crustal intrusions would be the largest. In a stratified intrusion setting, these would sit above olivine-rich lithologies because olivine is the first mineral to crystallise. This general model is also seen in terrestrial intrusions such as the layered mafic suites of the Bushveld Igneous Complex in South Africa (Eales & Cawthorn, 1996).

Lunning et al., (2015) presented data regarding anomalously Mg-rich olivines and orthopyroxenes (Mg#85-92) in four howardites from the Grosvenor Mountains, which were interpreted to represent the most primitive members of the diogenite suite. Although there does seem to be some connection between these high Mg grains and the more primitive end of the diogenite suite based on orthopyroxene composition and $\Delta^{17}\text{O}$ values (Lunning et al., 2015) (Fig. 2.6) – and may perhaps represent a discrete diogenitic lithology – a recent study by Hahn et al., (2018) on similar howardites from the Dominion Range (orthopyroxene Mg#75-90) established that there is no genetic link between the two groups on the bases of chemical composition and instead suggested that they sample the Vestan mantle though this has yet to

be proven. In either case, a source oxygen fugacity of $\Delta IW -2.05$ would allow formation of these grains (Fig. 2.6), although the majority are still offset with regards to Wo .

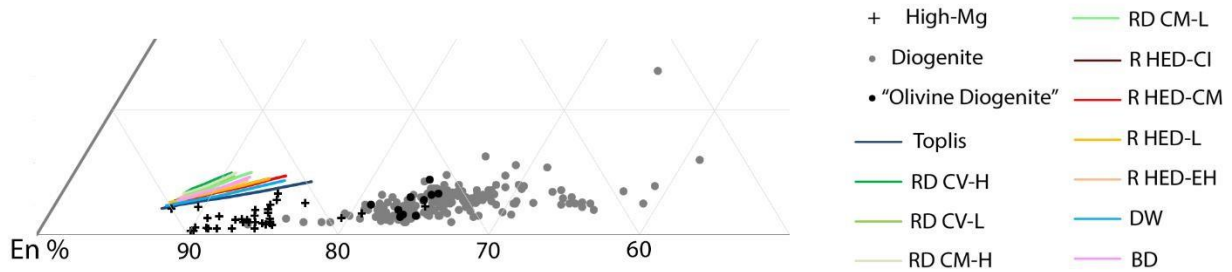


Figure 2.6. High Mg orthopyroxenes plotted against the global meteorite collection and pyroxenes generated by each of the starting compositions used in this study at $fO_2 \Delta IW -2.05$.

Oxygen fugacity is the only variable modelled in this system that has a strong effect on pyroxene composition. As the fO_2 of the starting bulk composition approaches the IW buffer, the orthopyroxenes produced become increasingly Fe-rich. This means that the dunitic to olivine orthopyroxenitic diogenites must have been sourced from regions with fO_2 conditions closer to the IW buffer ($\Delta IW > -1.20$) than the most magnesian orthopyroxenitic diogenites ($\Delta IW -1.60$ to -1.40). However, it is important to note that even in the most oxidised models, orthopyroxene compositions produced in the dunite-harzburgite part of the trends (i.e., only the most magnesian end; Fig. 5) are more magnesian than those of the officially classified ‘olivine diogenites’. As the initial degree of partial melt has negligible effect on composition, a range of starting compositions in the source that are poorer in Mg than those used here, in conjunction with relatively elevated oxygen fugacity, are needed to replicate the observed compositions.

Another argument supporting the notion that diogenites come from crustal intrusions is that olivine dominant mantle lithologies have not been detected in the large Veneneia and Rheasilvia impact basins at Vesta’s southern pole (Ammannito et al., 2013b), as had been expected prior to NASA’s Dawn mission. Although there are challenges in distinguishing an olivine content $< 25\%$ from the orthopyroxene spectra, no dunitic material was detected in

these impact basins (Beck et al., 2013), which instead revealed orthopyroxenitic diogenite and howardite compositions (Beck et al., 2017). As such, it seems that the crust of Vesta is thicker than initial models had suggested, perhaps up to 100 km (Yamaguchi et al., 2011; Jutzi et al., 2013; Clenet et al., 2014; Ermakov et al., 2014), meaning that these large-scale impacts have simply not penetrated the crust deeply enough to reach the mantle.

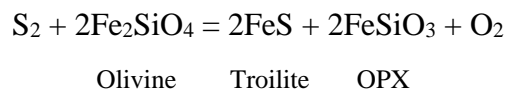
Olivine does, however, occur in the northern hemisphere in and around the Arruntia and Bellicia craters, and is proposed to be Vestan in origin and unrelated to the Rheasilvia impact (Ammanito et al., 2013b; Thangjam et al., 2014; Combe et al., 2015; Palomba et al., 2015). Topographic projections generated by Dawn's framing camera show that these two craters are considerably shallower than Rheasilvia (Yingst et al., 2014), further suggesting that mantle rocks have not been exposed. As such, the olivine detected in the northern craters – if it is indeed endogenic – may be part of a diogenitic pluton in a thick eucritic crust that has been excavated by the crater-forming impact. A stratigraphic intrusion model for the diogenites would explain why olivine is observed in relatively small craters in Vesta's northern hemisphere, but not in the Rheasilvia impact basin.

2.4.3. A Note on the Scarcity of Olivine-Bearing Diogenites in the Meteorite Collection

According to the Meteoritical Society Bulletin Database, dunitic to olivine-orthopyroxenitic diogenites make up < 3 % of all diogenite samples (11 out of 449), therefore only 0.6 % of the entire HED collection. This lack of olivine in the collection is mirrored by its absence in the large impact structures found at Vesta's south pole. The pMELTS models presented here can provide an explanation. Dunitic and harzburgitic diogenites only form over a relatively narrow temperature range under very hot conditions; because olivine is quickly exhausted from the melt, orthopyroxene is the dominant crystallising phase.

2.4.4. Implications of Heterogeneity in Vestan Mantle fO_2

Given that the $\Delta^{17}O$ data for diogenites indicate a well-homogenised mantle, an explanation is needed for the suggested variability in source fO_2 . If the Vestan mantle equilibrated with a large amount of melt, as implied by the volume of eucritic crust, it should have initially had a relatively homogenous fO_2 . As such, the process or processes that caused the fO_2 heterogeneity must have occurred late relative to this widespread melt extraction stage. The most likely driver of such a change is reaction between an exsolving fluid or gas phase and the mantle silicates. Given its abundance, the involvement of sulfur in this process is most plausible. A possible mechanism involves the following metasomatic reaction:



This reduction produces troilite and can drive the relatively small variations in oxygen fugacity needed to generate the spread of diogenite pyroxene compositions. Mantle metasomatism is a widespread process on Earth, where involvement of sulfur is important in modifying oxidation state (Rielli et al., 2017). There, metasomatism is highly heterogeneous such that domains experiencing extensive fluid flux are strongly affected and adjacent unaffected domains are unaffected (O'Reilly & Griffin, 2012), creating distinct variation in fO_2/fS_2 . Sulfidation has been reported in HEDs, such as diogenite Roda, howardite Melrose B (Srinivasan et al., 2016), and eucrite NWA 2339 (Zhang et al., 2013), as well as in enstatite chondrites (Fleet & McRae, 1987; Lehner et al., 2013), ordinary chondrites (Schrader et al., 2006; Tomkins, 2009), brachinites, lunar meteorites (Srinivasan et al., 2016), and ureilites (Langendam, 2016). Similar fO_2 -modifying reactions can be written involving fluid species such as H_2O , CO_2 and CH_4 (Langendam, 2016).

2.5. CONCLUSIONS

By compiling pyroxene composition data for 200 diogenites we found that ‘olivine diogenites’ have orthopyroxene compositions that are less magnesian than some orthopyroxenite diogenites. Because olivine should crystallise first from evolving basaltic magmas, olivine-bearing diogenites should have the most magnesian orthopyroxenes. The observation that this is not the case therefore implies that there was a degree of heterogeneity within the diogenite source region.

Our modelling of the effects of fractional crystallisation from a magma ocean situation of 11 starting compositions presented in literature and using previously estimated fO_2 conditions has shown that the pyroxenes produced are far too magnesian. The degree of initial partial melt has very limited effect on pyroxene composition and cannot account for the range of compositions observed in the meteorite collection. Subsequent modelling found that relatively slight changes in oxygen fugacity can cause large variations in orthopyroxene composition. In order to reproduce the observed orthopyroxene compositions of diogenites, we found that oxygen fugacities of ΔIW fO_2 -1.6 to -1.4 produced the best fit, but there must also have been some compositional variation to account for the full range of diogenite mineralogies and pyroxene compositions.

This variation in source region oxygen fugacity may have been the result of sulfidation reactions, in which sulfur reacts with olivine to produce troilite and orthopyroxene. This type of reduction reaction is commonly observed in a range of meteorite groups, including HEDs (Srinivasan et al., 2016), enstatite (Fleet & McRae, 1987) and ordinary (Schrader et al., 2006; Tomkins, 2009) chondrites, brachinites, and lunar meteorites (Srinivasan et al., 2016). This heterogeneity in source region fO_2 conditions, as well as the spread of diogenite compositions,

supports the theory that diogenites formed as magma chambers emplaced into the basaltic crust of Vesta, and were not formed via crystallisation from a global magma ocean.

The models also consistently produced orthopyroxene compositions that are too calcic, suggesting that the diogenite source is depleted in calcium. This can be accounted for by the removal of melt to produce the eucritic crust, and later generation of diogenite-forming melt from a Ca-poor source. This is in keeping with geochemical evidence that shows diogenites interacted with a feldspar-rich host rock (Barrat et al., 2010), further strengthening the argument for diogenites as crustal intrusions.

2.6. ACKNOWLEDGEMENTS & AUTHOR CONTRIBUTIONS

Funding for this project was provided as part of A.G.T.'s position at Monash University. The authors declare no competing interests. This project was developed by J.T.M with guidance from A.G.T. Modelling and writing were carried out by J.T.M. with editing assistance from A.G.T.

2.7. CHAPTER REFERENCES

Ammannito, E., De Sanctis, M.C, Capaccioni, F., Capria, M.T., Carraro, F., Combe, J.-P., Fonte, S., Frigeri, A., Joy, S.P., Longobardo, A., Magni, G., Marchi, S., McCord, T.B., McFadden, L.A., McSween, H.Y., Palomba, E., Pieters, C.M., Polanskey, C.A., Raymond, C.A., Sunshine, J.M., Tosi, F., Zambon, F., Russell, C.T. (2013a), Vestan lithologies mapped by the visual and infrared spectrometer on Dawn, *Meteoritics & Planetary Science*, **48**, 2185-2198

Ammannito, E., De Sanctis, M.C., Palomba, E., Longobardo, A., Mittlefehldt, D.W., McSween, H.Y., Marchi, S., Capria, M.T., Capaccioni, F., Frigeri, A., Pieters, C.M., Ruesch, O., Tosi, F., Zambon, F., Carraro, F., Fonte, S., Hiesinger, H., Magni, G., McFadden, L.A.,

- Raymond, C.A., Russell, C.T., Sunshine, J.M. (2013b), Olivine in an unexpected location on Vesta's surface, *Nature*, **504**, 122-125
- Ashcroft, H.O., Wood, B.J. (2015), An experimental study on partial melting and fractional crystallisation on the HED parent body, *Meteoritics & Planetary Science*, **50**, 1912-1924
- Barrat, J.-A. (2004), Determination of parental magmas of HED cumulates: The effects of interstitial melts, *Meteoritics & Planetary Science*, **39**, 1767-1779
- Barrat J.-A., Blichert-Toft, J., Gillet, P.H., Keller, F. (2000), The differentiation of eucrites: The role of in situ crystallisation, *Meteoritics & Planetary Science*, **35**, 1087-1100
- Barrat, J.-A., Yamaguchi, A., Zanda, B., Bollinger, C., Bohn, M., (2010), Relative chronology of crust formation on asteroid Vesta: Insights from the geochemistry of diogenites, *Geochimica et Cosmochimica Acta*, **74**, 6218-6231
- Beck , A.W., Lawrence, D.J., Peplowski, P.N., Viviano-Beck, C.E., Prettyman, T.H., McCoy, T.J., McSween, H.Y., Yamashita, N. (2017), Igneous lithologies on asteroid (4) Vesta mapped using gamma-ray and neutron data, *Icarus*, **286**, 35-45
- Beck, A.W., McCoy, T.J., Sunshine, J.M., Viviano, C.E., Corrigan, C.M., Hiroi, T., Mayne, R.G. (2013), Challenges in detecting olivine on the surface of 4 Vesta, *Meteoritics & Planetary Science*, **48**, 2155-2165
- Beck, A.W., McSween, H.Y. (2010), Diogenites as polymict breccias composed of orthopyroxene and harzburgite, *Meteoritics & Planetary Science*, **45**, 850-872
- Beck, A.W., Mittlefehldt, D.W., McSween, H.Y., Rumble III, D., Lee, C.A., Bodnar, R.J. (2011), MIL 03443, a dunite from asteroid 4 Vesta: Evidence for its classification and cumulate origin, *Meteoritics & Planetary Science*, **45**, 1133-1151

- Boesenberg, J.S., Delaney, J.S. (1997), A model composition of the basaltic achondrite planetoid, *Geochimica et Cosmochimica Acta*, **61**, 3205-3225
- Buckowski, D.L., Wyrick, D.Y., Toplis, M., Yingst, R.A., Williams, D.A., Garry, W.B., Mest, S., Kneissl, T., Scully, J.E.C., Nathues, A., De Sanctis, M.C., Le Corre, L., Reddy, V., Hoffmann, M., Ammannito, E., Frigeri, A., Tosi, F., Preusker, F., Roatsch, T., Raymond, C.A., Jaumann, R., Pieters, C.M., Russell, C.T. (2014), The unique geomorphology and physical properties of the Vestalia Terra plateau, *Icarus*, **244**, 89-103
- Clenet, H., Jutzi, M., Barrat, J.-A., Asphaug, E.I., Benz, W., Gillet, P. (2014), A deep crust-mantle boundary in the asteroid 4 Vesta, *Nature*, **511**, 303-306
- Combe, J.-P., McCord, T.B., McFadden, L.A., Ieva, S., Tosi, F., Longobardo, A., Frigeri, A., De Sanctis, M.C., Ammannito, E., Ruesch, O., Palomba, E., Fulchignoni, M., Raymond, C.A., Russell, C.T. (2015), Composition of the northern regions of Vesta analysed by the Dawn mission, *Icarus*, **259**, 53-71
- De Sanctis, M.C., Ammannito, E., Buckowski, D., Raymond, C.A., Jaumann, R., Mittlefehldt, D.W., Capaccioni, F., Capria, M.T., Frigeri, A., Magni, G., Tosi, F., Zambon, F., Russell, C.T. (2014), Compositional evidence of magmatic activity on Vesta, *Geophysical Research Letters*, **41**, 3038-344
- Domanik, K., Kolar, S., Musselwhite, D., Drake, M.J. (2004), Accessory silicate mineral assemblages in the Bilanga diogenite: A petrographic study, *Meteoritics & Planetary Science*, **39**, 567-579
- Dreibus, G., Wänke, H. (1980), The bulk compositions of the eucrite parent asteroid and its bearing on planetary evolution, *Zeitschrift für Naturforschung*, **35a**, 204-216

- Eales, H.V., Cawthorn, R.G. (1996), The Bushveld complex, *Developments in Petrology*, **15**, 181-229
- Elkins-Tanton, L.T., Weiss, B.P., Zuber, M.T. (2011), Chondrites as sample of differentiated planetesimals, *Earth and Planetary Science Letters*, **305**, 1-10
- Ermakov, A.I., Zuber, M.T., Smith, D.E., Raymond, C.A., Balmino, G., Fu, R.R., Ivanov, B.A. (2014), Constraints on Vesta's interior structure using gravity and shape models from the Dawn mission, *Icarus*, **240**, 146-160
- Fleet, M.E., MacRae, N.D. (1987), Sulfidation of Mg-rich olivine and the stability of niningerite in enstatite chondrites, *Geochimica et Cosmochimica Acta*, **51**, 1511-1521
- Fowler, G.W., Shearer, C.K., Papike, J.J., Layne, G.D. (1995), Diogenites as asteroidal cumulates: Insights from orthopyroxene trace element chemistry, *Geochimica et Cosmochimica Acta*, **59**, 3071-3084
- Ghiorso, M.S., Hirschmann, M.M., Reiners, P.W., Kress, V.C. III (2002), The pMELTS: A revision of MELTS aimed at improving calculation of phase relations and major elements partitioning involved in partial melting of the mantle at pressures up to 3 GPa, *Geochemistry, Geophysics, Geosystems*, **3**, 135
- Greenwood, R.C., Barrat, J.-A., Yamaguchi, A., Franchi, I.A., Scott, E.R.D., Bottke, W.F., Gibson, J.M. (2014), The oxygen isotope composition of diogenites: Evidence for early global melting on a single, compositionally diverse, HED parent body, *Earth and Planetary Science Letters*, **390**, 165-174
- Greenwood, R.C., Burbine, T.H., Miller, M.F., Franchi, I.A. (2017), Melting and differentiation of earlyformed asteroids: the perspective from high precision oxygen isotopes, *Chemie der Erde*, **77**, 1-43

- Greenwood, R.C., Franchi, I.A., Jambon, A., Buchanan, P.C. (2005), Widespread magma oceans on asteroidal bodies in the early solar system, *Nature*, **435**, 916-918
- Grove, T.L., Bartels, K.S. (1992), The relation between diogenite cumulates and eucrite magmas, *Proceedings of Lunar and Planetary Science*, **22**, 437-445
- Hahn, T.M., Lunning, N.G., McSween, H.Y., Bodnar, R.J., Taylor, L.A. (2018), Mg-rich harzburgites from Vesta: mantle residua or cumulates from planetary differentiation? *Meteoritics & Planetary Science*, **53**, 514-546
- Hoff, C., Jones, J.H., Le, L. (2014), Experimental Constraints on a Vesta Magma Ocean, *45th Lunar and Planetary Science Conference*, #1634
- Jurewicz, A.J.G., Mittlefehldt, D.W., Jones, J.H. (1995), Experimental partial melting of the St. Severn (LL) and Lost City (H) chondrites, *Geochimica et Cosmochimica Acta*, **59**, 391-408
- Jutzi, M., Asphaug, E., Gillet, P., Barrat, J.-A., Benz, W. (2013), The structure of the asteroid 4 Vesta as revealed by models of planet-scale collisions, *Nature*, **494**, 207-210
- Kawabata, Y., Nagahara, H. (2017), Crystallisation and cooling conditions for diogenite formation in the turbulent magma ocean of asteroid 4 Vesta, *Icarus*, **281**, 379-387
- Langendam, A.D. (2016), On the aggregation, differentiation and devolatilization of volatile-rich asteroids, PhD Thesis, Monash University
- Lehner, S.W., Petaev, M.I., Zolotov, M.Y., Buseck, P.R. (2013), Formation of niningerite by silicate sulfidation in EH3 chondrites, *Geochimica et Cosmochimica Acta*, **101**, 34-56
- Lunning, N.G., McSween, H.Y., Tenner, T.J., Kita, N.T., Bodnar, R.J. (2015), Olivine and pyroxene from the mantle of asteroid 4 Vesta, *Earth and Planetary Science Letters*, **418**, 126-135

- Mandler, B.E., Elkins-Tanton, L.T. (2013), The origin of eucrites, diogenites, and olivine diogenites: Magma ocean crystallisation and shallow magma chamber processes on Vesta, *Meteoritics & Planetary Science*, **48**, 2333-2349
- McCord, T.B., Adams, J.B., Johnson, T.V. (1970), Asteroid Vesta: Spectral Reflectivity and Compositional Implications, *Science*, **168**, 1445-1447
- McCord, T.B., Scully, J.E. (2015), The composition of Vesta from the Dawn mission, *Icarus*, **259**, 1-9
- McSween, H.Y., Ammannito, E., Reddy, V., Prettyman, T.H., Beck, A.W., De Sanctis, M.C., Nathues, A., Le Corre, L., O'Brien, D.P., Yamashita, N., McCoy, T.J., Mittlefehldt, D.W., Toplis, M.J., Schenk, P., Palomba, E., Turrini, D., Tosi, F., Zambon, F., Longobardo, A., Cappaccioni, F., Raymond, C.A., Russell, C.T. (2013), Composition of the Rheasilvia basin, a window into Vesta's interior, *Journal of Geophysical Research: Planets*, **118**, 335-346
- Mittlefehldt, D.W. (1994), The genesis of diogenites and HED parent body petrogenesis, *Geochimica et Cosmochimica Acta*, **58**, 1537-1552
- Mittlefehldt, D.W., Beck, A.W., Lee, C.A., McSween, H.Y., Buchanan, P.C. (2012), Compositional constraints on the genesis of diogenites, *Meteoritics & Planetary Science*, **47**, 72-98
- O'Reilly SY, Griffin WL, 2012. Mantle Metasomatism. In: Metasomatism and the chemical transformation of rock. Eds: D.E. Harlov, H. Austrheim. Springer-Verlag Berlin Heidelberg. 806 p

- Peslier, A.H., Brandon, A.D., Tarduno, J.A., Mittlefehldt, D.W. (2015), Petrology of diogenite NWA 5480, a pristine olivine-rich deformed harzburgite, *46th Lunar and Planetary Science Conference*, #1904
- Pringle, E.A., Savage, P.S., Badro, J., Barrat, J.-A., Moynier, F. (2013), Redox state during core formation on asteroid 4-Vesta, *Earth and Planetary Science Letters*, **373**, 75-82
- Rayman, M.D., Mase, R.A. (2014), Dawn's exploration of Vesta, *Acta Astronautica*, **94**, 159-167
- Raymond, C. A., Russell, C. T. and McSween, H. Y. (2017) "Dawn at Vesta: Paradigms and Paradoxes," in Elkins-Tanton, L. T. and Weiss, B. P. (eds) *Planetesimals: Early Differentiation and Consequences for Planets*. Cambridge: Cambridge University Press (Cambridge Planetary Science), pp. 321–339
- Rielli, A., Tomkins, A.G., Nebel, O., Brugger, J., Etschmann, B., Zhong, R., Yaxley, G. and Paterson, D. 2017. Evidence of sub-arc mantle oxidation by sulfur and carbon. *Geochemical Perspectives Letters*, **3**, 124-132
- Righter, K., Drake, M.J. (1997), A magma ocean on Vesta: Core formation and petrogenesis of eucrites and diogenites, *Meteoritics & Planetary Science*, **32**, 929-944
- Ruzicka, A., Snyder, G.A., Taylor, L.A. (1997), Vesta as the howardite, eucrite and diogenite parent body: Implications for the size of a core and for large-scale differentiation, *Meteoritics & Planetary Science*, **32**, 825-840
- Sack, R.O., Azeredo, W.J., Lipschutz, M.F. (1991), Olivine diogenites: the mantle of the eucrite parent body, *Geochimica et Cosmochimica Acta*, **55**, 1111-1120

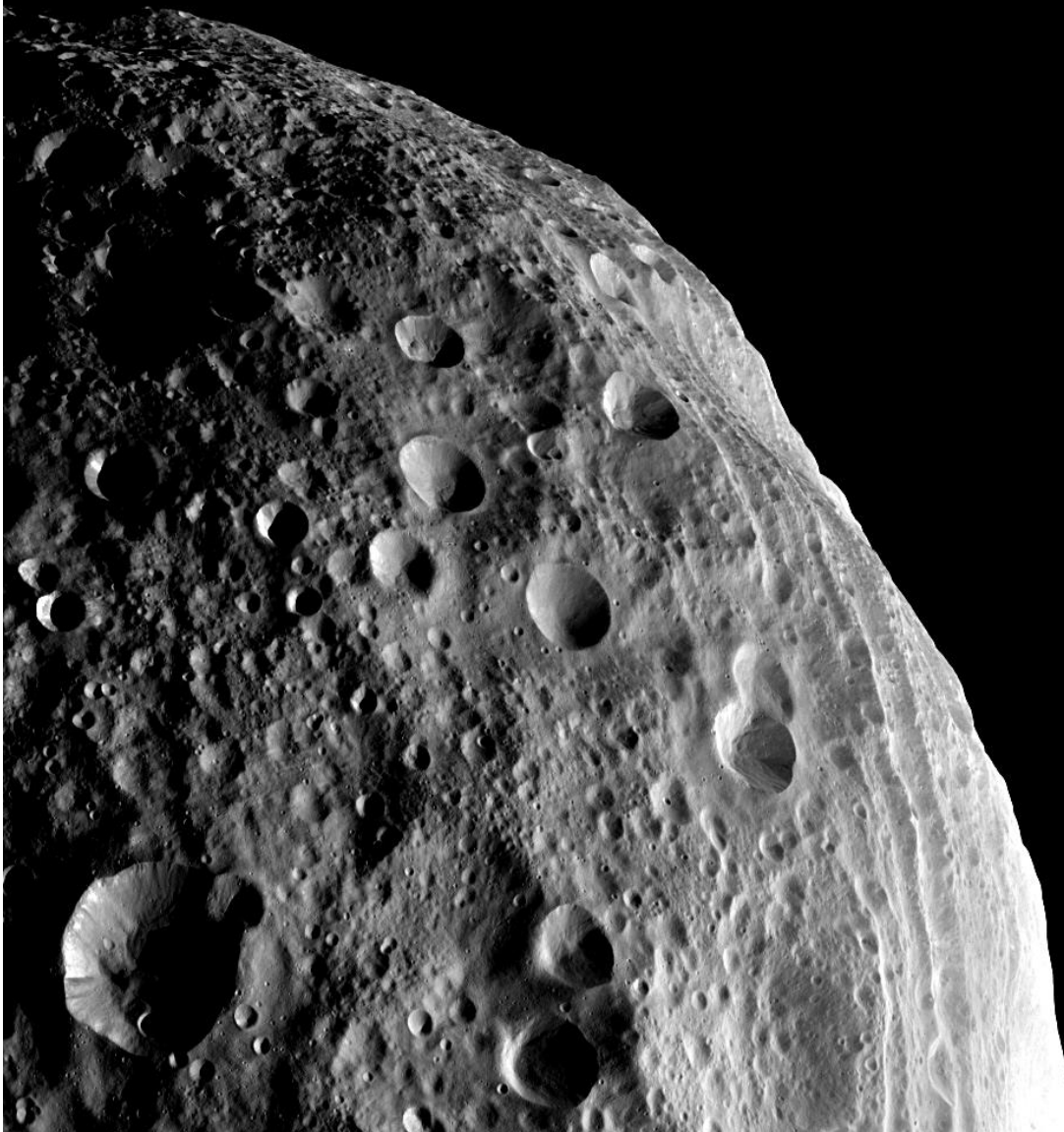
- Schiller, M., Baker, J., Creech, J., Paton, C., Millet, M.-A., Irving, A., Bizzaro, M. (2011), Rapid timescales for magma ocean crystallisation on the howardite-eucrite-diogenite parent body, *The Astrophysical Journal Letters*, **740**, L22
- Schrader, D.L., Schmidt, B.E., Lauretta, D.S. (2006), Oxidation and sulfidation-oxidation of Fe-based alloys in He-H₂S-CO₂ gas mixtures, *Lunar 37th Lunar and Planetary Science Conference*, #2256
- Shearer, C.K., Burger, P., Papike J.J. (2010), Petrogenetic relationships between diogenites and olivine diogenites: Implications for magmatism on the HED parent body, *Geochimica et Cosmochimica Acta*, **74**, 4865-4880
- Srinivasan, P., Shearer, C.K., McCubbin, F.M., Bell, A.S., Agee, C.B. (2016), Examining metasomatism in low fO_2 environments: exploring sulfidation reactions in various parent bodies, *47th Lunar and Planetary Science Conference*, #1623
- Steenstra, E., Knibbe, J.S., Rai, N., van Westrenen, W. (2016), Constraints on core formation in Vesta from metal-silicate partitioning of siderophile elements, *Geochimica et Cosmochimica Acta*, **177**, 4861
- Takeda, H. (1997), Mineralogical records of early planetary processes on the howardite, eucrite, diogenite parent body with reference to Vesta, *Meteoritics & Planetary Science*, **32**, 841-853
- Thangjam, G., Nathues, A., Mengel, K., Hoffmann, M., Schäfer, M., Reddy, V., Cloutis, E.A., Christensen, U., Sierks, H., le Corre, L., Vincent, J.-B., Russell, C.T. (2014), Olivine-rich exposures at Bellicia and Arruntia craters on (4) Vesta from Dawn FC, *Meteoritics & Planetary Science*, **49**, 18311850

- Tharp, T.M., Loucks, R.R., Sack, R.O. (1998), Modeling compaction of olivine cumulates in the Muskox intrusion, *American Journal of Science*, **298**, 758-790
- Thomas, J.H., Rau, R.L., Skelton, R.T., Kavanagh, R.W. (1984), Half-life of ^{26}Al , *Physical Review C*, **30**, 385-387
- Tomkins, A.G. (2009), What metal-troilite textures can tell us about post-impact metamorphism in chondrite meteorites, *Meteoritics & Planetary Science*, **44**, 1133-1149
- Toplis, M.J., Mizzon, H., Monnereau, M., Forni, O., McSween, H.Y., Mittlefehldt, D.W., McCoy, T.J., Prettyman, T.H., De Sanctis, M.C., Raymond, C.A., Russell, C.T. (2013), Chondritic models of 4 Vesta: Implications for geochemical and geophysical properties, *Meteoritics & Planetary Science*, **48**, 2300-2315
- Walker, D., Jurewicz, S., Watson, E.B. (1988), Adcumulus dunite growth in a laboratory thermal gradient, *Contributions To Mineralogy and Petrology*, **99**, 306-319
- Warren, P.H. (1997), Magnesium oxide-iron oxide mass balance constraints and a more detailed model for the relationship between eucrites and diogenites, *Meteoritics & Planetary Science*, **32**, 945-963
- Wiechert, U.H., Halliday, A.N., Palme, H., Ruml, D. (2004), Oxygen isotope evidence for rapid mixing of the HED meteorite parent body, *Earth and Planetary Science Letters*, **221**, 373-382
- Wilson, L., Keil, K. (1996), Volcanic eruptions and intrusions on the asteroid 4 Vesta, *Journal of Geophysical Research*, **101(E8)**, 18927-18940
- Wilson, L., Keil, K. (2012), Volcanic activity on differentiated asteroids: A review and analysis, *Chemie der Erde*, **72**, 289-321

- Yamaguchi, A., Barrat, J.-A., Ito, M., Bohn, M. (2011), Posteuclitic magmatism on Vesta: Evidence from the petrology and thermal history of diogenites, *Journal of Geophysical Research*, **116**, E08009
- Yamaguchi, A., Barrat, J.-A., Shirai, N., Ebihara, M. (2015), Petrology and geochemistry of Northwest Africa 5480 diogenite and evidence for a basin-forming event on Vesta, *Meteoritics & Planetary Science*, **50**, 1260-1270
- Yingst, R.A., Mest, S.C, Berman, D.C., Garry, W.B., Williams, D.A, Buckowski, D., Jaumann, R., Pieters, C.M., De Sanctis, M.C, Frigeri, A., Le Corre, L., Preusker, F., Raymond, C.A., Reddy, V., Russell, C.T., Roatsch, T., Schenk, P.W. (2014), Geologic mapping of Vesta, *Planetary and Space Science*, **103**, 2-23
- Zhang, A.C., Wang, R.C., Hsu, W.B., Bartoschewitz, R. (2013), Record of S-rich vapors on asteroid 4 Vesta: Sulfurization in the Northwest Africa 2339 eucrite, *Geochimica et Cosmochimica Acta*, **109**, 113
- Zuber, M.T., McSween, H.Y., Binzel, B.P., Elkins-Tanton, L.T., Konopliv, A.S., Pieters, C.M., Smith, D.E. (2011), Origin, internal structure and evolution of 4 Vesta, *Space Science Reviews*, **163**, 77-93

“Man must rise above Earth to the top of the atmosphere and beyond, for only then will he fully understand the world in which he lives”

Socrates



Chapter 3

A Model for Evolving Crust on 4 Vesta through Combined Compositional and Thermal Modelling[†]

Jennifer T. Mitchell¹, Andrew G. Tomkins¹, Christopher
Newton² & Timothy E. Johnson³

¹School of Earth, Atmosphere and Environment, Monash University, Australia

²School of Physics & Astronomy, Monash University, Australia

³School of Earth & Planetary Sciences, Curtin University, Australia

[†]Accepted in *Earth and Planetary Science Letters*, January 2021

ABSTRACT

Combined phase equilibria and thermal modelling has been used to investigate the evolution of asteroid 4 Vesta. Orthopyroxene compositions of 200 natural diogenite meteorites are used as a basis for constructing a staged mantle melting model for Vesta, which is then used to develop a staged thermal evolution model. Our pMELTS models find that removal of 15-20 % of a mean eucrite component from an initial Vestan mantle composition allows a second stage of melting that crystallises low-calcium orthopyroxenes that match the observed compositions of those in natural diogenites, whereas single stage melting produces orthopyroxenes that are too calcic. Using the compositions generated by the pMELTS modelling, THERMOCALC models were created for an initial Vestan mantle composition and an evolved composition generated by a melt extraction stage. These models suggest that melt production for second-stage diogenite generation required considerably hotter temperatures (>1340 °C) than for eucrites (<1240 °C). Staged and layered thermal evolution models developed using these composition and temperature constraints, based on the decay of ^{26}Al and ^{60}Fe , suggest that Vesta accreted 1.50 to 1.75 Myr after calcium-aluminium inclusion (CAI) formation. Earlier accretion results in conditions that are inconsistent with the petrology of the HED meteorites, whereas later accretion predicts temperatures that are insufficient to produce diogenites. We suggest that upward migration of ^{26}Al -rich melt initially created a convecting shallow magma ocean of <20 km depth which rapidly crystallised to form a ^{26}Al -rich eucritic crust that acted as a hot insulating lid. The second stage of crust formation began once the depleted mantle residue reached high enough temperatures to produce diogenite-forming magmas. These results further support the view that diogenites likely formed as crustal intrusions rather than as magma ocean cumulates.

3.1. INTRODUCTION

Vesta is the largest differentiated rocky asteroid in the Solar System, almost qualifying as a minor planet given its impact-modified near-spheroidal shape. As such, determining the petrogenesis of its crust is important to the study of differentiated protoplanetary bodies. The howardite-eucrite-diogenite (HED) clan of meteorites that are likely sourced from asteroid 4 Vesta (Burratti et al., 2013; McSween et al., 2013; McCoy et al., 2015) and are the most common achondrites in the global meteorite collection. Both eucrites and diogenites are igneous lithologies, whereas howardites are mechanical breccias produced through repeated impacting of the Vestan surface. Eucrites range from basaltic rocks to samples preserving cumulate textures and form much of Vesta's crust. They are composed primarily of calcic plagioclase and low-Ca pyroxenes containing augite lamellae, as well as minor metal and sulfides. Eucrites are further subdivided into Main Group, Stannern trend, and Nuevo Laredo trend based on major and incompatible element ratios (Barrat et al., 2007). Many eucrites experienced high-temperature metamorphism that in some cases led to secondary melting, which has largely been considered to be the consequence of serial magmatism superimposed on heating associated with impacts (Yamaguchi et al., 1996). Diogenites are orthopyroxenitic cumulates with accessory plagioclase, sulfides, and metals (Mittlefehldt, 1994), although some rare samples of harzburgitic and dunitic samples have been reported (Beck et al., 2011). These are thought to have formed through crystal settling either from a global magma ocean (Righter & Drake, 1997; Ruzicka et al., 1997), within discrete crustal magma chambers (Beck et al., 2011; Mandler & Elkins-Tanton, 2013; Clenet et al., 2014).

A genetic relationship between diogenites and eucrites has long been argued. In the magma ocean scenario, large-scale crystal settling and fractionation creates an 'onion-skin' layering, with basaltic eucrites extruded to form the upper crust, grading down through cumulate eucrites

and diogenites that comprise the lower crust and upper mantle (Mandler & Elkins-Tanton, 2013). Conversely, the serial magmatism scenario suggests that diogenites represent cumulates of late-stage magmas that intruded into an older eucrite crust, creating a diverse range of lithologies (Yamaguchi et al., 2011; Barrat & Yamaguchi, 2014). NASA's Dawn mission produced some key insights. In particular, the lack of olivine in Vesta's south polar impact basins (Ammannito et al., 2013), combined with the sparsity of harzburgitic and dunitic diogenites, calls into doubt the idea that all HEDs come from rocks crystallised from a homogeneous global magma ocean because temperatures sufficient for >50% melting (i.e., a magma ocean) generate magmas that should produce olivine-rich cumulates. Similarly, unlike the Moon, rocks with abundant flotationally accumulated plagioclase (anorthosites) are not known amongst the HED meteorite collection, nor observed by Dawn. This observation could be taken to imply that there was no magma ocean. However, the much lower gravity of Vesta and the small density difference between basalt and plagioclase, means that Stokes Law plagioclase flotation may have been too inefficient to form anorthosites (cf. Elkins-Tanton, 2012). Nonetheless, the plagioclase-rich basalts that dominate the eucrites are what one might expect of a modest degree of partial melting of a primary chondritic source; that is, the >50% melting of the magma ocean scenario is not needed to explain them. And furthermore, the observation that dense FeNi metal grains are found in nearly all diogenites and eucrites implies that core formation was inefficient (Tomkins et al., 2013), which is more consistent with modest partial melting, rather than the existence of a prolonged magma ocean. Since geochemical studies have found that diogenites and eucrites may not be cogenetic (Barrat et al., 2008; Barrat and Yamaguchi, 2014), it is likely that the magmatic evolution of Vesta was more complex than originally thought.

Here, we combine thermodynamic modelling using the pMELTS (Ghiorso et al., 2002) and THERMOCALC (Powell & Holland, 1988) software packages with thermal modelling based on decay of the short-lived isotopes ^{26}Al and ^{60}Fe (e.g., Moskovitz & Gaidos, 2011; Mare et al., 2014) to generate models for the early evolution of Vesta based on modest degrees of partial melting. These allow us to explore the relationships between eucrite and diogenite meteorites, and the proportion of melting in the Vestan mantle needed to form them.

3.2. METHODS

Recently, we (Mitchell & Tomkins, 2019) developed a pMELTS (Ghiorso et al., 2002) model to investigate plausible formation mechanisms of diogenite meteorites, using 11 starting bulk compositions previously proposed for Vesta (Boesenburg & Delaney 1997; Righter & Drake 1997; Ruzicka et al. 1997; Dreibus & Wänke 1980; Toplis et al., 2013). In that study, we suggested that variable oxygen fugacity in the magma source region played a key role in controlling the compositions of orthopyroxenes in diogenites. However, the orthopyroxene compositions predicted by the models were consistently enriched in Ca relative to natural diogenites, implying an additional control on the magmatic evolution of Vesta.

3.2.1 New pMELTS modelling

To better understand diogenite genesis and generate a better match between modelled and observed orthopyroxene compositions, we started by extracting differing proportions of an average eucrite composition (mean eucrite of Mittlefehldt et al., 1998) from the bulk Vesta compositions used in Mitchell and Tomkins (2019). This is essentially equivalent to extracting differing amounts of basaltic crust from the mantle. A range of Ca-depleted starting bulk compositions were produced reflecting 5, 10, 15, and 20 % eucrite removal (Table A1). We then modelled partial melting of these modified starting compositions – essentially equivalent

to a second stage of melting of a depleted Vestan mantle – using the pMELTS software v.5.6.1 (Ghiorso et al., 2002). In keeping with previous thermal models of Vesta (Ghosh & McSween, 1998; Formisano et al., 2013), volatiles are considered to be evaporated and are not considered in the bulk compositions used here.

The models were run at a pressure of 86.59 MPa (equivalent to ~100 km depth on Vesta), oxygen fugacities (fO_2) -1.60 to -1.20 log units below the iron-wüstite buffer (ΔIW) to match the orthopyroxene compositions of diogenites as described by Mitchell & Tomkins (2019), and up to temperatures sufficient to produce 40 ± 0.1 vol% melt. The degree of initial partial melt has a negligible effect on major element compositions of pyroxenes produced by the model, and higher temperatures were selected for this stage of modelling to fully explore the range of pyroxene compositions that could be generated over time. The resulting melt compositions were then modelled separately from the residue, and cooled in 20 °C steps, for which the abundance of all crystallising phases was recorded and pyroxene compositions calculated. The resulting pyroxene compositions (Table A2; Fig.3.1) were then compared to those of 200 natural diogenite orthopyroxenes (data from Meteoritical Bulletin Database). From this comparison, a close match between modelled and observed orthopyroxene compositions was achieved by using the Ruzicka (R) HED CI bulk composition minus 15 % eucrite at fO_2 ΔIW -1.20, which we refer to hereafter as “R-HED-CI –15”. This in itself is an important result, indicating that diogenite pyroxene compositions with can be explained by considering partial melting of a Vestan mantle that had already experienced ~15% silicate melt removal (plus an undetermined percentage of metallic melt removal).

The next step in our analysis involved investigating how hot the Vestan mantle would need to get to go through this second stage of melt generation. For this step, the R-HED-CI –15

composition was modelled using the software THERMOCALC (Powell and Holland, 1988), which can be used to investigate, amongst other things, partial melting and crystallisation of a wide range of planetary materials via P - T or T - X pseudosections (Johnson et al., 2016, 2021; Tomkins et al., 2020).
surfaces.

3.2.2 THERMOCALC modelling

Two pressure-temperature pseudosections were constructed using THERMOCALC 3.50 (Powell and Holland, 1988) utilising the end-member thermodynamic data of Holland & Powell (2011; ds633 dataset produced in June, 2017) and activity–composition models of Holland et al. (2018), which enable calculation of subsolidus to suprasolidus (melt-bearing) phase equilibria for bulk compositions ranging in composition from peridotite to granite. The two modelled bulk compositions (Table 3.1) are an undepleted composition prior to eucrite extraction (R-HED-CI and a depleted composition based on extraction of 15% eucrite melt (R-HED-CI–15) as described above.

Table 3. 1. Compositions (wt%) used in THERMOCALC modelling, normalised to 100%.

	Undepleted (R-HED-CI)	Depleted (R-HED-CI–15)	Post-Diogenite Residue
SiO₂	45.34	44.64	42.87
TiO₂	0.18	0.1	0.10
Al₂O₃	3.29	1.56	1.69
Cr₂O₃	0.85	0.93	0.99
FeO	14.34	13.76	13.32
MnO	0.4	0.38	0.35
MgO	32.67	37.1	39.18
CaO	2.78	1.45	1.49
Na₂O	0.12	0.06	
K₂O	0.01		
P₂O₅	0.02	0.02	

Although these models permit calculations in the $K_2O-Na_2O-CaO-FeO-MgO-Al_2O_3-SiO_2-H_2O-TiO_2-Fe_2O_3-Cr_2O_3$ (KNCFMASHTOCr) chemical system, we use an anhydrous and ferric iron-free subset (i.e., in the KNCFMASHTOCr system) that is appropriate to diogenites and other Fe-metal-bearing meteorites. Phase abbreviations follow Whitney and Evans (2010).

3.2.3 Thermal evolution modelling

The bulk silicate compositions and the THERMOCALC modelling were used as the basis for the construction of thermal evolution models for Vesta based on the decay of ^{26}Al and ^{60}Fe . In the THERMOCALC modelling, the initial undepleted composition (R-HED-CI) transitioned to the depleted composition (R-HED-CI-15) at 1240 °C, representing 15 % melt extraction to form the initial eucrite crust, and concurrent extraction of the core. The system transitions again at 1340 °C, representing the extraction of diogenite melt (Table 1). The physical parameters used in this study were based on the model of Vesta's structure by Russell et al., (2012), utilising a three-zone onion-shell geometry with a total radius of 260 km (i.e., the approximate radius of Vesta), a core radius of 116 km was calculated, equivalent to 18 % of Vesta's mass (Russell et al., 2012), and an initial single-plate lid crust of 17 km thickness with a composition and thickness based on 15 % melt removal as established in the pMELTS modelling.

We assumed instantaneous accretion based on the work by Henke et al., (2013) and references therein, who found that extremely rapid accretion provides the most satisfactory explanation for the thermal history of asteroids. Longer durations of accretion slightly increase the length of the initial heating period. Instantaneous segregation of melt was also assumed following Ghosh & McSween (1998). Heat generation was modelled using the one-dimensional heat equation with internal heat sources (Moskovitz and Gaidos 2011):

$$\frac{\partial T}{\partial t} = \frac{1}{r^2} \frac{\partial}{\partial r} \left(r^2 k \frac{\partial T}{\partial r} \right) + \frac{Q(t)}{c}$$

such that the internal heat source $q(t)$ was governed by:

$$q(t) = f_{al} \left[\frac{Al^{26}}{Al^{27}} \right] \frac{E_{Al}}{\tau_{Al}} e^{-\frac{t}{\tau_{Al}}} + f_{fe} \left[\frac{Fe^{60}}{Fe^{56}} \right] \frac{E_{Fe}}{\tau_{Fe}} e^{-\frac{t}{\tau_{Fe}}}$$

Where T is temperature (K), t is time in years, r is the radial distance from the centre of model (meters). The remaining variables are defined in Table 3.2.

Table 3.2. Symbols, definitions, and values used in the thermal evolution modelling (after Formisano et al., 2013; Mare et al., 2014).

Symbol	Definition	Value	Units
κ	thermal conductivity	3.20E7	$J m^{-1} yr^{-1} K^{-1}$
		Regolith: 3.2E6	
		silicate melting: 12.6E7	
ρ	Density	Initial (LL): 3440	$kg m^{-3}$
		Core: 7100	
		Mantle: 3400	
c	Specific heat capacity at constant pressure	Silicate: 927	$J kg^{-1} K^{-1}$
		Metal: 578	
		Sulfide: 699	
		Conjoined: 645	
f_{Al}	Chondritic abundance of Al	Vesta: 2.65E23	kg^{-1}
f_{Fe}	Chondritic abundance of Fe	Vesta: 2.12E24	kg^{-1}
$\left[\frac{Al^{26}}{Al^{27}} \right]$	Initial abundance of ^{26}Al	5.00E-05	-
$\left[\frac{Fe^{60}}{Fe^{56}} \right]$	Initial abundance of ^{60}Fe	1.15E-08	-
τ_{Al}	^{26}Al half-life	0.717	Myr
τ_{Fe}	^{60}Fe half-life	2.62	Myr
E_{Al}	^{26}Al decay energy per atom	6.42E-13	J
E_{Fe}	^{60}Fe decay energy per atom	4.87E-13	J
T_{init}	Initial model temperature	180	K
T_{ext}	External temperature	180	K

The main components of this model follow Mare et al., (2014) and Moskovitz & Gaidos (2011). As with the Mare et al., (2014) model, we consider thermal buffering caused by melting of silicates, metal and sulfide grains (i.e. latent heat of fusion). The silicates and conjoined metal-sulfide grains were considered to melt in five steps, whereas isolated sulfide and metal grains were modelled in one melting step. Moreover, utilizing the high-resolution X-Ray computed tomography results for LL chondrites (similar FeO content and thus oxidation state as Vesta) from Mare et al., (2014), only metallic Fe was divided into multiple melting steps under the assumption that 80 wt% of Fe existed as conjoined grains, with the remaining 20 wt% split into FeS (40 wt%) and FeNi metal (60 wt%).

Our model also considers ^{26}Al migration in the silicate melt, an important component of the Moskovitz & Gaidos (2011) investigation, which treated extraction of ^{26}Al from the mantle as a function of time. The implementation of ^{26}Al migration in our model occurs via instantaneous formation of the core, mantle and an initial crust/hot lid at 1240 °C, as established by our THERMOCALC modelling and is in keeping with previous thermochemical studies (Ghosh & McSween (1998) and references therein). The thermal model begins as a single-zone system representing an initially homogenous bulk Vesta composition that allows heating by ^{26}Al and ^{60}Fe decay throughout the body. When the initial system reaches 1240 °C, the model transitions to the three-zone system with temperature evolving in the core, mantle, and crust, reflecting their different concentrations of ^{60}Fe and ^{26}Al and associated heating. A third stage occurs when 1340 °C is reached and a mean diogenite component (Mittlefehldt, 1994) is moved from the mantle into the crust. Models were produced for accretion at 0.5, 1.0, 1.25, 1.5, 1.75, 2.0 and 2.5 million years after the formation of CAIs at T_0 , representing the timing of initial condensation of the Solar System ($T_0 = 4568.2$ Ma; Bouvier & Wadhwa, 2010). The abundances of ^{26}Al and ^{60}Fe at each stage of the model are compiled in Table 3.3.

Table 3.3. wt% of ^{26}Al and ^{60}Fe at each compositional stage for the accretion times used in this study, extracted from the thermal evolution model. Undepleted refers to the initial composition of Vesta, depleted refers to the mantle composition post-initial eucrite extraction, and residue refers to the mantle composition after diogenite extraction.

		^{26}Al (wt%)	^{60}Fe (wt%)
$T_0 = + 0.05$ Myr	<i>Undepleted</i>	4.241×10^{-5}	1.881×10^{-7}
	<i>Depleted</i>	2.038×10^{-5}	9.623×10^{-8}
	<i>Residue</i>	2.205×10^{-5}	9.319×10^{-8}
$T_0 = + 1.00$ Myr	<i>Undepleted</i>	2.610×10^{-5}	1.630×10^{-7}
	<i>Depleted</i>	1.254×10^{-5}	8.338×10^{-8}
	<i>Residue</i>	1.357×10^{-5}	8.075×10^{-8}
$T_0 = + 1.25$ Myr	<i>Undepleted</i>	2.048×10^{-5}	1.518×10^{-7}
	<i>Depleted</i>	9.837×10^{-6}	7.762×10^{-8}
	<i>Residue</i>	1.065×10^{-5}	7.517×10^{-8}
$T_0 = + 1.50$ Myr	<i>Undepleted</i>	1.606×10^{-5}	1.413×10^{-7}
	<i>Depleted</i>	7.717×10^{-6}	7.225×10^{-8}
	<i>Residue</i>	8.352×10^{-6}	6.997×10^{-8}
$T_0 = + 1.75$ Myr	<i>Undepleted</i>	1.260×10^{-5}	1.315×10^{-7}
	<i>Depleted</i>	6.054×10^{-6}	6.726×10^{-8}
	<i>Residue</i>	6.552×10^{-6}	6.513×10^{-8}
$T_0 = + 2.00$ Myr	<i>Undepleted</i>	6.887×10^{-6}	1.224×10^{-7}
	<i>Depleted</i>	4.749×10^{-6}	6.261×10^{-8}
	<i>Residue</i>	5.140×10^{-6}	6.063×10^{-8}
$T_0 = + 2.50$ Myr	<i>Undepleted</i>	6.085×10^{-6}	1.061×10^{-7}
	<i>Depleted</i>	2.923×10^{-6}	5.425×10^{-8}
	<i>Residue</i>	3.163×10^{-6}	5.254×10^{-8}

3.3. RESULTS

3.3.1 pMELTS Modelling

Figure 3.1 shows the results of the pMELTS modelling. From this it can be seen that removal of a eucrite component from the mantle depletes it in CaO and lowers the wollastonite (Wo ; CaSiO_3) content in orthopyroxenes produced during the second stage of magma generation and crystallisation. We find that between 15-20 % eucrite removal, at $f\text{O}_2$ between $\Delta\text{IW} -1.60$

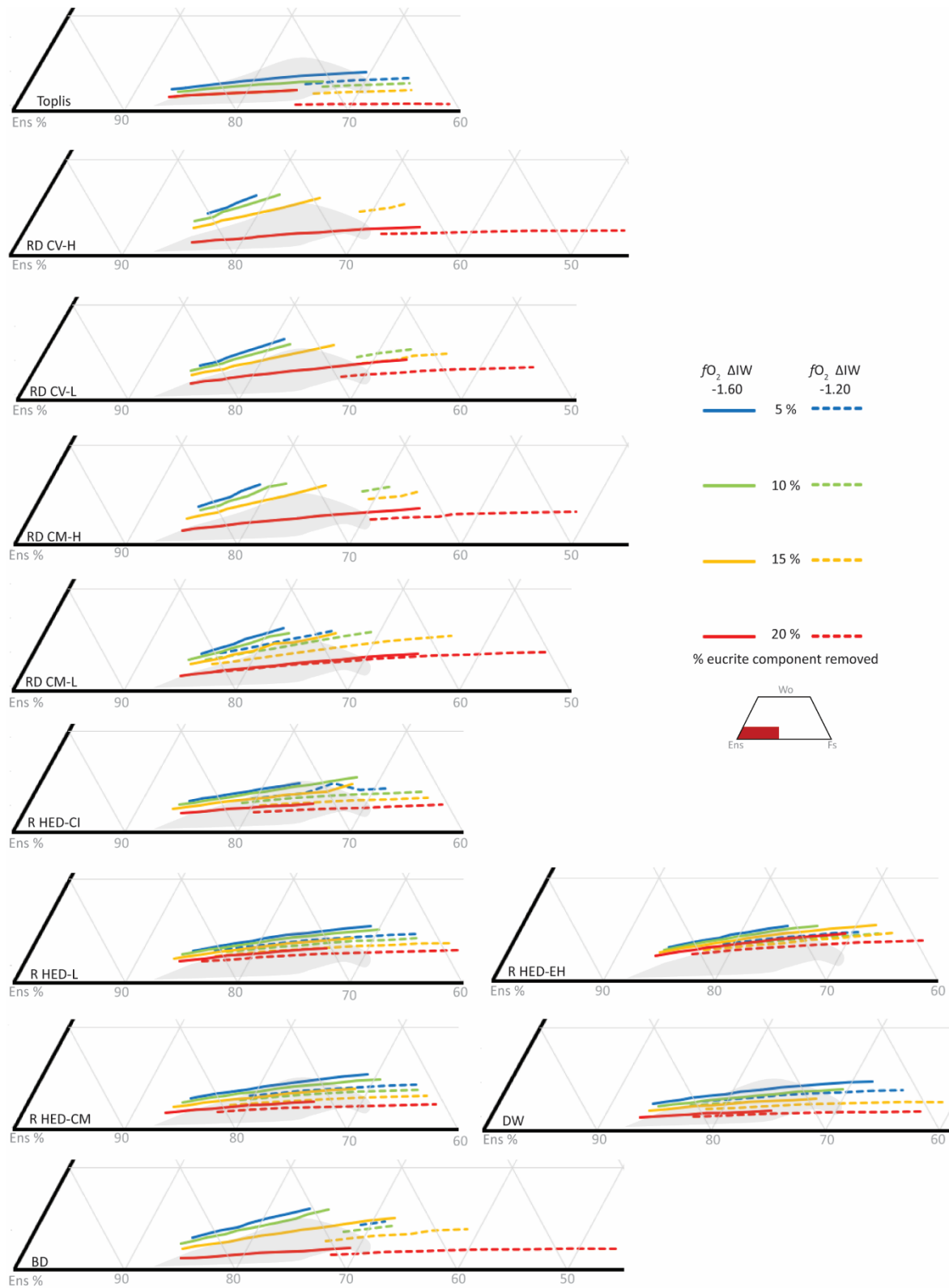


Figure 3.1. Orthopyroxene compositions generated through pMELTS modelling of each silicate starting bulk composition and the adjustments of each composition to reflect 5-20% eucrite removal from the diogenite source region. fO_2 conditions determined in Mitchell & Tomkins (2019). The shaded area represents 200 natural diogenite compositions (data from the Meteoritical Society Bulletin Database). Starting compositions: Toplis, Toplis et al., (2013); RD, Righter & Drake (1997); R, Ruzicka et al., (1997), DW, Dreibus & Wänke (1980); BD, Boesenberg & Delaney (1997). Pyroxene compositions are compiled in Table A1.

and -1.20, produces model orthopyroxene compositions that closely match those observed in diogenites. The bulk composition that provides the closest match is R-HED-CI, although several others also provide good matches. As expected, increasing the amount of eucrite removed from the starting composition also increases the temperature required to reach a given percentage of partial melting, as well as the temperature at which orthopyroxenites are first produced during crystallisation of the resulting magma.

3.2 THERMOCALC modelling

The THERMOCALC models (Fig. 3.2) allow a comparison of the chemical evolution of the mantle, the extent of melting and temperatures required to generate the depleted and undepleted bulk compositions, and a comparison with the pMELTS models. In the model for the undepleted initial bulk silicate Vesta starting composition (R-HED-CI, Fig. 3.2A), the temperature required for 15% melting is slightly cooler than that in the pMELTS model (~1200 °C rather than 1240 °C at 0.86 kbar), which likely reflects the different thermodynamic datasets and activity–composition models used. In nature, a small amount of early melt migration would shift the bulk composition to slightly depleted values, thereby shifting the temperature required to reach 15% cumulative melt to slightly higher values. For this reason, we elect to use 1240 °C as the temperature at which core and crust separation occurs in the thermal evolution models.

In the thermodynamic model for the depleted composition (R-HED-CI –15, Fig. 3.2B), the solidus is unexpectedly lowered slightly, but complete consumption of calcic pyroxene and plagioclase occurs at lower T . Compared to the undepleted bulk composition, much higher temperatures are required to achieve modest proportions of melt. Peridotitic residues, mainly olivine and minor orthopyroxene (i.e., similar to ureilites, which contain olivine, pigeonite

and/or orthopyroxene), and then pyroxene-absent dunite residues (i.e., akin to the silicate component of main group pallasites) are achieved as melting progresses from 15 to 25%. For the thermal evolution models, 1340 °C is taken to be the temperature when a diogenite-forming melt is extracted, representing ~20% melting at 0.86 kbar.

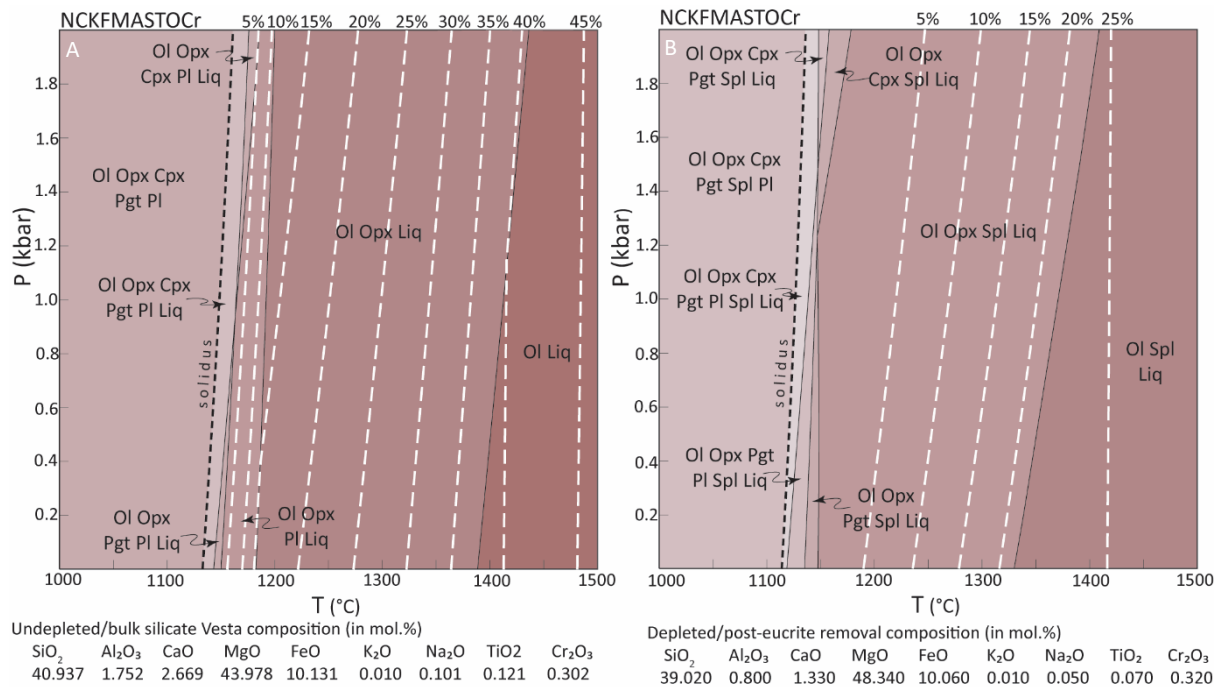


Figure 3.2. THERMOCALC pseudosections of (A) the undepleted, initial bulk silicate R-HED-CI composition and (B) the depleted R-HED-CI-15 composition. The white dashed lines represent melt contours of 5-45% partial melting in the system under these conditions. Spinel appears on (B) as the mean eucrite component used in this study does not account for Cr₂O₃, meaning that it becomes a higher fraction of the normalised depleted composition. Spinel is not a major phase in these compositions and should not be considered as such. Abbreviations: Ol, olivine; Opx, orthopyroxene; Cpx, clinopyroxene; Pgt, pigeonite; Pl, plagioclase; Spl, spinel; Liq, liquid.

3.3 Thermal evolution modelling

As in previous studies (Ghosh & McSween, 1998; Formisano et al., 2013), thermal modelling of Vesta's evolution (Fig. 3.3) finds that the time of accretion relative to T_0 greatly affects maximum mantle temperatures, with later accretion times resulting in lower temperatures due to the short half-life of ²⁶Al. Models in which accretion occurs at $T_0 + 1.5$ Myr or earlier achieve mantle temperatures that are significantly higher than those required for diogenite formation. The model for accretion at $T_0 + 1.75$ Myr does not achieve mantle temperatures of 1340 °C

that are required to produce dunitic diogenite compositions, but can generate melts that would produce harzburgitic to orthopyroxenitic diogenite at a lower degree of partial melting. The model for accretion at $T_0 + 2.0$ Myr does not reach temperatures capable of producing diogenite melts, and accretion at $T_0 + 2.5$ Myr (not shown) does not reach temperatures high enough to cause widespread silicate melting.

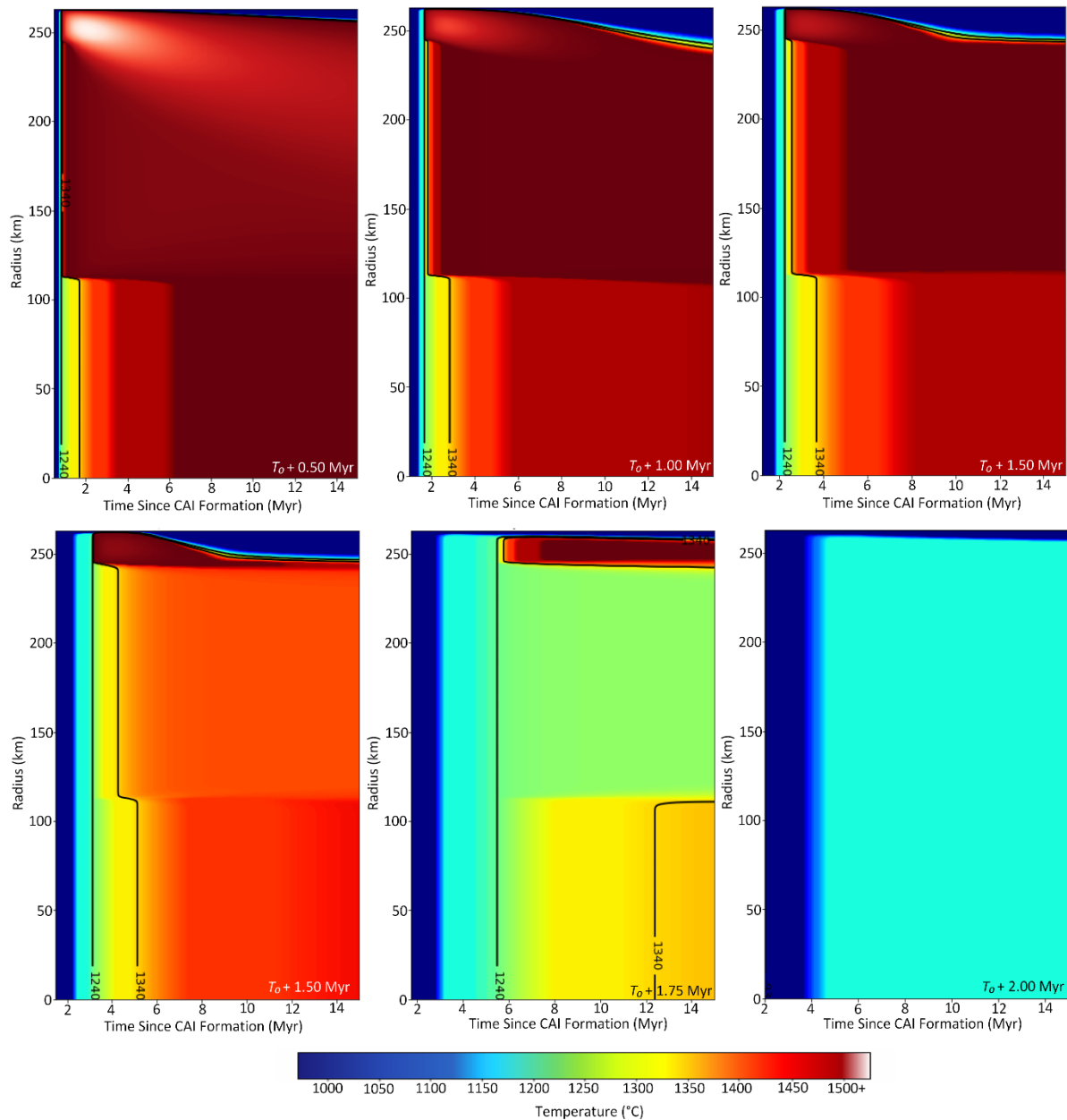


Figure 3.3. Thermal models of Vesta at various accretion ages, showing the variations in heat production and temperature caused by the decay of ^{26}Al and ^{60}Fe through time relative to CAI formation. The 1240 and 1340 ($^{\circ}\text{C}$) lines show the first instance of conditions reaching the temperatures required for the initial stage of eucrite and diogenite magmatism respectively, as established in the THERMOCALC models.

The models predict that the highest temperatures from occur in the ^{26}Al -enriched crust. These temperatures are often unreasonably high, and we infer that convection occurs. The effects of convective heat loss are not included in the models but are discussed below. Maximum temperatures reached are as follows: $T_0 + 0.50$ Myr 25,262 °C; + 1.00 Myr 10,793° C; + 1.25 Myr 6,289 °C; + 1.50 Myr 3,412 °C; + 1.75 Myr 1,535 °C. No crust is generated through mantle melting at $T_0 + 2.00$ – 2.50 Myr, where mantle temperatures reach 1189 °C and 962 °C respectively.

3.4. DISCUSSION

The combined models presented in this study imply that Vesta accreted at $T_0 + 1.5 - 1.75$ Myr, seemingly contemporaneous with the ureilite parent body (cf. Budde et al., 2015). The temperatures required to generate the first eucrite melts from a chondritic starting composition occur at approximately $T_0 + 3 - 5$ Myr. The mineral associations and textures in primitive achondrites suggest that silicate melt migration typically occurs at melt fractions of 10-20 %, where melt can form interconnected networks and drain from the source (Tomkins et al., 2020). Thus, the earliest eucrites are expected to be the product of moderate degrees of partial melting of a primitive source. In primitive achondrites, the metal-sulfide assemblage tends to form connected networks within the silicate melt network, implying that core segregation proceeds at the same time as silicate melt extraction (Tomkins et al., 2020). In addition, previous modelling has suggested that cores form contemporaneously with extraction of the initial crust, particularly when the percentage of metal-sulfide melt is higher (Bagdassarov et al., 2009). The process of core and crust formation depletes the mantle in some, but not all, of the heat-producing elements.

Our modelling shows that, after formation of a modestly depleted mantle by extraction of a eucritic crust and a metallic core, sufficient ^{26}Al and ^{60}Fe remained in the mantle for significant heating to continue, and that the mantle was insulated by the crust. Very early accretion, before $\sim T_0 + 1.5$ Myr, would result in extreme heating ($>1500^\circ\text{C}$) and formation of a global magma ocean. The pMELTS and THERMOCALC models indicate that these temperatures would consume all plagioclase and pyroxene and a significant proportion of olivine. Such melting would produce komatiite-like lavas (i.e., producing olivine-rich rocks), olivine-rich cumulates, and a dunitic mantle. Since meteorites with comparable mineralogy are almost completely lacking amongst the nearly 2400 HED meteorites (there are a small number of olivine-rich diogenites, which can form from melts generated by cooler melting), it is unlikely that the mantle ever reached the temperatures needed to form such melts. As suggested in the Introduction, the widespread presence of metal particles in HED meteorites also implies inefficient core formation and a lower degree of partial melting in the mantle.

Accretion at $T_0 + 1.5$ – 1.75 produces appropriate second-stage heating for diogenite magmatism. Accretion at $T_0 + 1.5$ Myr leads to mantle temperatures of up to $\sim 1400^\circ\text{C}$ and the generation of voluminous olivine-rich diogenite-forming magma during the second stage of melting. Accretion at $T_0 + 1.75$ Myr would generate temperatures sufficient to form a eucritic crust, and the entire mantle would produce 15–20% melt during second-stage melting, sufficient to generate a second pulse of diogenite-forming intrusions into the eucritic crust. As accretion at $T_0 + 2.0$ Myr results in a body that produces only low degrees of partial melting (maximum mantle $T = 1189^\circ\text{C}$), this model cannot explain the meteorite population from Vesta. Such a body might be expected to produce a small amount of plagiobasalt crust, but not diogenitic intrusions.

The crustal temperatures predicted by the thermal models are implausibly high. As our models only consider diffusive heat loss, we infer that convection within an extensively molten early-formed crust and evaporative heat loss would have promoted more rapid cooling at the surface. Eucrites are strongly depleted in moderately- to highly-volatile elements, which requires a component of evaporative mass loss (cf. Ruzicka et al., 2001; Sossi et al., 2019). Once solidified, this initial crust would have acted as a lid that insulated the mantle. Continued ^{26}Al decay, magmatic heat from diogenite intrusions and impact heating are expected to have produced high-temperature metamorphism and secondary melting within this early crust. Of these, the most important contributor to crustal melting may have been the high ^{26}Al , since the temperature of the diogenite-forming magmas is only a small amount above those needed to form the eucrites. Supporting this suggestion is the evidence of widespread crustal metamorphism affecting the eucrites, with inferred temperatures of 700 to 1000°C, including evidence for some partial melting (Yamaguchi et al., 1996; 2009). Impacts may have had the overall effect of increasing the cooling rate of the crust: they locally heat a small volume of material at the site of impact, but by removing a large amount of material they expose the hotter deeper remainder to lower temperatures than otherwise, thereby increasing the rate of cooling for asteroids overall (Ciesla et al., 2013).

Combining the thermal models with the observed range of meteorites provides an effective way to date the accretion of Vesta. The most consistent scenario requires accretion between 1.50 and 1.75 Myr following CAI formation to produce an initial crust consisting of plagiobasalt (eucrites) at approximately $T_0 + 3\text{-}5$ Myr that is later intruded by hotter more ultramafic magmas that fractionated to form cumulate diogenite material around $T_0 + 5$ Myr and onwards (Fig. 3.4). An important difference between the $T_0 + 1.5$ Myr and $T_0 + 1.75$ Myr models is the amount of diogenite-forming magma that is produced. If the proportion of

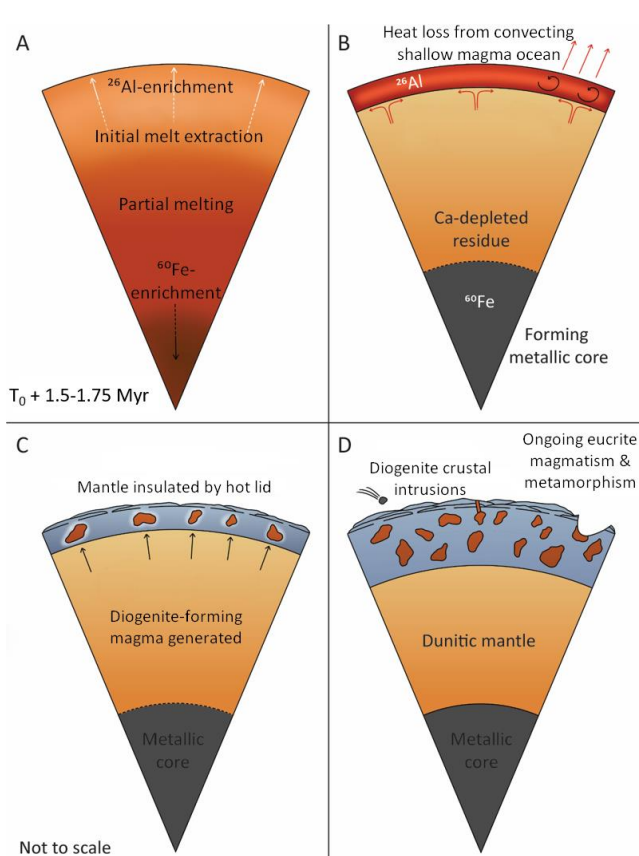


Figure 3.4. A simplified schematic of Vesta's evolution as envisaged from modelling presented in this study. A) Vesta accretes at $T_0 + 1.50\text{--}1.75$ Myr from a chondritic precursor and is heated through decay of ^{26}Al and ^{60}Fe . An initial eucrite-like melt composition is extracted at $1240\text{ }^\circ\text{C}$ (15 % melt); B) ^{26}Al is predominantly incorporated into the shallow magma layer, which crystallises rapidly through convective and evaporative heat loss; C) The insulated mantle heats to $1340\text{ }^\circ\text{C}$, generating melt compositions capable of crystallising dunitic to noritic diogenites, from a non-homogenised mantle. Eucrite magmatism is ongoing, and crustal metamorphism occurs through ^{26}Al decay; D) Secondary intrusions crystallise diogenites and additional eucrite material, thickening Vesta's crust, resulting in a deep crust-mantle boundary and lack of mantle exposure in the Rheasilvia impact basin. Impact gardening produces howardites and liberates HED meteorites. Dyking allows for the transport of diogenite material to the surface, resulting in features such as Brumalia Tholus.

diogenite in the crust is high, the $T_0 + 1.5$ Myr model is more likely to be true, whereas accretion at $T_0 + 1.75$ Myr is more consistent with a low proportion of diogenite. The second stage of magmatism can also produce eucritic compositions from crustal magma chambers following extraction of cumulate diogenite material, which would increase the eucrite:diogenite ratio. In the global meteorite collection as of early 2021, there are 503 diogenites and 1427 eucrites. This might imply that diogenite magmatism was relatively short-lived compared to eucrite magmatism. However, the entire crust of Vesta is unlikely to have been representatively sampled. Numerical modelling of dyke and sill formation on asteroids shows that melt transport is efficient at low gravity (Wilson & Keil, 2012), and petrological analysis of primitive achondrites suggests that melt networks form at low degrees of partial

melting (Tomkins et al., 2020). Thus, although we have modelled a two-stage crust formation process involving melt extraction at 15–20% melting, lower degrees of melting may be relevant

(Wilson & Keil, 2012), in which case models considering later times of accretion may be more appropriate.

It is also noteworthy that the $T_0 + 1.50$ and $T_0 + 1.75$ Myr accretion models result in different mantle compositions. In the former, mantle temperatures are sufficient to produce a highly-depleted dunitic mantle (Fig. 3.2B) akin to pallasite silicates, whereas accretion at $T_0 + 1.75$ Myr results in a cooler, peridotite mantle with olivine–pyroxene proportions similar to those in ureilites. The maximum temperature recorded by ureilites is $\sim 1280^\circ\text{C}$ and the parent body may have been of comparable size (Collinet and Grove, 2020), which is more consistent with the $T_0 + 1.75$ Myr model. However, as there has been insufficient sampling of Vesta’s mantle, it is not possible to use its composition as a way of distinguishing the most appropriate time-of-accretion. Nonetheless, the relatively thick crust (Clenet et al., 2014) implies more voluminous magmatism, so we favour a complex crustal structure composed of abundant diogenitic intrusions emplaced into an early-formed eucritic crust (i.e., closer to the $T_0 + 1.5$ Myr model), resulting in a dunitic mantle.

Previous thermal models of Vesta have suggested a wide range of timescales for accretion. The thermal model of Ghosh & McSween (1998) suggested that Vesta accreted at $T_0 + 2.85$ Myr, whereas that of Formisano et al. (2013) prefers an accretion age of $T_0 + 0.5\text{--}1.4$ Myr. These discrepancies may be explained by the higher proportion of ^{26}Al used in the Ghosh & McSween (1998) model, as well as the larger core sizes used in both studies, which involve higher amounts of ^{60}Fe . As in previous studies, our thermal modelling shows that the time of accretion – and thereby the amount of ^{26}Al and ^{60}Fe available to generate heat – is the key determining factor in reaching high temperatures. The Formisano et al., (2013) model requires 50 % silicate melting, which is inconsistent with the lithologies observed on Vesta and in the HED meteorite

collection. This high degree of partial melting requires a much higher abundance of ^{26}Al , and an early accretion time. The compositional and THERMOCALC modelling presented in this study finds that HED lithologies can be generated with <20 % partial melting, requiring less ^{26}Al to produce silicate melting. Consequently, the time of accretion of Vesta is unlikely to be as early as suggested by Formisano et al., (2013). Similarly, the higher proportion of ^{26}Al used in the Ghosh & McSween (1998) model means that later accretion is required to be consistent with the meteorite petrology. The Ghosh & McSween (1998) model also does not consider diogenite genesis, which affects the timing and extent of ^{26}Al extraction to the crust.

Both the Ghosh & McSween (1998) and the Formisano et al. (2013) models include a veneer of unmelted chondritic material early in Vesta's history. In contrast, our model suggests that the initial eucritic crust of Vesta would have functioned as an insulating hot (i.e. volcanically-active) stagnant lid. Stagnant lids occur when the outermost layers of an asteroid or planetary body become too viscous to convect as a result of cooling and crystallisation and are thought to have formed on many planetary bodies early in the Solar System's history (Solomatov & Moresi, 2000). Our model suggests that much of the ^{26}Al would have been concentrated in this outer layer (Fig. 3.4). Heat generation within this early-formed crust would have reduced heat loss from the mantle and maintained elevated temperatures in Vesta's interior for longer than in cold (volcanically inactive or sluggish) lid models. This enhanced heat retention under a crystallised crust would perhaps follow a shallow magma ocean stage. The thermal models of Neumann et al., (2014) are comparable; in these, concentration of ^{26}Al in the upper levels of Vesta's crust creates a superheated molten layer, up to a few tens of kilometers thick, that undergoes convection to rapidly lose heat within 1.5 million years of Vesta's accretion. Both the timing of the formation of this shallow magma ocean and its geometry are broadly

consistent with the results of our modelling, where the extraction of the initial ^{26}Al -enriched melt occurs approximately 1.5 million years after Vesta's accretion.

Dating of HED meteorites indicates that Vesta underwent a period of prolonged magmatism following early extraction of the primary eucrite crust. Ongoing crustal growth by addition of melt/magma is thought to have occurred through emplacement of sills and dykes (Wilson & Keil, 2012), and late-stage crustal intrusions have been suggested by a number of authors (Mittlefehldt, 1994; Barrat et al., 2008; Yamaguchi et al., 2011). Features such as Brumalia Tholus on Vesta's surface have been interpreted to represent dyke-fed intrusions within the crust (Buckowski et al., 2014). Dating of basaltic eucrites using the ^{26}Al – ^{26}Mg system has produced ages of approximately 2.66 Myr after CAI formation (Hublet et al., 2017). Similarly, ^{26}Al – ^{26}Mg ages for cumulate eucrites finds that they post-date earlier basaltic eucrite magmatism at 5.48–7.25 Myr after CAI formation (Hublet et al., 2017). This staged magmatism is further supported by dating of zircons in eucrites, which suggests that magmatism continued for several tens of millions of years (Misawa et al., 2005; Roszjar et al., 2016; Jourdan et al., 2020). These data accord with the evidence for complex post-crystallisation processes, including widespread crustal metamorphism (Yamaguchi et al., 1996; Yamaguchi et al., 2009) and impact modification (Yamaguchi et al., 2001), which tend to overprint thermometers with low closure temperatures (Wadhwa et al., 2009). Geochronological studies of diogenites also support our models, in that diogenites appear to have crystallised after extinction of ^{26}Al (i.e., after seven half-lives, or $T_0 + 5$ Myr), significantly post-dating eucrites (Hublet et al., 2017).

Trace element anomalies recorded in some diogenites suggest that they interacted with eucritic crust, and therefore post-date eucrite magmatism (Barrat et al., 2008). Similarly, the wide range of diogenite orthopyroxene compositions requires multiple source compositions (Mittlefehldt,

1994), including localised variations in oxygen fugacity (Mitchell & Tomkins, 2019). Although some previous studies focusing on the geochemistry of diogenites have suggested that they were produced by remelting of magma ocean cumulates rather than primary mantle melting (Mittlefehldt, 1994; Barrat et al., 2008; Mittlefehldt et al., 2012), these have tended to point out simply that a heterogeneous source is required as a basis for making this suggestion. Modest partial melting in the mantle and early melt extraction would inhibit homogenisation, so a chemically heterogeneous mantle would be an expected outcome of our model. Again, this suggestion is comparable with observations from ureilites, which despite high temperatures, have geochemistry and isotopic characteristics indicating considerable mantle heterogeneity (Barrat et al., 2017; Sanders et al., 2017).

Magmatic differentiation occurred on numerous planetesimals early in the early Solar System's history, including the parent bodies of the fractionated iron meteorites, pallasites, ureilites, brachinites, aubrites, angrites and many ungrouped achondrites. The brachinites and ureilites are thought to represent mantle residues (Keil, 2014; Collinet and Grove 2020), but are mineralogically distinct from the pigeonite- and augite-absent harzburgitic residues generated by second-stage melting presented here. They are, however, mineralogically similar to the residue produced by the first stage of melting, being rich in olivine and containing appreciable concentrations of pyroxene (albeit higher proportions of calcic pyroxene). Dating of ureilites using ^{26}Al – ^{26}Mg (Budde et al., 2015) suggests that accretion and silicate melt extraction were contemporaneous with our modelled ages for accretion and melting of Vesta; comparable data for brachinites have not yet been published.

3.5. CONCLUSIONS

The models for Vesta presented here provide insights into the processes of magmatism in the early solar system and the genesis of HED meteorites and provide updates to previous evolution models by considering diogenites as complex products of remelting rather than magma ocean cumulates. In order to explain the range of observed natural diogenite compositions and their relationship to eucrites, Vesta's evolution must have been more complex than a single stage of fractional crystallisation from a homogeneous global magma ocean. The vast majority of diogenites are orthopyroxenites, so it is unlikely that they represent the Vestan mantle. In addition, they are too depleted in Ca to represent cumulates from a globally homogeneous magma ocean.

A key interpretation of the thermal models presented here is that the timing of Vesta's accretion played a pivotal role in determining its magmatic evolution due to the rapidly changing abundance of short-lived ^{26}Al . We find that, in order to be consistent with the petrology of the HED meteorites, Vesta most likely accreted between 1.50 and 1.75 Myr after CAI formation. Models proposing earlier accretion times in which ^{26}Al was more abundant reach implausibly high temperatures that would have resulted in magma oceans that would crystallise rocks not known amongst the nearly 2400 HED meteorites. Models of later accretion do not reach temperatures sufficiently high to generate the basaltic crust of Vesta.

Magmatism on Vesta can be approximated using a two-stage evolution model. The first stage generated an initial eucrite-like melt that was efficiently extracted when melt fractions reached 15–20 % at temperatures of 1200–1240 °C to form an ^{26}Al -enriched shallow magma ocean that quickly crystallised via convection and evaporative cooling to leave a hot stagnant lid. This ^{26}Al enrichment allowed the crust to generate significant radiogenic heat, slowing the rate of heat loss from Vesta's mantle, and promoting widespread metamorphism and secondary

melting within the crust. This insulation also allowed the mantle to undergo prolonged radiogenic heating until temperatures were high enough (≥ 1340 °C) to trigger a second stage of magmatism characterised by diogenite formation and ongoing eucrite extraction. Future iterations of the models presented here will be designed to also consider convection.

Although the majority of diogenites are orthopyroxenites, there are rare dunitic samples that require higher temperatures and ongoing eucrite magmatism. An expected outcome of melt extraction after modest extents of partial melting are heterogeneous mantle, diogenite and eucrite compositions. Diogenite magmas were emplaced into the older eucrite crust as discrete intrusions, which underwent fractional crystallisation at a range of fO_2 values controlled by source heterogeneity to generate the diverse range of orthopyroxene compositions recorded in diogenites. This stage served to thicken the crust sufficiently that the Vestan mantle was not exposed by the Rheasilvia impact.

3.6. ACKNOWLEDGEMENTS & AUTHOR CONTRIBUTIONS

Funding for this study was provided as part of A.G.T.'s positional at Monash University. T.E.J acknowledges an Open Fund (GPMR201903) from the State Key Laboratory of Geological Processes and Mineral Resources, China University of Geosciences, Wuhan.

3.7. CHAPTER REFERENCES

Ammanito, E., De Sanctis, M.C., Palomba, E., Longobardo, A., Mittlefehldt, D.W., McSween, H.Y., Marchi, S., Capria, M.T., Capaccioni, F., Frigeri, A., Pieters, C.M., Reusch, O., Tosi, F., Zambon, F., Carraro, F., Fonte, S., Hiesinger, H., Magni, G., McFadden, L.A., Raymond, C.A., Russell, C.T., Sunshine, J.M. (2013), Olivine in an unexpected location on Vesta's surface, *Nature*, **504**, 122-125

- Arai, T., Maruyama, S. (2017), Formation of anorthosite on the Moon through magma ocean fractional crystallization, *Geoscience Frontiers*, **8**, 299-308
- Ashcroft, H.O., Wood, B.J. (2015), An experimental study on partial melting and fractional crystallisation on the HED parent body, *Meteoritics & Planetary Science*, **50**, 1912-1924
- Bagdassarov, N., Solferino, G., Golabek, G.J., Schmidt, M.W. (2009), Centrifuge assisted percolation of Fe-S melts in partially molten peridotite: time constraints for planetary core formation, *Earth and Planetary Science Letters*, **288**, 84-95
- Barrat, J.-A. (2004), Determination of parental magmas of HED cumulates: The effects of interstitial melts, *Meteoritics & Planetary Science*, **39**, 1767-1779
- Barrat, J.-A., Bilchert-Toft, J., Gillet, P.H., Keller, F. (2000), The differentiation of eucrites: The role of *in situ* crystallization, *Meteoritics & Planetary Science*, **35**, 1087-1100
- Barrat, J.-A., Sansjofre, P., Yamaguchi, A., Greenwood, R.C., Gillet, P. (2017), Carbon isotopic variation in ureilites: evidence for an early volatile-rich inner solar system, *Earth and Planetary Science Letters*, **478**, 143-149
- Barrat, J.-A., Yamaguchi, A. (2014), Comment on “the origins of eucrites, diogenites, and olivine diogenites: magma ocean crystallization and shallow magma processes on Vesta” by B.E. Mandler and L.T. Elkins-Tanton, *Meteoritics & Planetary Science*, **49**, 466-472
- Barrat, J.-A., Yamaguchi, A., Greenwood, R.C., Benoit, M., Cotton, J., Bohn, M., Franchi, I.A. (2008), Geochemistry of diogenites: Still more diversity in their parental melts, *Meteoritics & Planetary Science*, **43**, 1759-1775

- Barrat, J.-A., Yamaguchi, A., Zanda, B., Bolinger, C., Bohn, M. (2010), Relative chronology of crust formation on asteroid Vesta: insights from the geochemistry of diogenites, *Geochimica et Cosmochimica Acta*, **74**, 6218-6231
- Barrat, J.-A., Yamaguchi, A., Greenwood, R.C., Bohn, M., Cotton, J., Benoit, M., Franchi, I.A. (2007), The Stannern trend eucrites: Contamination of main group eucritic magmas by crustal partial melts, *Geochimica et Cosmochimica Acta*, **71**, 4108-4124
- Beck, A.W., Mittlefehldt, D.W., McSween, H.Y., Ruml, III, D., Lee, C.A., Bodnar, R.J. (2011), MIL 03443, a dunite from asteroid Vesta: Evidence for its classification and cumulate origin, *Meteoritics & Planetary Science*, **45**, 1133-1151
- Boesenberg, J.S., Delaney, J.S. (1997), A model composition of the basaltic achondrite planetoid, *Geochimica et Cosmochimica Acta*, **61**, 3205-3225
- Bouvier, A., Wadhwa, M. (2010), The age of the Solar System redefined by the oldest Pb-Pb age of a meteoritic inclusion, *Nature Geoscience*, **3**, 637-641
- Buckowski, D.L., Wyrick, D.Y., Toplis, M., Yingst, R.A., Williams, D.A., Garry, W.B., Mest, S., Kneissl, T., Scully, J.E.C., Nathues, A., De Sanctis, M.C., LeCorre, L., Reddy, V., Hoffmann, M., Ammannito, E., Frigeri, A., Tosi, F., Preusker, F., Roatsch, T., Raymond, C.A., Jaumann, R., Pieters, C.M., Russell, C.T. (2014), The unique geomorphology and physical properties of the Vestalia Terra plateau, *Icarus*, **244**, 89-103
- Budde, G., Kruijer, T.S., Fischer-Gödde, M., Irving, A.J., Kleine, T. (2015), Planetesimal differentiation revealed by the Hf-W systematics of ureilites, *Earth and Planetary Science Letters*, **430**, 316-325

- Burratti, B.J., Dalba, P.A., Hicks, M.D., Reddy, V., Sykes, M.V., McCord, T.B., O'Brien, D.P., Pieters, C.M., Prettyman, T.H., McFadden, L.A., Nathues, A., Le Corre, L., Marchi, S., Raymond, C.A., Russell, C.T. (2013), Vesta, vestoids, and the HED meteorites: interconnections and differences based on Dawn Framing Camera observations, *Journal of Geophysical Research: Planets*, **118**, 1991-2003,
- Clenet, H., Jutzi, M., Barrat, J.A., Asphaug, E.I., Benz, W., Gillet, P. (2014), A deep-crust mantle boundary in the asteroid 4 Vesta, *Nature*, **511**, 303-306
- Collinet, M., Grove, T.L. (2020), Incremental melting in the ureilite parent body: initial composition, melting temperatures, and melt compositions, *Meteoritics & Planetary Science*, **55**, 832-856
- Downes, H., Mittlefehldt, D.W., Kita, N.T., Valley, J.W. (2008), Evidence from polymict ureilite meteorites for a disrupted and re-accreted single ureilite parent asteroid gardened by several distinct impactors, *Geochimica et Cosmochimica Acta*, **72**, 4825-4844
- Dreibus, G., Wänke, H. (1980), The bulk compositions of the eucrite parent asteroid and its bearing on planetary evolution, *Zeitschrift für Naturforschung*, **35a**, 204-216
- Formisano, M., Federico, C., Turrini, D., Coradini, A., Capaccioni, F., De Sanctis, M.C., Pauselli, C. (2013), The heating history of Vesta and the onset of differentiation, *Meteoritics & Planetary Science*, **48**, 2316-2332
- Ghiorso, M.S., Hirschmann, M.M., Reiners, P.W., Kress, III, V.C. (2002), The pMELTS: A revision of MELTS aimed at improving calculation of phase relations and major elements partitioning involved in partial melting of the mantle at pressures up to 3 GPa, *Geochemistry, Geophysics, Geosystems*, **3**, 1-35

- Ghosh, A., McSween, H.Y. (1998), A thermal model for the differentiation of asteroid 4 Vesta, based on radiogenic heating, *Icarus*, **134**, 187-206
- Henke, S., Gail, H.-P., Trieflodd, M., Schwarz, W.H. (2013), Thermal evolution model for the H chondrite asteroid-instantaneous protracted accretion, *Icarus*, **226**, 212-228
- Holland, T.J.B. and Powell, R. (2011), An improved and extended internally consistent thermodynamic dataset for phases of petrological interest, involving a new equation of state for solids. *Journal of Metamorphic Geology*, **29**, 333-383
- Hublet, G., Debaille, V., Wimpenny, J., Yin, Q.-Z. (2017), Differentiation and magmatic activity in Vesta evidenced by ^{26}Al - ^{26}Mg dating in eucrites and diogenites, *Geochimica et Cosmochimica Acta*, **218**, 73-97
- Johnson, T.E., Benedix, G.K., Bland, P.A. (2021), Metamorphism and partial melting of ordinary chondrites: calculated phase equilibria, *Earth and Planetary Science Letters*, **433**, 21-30
- Johnson, T.E., Morrissey, L.J., Nemchin, A.A., Gardiner, N.J., Snape, J.F. (2021), The phases of the Moon: modelling crystallisation of the lunar magma ocean through equilibrium thermodynamics, *Earth and Planetary Science Letters*, **556**, 116721
- Jourdan, F., Kennedy, T., Benedix, G.K., Eroglu, E., Mayer, C. (2020), Timing of the magmatic activity and upper crustal cooling of differentiated asteroid 4 Vesta, *Geochimica et Cosmochimica Acta*, **273**, 205-225
- Mandler, B.E., Elkins-Tanton, L.T. (2013), The origin of eucrites, diogenites, and olivine diogenites: magma ocean crystallization and shallow magma chamber processes on Vesta, *Meteoritics & Planetary Science*, **48**, 2333-2349,

- Mare, E.R., Tomkins, A.G., Godel, B.M. (2014), Restriction of parent body heating by metal-troilite melting: Thermal models for the ordinary chondrites, *Meteoritics & Planetary Science*, **49**, 636-651
- McCoy, T.J., Beck, A.W., Prettyman, T.H., Mittlefehldt, D.W. (2015), Asteroid (4) Vesta II: exploring a geologically and geochemically complex world with the Dawn Mission, *Chemie der Erde*, **75**, 273-285
- McSween, H.Y., Binzel, P., De Sanctis, M.C., Ammannito, E., Prettyman, T.H., Beck, A.W., Reddy, V., Le Corre, L., Gaffey, M.J., McCord, T.B., Raymond, C.A., Russell, C.T., the Dawn Science Team (2013), Dawn; the Vesta-HED connection; and the geologic context for eucrites, diogenites, and howardites, *Meteoritics & Planetary Science*, **48**, 2090-2104
- Misawa, K., Yamaguchi, A., Kaiden, H. (2005), U-Pb and ^{207}Pb - ^{206}Pb ages of zircons from basaltic eucrites: implications for early basaltic volcanism on the eucrite parent body, *Geochimica et Cosmochimica Acta*, **69**, 5847-5861
- Mitchell, J.T., Tomkins, A.G. (2019), On the source of diogenites and olivine diogenites: compositional diversity from variable $f\text{O}_2$, *Geochimica et Cosmochimica Acta*, **258**, 37-49
- Mittlefehldt, D.W. (1994), The genesis of diogenites and HED parent body petrogenesis, *Geochimica et Cosmochimica Acta*, **58**, 1537-1552
- Mittlefehldt, D.W., McCoy, T.J., Goodrich, C.A., Kracher, A. (1998), Planetary Materials (Mineralogical Society of America, Reviews in Mineralogy, Vol. 36), EOS Transactions

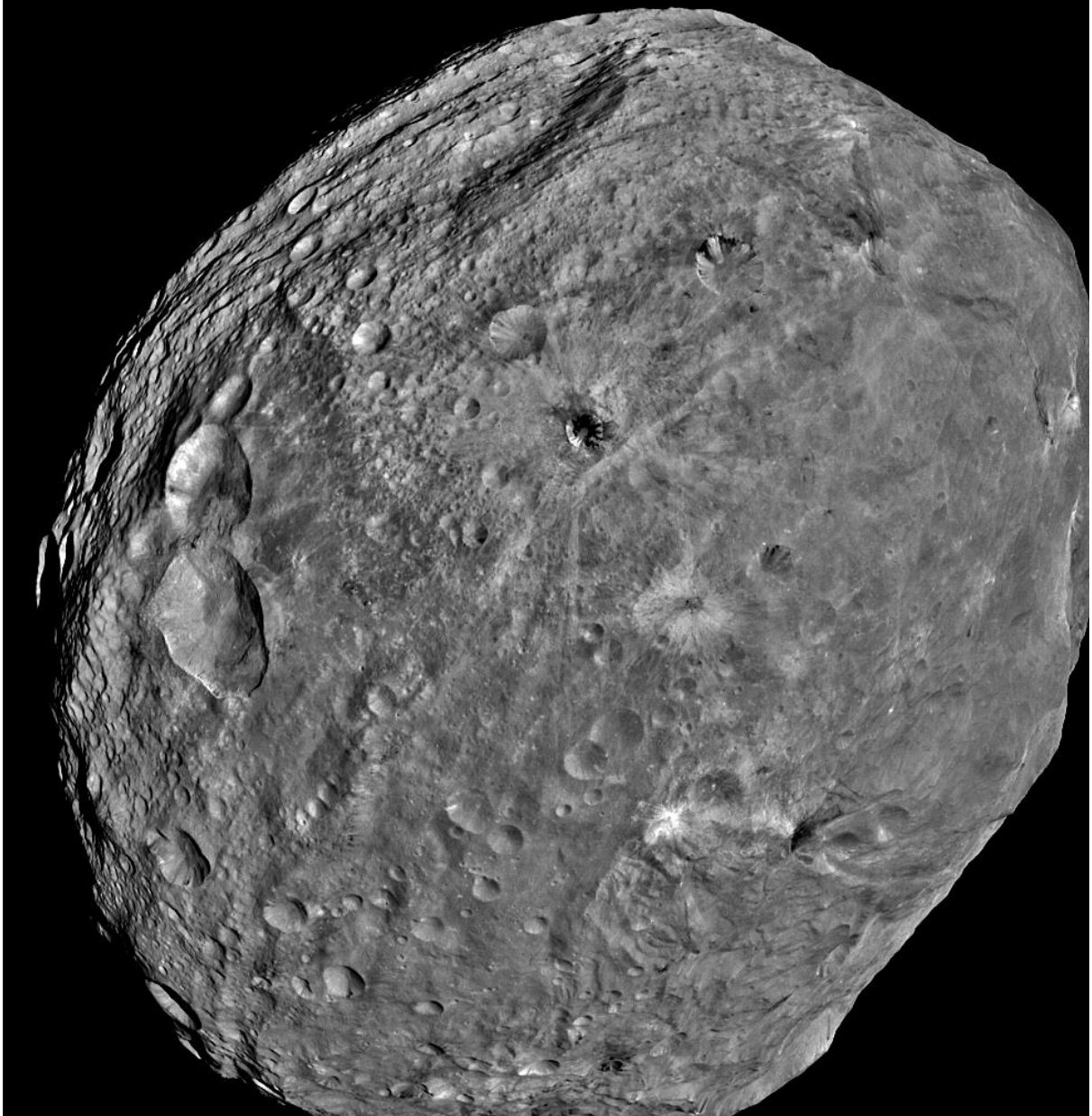
- Mittlfehltdt, D.W., Beck, A.W., Lee, C.A., McSween, H.Y., Buchanan, P.C. (2012), Compositional constraints on the genesis of diogenites, *Meteoritics & Planetary Science*, **47**, 72-
- Moskovitz, N., Gaidos, E. (2011), Differentiation of planetesimals and the thermal consequences of melt migration, *Meteoritics & Planetary Science*, **46**, 903-918
- Neumann, W., Breuer, D., Spohn, T. (2014), Differentiation of Vesta: implications for a shallow magma ocean, *Earth and Planetary Science Letters*, **395**, 267-280
- Powell, R., Holland, T. (1988), An internally consistent dataset with uncertainties and correlations: 3. Applications to geobarometry, worked examples and a computer program. *Journal of Metamorphic Geology*, **6**, 173-204
- Righter, K., Drake, M.J. (1997), A magma ocean on Vesta: Core formation and petrogenesis of eucrites and diogenites, *Meteoritics & Planetary Science*, **32**, 929-944
- Roszjar, J., Whitehouse, M.J., Srinivasan, G., Mezger, K., Schere, E.E., Van Orman, J.A., Bischoff, A. (2016), Prolonged magmatism on 4 Vesta inferred from Hf-W analyses of eucrite zircon, *Earth and Planetary Science Letters*, **452**, 216-226
- Russell, C.T., Raymond, C.A., Coradini, A., McSween, H.Y., Zuber, M.T., Nathues, A., De Sanctis, M.C., Jaumann, R., Konopliv, A.S., Preusker, F., Asmar, S.W., Park, R.S., Gaskell, R., Keller, H.U., Mottola, S., Roatsch, T., Scully, J.E.C., Smith, D.E., Tricarico, P., Toplis, M.J., Christensen, U.R., Feldman, W.C., Lawrence, D.J., McCoy, T.J., Prettyman, T.H., Reedy, R.C., Sykes, M.E., Titus, T.N. (2012), Dawn at Vesta: testing the protoplanetary paradigm, *Science*, **336**, 684-686

- Ruzicka, A., Snyder, G.A., Taylor, L.A. (1997), Vesta as the howardite, eucrite, and diogenite parent body: Implications for the size of a core and for large-scale differentiation, *Meteoritics & Planetary Science*, **32**, 825-840
- Ruzicka, A., Snyder, G.A., Taylor, L.A. (2001), Comparative geochemistry of basalts from the Moon, Earth, HED asteroid, and Mars: implications for the origin of the Moon, *Geochimica et Cosmochimica Acta*, **65**, 979-997,
- Sanders, I.S., Scott, E.R.D., Delaney, J.S. (2017), Origin of mass-independent oxygen isotope variation among ureilites: clues from chondrites and primitive achondrites, *Meteoritics & Planetary Science*, **52**, 690-708
- Solomatov, V.S., Moresi, L.-N. (2000), Scaling of time-dependent stagnant lid convection: application to small-scale convection on Earth and other terrestrial planets, *Journal of Geophysical Research*, **105**, 21,795-21,817
- Sossi, P.A., Klemme, S., O'Neill, H. St.C., Berndt, J., Moynier, F. (2019), Evaporation of moderately volatile elements from silicate melts: experiments and theory, *Geochimica et Cosmochimica Acta*, **260**, 204-231
- Tomkins, A.G., Johnson, T.E., Mitchell, J.T. (2020), A review of the chondrite-achondrite transition, and a metamorphic facies series for equilibrated primitive stony meteorites, *Meteoritics & Planetary Science*, **54**, 857-885
- Tomkins, A.G., Weinberg, R.F., Schaefer, B.F., Langendam, A. (2013), Disequilibrium melting and melt migration driven by impacts: implications for rapid planetesimal core formation, *Geochimica et Cosmochimica Acta*, **100**, 41-59,
- Toplis, M.J., Mizzon, H., Monnereau, M., Forni, O., McSween, H.Y., Mittlefehdt, D.W., McCoy, T.J., Prettyman, T.H., De Sanctis, M.C., Raymond, C.A., Russell, C.T. (2013),

- Chondritic models of 4 Vesta: Implications for geochemical and geophysical properties, *Meteoritics & Planetary Science*, **48**, 2300-2315
- Wadhwa, M., Amelin, Y., Bogdanovski, O., Shukolyukov, A., Lugmair, G.W., Janney, P. (2009), Ancient relative and absolute ages for a basaltic meteorite: implications for timescales of planetesimal accretion and differentiation, *Geochimica et Cosmochimica Acta*, **73**, 5189-5201
- Whitney, D.L., Evans, B.W. (2010), Abbreviations for names of rock-forming minerals, *American Mineralogist*, **95**, 185-187
- Wilson, L., Keil, K. (2012), Volcanic activity on differentiated asteroids: A review and analysis, *Chemie der Erde*, **72**, 289-321
- Yamaguchi, A., Barrat, J.A., Ito, M., Bohn, M. (2011), Posteuclitic magmatism on Vesta: Evidence from the petrology and thermal history of diogenites, *Journal of Geophysical Research*, **116**, E08009
- Yamaguchi, A., Taylor, G.J., Keil, K. (1996), Global crustal metamorphism of the Eucrite Parent Body, *Icarus*, **124**, 97-112
- Yamaguchi, A., Taylor, G.J., Keil, K., Floss, C., Crozaz, G., Nyquist, L.E., Bogard, D.D., Garrison, D.H., Reese, Y.D., Wiesmann, H., Shih, C-Y. (2001), Post-crystallization reheating and partial melting of eucrite EET90020 by impact into the hot crust of asteroid 4Vesta ~4.50 Ga ago, *Geochimica et Cosmochimica Acta*, **65**, 3577-3599

*"To confine our attention to terrestrial matters
would be to limit the human spirit."*

Stephen Hawking



Chapter 4

A Comparison of Petrofabrics in Ureilites and Diogenites: Implications for Distinguishing Between Mantle Residue, Magma Cumulate, and Impact Melt Origins

Jennifer T. Mitchell¹, Andrew G. Tomkins¹, Natasha R.
Stephen², Floriana Salvemini³, Vladimir Luzin³, Helen E.A.
Brand⁴, Anton Maksimenko⁴

¹School of Earth, Atmosphere and Environment, Monash University, Australia

²Plymouth Electron Microscopy Centre, University of Plymouth, United Kingdom

³Australian Nuclear Science and Technology Organisation (ANSTO), Australia

⁴Australian Synchrotron, Australia

ABSTRACT

The use of petrofabric analysis is underutilised in planetary science and meteoritics. Here, we combine novel imaging and analytical techniques to determine key differences between the petrofabrics of ureilites (mantle residues) and diogenites (crustal cumulates). Optical microscopy of ureilites NWA 3140 and Watson 018 identified a shape-preferred orientation and elongation of the grain aspect ratio. DINGO neutron tomography and KOWARI strain scanner analysis confirm this lineation. We propose that the lineation observed in these samples was caused by high temperature pencil-glide during mantle shearing, updating previous views with reference to modern interpretations of ureilite petrogenesis. Imaging and Medical Beamline (IMBL) analysis of orthopyroxenite diogenites Dhofar 700, NWA 7977 and 8265 reveals abundant high-density accessory phases (sulfides, chromite, FeNi metals) throughout all samples, as well as rare low-density phase in NWA 7977, likely plagioclase or silica. Shock veins can also be identified using this technique. Diogenite foliations reported in literature are not detectable in IMBL, and we find that such alignment features are most likely due to shearing during magma migration through a complex network of dykes and the re-intrusion and subsequent mixing of magmas into crustal reservoirs, providing further compositional diversity during diogenite crystallisation as required by the wide range of natural diogenite compositions. Optical microscopy EBSD analysis of harzburgite diogenite NWA 5480 shows a pervasive poikilitic texture throughout the sample, with numerous dunite clastic in an orthopyroxene matrix. There is no evidence of grain orientation in this sample, and we conclude that NWA 5480 represents an impact melt sheet that has entrained a pre-existing dunite-harzburgite lithology. This is in contrast to previous studies that suggest NWA 5480 represents the Vestan mantle. Instead, we propose that Vesta's mantle is composed of high-Mg olivine and would likely display grain elongation and orientations similar to that of the ureilites studied here.

4.1. INTRODUCTION

Achondrite meteorites record a vast array of igneous and metamorphic processes occurring in the early Solar System, revealing complex evolutionary histories across many parent bodies. Investigating the behaviour of magmatism in the early Solar System allows us to better understand planet-forming processes. This study focuses on diogenites and ureilites, as they offer an opportunity to compare the textural features of ultramafic samples from different settings. Diogenites are predominately orthopyroxenitic cumulates, with rare examples of dunitic compositions, associated with asteroid 4 Vesta (McCord et al., 1970; De Sanctis et al., 2013). They are thought to represent either the results of mineral settling from a global magma ocean (Richter & Drake, 1997; Ruzicka et al., 1997; Takeda, 1997; Warren, 1997) or multiple crustal intrusions from diverse magmatic sources (Grove & Bartels, 1992; Domanik et al., 2004; Mandler & Elkins-Tanton, 2013; Clenet et al., 2014; Yamaguchi et al., 2015; *Chapter 2-3*, Mitchell & Tomkins, 2019). Ureilites are the carbon-rich pigeonite-olivine mantle residues of melt extraction from a catastrophically disrupted parent body (Goodrich et al., 2004; Downes et al., 2008). As such, these meteorites can reveal details about igneous and magmatic processes in the early Solar System.

Meteorite petrofabrics can preserve information about melt flow and mechanical disruptions to the system. For instance, electron backscatter diffraction analysis (EBSD) has been used to distinguish between magmatic flow and mineral settling/compaction in Martian nakhlites (Daly et al., 2019) and brachinite-like ungrouped achondrites (Hasegawa et al., 2019), as well as investigating the effects of shock metamorphism across various meteoritic mineral phases (Darling et al., 2016; Tomioka & Miyahara, 2017; Chen et al., 2019). However, EBSD can only provide information about a two-dimensional surface. The use of neutron and X-Ray

imaging allows researchers to analyse larger three-dimensional samples without damage and material loss. Neutron tomography recently has been used to investigate the internal structures of pallasites (Kichanov et al., 2018) and the relationship between kamacite and taenite crystals in iron meteorites (Caporali et al., 2016), showing great potential for the study of extra-terrestrial materials.

Here, we investigate the petrofabrics of diogenites Dhofar (Dho) 700, Northwest Africa (NWA) 7977 and 8265, and ureilites Northwest Africa 3140 and Watson 018 to determine processes occurring in asteroidal crustal intrusions and mantles respectively. We also examine Northwest Africa 5480, an unusual harzburgitic diogenite thought to represent either a sample of the Vestan mantle (Tkalcic et al., 2013) or a large-scale impact melt (Yamaguchi et al., 2015) to determine a likely provenance.

4.2. SAMPLES & METHODS

Three diogenite (Dho 700, NWA 7977, NWA 8265) and two ureilites (NWA 3140, Watson 018) whole-stone samples were selected for use in this study, as well as two ureilite thin sections of the same samples and an additional diogenite (NWA 5480). All samples are part of the Monash University meteorite collection.

The whole-stone diogenites used in this study are all orthopyroxenites, measuring approximately 3 cm³. Dho 700 is an unbrecciated unequilibrated diogenite, and one of the most ferroan diogenites in the global meteorite collection, displaying a granular texture composed of zoned orthopyroxene (En₆₂₋₇₁Wo_{2.5-7}) with accessory clinopyroxene (En₅₅₋₆₆Wo₈₋₂₅), olivine, plagioclase, silica, troilite, chromite, and FeNi metal (Russell et al., 2003; Barrat et al., 2008; Yamaguchi et al., 2011). Earlier petrological studies of Dhofar 700 identified thin chains of chromite grains that occur along healed fractures, and tiny troilite inclusions that are isolated in the orthopyroxene (Yamaguchi et al., 2011). NWA 7977 is composed of coarse-grained

orthopyroxene ($\text{En}_{72}\text{Fs}_{18}\text{Wo}_3$) with accessory troilite, chromite, silica, and FeNi metal (Ruzicka et al., 2015). NWA 8265 is similar in composition to NWA 7977, with orthopyroxene ($\text{En}_{74}\text{Wo}_3$), and accessory olivine, chromite, and troilite (Ruzicka et al., 2017). A polished 2.5 x 1.5 cm thin section of NWA 5480 was also used in this study. This is a harzburgitic diogenite (olivine $\text{Fa}_{30.2}\text{Fo}_{69.8}$, orthopyroxene $\text{En}_{575.2}\text{Fs}_{24.8}\text{Wo}_{1.8}$) with accessory chromite (Weisberg et al., 2009; Yamaguchi et al., 2015).

Our samples of ureilites NWA Africa 3140 and Watson 018 both measure approximately 2 cm³. NWA 3140 is composed of olivine ($\text{Fa}_{22.2-13.8}$), pigeonite ($\text{Fs}_{17.9}\text{Wo}_{9.1}$), interstitial metal and carbon phases including diamond (Russell et al., 2005). Watson 018 is also composed of olivine ($\text{Fa}_{20.4}$), pigeonite ($\text{Fs}_{16.9-17.2}\text{Wo}_{8.6}$), graphite and diamond, and has small metal blebs amongst the olivine (Bouvier et al., 2017). Petrological thin sections of both meteorites were also used in this study.

4.2.1. Optical Microscopy

The petrological thin section of diogenite NWA 5480 and ureilites NWA 3140 and Watson 018 were initially analysed using optical microscopy in both plane- and cross-polarised light at Monash University, Australia. We established areas of interest in the NWA 5480 thin section for further study in EBSD and recorded textural and compositional relationships across the sample. NWA 3140 and Watson 018 were studied further as whole rock samples using neutron scattering techniques.

4.2.2. Imaging & Medical Beamline

Analysis of diogenites Dho 700, NWA 7977, and NWA 8265 by X-ray computed tomography (XRCT) was conducted at the Imaging and Medical Beamline (IMBL) of the Australian Synchrotron. Although IMBL is predominately designed to image biological samples, it can

also be used in the study of inorganic materials. The potential uses of IMBL in planetary geology are explored in this study.

Samples were analysed at 90 keV beam energy using a 105 mm ruby detector, 20 μm screen, sample-to-detector distance of 0.7 m, and pixel size of 17.8 μm . Samples were stacked in plastic tubes and separated using polystyrene foam to allow data from multiple samples (exported as .tif files) to be collected in a single run. Similar to backscatter electron (BSE) imaging where the greyscale relates to atomic mass, the greyscale of the images produced by XRCT are dependent on density, measured as a function of X-ray absorption (denser materials block X-rays more effectively). High-density minerals appear as light greys and whites, whilst low-density materials as dark grey. Voids appear black.

The images collected were later imported into the Fiji (ImageJ) software (Schneider et al., 2012) and compiled into video files showing progression through each sample. Areas of specific interest were identified and individual frames were selected for brightness/contrast corrections to best show the variations in density. Accessory phases identified in these images were later colour coded to highlight distribution patterns and grain sizes.

4.2.3. Neutron Scattering Techniques; DINGO Neutron Tomography and KOWARI Strain Scanner

Neutron scattering techniques are somewhat new to the field of meteoritics and have traditionally been used to detect hydrogen-bearing phases within a sample. DINGO, part of the OPAL multi-purpose nuclear reactor run by ANSTO, Australia, is a neutron radiography, tomography, and imaging instrument (Garbe et al., 2015). DINGO utilises neutron radiation to image contrasts in neutron absorption and scattering in three-dimensional samples across a wide range of materials and fields of study. The total linear attenuation coefficient (μ) describes

the fraction of the neutron beam that is absorbed or scattered per unit thickness of the sample.

This is defined as follows (Yilmaz et al., 2011):

The transmitted intensity $I(\lambda)$ of the neutron beam with incident intensity $I_0(\lambda)$ follows the Beer-Lambert Law;

$$I(\lambda) = I_0(\lambda)e^{-\sum_i(\mu(\lambda)d)_i}$$

where $\mu(\lambda)$ is the total linear attenuation coefficient for a given isotope, i , that the neutron beam interacts with within the sample thickness, d . At neutron wavelength λ , the total linear attenuation coefficient $\mu(\lambda)$ of an isotope is defined as;

$$\mu(\lambda) = \sigma_t(\lambda) \frac{\rho N_A}{M}$$

where $\sigma_t(\lambda)$ is the total cross-section for neutron absorption and scattering, ρ is the density, N_A is Avogadro's number, and M is atomic mass.

DINGO neutron tomography analysis of diogenites Dho 700, NWA 7977, NWA 8265, and ureilites NWA 3140 and Watson 018 was carried out using a pixel size of 14.7 μm and a 30 μm thick scintillation screen, with a field of view of 74 x 43 mm^2 to image the entirety of the samples selected for study. A total of 1800 projections were acquired at 0.1° intervals over 360° with an exposure time of 19 seconds per acquisition. Neutron tomography data generated by DINGO is collected as greyscale images where the gradient is reflective of the total neutron attenuation coefficient. This allows different phases within the sample to be highlighted because each mineral has unique absorption characteristics. Hydrogen is particularly effective at blocking neutrons, and this feature allows effective mapping of hydrated mineral phases in geological samples. The images produced via neutron tomography are thus quite distinct to those produced by X-ray tomography.

The KOWARI strain scanner, another non-destructive neutron-source instrument at OPAL, analyses the residual stress in the 3D crystal lattice of samples through neutron scattering (Brule & Kirstein, 2006; Kirstein et al., 2009). KOWARI analysis of ureilites NWA 3140 and Watson 018 was undertaken using wavelength $\lambda = 1.5 \text{ \AA}$, using a Si(400) monochromator at 67° , measurements on $\sim 3^\circ \times 3^\circ$ sphere to maximise grain statistics, detector Bragg angle $2\theta = 36^\circ$, and detector coverage $\sim 11^\circ$. This set up covers many diffraction peaks of the olivine spectrum, appropriate for the study of ureilites. The indices in which data are reported relate to the following crystallographic axes of olivine: $a = 10.236 \text{ \AA}$; $b = 6.00 \text{ \AA}$; $c = 4.7668 \text{ \AA}$.

4.2.4. Electron Backscatter Diffraction

The thin section of NWA 5480 was polished using a Buehler Vibromet and carbon-coated prior to analysis at Plymouth Electron Microscopy Centre, University of Plymouth, United Kingdom. Imaging was conducted using a Zeiss Crossbeam 550 using an accelerating voltage of 15 kV and 10 nA. EBSD analysis used an Oxford Instruments Symmetry detector paired with AZtec software. An Oxford Instruments UltiMax 170 detector was used to assist with phase identification via EDS. Operating procedures were varied to optimise the diffraction signal and are reported individually for each data set. The analyses used standard phases from both the International Crystal Structure Database (ICSD) and American Mineralogist; olivine ICSD[83791], Haiber et al., (1997); pyroxene variety enstatite, Yang & Ghose, (1995); chromite ICSD[432691], Shirone et al., (1964). Post-processing was completed using AZtecCRYSTAL, with a minimal data-cleaning regime applied to each map. The minimum hit rate for raw data was approximately 85% before processing. Crystallographic preferred orientations (CPO) of minerals were analysed in reference to their major crystallographic axes: $\langle a \rangle = \{100\}$; $\langle b \rangle = \{010\}$; $\langle c \rangle = \{001\}$. Data were plotted on upper hemisphere equal area projections (pole figures) and contoured with respect to the density of data points, expressed as multiples of uniform density (m.u.d.).

4.3. RESULTS

4.3.1. Optical Microscopy

Optical microscopy of diogenite NWA 5480 (Fig. 4.1) identified a heterogeneous distribution of olivine and orthopyroxene across the thin section, with minor amounts of fine-grained opaque phases such as iron sulfide, chromite, and Fe-Ni metals. Olivine occurs as irregular, sub-angular to sub-rounded grains and multi-grain clasts measuring up to 3 mm in a crystalline orthopyroxene matrix. These clasts typically display adcumulate textures with both rounded boundaries and granulitic areas (average grain size 300 μm). The olivine maintains sharp contacts with the orthopyroxene matrix, and commonly contains fine inclusion trails, identified in plane-polarised light. Olivine also occurs as pervasive blebby chadacrysts (<20 μm) throughout the orthopyroxene matrix across the whole sample with no apparent orientation.

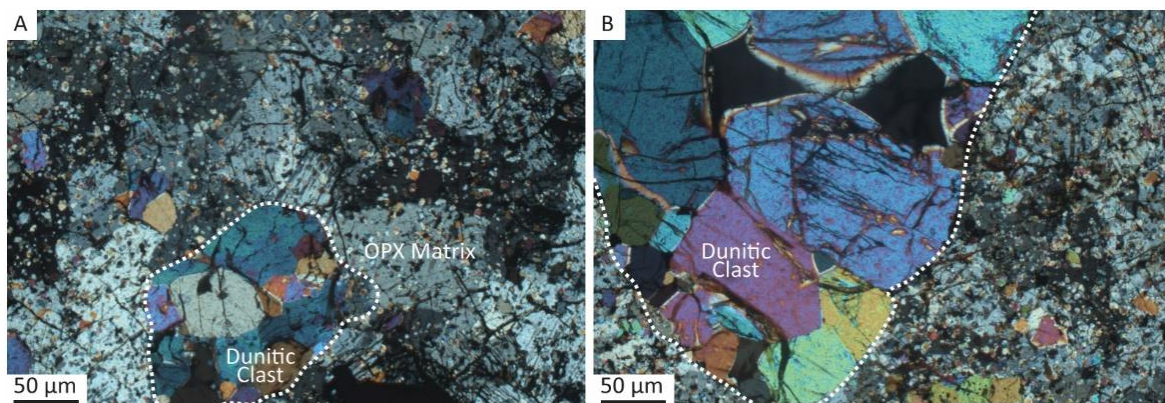


Figure 4.1. Photomicrographs of NWA 5480. A) Cross-polarised light image of a small dunitic clast and fragments in relation to the coarse orthopyroxenite matrix with pervasive olivine oikocrysts; B) Cross-polarised light image of a dunitic clast and the pervasive olivine oikocrysts that are present throughout the poikilitic matrix orthopyroxene.

The orthopyroxene-dominated matrix is composed of irregular interlocking grains, measuring <1 mm along the longest axis, with no observed twinning nor exsolution. No shape preferred orientation (SPO) of any mineral phase was noted in optical microscopy.

Ureilite Watson 018 (Fig. 4.2) displays a phaneritic texture of anhedral angular olivine and pigeonite grains, measuring up to approximately 7 mm along the longest axis, bounded by

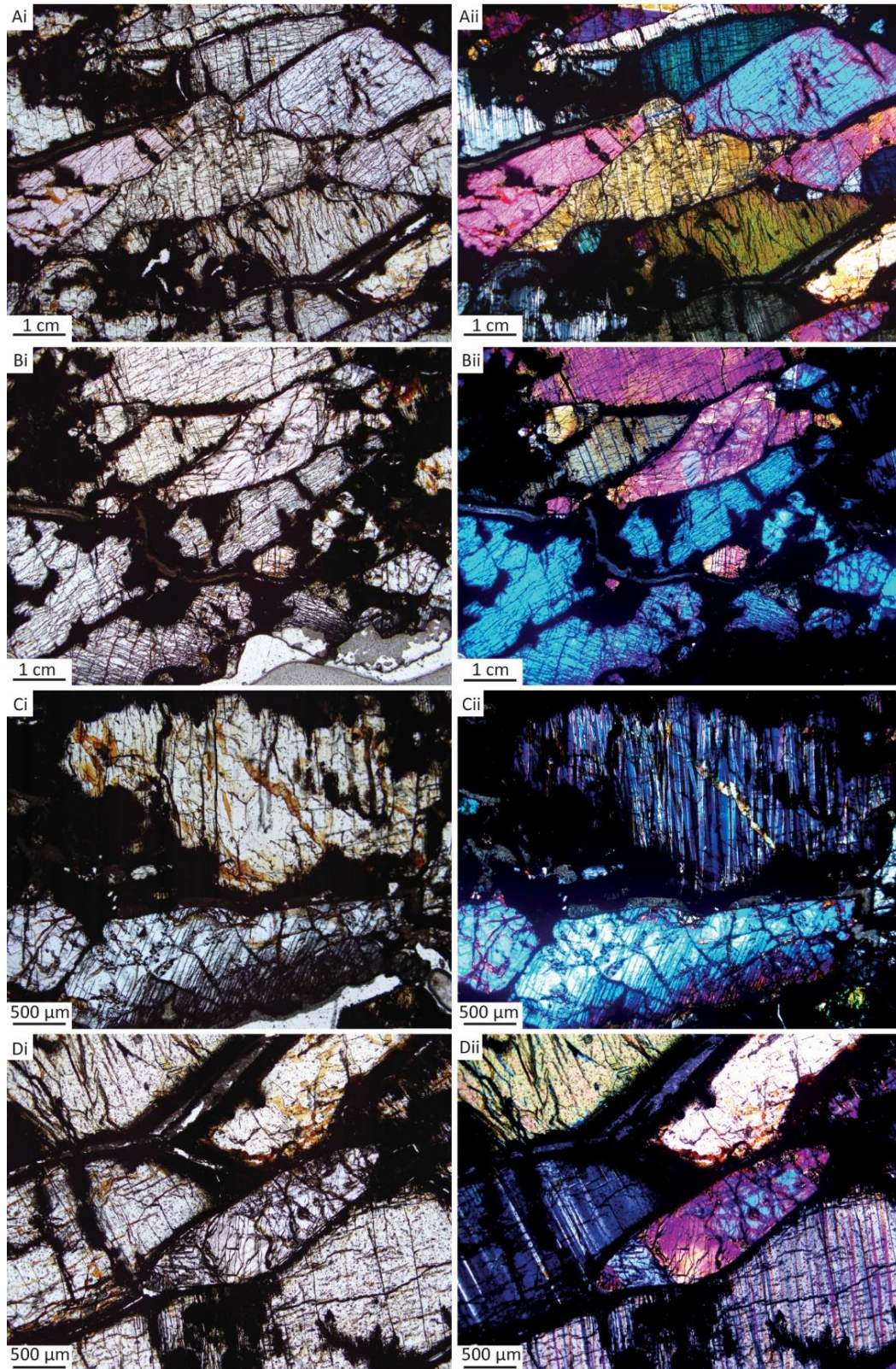


Figure 4.2. Photomicrographs of Watson 018 in i) plane-polarised light and ii) cross-polarised light. A) Olivine and pigeonite grains exhibiting elongation and shape-preferred orientation approximately NE-SW relative to the image, best compared to the Z axis defined by the DINGO data (Fig. 6). Pigeonite shows lamellar twinning and the central olivine grain shows polysynthetic twinning; B) Olivine grains near the edge of the sample, showing a distinct elongation; C) Pigeonite grains with extensive polysynthetic shock twinning; D) Polysynthetic twinning of elongated olivine grains. Opaque phases are graphite and metal/sulphide accessory phases.

graphite. Mineral grains show an elongation of the grain aspect ratio across the sample. A number of olivine grains have polysynthetic twins, and extinction is undulose in places. Pigeonite displays lamellar twinning. Both olivine and pigeonite grains showing a consistent elongation and shape preferred orientation across the sample section, which has been cut close to the Z axis of the DINGO data (Fig. 4.6).

The thin section of NWA 3140 (Fig. 4.3) shows a relatively equigranular texture of olivine (2-3 mm on average) and opaque phases (graphite, metal/sulphide accessory phases). The

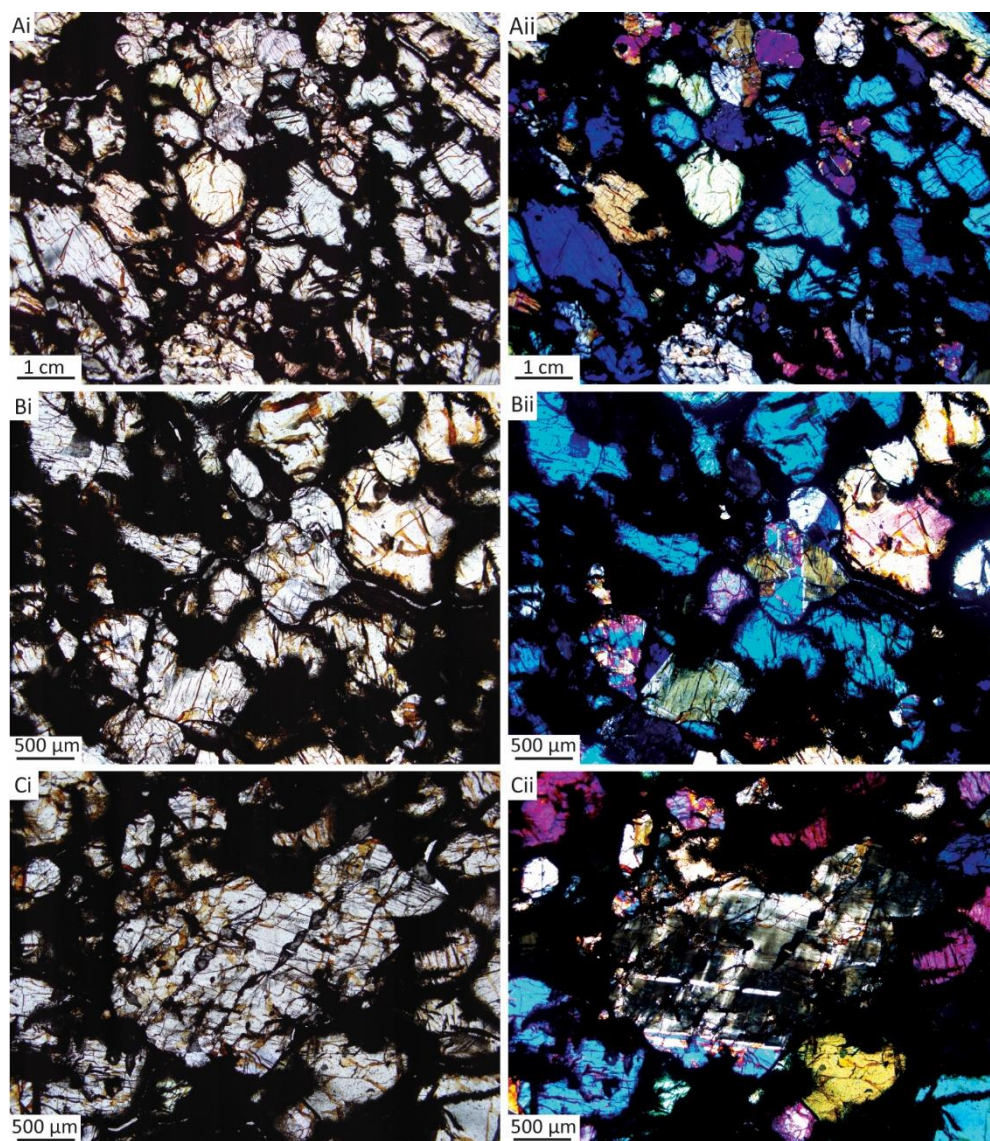


Figure 4.3. Photomicrographs of NWA 3140 in i) plane-polarised light and ii) cross-polarised light. A) Olivine grains showing a slight alignment NW-SE relative to the picture, best related to x-axis (blue) in DINGO data (Fig.6); B) Rare polysynthetic twinning of central olivine grain; C) Shocked pigeonite grain. Opaque material is graphite and metallic accessory phases.

orientation of this thin section is similar to the X axis of the DINGO data (Fig.6) and does not effectively show any foliation or lineation. However, a slight alignment can be observed in some of the elongated olivine grains. Polysynthetic twins are rare in this sample. Extinction is slightly undulose, and there are sparse examples of shocked grains.

4.3.2. Imaging & Medical Beamline

A total of 1485 images were collected of Dhofar 700, 1393 of NWA 7977, and 1153 of NWA 8265. Both Dhofar 700 and NWA 8265 were off centre during the run time, and some of the sample is obscured as a result. However, the majority of both samples are observed. NWA 7977 was correctly centred, and the full sample is visible in the data. All samples display high and mid density accessory phases, thought to be FeNi metals and sulphide/chromite respectively. Sulphide phases and chromite cannot be differentiated here due to their similar density. Fracture networks are observed in all samples, and the widest of these fractures sometimes contain low-density weathering products, which appear as very dark grey vein-like features in the IMBL density greyscale. The pyroxenes are crystalline and do not vary in density, so it is not possible to determine pyroxene grain sizes using this technique.

Dhofar 700 contains the lowest abundance of accessory phases. Both FeNi metal (< ~1 mm) and sulphide (< ~2 mm) grains are observed as sparse inclusions within orthopyroxene and are predominantly concentrated in a shock vein that can be traced through approximately 1/3 of the sample (Fig. 4.4).

NWA 7977 contains abundant FeNi metal (< ~3 mm) and sulphide/chromite (< ~3 μm) throughout the sample, with a number of very fine sulphide veins composed of elongate grains observed throughout the sample that are oriented NW-SE with respect to the view shown in Figure 4.4. The FeNi metal grains are typically larger than the sulphide/chromite grains. This is the only sample examined in this study to contain a rare low-density accessory phase within

the orthopyroxene, thought to be plagioclase as it does not appear to be associated with fracturing or other shock effects.

NWA 8265 contains fine sulphide and FeNi metal grains with no apparent pattern to their distribution (Fig. 4.4). The FeNi metal grains are typically larger than the sulphides in this sample, measuring up to approximately 1.5 μm and 4 μm respectively. There are some fine sulphide veins that appear to infill fractures in places.

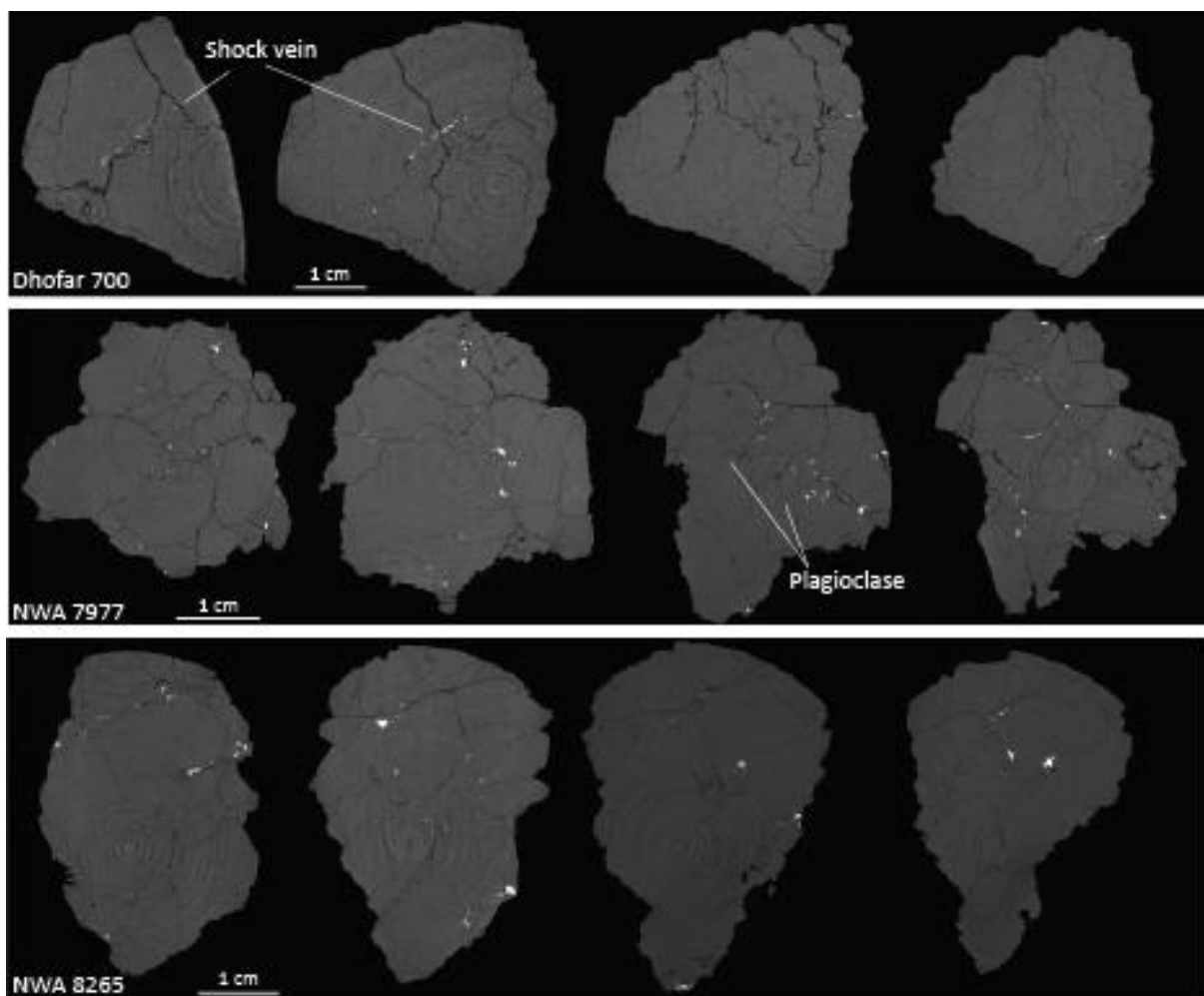


Figure 4.4. X-Ray computed tomography images from IMBL of diogenites Dhofar 700, NWA 7977, and NWA 8265. High density phases such as FeNi metals show as white and sulfides appear as light grey. Low density phases such as plagioclase or silica appear as darker grey than the dominant orthopyroxene.

4.3.3. Neutron Scattering Techniques; DINGO Neutron Tomography and KOWARI Strain Scanner

The lack of variation in mineralogy in diogenites Dhofar 700, NWA 7977, and NWA 8265 (Fig. 4.5) means that it is not possible to determine grain size nor clear inferences about internal structure from DINGO data. However, all samples show weathering infill in fractures (appearing as white) and metal and sulphide accessory phases (black). Although the shock vein in Dhofar 700 does appear in this data set, it is significantly less apparent than in the IMBL data output.

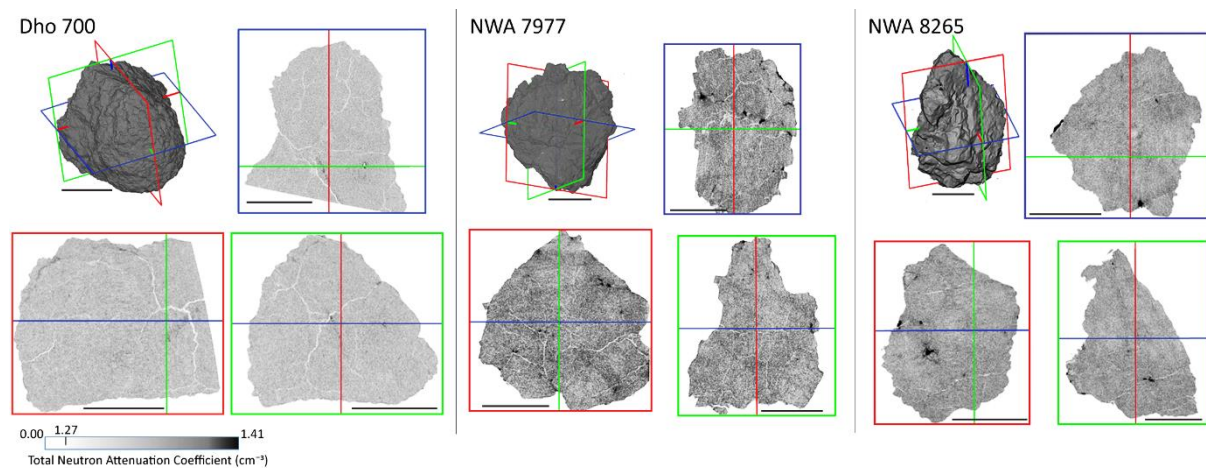


Figure 4.5. DINGO data of diogenites Dhofar 700, NWA 7977 and NWA 8265. Metals and sulfides appear as black, orthopyroxene as grey, and fracture infill as white.

In contrast, the DINGO analysis of ureilites NWA 3140 and Watson 018 clearly shows the internal structure of these samples due to the differences in neutron attenuation between the silicate and carbon-rich phases present in ureilites. In this instance, the olivine appears as light grey and the carbon as dark grey to black, highlighting clear grain boundaries (Fig. 4.6). Silicate grains in Watson 018 range in size from submillimetre to 5 mm, whereas silicate grains in NWA 3140 are typically 2-3 mm along the longest axis. A clear lineation was observed in both samples, where the olivine grains are elongated and aligned. KOWARI strain scanner analysis finds that both ureilite samples studied here show similar alignments in (301), (311), and (121) (Fig. 4.6), both strongest in (301), the olivine c-axis. Watson 018 has a stronger lineation as

ascribed by higher I values (sharpness of texture compared to the background) and density of data (max. number). As the ureilites studied here are whole-rock samples, the KOWARI data also includes the graphite and accessory phases. However, as olivine is the dominant phase, we can infer that the data can be largely considered in terms of olivine orientation.

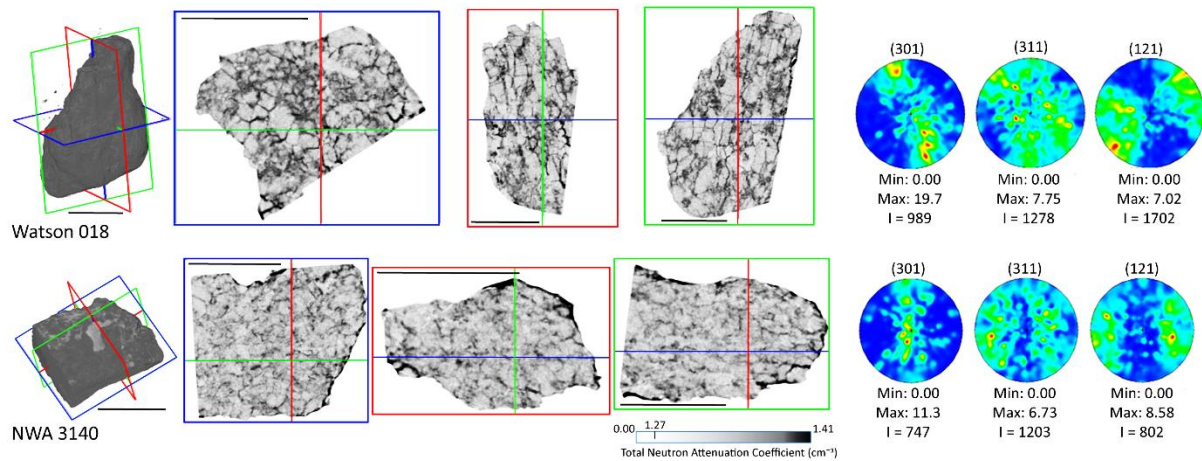


Figure 4.6. DINGO and KOWARI strain scanner data for ureilites Watson 018 and NWA 3140. DINGO data shows clear mineral elongation and long-axis alignment in 2 axes (red, green), perpendicular to short-axis (blue). In these images, graphite, metals, and sulphides appear as black, and olivine and pigeonite as grey. Both samples display similar alignments, strongest in (301) and (121). Max = 1 represents a random orientation and Max = >1 signifies an alignment. The I value refers to the sharpness of the texture relative to the background. Higher I values relate to stronger, more defined textures.

4.3.4. Electron Backscatter Diffraction

The pyroxenes of NWA 5480 range of $\text{En}_{74.33-79.23}\text{Fs}_{16.69-23.51}\text{Wo}_{1.40-2.62}$ (Mg# 65-70), with a mean of $\text{En}_{76.62}\text{Fs}_{21.34}\text{Wo}_{1.95}$ (n=28). This is in keeping with the composition recorded in the Meteoritical Society Bulletin Database ($\text{En}_{73.4}\text{Fs}_{24.8}\text{Wo}_{1.8}$), and thus NWA 5480 is one of the more Mg-rich diogenites in the global meteorite collection (Fig. 4.7). Olivine compositions are $\text{Fa}_{23.40-27.53}\text{Fo}_{76.6-72.47}$ (Mg#60-65), with a mean at $\text{Fa}_{25.84}\text{Fo}_{74.16}$ (n=23). Compositions for both olivine and pyroxene are compiled in Table 4.1. No compositional zoning is observed in the sample. These values are consistent with other olivine-bearing diogenite compositions recorded in the Meteoritical Society Bulletin Database.

Five sites were selected for analysis by EBSD. Two large area montages focused on dunite clasts and the surrounding orthopyroxene matrix (Fig. 4.8A-B) and three higher magnification

Table 4.1. Pyroxene and olivine compositions of NWA 5480.

Pyroxene						Olivine			
Ens	Fs	Wo	Ens	Fs	Wo	Fa	Fo	Fa	Fo
77.58	20.12	2.3	74.98	22.87	2.15	26.18	73.82	23.4	76.6
75.43	21.94	2.62	78.82	16.69	1.49	25.79	74.21	23.69	76.31
75.41	22.55	2.04	79.23	19.44	1.34	27.53	72.47	23.95	76.05
75.96	21.96	2.08	78.43	20.03	1.63	26.84	73.16	26.78	73.22
76.17	21.59	2.24	79.03	19.28	1.69	26.39	73.61	26.66	73.34
76.58	21.16	2.26	78.76	19.83	1.41	25.8	74.2	26.87	73.13
76.08	22.02	1.9	78.8	19.53	1.68	25.61	74.39	26.74	73.26
75.6	22.08	2.32	78.69	19.91	1.4	26.19	73.81	26.95	73.05
75.43	22.49	2.08	75.23	22.71	2.06	27.33	72.67	27.01	72.99
77.51	20.41	2.09	75.38	22.55	2.07	25.81	74.19		
77.49	21.03	1.47	74.33	23.51	2.16	26.69	73.31		
75.25	23	1.75	75.71	22.07	2.23	25.27	74.73		
75.82	22.14	2.03	75.4	22.56	2.04	23.43	76.57		
76.49	21.5	2.01	75.72	22.5	2.04	23.44	76.56		

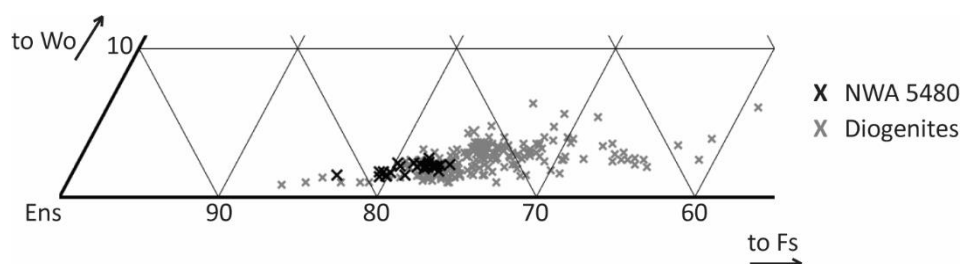


Figure 4.7. Pyroxene compositions of NWA 5480 compared to natural diogenite compositions (data from Meteoritical Bulletin Database).

areas centred on the poikiloblastic orthopyroxene (indexed as enstatite) matrix and olivine chadacrysts (Fig. 4.8C-E). The two large area montages indexed 2714 and 882 grains, respectively, at a hit rate >79.7 % and the higher magnification scans indexed 1642, 228, and 375 grains at hit rates upwards of 88.3 %.

Band contrast and phase mapping of the dunite clasts found granular textures with 120° triple junctions. The olivine chadacrysts are completely separate to the dunite clasts and are restricted entirely to the orthopyroxene matrix. Neither the dunite clasts nor orthopyroxene matrix record a preferred orientation. No alignment was observed in the olivine chadacrysts.

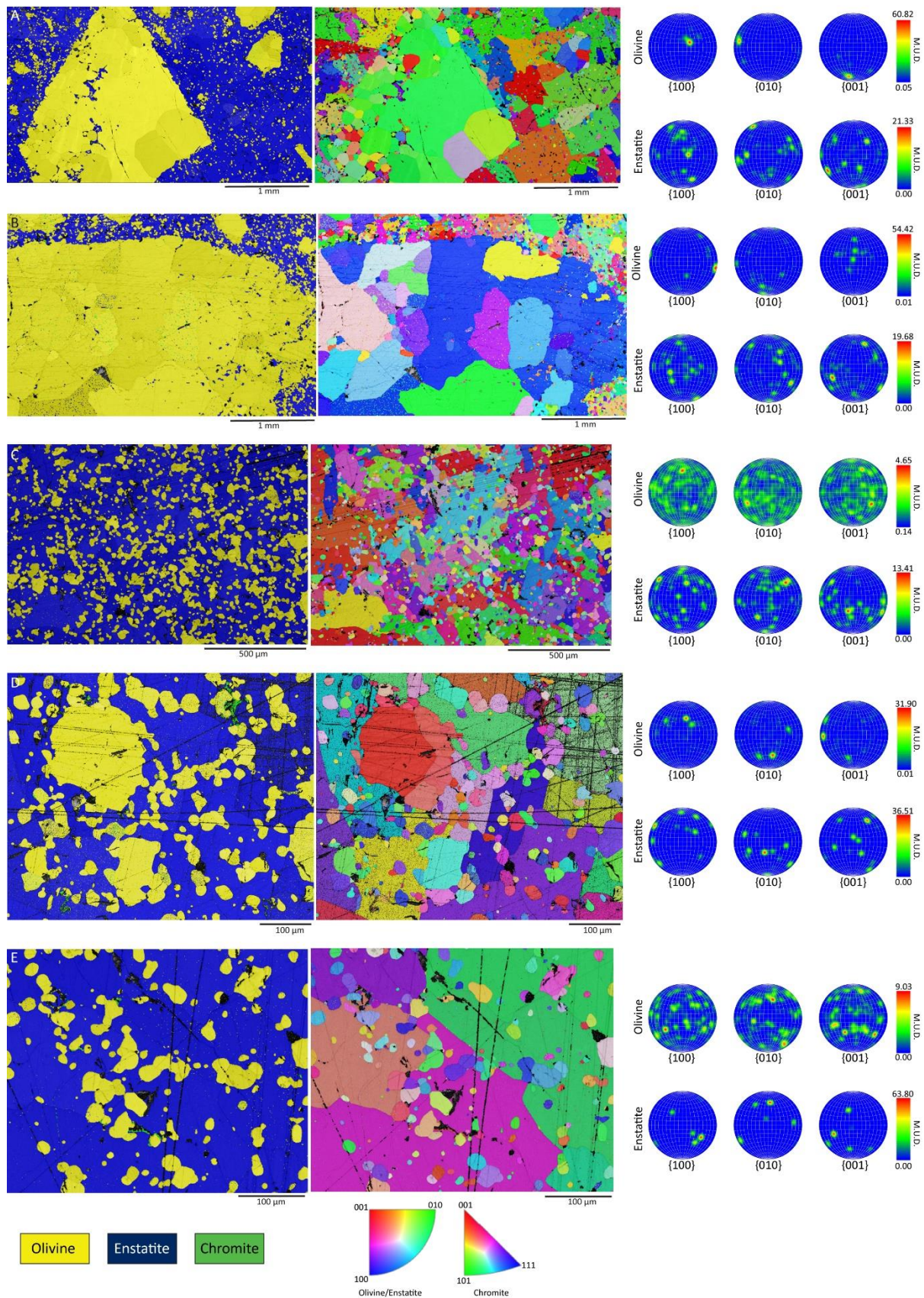


Figure 4.8. EBSD phase maps (left) indexed for olivine, enstatite (orthopyroxene) and chromite, and IPF maps (right) of NWA 5480 with associated pole figures. A-B) large area maps focused on dunite clasts and their relationship with the surrounding matrix; C-E) higher magnification images of the orthopyroxene matrix and olivine poikiloblasts. {100} relates to the a-axis, {010} to the b-axis, and {001} to the c-axis.

4.4. DISCUSSION

4.4.1. Mineral Alignment in Asteroidal Mantles

Magmatic lineations (Fig. 4.9) develop when the long-axis (c-axis) of crystals align due to shearing, typically approximately parallel to the shear direction, with the short axes (a/b-axis) alignment forming perpendicular to this (Nicolas, 1992; Bhattacharyya, 1996; Paterson, 1988; Mizukami et al., 2004). DINGO neutron tomography and KOWARI strain scanner data of NWA 3140 and Watson 018 presented in this study show a clear lineation that is consistent with reports of lineations in other ureilite samples (Berkley et al., 1976, 1980; Goodrich et al., 1984; Takeda, 1986; Lorenz et al., 2019). The lineation of ureilites, defined by the c-axis of olivine, was previously proposed to have been generated through laminar flow in a dynamic melt (Berkley et al., 1976, 1980) or through compaction processes in a crustal magma chamber (Walker & Agee, 1988). However, since these initial studies, limited work has been done on investigating other possible causes of this alignment. Additionally, both the Berkley et al., (1976) and Walker & Agee (1988) model are now out of date because ureilites are widely accepted to be the mantle residues of silicate melt extraction (Kita et al., 2004; Goodrich et al., 2007; Barrat et al., 2015, 2016; Collinet & Grove, 2020).

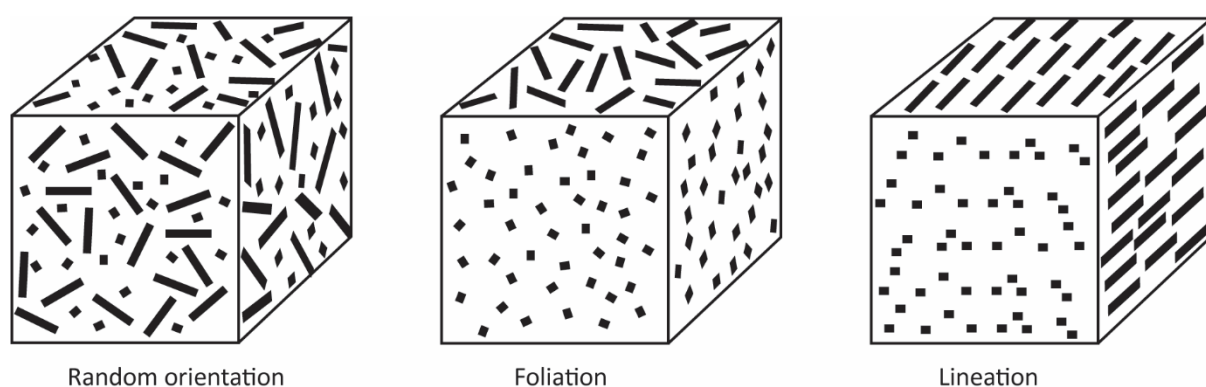


Figure 4.9. Differences in crystal orientation between random (no) orientation, foliation, and lineation. Magmatic foliation occurs when minerals settle and compact, developing a short-axis alignment in one or two axes perpendicular to the settling motion in a plane. Lineation develops during shearing etc. to create a long-axis alignment in two planes.

The shape preferred orientations observed in the DINGO neutron tomography data of NWA 3140 and Watson 018 suggest that these samples underwent shearing to elongate and align the mineral grains approximately parallel to the direction of shear, as has been observed in experimental modelling of the behaviour of olivine during shearing (Zhang et al., 2000). Shear-induced crystallographic alignment of olivine has also been observed in samples from the Earth's mantle (Mainprice & Nicolas, 1989; Mancktelow et al., 2002; Sawaguchi & Ishii, 2003; Arbaret et al., 2007). There, peridotites develop a crystallographic preferred orientation through mantle flow where diffusion creep, dislocation creep, and grain boundary accommodated sliding occur as a function of stress and grain size (Chatzaras et al., 2016) during solid-state plastic deformation (Ismail & Mainprice, 1998; Tommasi et al., 2000; Warren & Hirth, 2006). It is not unlikely that similar processes can occur in an asteroidal setting. Compaction, as suggested by Walker & Agee (1988), is therefore an unlikely mechanism to generate this texture as this process results in a short-axis alignment (Naslund & McBirney, 1996; Paterson et al., 1998; 1989), not a long-axis alignment as observed in the ureilites studied here.

The data produced for NWA 3140 and Watson 018 by the KOWARI strain scanner are most similar to the orientation characteristics produced by the 'pencil-glide' system, where plastic deformation through shearing in the [100] direction is accommodated by multiple planes (Raleigh, 1968; Ismail & Mainprice, 1998; Tommasi et al., 2000; Mahendran et al., 2019). Pencil-glide occurs at upwards of 1000 °C (Raleigh, 1968) – achievable in the ureilite parent body mantle prior to disruption (Goodrich et al., 2004, 2007) – with moderate strain rates in near melt-free conditions (Carter & Ave'Lallemant, 1970; Holtzman et al., 2003). Both Watson 018 and NWA 3140 are residual assemblages, meaning that melt has been removed as evidenced by the lack of plagioclase in these samples (Cohen et al., 2004), and as the deformation regime suggested here requires low-absent melt conditions, we can infer that the deformation must have after occurred melt extraction.

Therefore, we suggest that the lineation in ureilites represents shearing forces in the UPB mantle that were present after melt extraction. Pencil-glide has also been reported in olivine from pallasite meteorites (Klosterman & Buseck, 1973) – stony iron meteorites representing the core-mantle boundary of disrupted differentiated asteroids (Boesenberg et al., 2012) – which suggests that solid-state deformation was a widespread mantle process across asteroid bodies of various sizes. The study of additional ureilites may add further weight to this view, particularly through the use of techniques such as the KOWARI strain scanner in which whole-stone samples can be analysed thus reducing observation biases resulting from available cut surfaces.

4.4.2. Mineral Alignment in Asteroidal Magma Chambers

Magmatic foliations (Fig. 4.9) are developed through gravitational settling and compaction of crystals in a stagnant magma chamber/intrusion (Daly et al., 2019) and appears as an alignment of one or two crystal axes – typically short-axis – in a plane (Naslund & McBirney, 1996; Paterson et al., 1998; 1989). On Earth, magmatic foliations are often best observed in ultramafic-mafic intrusive complexes (Jackson, 1961; George, 1978; McBirney & Noyes, 1979; Vukmanovic et al., 2018), and they have also recently been identified in Martian nakhlites MIL 03346 and Lafayette (Daly et al., 2019). Modelling of convecting magma chambers has suggested that a stagnant layer exists at the bottom of intrusions (Jaupart & Brandeis, 1986). This layer produces a magmatic foliation, whilst the actively convecting regime would develop a further foliation displayed as an additional alignment of the long-axis parallel to the direction of movement within the magma body (Bhattacharyya, 1966; Correa-Gomes et al., 20011; Vukmanovic et al., 2018; Daly et al., 2019).

The rate of mineral settling is approximated by Stokes' Law, where the terminal velocity of a spherical particle (v_s) settling through a liquid – in this case a magma – is defined as follows:

$$v = \frac{2(\rho_p - \rho_f)gr^2}{9\mu}$$

Where v = downward settling velocity of the crystal, ρ_p = density of the particle, ρ_f = density of the fluid, μ = dynamic viscosity, g = gravitational acceleration, and r = radius of the particle. As such, the rate of mineral settling is partly dependent on the strength of gravity, reducing the rate at which minerals settle. The effects of this in addition to cooling of the melt are presented in Walker et al., (1978) with regards to eucrite melts in particular, finding that the accumulation of crystals slows as the process nears completion. Despite this, Ruzicka et al., (1997) presented a model for mineral settling in a non-turbulent global magma ocean on Vesta, where 1 mm particles settle relatively quickly early in Vesta's history at a maximum of 21.5 km/year in a melt crystallising olivine, with diogenite-like compositions accumulating at a rate of > 0.137 km/year before slowing down as the melt evolves and cool, becoming increasingly viscous. Although diogenites likely represent crustal magma chambers as opposed to a magma ocean cumulates (see *Chapter 2* and *Chapter 3*), we can infer that these melt bodies also underwent similar rates of mineral settling as the variables applicable to Stokes' Law remain the same. There are modifications to Stokes' Law applicable to dense phases settling through crystal-bearing magmas (e.g., Chung and Mungall, 2009), but these are not considered to be applicable to orthopyroxene accumulation because there are not expected to be lower density crystals in the magma at the same time.

The IMBL and DINGO data for diogenites Dho 700, NWA 7977 and 8265 do not appear to show a shape-preferred orientation within these samples. The apparent lack of a lineation suggests that they may represent crystal settling in a stagnant regime. The lack of foliation is more difficult to reconcile but may be consistent with the low gravity environment where compaction would be minimised. However, without conclusive crystallographic alignment data – be it EBSD or KOWARI – it is not possible to draw firmer conclusions. This stage of

the project was heavily impacted by the Covid-19 pandemic and data collection was not able to be completed due to multiple facility shut-downs.

Alignment data for three olivine-bearing diogenites is presented in Tkalcec & Brenker (2014) wherein EBSD analysis of NWA 5480, NWA 5784, and Miller Range (MIL) 07001,6 was performed. The authors identify a foliation in all three samples (weakest in MIL 07001,6) that they propose is the result of solid-state plastic deformation in Vesta's upper mantle, dominated by shearing, although they did not rule out a magma chamber origin for MIL 07001,6. They proposed that the deformation observed in these samples studied required high temperatures (1196-1299 °C) to occur, and is used in support of their argument for a mantle origin. However, as established in *Chapter 2* (Mitchell & Tomkins, 2019) and *Chapter 3*, and by other authors (e.g. Grove & Bartels, 1992; Mittlefehldt, 1994; Yamaguchi et al., 2015), diogenites – including olivine-bearing diogenites – most likely represent multiple discrete crustal intrusions. Similarly, samples from terrestrial magma chambers show evidence of this same mechanism of olivine deformation (Yao et al., 2017). Additionally, it would be expected that the proposed mantle shearing and solid-state deformation as seen in ureilites generates a lineation as opposed to a foliation (Fig. 4.9).

The development of the foliation reported by Tkalcec & Brenker (2014) leads to the consideration of more complex magmatic structures on Vesta. Numerical modelling of dyke propagation on Vesta finds that the low gravity environment coupled with HED rheologies allows for the development of extensive crustal intrusions (Wilson & Keil, 1996). This result is consistent with widespread development of magma reservoirs in the upper lithosphere where gravitational settling can occur to produce cumulates (Wilson & Keil, 2012). These reservoirs were likely fed by a number of dykes due to fracturing of the host rock during initial emplacement (Wilson & Keil, 1996; Abdelmalak et al., 2012; Hou, 2012; Rivalta et al., 2015). The THERMOCALC modelling presented in *Chapter 3* finds that the temperatures proposed

in Tkalcec & Brenker (2014) are consistent with olivine-orthopyroxenitic and harzburgitic diogenite crystallisation, and even at the highest pressures modelled, the system contains up to approximately 15 % liquid. This temperature requirement is therefore not immediately indicative of a mantle environment, and we can infer that some degree of convection would occur in parts of these intrusions. As stated previously, convecting magma chambers can develop a stagnant regime near the base (Jaupart & Bandeis, 1986), developing a gravitational settling magmatic foliation, while other regions of the intrusion record evidence of a dynamically circulating magma during crystallisation (Žák et al., 2005, 2008; Correa-Gomes et al., 2011; Vukmanovic et al., 2018; Daly et al., 2019). Additionally, the recharge of magma from the multiple feeder dykes and subsequent mixing can also cause motion within magma chambers, as well as scouring of chamber walls and fast compaction to re-orient and deform pre-existing crystals (Bergantz, 2000; Yao et al., 2019) to generate shape and lattice preferred orientations.

As such, the alignments reported in olivine-bearing diogenites may be the result of multiple processes occurring during magmatism and crystallisation. Orientation-forming stresses such as shearing can occur during magma transport and emplacement and rapid compaction (Yao et al., 2017), further exacerbated by magma recharge from multiple feeder dykes (Wilson & Keil, 1996; 2012; Bergantz, 2000). External stressors can also contribute to developing multiple magmatic fabrics (Žák et al., 2005, 2008; Correa-Gomes et al., 2011). Diogenite meteorite samples represent only small parts of a larger system, meaning that the foliations reported by Tkalcec & Brenker (2014) may or may not be a consistent feature of the class. Further analysis of both olivine-bearing and orthopyroxenitic diogenites is required to decipher the mechanisms at play during syn- and post-crystallisation processes. Mineral compositions are therefore perhaps the best way to distinguish mantle rocks from crustal intrusions, and this is discussed

in greater detail in the next section regarding the provenance of harzburgitic diogenite NWA 5480.

4.4.3. An Impact Melt Sheet Origin for NWA 5480

NWA 5480 has been proposed to represent either a sample of the Vestan mantle (Tkalcec et al., 2013; Tkalcec & Brenker, 2014, 2015), or an impact-melt (Yamaguchi et al., 2015). Although these are two distinctly different interpretations, they are not mutually exclusive because it is plausible that a mantle component underwent impact melting. Tkalcec et al., (2013) and Tkalcec & Brenker (2014, 2015) suggested that the olivine in NWA 5480 underwent a number of stages of plastic deformation through mantle shear within 50 Myr of CAI formation, as well as a period of remelting and slow cooling to produce the coarse-grained poikilitic texture observed throughout the sample. EBSD data presented in these studies show a weak foliation in olivine grains with M-index values < 0.19 , where $M = 1$ indicates a single crystal fabric and $M = 0$ represents a random fabric (Skemer et al., 2005). These values are roughly comparable to those of a number of ungrouped achondrites (Hasegawa et al., 2019) and to terrestrial peridotite samples (Warren et al., 2008).

Yamaguchi et al., (2015) suggested that the heterogeneous and poikilitic nature of NWA 5480 is the result of a large impact event – such as might occur during the formation of Rheasilvia. A very large impact may have caused remelting of a harzburgitic target rock, with olivine-rich domains less effected by melting than orthopyroxene. These authors also highlighted that lattice preferred orientation in olivine can be produced by more than one process. For instance, impact processes could generate the strain that Tkalcec et al., (2013) and Tkalcec & Brenker (2015) observed in the olivine crystals. Also, grazing impacts (Asphaug et al., 2006; Consolmagno et al., 2015) could be responsible for shearing in the deep crust and upper mantle of Vesta (Yamaguchi et al., 2015), although this mechanism is disputed by Tkalcec & Brenker,

(2019). Yamaguchi et al., (2015) also calculated that NWA 5480 cooled at a depth of several tens of metres based on the work of Miyamoto (1997), significantly shallower than some eucrites (Miyamoto & Takeda, 1994) and certainly not at mantle depths (Jutzi et al., 2013; Clenet et al., 2014). Yamaguchi et al., (2015) compared the petrographic textures observed in NWA 5480 to those of chondritic melt breccias and found a number of similarities including irregularly shaped clasts and grains, flow textures, and the growth of fine grains at favourable nucleation sites around larger clasts and fragments.

EBSD analysis of the dunite clasts in NWA 5480 (Fig. 4.8) presented in this study did not find evidence of preferred orientation. The random crystal orientation in these clasts suggests that the olivine crystals in the clasts did not undergo shearing during crystallisation, which is especially apparent when compared to the distinct lineation observed in ureilites. Although a foliation has been reported for this sample by Tkalcec et al., (2013) and Tkalcec & Brenker (2014, 2015), as discussed previously there are a number of ways for this texture to develop in non-mantle environments and cannot be used to signify a mantle origin. The adcumulate textures observed within the NWA 5480 dunite clasts suggests that the precursor lithology underwent compaction in a magma chamber, which drove off interstitial liquid (Schmidt et al., 2012; Holness et al., 2017; Yao et al., 2017; Vukmanovic et al., 2018) – a process that clearly occurred on Vesta given the presence of other adcumulate HED samples (Lovering, 1975; Hsu & Corzaz, 1997; Barrat et al., 2006). However, the heterogeneous distribution of crystalline olivine and orthopyroxene with no apparent alignment suggests that NWA 5480 had a more complex history.

The poikiloblastic texture and mineralogical heterogeneity of NWA 5480 is unusual in diogenites, immediately suggesting that this meteorite formed in a setting distinct from most diogenites. On Earth, poikilitic textures with orthopyroxene oikocrysts and olivine chadacrysts are common in multi-staged mafic and ultramafic intrusions (Wager et al., 1960; Barnes et al.,

2016), and they are also common to ultramafic shergottites where they are thought to represent deep cumulate processes in the Martian crust (Combs et al., 2019; Udry et al., 2020). Detailed studies of many large and contextualised samples on Earth suggest that this texture develops through infiltration of orthopyroxene-saturated melt through olivine cumulate with the olivine being partly resorbed in a peritectic reaction (Barnes et al., 2016; Kaufmann et al., 2018). In the case of NWA 5480, the preservation of minor element zoning in olivine, pyroxene, and chromite combined with the finer-than-typical grain size of the orthopyroxene (diogenites are typically medium to coarse grained) suggests comparatively rapid cooling of the sample; likely in a near-surface environment (Miyamoto, 1977; Yamaguchi et al., 2015). We suggest that the dunite clasts likely represent a pre-existing cumulate lithology that has been brecciated and entrained into a new melt, around which large orthopyroxene crystals grew. The olivine chadacrysts likely represent pre-existing crystals that were partly resorbed during melt infiltration (Barnes et al., 2016).

Both the olivine and orthopyroxene compositions of NWA 5480 are not the most primitive of the HEDs in the global meteorite collection (Fig. 4.7) as would be expected from a sample of the Vestan mantle (Mitchell & Tomkins, 2019), and instead plot with other olivine-bearing diogenite samples. Vesta's mantle should be composed of Mg-rich residual olivine compared to the compositions of olivine formed in crustal cumulates. High-Mg olivine (Mg# 80-92) and pyroxene (Mg# 85-92) fragments have been identified in howardites that cannot be ascribed to an established Vestan lithology and are proposed to have a mantle origin (Lunning et al., 2015; Hahn et al., 2018). Mg# values for NWA 5480 generated in this study are significantly lower (olivine Mg# 60-65; pyroxene Mg# 65-70), and the pyroxene compositions are in keeping with other olivine-bearing diogenites (Mitchell & Tomkins, 2019). Yamaguchi et al., (2015) showed that NWA 5480 cooled rapidly at a rate of several tens of °C/year – much faster than eucrite

crystallisation (Takeda, 1997) – meaning that there was little time for compositions to evolve in the melt (Cassanelli & Head, 2016).

Given the above points, we suggest that a mantle origin for NWA 5480 is unlikely. Instead, we propose that NWA 5480 most likely represents a large impact melt sheet that resulted from an impact into a diogenitic target rock with dunitic components, to satisfy the rapid cooling rate. The lack of a mantle exposure on Vesta (Ammannito et al., 2013; Ermakov et al., 2014; Ruesch et al., 2014), coupled with the FeO-rich olivine composition, implies that the target rock was diogenite-like material. A large impact would be needed to generate a hot, large volume melt sheet (Yamaguchi et al., 2015), likely requiring a crater some hundreds of kilometres in diameter (Warren et al., 1996; Keil et al., 1997). The most likely source for NWA 5480 is therefore the Rheasilvia or Veneneia impact basins. Rheasilvia is approximately 500 km wide and excavated material from a depth of 60-100 km where the crater overlaps with the older 400 km diameter Veneneia impact basin (Ivanov & Melosh, 2013; Jutzi et al., 2013; Clenet et al., 2014), and is floored by predominately orthopyroxene-dominated breccias (McSween et al., 2013; Ammannito et al., 2015). Imaging carried out by NASA's Dawn probe finds a number of craters within the Rheasilvia basin, allowing for material – possibly NWA 5480 – to be liberated after the melt sheet had cooled and solidified.

Although Vesta's mantle is seemingly unsampled outside of potential mineral fragments in howardites (Lunning et al., 2015; Hahn et al., 2015), it is possible to draw some conclusions as to what would be expected. The mantle is most likely composed of high-Mg olivine beneath a crust thickened by serial magmatism and intrusions (Yamaguchi et al., 2011; Clenet et al., 2014), and was not sufficiently uplifted during the Veneneia and Rheasilvia impact events to be exposed at the surface (Ermakov et al., 2014). Mantle samples would be distinguishable from typical diogenites due to the lack of major orthopyroxene, coarse equigranular textures, elevated Mg contents, and possibly a consistent high-temperature/high-pressure lineation

across numerous samples – as seen in ureilites and terrestrial mantle samples – developed during mantle shear.

4.5. CONCLUSIONS

The study of meteorite petrofabrics allows us to interrogate a multitude of magmatic and deformational processes that occurred in the early Solar System. Here, we have combined optical microscopy, EBSD, Synchrotron source X-Ray imaging, and neutron scattering techniques to investigate variations in achondrite petrofabrics from two distinct bodies – Vesta and the ureilite parent body – to compare mechanisms responsible for the development of mineral alignment in mantle, magma chamber, and impact melt sheet settings.

Optical microscopy and neutron scattering analysis of ureilites NWA 3140 and Watson 018 has identified a clear shape- and crystal-preferred orientation indicative of high temperature shear deformation in a mantle setting after melt extraction, updating previous interpretations with regards to modern ureilite genesis theories.

Although data collection of diogenite samples was disrupted by the Covid-19 pandemic, we have utilised literature to evaluate reported plastic deformation in context of crustal magma chambers. We conclude that the reported foliation in some diogenite samples may be the result of complex ongoing magmatism, involving the re-intrusion of melt into crustal magma reservoirs and shearing during melt migration. Because magma chambers and crustal intrusions undergo a wide range of processes, and individual diogenite meteorites only sample localised areas, it is likely that diogenites record multiple fabrics across the group.

Based on the use of optical microscopy and EBSD, and comparison with published research on similar rocks from multi-stage ultramafic intrusions on Earth, we suggest that an impact melt sheet origin is the most likely explanation for diogenite NWA 5480. This meteorite has a poikilitic texture with orthopyroxene oikocrysts enveloping olivine chadacrysts in matrix

containing dunitic clasts – very unusual for a diogenite. The minerals in these components are unoriented in all areas analysed, and the mineral compositions are not primitive enough to satisfy a mantle origin. Instead, we propose that NWA 5480 represents scenario where a high temperature impact melt derived from a diogenitic target incorporated pre-existing dunitic clasts, reacting with and partly resorbing the olivine to form the orthopyroxene oikocrysts.

Finally, we reiterate that it does not appear likely that a sample of Vesta’s mantle exists in the global meteorite collection. Based on our findings here, we expect the Vestan mantle to be composed of high Mg, coarse-grained olivine that likely records evidence of high temperature-high pressure deformation comparable to the textures seen in ureilites.

4.6. ACKNOWLEDGEMENTS AND AUTHOR CONTRIBUTIONS

Funding for this study was provided part of A.G.T.’s position at Monash University. This project was developed by J.T.M. Optical microscopy was carried out by J.T.M. and A.G.T. DINGO neutron tomography was run by F.S. and KOWARI strain scanner by V.L. IMBL data was collected by J.T.M. and H.E.A.B. with assistance from A.M. EBSD analysis was carried out by N.R.S.

4.7. CHAPTER REFERENCES

Abdelmalak, M.M., Mourgues, R., Galland, O., Bureau, D. (2012), Fracture mode analysis and related surface deformation during dyke intrusion: results from 2D experimental modelling, *Earth and Planetary Science Letters*, **359**, 93-105

Ammannito, E., De Sanctis, M.C., Combe, J.-Ph., Frigeri, A., Jaumann, R., Longobardo, A., McSween, H.Y., Palomba, E., Tosi, F., Raymond, C.A., Russell, C.T., the Dawn Science Team (2015), Compositional variations in the Vestan Rheasilvia basin, *Icarus*, **259**, 194-202

- Ammannito, E., De Sanctis, M.C., Palomba, E., Longobardo, A., Mittlefehldt, D.W., McSween, H.Y., Marchi, S., Capria, M.T., Capaccioni, F., Frigeri, A., Pieters, C.M., Ruesch, O., Tosi, F., Zambon, F., Carraro, F., Fonte, S., Hiesinger, H., Magni, G., McFadden, L.A., Raymond, C.A., Russell, C.T., Sunshine, J.M. (2013), Olivine in an unexpected location on Vesta's surface, *Nature*, **504**, 122-125
- Arbaret, L., Bystricky, M., Champallier, R. (2007), Microstructures and rheology of hydrous synthetic magmatic suspensions deformed in torsion at high pressure, *Journal of Geophysical Research*, **112**, B10208
- Asphaug, E. (2010), Similar-sized collisions and the diversity of planets, *Chemie der Erde*, **70**, 199-219
- Asphaug, E., Agnor, C.B., Williams, Q. (2006), Hit-and-run planetary collisions, *Nature*, **439**, 155-160
- Barnes, S.J., Mole, D.R., Le Vaillant, M., Campbell, M.J., Verrall, M.R., Roberts, M.P., Evans, N.J. (2016), Poikilitic textures, heteradcumulates and zoned orthopyroxenes in the Ntaka ultramafic complex, Tanzania: implications for crystallization mechanism of oikocrysts, *Journal of Petrology*, **57**, 1171-1196
- Barrat, J.-A., Beck, P., Bohn, M., Cotton, J., Gillet, Ph., Greenwood, R.C., Franchi, I.A. (2006), Petrology and geochemistry of the fine-grained, unbrecciated diogenite Northwest Africa 4215), *Meteoritics & Planetary Science*, **41**, 1045-1057
- Barrat, J.-A., Jambon, A., Yamaguchi, A., Bischoff, A., Rouget, M-L., Liorzou, C. (2016), Partial melting of a C-rich asteroid: lithophile trace elements in ureilites, *Geochimica et Cosmochimica Acta*, **194**, 163-178

- Barrat, J.-A., Rouxel, O., Wang, K., Moynier, F., Yamaguchi, A., Bischoff, A., Langlade, J. (2015), Early stages of core segregation recorded by Fe isotopes in an asteroidal mantle, *Earth and Planetary Science Letters*, **419**, 93-100
- Barrat, J.-A., Yamaguchi, A., Greenwood, R.C., Benoit, M., Cotton, J., Bohn, M., Franchi, I.A. (2008), Geochemistry of diogenites: still more diversity in their parental melts, *Meteoritics & Planetary Science*, **43**, 1759-1775
- Berganz, G.W. (2000), On the dynamics of magma mixing by reintrusion: implications for pluton assembly processes, *Journal of Structural Geology*, **22**, 1297-1309
- Berkley, J.L., Gassaway-Brown, H., Keil, K., Carter, N.L., Mercier, J.-C.C. (1976), The Kenna ureilite: an ultramafic rock with evidence for igneous, metamorphic, and shock origin, *Geochimica et Cosmochimica Acta*, **40**, 1429-1437
- Berkley, J.L., Taylor, J.T., Keil, K., Harlow, G.E., Prinz, M. (1980), The nature and origin of ureilites, *Geochimica et Cosmochimica Acta*, **44**, 1579-1597
- Bhattacharyya, D.S. (1966), Orientation of mineral lineation along the flow direction in rocks, *Tectonophysics*, **3**, 29-33
- Boesenberg, J.S., Delaney, J.S., Hewins, R.H. (2012), A petrological and chemical re-examination of Main Group pallasite formation, *Geochimica et Cosmochimica Acta*, **89**, 134-158
- Bouvier, A., Gattacceca, J., Grossman, J., Metzler, K. (2017), The meteoritical bulletin, No. 105, *Meteoritics & Planetary Science*, **52**, 2411
- Brule, A., Kirstein, O. (2006), Residual stress diffractometer KOWARI at the Australian research reactor OPAL: status of the project, *Physica B*, **385-386**, 1040-1042

- Carter, N.L., Ave'Lallemant, H.G. (1970), High temperature flow of dunite and peridotite, *Geological Society of America Bulletin*, **80**, 2181-2202
- Cassanelli, J.P., Head, J.W. (2016), Did the Orientale impact melt sheet undergo large-scale igneous differentiation by crystal settling, *Geophysical Research Letters*, **43**, 11156-11165
- Chatzaras, V., Kruckenberg, S.C., Cohen, S.M., Medaris, L.G., Withers, A.C., Bagley, B. (2016), Azial-type olivine crystallographic preferred orientations: the effect of strain geometry on mantle texture, *Journal of Geophysical Research: Solid Earth*, **121**, 4895-4922
- Chen, D.-L., Zhang, A.-I., Pang, R.-L., Chen, J.-N., Li, Y. (2019), Shock-induced phase transformation of anorthitic plagioclase in the eucrite meteorite Northwest Africa 2650, *Meteoritics & Planetary Science*, **54**, 1548-1562
- Chung, H.-Y., Mungall, J.E. (2009), Physical constraints on the migration of immiscible fluids through partially molten silicates, with special references to magmatic sulphide ores, *Earth and Planetary Science Letters*, **286**, 14-22
- Clenet, H., Jutzi, M., Barrat, J.A., Ashpaug, E.I., Benz, W., Gillet, P. (2014), A deep crust-mantle boundary in the asteroid 4 Vesta, *Nature*, **511**, 303-306
- Cohen, B.A., Goordich, C.A., Keil, K. (2004), Feldspathic clast population in polymict ureilites: stalking the missing basalts from the ureilite parent body, *Geochimica et Cosmochimica Acta*, **68**, 4249-4266
- Collinet, M., Grove, T.L. (2020), Incremental melting in the ureilite parent body: initial composition, melting temperatures, and melt compositions, *Meteoritics & Planetary Science*, **55**, 832-856

- Combs, L.M., Udry, A., Howarth, G.H., Righter, M., Lapen, T.J., Gross, J., Ross, D.K., Rahib, R.R., Day, J.M.D. (2019), Petrology of the enriched poikilitic shergottite Northwest Africa 10169: insight into the martian interior, *Geochimica et Cosmochimica Acta*, **266**, 435-462
- Consolmagno, G.J., Golabek, G.J., Turrini, D., Jutzi, M., Sirono, S., Svetsov, V., Tsiganis, K. (2015), Is Vesta intact and pristine protoplanet? *Icarus*, **254**, 190-201
- Correa-Gomes, L.C., Souza Filho, C.R., Martins, C.J.F.N., Oliveira, E.P. (2001), Development of symmetrical and asymmetrical fabrics in sheet-like igneous bodies: the role of magma flow and wall-rock displacements in theoretical and natural cases, *Journal of Structural Geology*, **23**, 1415-1428
- Daly, L., Piazzolo, S., Lee, M.R., Griffin, S., Chung, P., Campanaka, F., Cohen, B.E., Hallis, L.J., Trimby, P.W., Baumgartner, R., Forman, L.V., Benedix, G.K. (2019), Understanding the emplacement of Martian volcanic rocks using petrofabrics of the nakhlite meteorites, *Earth and Planetary Science Letters*, **520**, 220-230
- Darling, J.R., Moser, D.E., Barker, I.R., Tait, K.T., Chamberlain, K.R., Schmitt, A.K., Hyde, B.C. (2016), Variable microstructural response of baddeleyite to shock metamorphism in young basaltic shergottite NWA 5298 and improved U-Pb dating of solar system events, *Earth and Planetary Science Letters*, **444**, 1-12
- De Sanctis, M.C., Ammannito, E., Capria, M.T., Capaccioni, F., Combe, J.-P., Frigeri, A., Longobardo, A., Magni, G., Marchi, S., McCord, T.B., Palomba, E., Tosi, D., Zambon, F., Carraro, F., Fonte, S., Li, Y.J., McFadden, L.A., Mittlefehldt, D.W., Pieters, C.M., Jaumann, R., Stephan, K., Raymond, C.A., Russell, C.T. (2013), Vesta's mineralogical composition as revealed by the visible and infrared spectrometer on Dawn, *Meteoritics & Planetary Science*, **48**, 2166-2184

- Domanik, K., Kolar, S., Musselwhite, D., Drake, M.J. (2004), Accessory silicate mineral assemblages in the Bilanga diogenite: a petrographic study, *Meteoritics & Planetary Science*, **39**, 567-579
- Downes, H., Mittlefehldt, D.W., Kira, N.T., Valley, J.W. (2008), Evidence from polymict ureilite meteorites for a disrupted and re-accreted single ureilite parent asteroid gardened by several distinct impactors, *Geochimica et Cosmochimica Acta*, **72**, 4825-4844
- Ermakov, A.I., Zuber, M.T., Smith, D.E., Raymond, C.A., Balmino, G., Fu, R.R., Ivanov, B.A. (2014), Constrains on Vesta's interior structure using gravity and shape models from the Dawn mission, *Icarus*, **240**, 146-160
- Garbe, U., Randall, T., Hughes, C., Davidson, G., Pangelis, S., Kennedy, S.J. (2015), A new neutron radiography/tomography/imaging station DINGO at OPAL, *Physics Procedia*, **69**, 27-32
- George, R.G. (2018), Structural petrology of the Olympus ultramafic complex in the Troodos ophiolite, Cyprus, *Geological Society of America Bulletin*, **89**, 845-865
- Goodrich, C.A. (1992), Ureilites: a critical review, *Meteoritics*, **27**, 327-352
- Goodrich, C.A., Keil, K., Berkley, J.L., Laul, J.C., Smith, M.R., Wacker, J.F., Clayton, R.N., Mayeda, T.K. (1984), Roosevelt County 027: a low-shock ureilite with interstitial silicates and high noble gas concentrations, *Meteoritics*, **22**, 191-218
- Goodrich, C.A., Scott, E.R.D., Fioretti, A.M. (2004), Ureilitic breccias: clues to the petrologic structure and impact disruption of the ureilite parent asteroid, *Chemie der Erde*, **64**, 283-327

- Goodrich, C.A., Van Orman, J.A., Wilson, L. (2007), Fractional melting and smelting on the ureilite parent body, *Geochimica et Cosmochimica Acta*, **71**, 2876-2895
- Grove, T.L., Bartels, K.S. (1992), The relation between diogenite cumulates and eucrite magmas, *Proceedings of Lunar and Planetary Science*, **22**, 437-445
- Greenwood, R.C., Franchi, I.A., Jambon, A., Barrat, J.-A., Burbine, T.H. (2006), Oxygen isotope variation in stony-iron meteorites, *Science*, **313**, 1763-1765
- Hahn, T.M., Lunning, N.G., McSween, H.Y., Bodnar, R.J., Taylor, L.A. (2018), Mg-rich harzburgites from Vesta: mantle residua or cumulates from planetary differentiation, *Meteoritics & Planetary Science*, **53**, 514-546
- Haiber, M., Ballone, P., Parrinella, M. (1997), Structure and dynamics of protonated Mg₂SiO₄; an ab-initio molecular dynamics study, *American Mineralogist*, **82**, 913-922
- Haswgawa, H., Mikouchi, T., Yamaguchi, A., Yasutake, M., Greenwood, R.C., Franchi, I.A. (2019), Petrological, petrofabric, and oxygen isotopic study of five ungrouped meteorites related to brachinites, *Meteoritics & Planetary Science*, **54**, 752-767
- Hiroshi, T. (1997), Mineralogical records of early planetary processes on the howardite, eucrite, diogenite parent body with reference to Vesta, *Meteoritics & Planetary Science*, **32**, 841-853
- Holness M.B., Vukmanovic, Z., Mariani, E. (2017), Assessing the role of compaction in the formation of adcumulates: a microstructural perspective, *Journal of Petrology*, **58**, 643-674
- Holtzman, B.K., Kohlstedt, D.L., Zimmerman, M.E., Heidelbach, F., Hiraga, T., Hustoft, J. (2003), Melt segregation and strain partitioning: implications for seismic anisotropy and mantle flow, *Science*, **301**, 1227-1230

- Hou, G. (2012), Mechanism for three types of mafic dyke swarms, *Geoscience Frontiers*, **3**, 217-223
- Hsu, W., Crozaz, G. (1997), Mineral chemistry and the petrogenesis of eucrite: II cumulate eucrites, *Geochimica et Cosmochimica Acta*, **61**, 1293-1302
- Ismail, W.B., Mainprice, D. (1998), An olivine fabric database: an overview of upper mantle fabrics and seismic anisotropy, *Tectonophysics*, **296**, 145-157
- Ivanov, B.A., Melosh, H.J. (2013), Two-dimensional numerical modeling of the Rheasilvia impact formation, *Journal of Geophysical Research: Planets*, **118**, 1545-1557
- Jackson, E. (1961), Primary textures and mineral association in the ultramafic zone of the Stillwater complex, Montana, 2230-7102
- Jaupart, C., Brandeis, G. (1986), The stagnant bottom layer of convecting magma chambers, *Earth and Planetary Science Letters*, **80**, 183-199
- Jutzi, M., Asphaug, E., Gillet, P., Barrat, J.-A., Benz, W. (2013), The structure of the asteroid 4 Vesta as revealed by models of planet-scale collisions, *Nature*, **494**, 207-210
- Kaufmann, F.E.D., Vukmanovic, Z., Holness, M.B., Hecht, L. (2018), Orthopyroxene oikocrysts in the MG1 chromitite layer of the Bushveld Complex: implications for cumulate formation and recrystallisation, *Contributions to Mineralogy and Petrology*, **173**, 17
- Keil, K., Stöffler, D., Love, S.G., Scott, E.R.D. (1997), Constraints on the role of impact heating and melting in asteroids, *Meteoritics & Planetary Science*, **32**, 349-363
- Kirstein, O., Luzin, V., Garbe, U. (2009), The strain-scanning diffractometer KOWARI, *Neutron News*, **20**, 34-36

- Kita, N.T., Ikeda, Y., Togashi, S., Liu, Y., Morishita, Y., Weisberg, M.K. (2004), Origin of ureilites inferred from a SIMS oxygen isotopic and trace element study of clasts in the Dar al Gani 319 polymict ureilite, *Geochimica et Cosmochimica Acta*, **68**, 4213-4235
- Klosterman, M.J., Buseck, P.R. (1973), Structural analysis of olivine in pallasitic meteorites: deformation in planetary interiors, *Journal of Geophysical Research*, **78**, 7581-7588
- Lorenz, C.A., Shiryaev, A.A., Vlasov, I.I., Borisovsky, S.E. (2019), Metamorphism of four desert ureilites and luminescence spectroscopy of defects in ureilitic diamonds, *Meteoritics & Planetary Science*, **54**, 1197-1214
- Lovering, J.F. (1975), The Moama eucrite – a pyroxene-plagioclase adcumulate, *Meteoritics*, **10**, 101-114
- Lunning, N.G., McSween, H.Y., Tenner, T.J., Kita, N.T., Bodnar, R.J. (2015), Olivine and pyroxene from the mantle of asteroid 4 Vesta, *Earth and Planetary Science Letters*, **418**, 126-135
- Mahendran, S., Carrez, Ph., Cordier, P. (2019), On the glide of [100] dislocation and the origin of pencil glide' in Mg₂SiO₄ olivine, *Philosophical Magazine*, **99**, 2751-2769
- Mainprice, D., Nicolas, A. (1989), Development of shape and lattice preferred orientations: application to the seismic anisotropy of the lower crust, *Journal of Structural Geology*, **11**, 175-189
- Mancktelow, N.S., Arbaret, L., Pennacchioni, G. (2002), Experimental observations on the effect of interface slip on rotation and stabilisation of rigid particles in simple shear and a comparison with natural mylonites, *Journal of Structural Geology*, **24**, 567-585

- Mandler, B.E., Elkins-Tanton, L.T. (2013), The origin of eucrite, diogenites, and olivine diogenites: magma ocean crystallization and shallow magma chamber processes on Vesta, **48**, 2333-2349
- McBirney, A.R., Noyes, R.M. (1979), Crystallization and layering of the Skaergaard intrusion, *Journal of Petrology*, **20**, 487-554
- McCord, T.B., Adams, J.B., Johnson, T.V. (1970), Asteroid Vesta: spectral reflectivity and compositional implications, *Science*, **168**, 1445-1447
- McSween, H.Y., Ammannito, E., Reddy, V., Prettyman, T.H., Beck, A.W., De Sanctis, M.C., Nathues, A., Le Corre, L., O'Brien, D.P., Yamashita, N., McCoy, T.J., Mittlefehldt, D.W., Toplis, M.J., Schenk, P., Palomba, E., Turrini, D., Tosi, F., Zambon, F., Longobardo, A., Cappaccioni, F., Raymond, C.A., Russell, C.T. (2013), Composition of the Rheasilvia basin, a window into Vesta's interior, *Journal of Geophysical Research: Planets*, **118**, 335-346
- Mitchell, J.T., Tomkins, A.G. (2019), On the source of diogenites and olivine diogenites: compositional diversity from variable fO_2 , *Geochimica et Cosmochimica Acta*, **258**, 37-49
- Mittlefehldt, D.W. (1994), The genesis of diogenites and HED parent body petrogenesis, *Geochimica et Cosmochimica Acta*, **58**, 1537-1552
- Miyamoto, M. (1997), Chemical zoning of olivine in several pallasites, *Journal of Geophysical Research*, **102**, 21613-21618
- Miyamoto, M., Takeda, H. (1994), Evidence for excavation of deep crustal material of a Vesta-like body from Ca compositional gradients in pyroxene, *Earth and Planetary Science Letters*, **122**, 343-349

- Mizukami, T., Wallis, S.R., Yamamoto, J. (2004), Natural examples of olivine lattice preferred orientation patterns with a flow-normal a-axis maximum, *Nature*, **427**, 432-436
- Naslund, H.R., McBirney, A.R. (1996), Mechanisms of formation of igneous layering, *Developments in Petrology*, **15**, 1-43
- Nicolas, A. (1992), Kinematics in magmatic rocks with special reference to gabbros, *Journal of Petrology*, **33**, 891-915
- Paterson, S.R., Fowler, T.K., Schmidt, K.L., Yoshinobu, A.S., Yuan, E.S., Miller, R.B. (1998), Interpreting magmatic fabric patterns in plutons, *Lithos*, **44**, 53-82
- Paterson, S.R., Vernon, R.H., Tobisch, O.T. (1989), A review of criteria for the identification of magmatic and tectonic foliations in granitoids, *Journal of Structural Geology*, **11**, 349-363
- Raleigh, C.B. (1968), Mechanisms of plastic deformation of olivine, *Journal of Geophysical Research*, **73**, 5391-5406
- Righter, K., Drake, M.J. (1997), A magma ocean on Vesta: core formation and petrogenesis of eucrites and diogenites, *Meteoritics & Planetary Science*, **32**, 929-944
- Rivalta, E., Taisne, B., Bungler, A.P., Katz, R.F. (2015), A review of mechanical models of dike propagation: schools of thought, results and future directions, *Tectonophysics*, **638**, 1-42
- Ruesch, O., Hiesinger, H., De Sanctis, M.C., Ammannito, E., Palomba, E. Longobardo, A., Zambon, F., Tosi, F., Capria, M.T., Capaccioni, F., Frigeri, A., Fonte, S., Magni, G., Raymond, C.A., Russell, C.T. (2014), Detections and geologic context of local enrichments in olivine on Vesta with VIR/Dawn data, *Journal of Geophysical Research: Planets*, **119**, 2078-2108

- Russell, S.S., Zipfel, J., Folco, L., Jones, R., Grady, M.M., McCoy, T., Grossman, J.N. (2003), The meteoritical bulletin, No. 87, 2003 July, *Meteoritics & Planetary Science*, **38**, A189-A248
- Russell, S.S., Zolensky, M., Righter, K., Folco, L., Jones, R., Connolly, H.C., Grady, M.M., Grossman, J.N. (2005), The meteoritical bulletin, No. 89, *Meteoritics & Planetary Science*, **40**, A201-263
- Ruzicka, A., Grossman, J., Bouvier, A., Agee, C.B. (2017), The meteoritical bulletin, No. 103, *Meteoritics & Planetary Science*, **52**, 1014
- Ruzicka, A., Grossman, J., Bouvier, A., Herd, C.D.K., Agee, C.B. (2015), The meteoritical bulletin, No. 102, *Meteoritics & Planetary Science*, **52**, 1662
- Ruzicka, A., Snyder, G.A., Taylor, L.A. (1997), Vesta as the howardite, eucrite and diogenite parent body: implications for the size of a core and for large-scale differentiation, *Meteoritics & Planetary Science*, **32**, 825-840
- Sawaguchi, T., Ishii, K. (2003), Three-dimensional numerical of lattice- and shape-preferred orientation of orthopyroxene porphyroclasts in peridotites, *Journal of Structural Geology*, **25**, 1425-1444
- Schneider, C.A., Rasband, W.S., Eliceiri, K.W. (2012), NIH Image to ImageJ: 25 years of image analysis, *Nature Methods*, **9**, 671-675
- Scott, E.R.D. (1977), Formation of olivine-metal textures in pallasite meteorites, *Geochimica et Cosmochimica Acta*, **41**, 693-710
- Shirone, G., Cox, D.E., Pickart, S.J. (1964), Magnetic structures in FeCr₂S₄ and FeCr₂O₄, *American Mineralogist*, **80**, 9-20

- Skemer, P., Katayama, I., Jiang, Z., Karato, S. (2005), The misorientation index: development of a new method for calculating the strength of lattice-preferred orientation, *Tectonophysics*, **411**, 157-167
- Takeda, H. (1986), Mineralogy of Antarctic ureilites and a working hypothesis for their origin and evolution, *Earth and Planetary Science Letters*, **81**, 358-370
- Takeda, H. (1997), Mineralogical records of early planetary processes on the howardite, eucrite, diogenite parent body with reference to Vesta, *Meteoritics & Planetary Science*, **32**, 841-853
- Thangjam, G., Nathues, A., Mengel, K., Hoffmann, M., Schäfer, M., Reddy, V., Cloutis, E.A., Christensen, U., Sierks, H., Le Corre, L., Vincent, J.-B., Russell, C.T. (2014), Olivine-rich exposures at Bellicia and Arruntia craters on (4) Vesta from Dawn FC, *Meteoritics & Planetary Science*, **49**, 1831-1850
- Tkalcec, B.J., Brenker, F.E. (2014), Plastic deformation of olivine-rich diogenites and implications and mantle processes on the diogenite parent body, *Meteoritics & Planetary Science*, **49**, 1202-1213
- Tkalcec, B.J., Brenker, F.E. (2015), Asteroidal processed recorded by polyphase deformation in harzburgitic diogenite NWA 5480, *Journal of Structural Geology*, **77**, 138-150
- Tkalcec, B.J., Brenker, F.E. (2019), Absence of olivine orientation fabric in highly shocked Martian dunite, *Meteoritics & Planetary Science*, **54**, 267-279
- Tkalcec, B.J., Golabek, G.J., Brenker, F.E. (2013), Solid-state plastic deformation in the dynamic interior of a differentiated asteroid, *Nature Geoscience*, **6**, 93-97
- Tomioka N., Miyahara, M. (2017), High-pressure minerals in shocked meteorites, *Meteoritics & Planetary Science*, **52**, 2017-2039

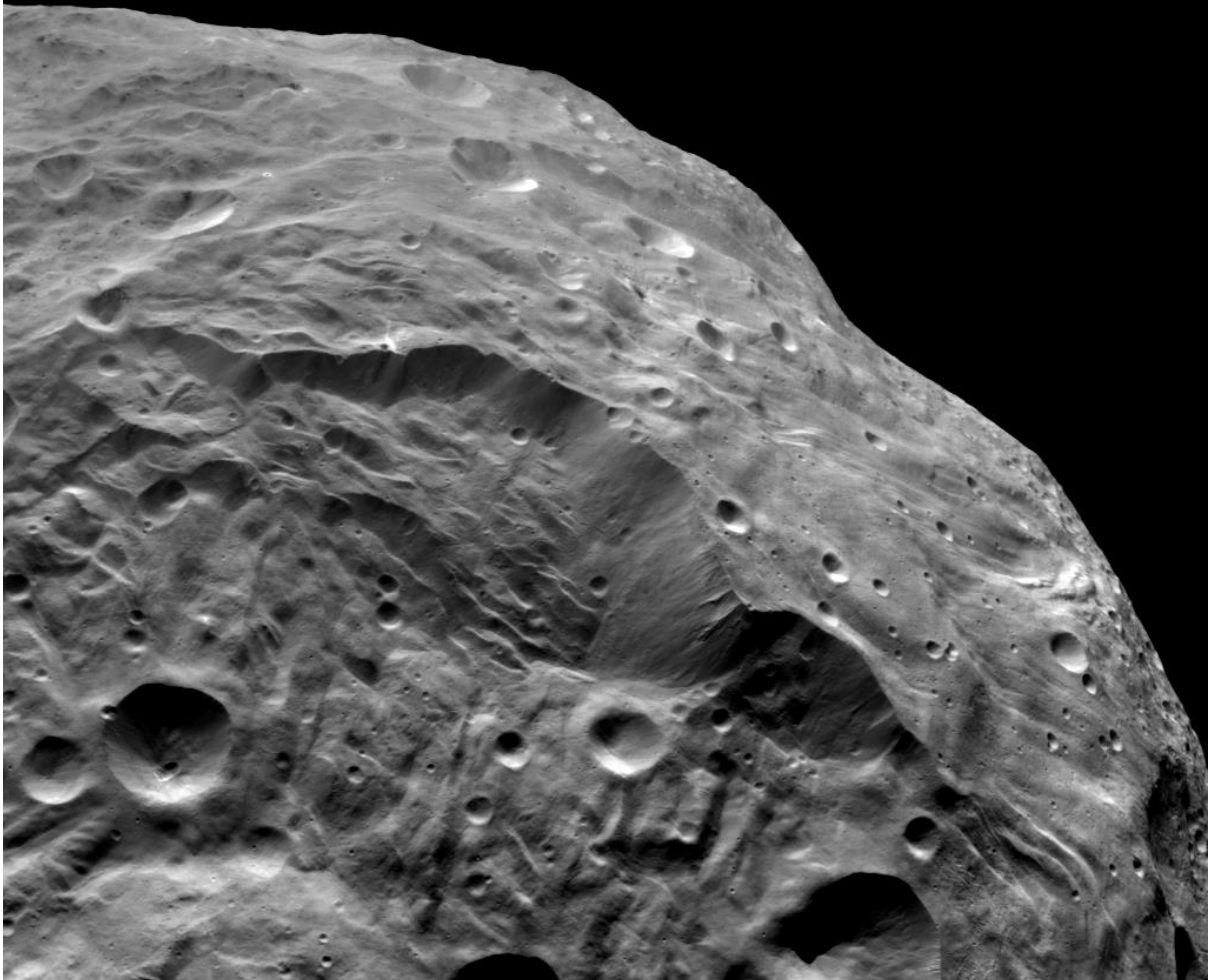
- Tommasi, A., Mainprice, D., Canova, G., Chastel, Y. (2000), Viscoplastic self-consistent and equilibrium-based modeling of olivine lattice preferred orientations: implications for the upper mantle seismic anisotropy, *Journal of Geophysical Research*, **105**, 7893-7908
- Turcotte, D.L., Schubert, G. (1982), *Geodynamics: Application of Continuum Physics to Geological Problems*, John Wiley & Sons, New York, New York, 450pp
- Udry, A., Howarth, G.H., Herd, C.D.K., Day, J.M.D., Lapen, T.J., Filiberto, J. (2020), What martian meteorites reveals about the interior and surface of Mars, *Journal of Geophysical Research: Planets*, **125**, e02020JE006523
- Vukmanovic, Z., Holness, M.B., Monks, M., Andersen, J.C.Ø. (2018), The Skaegaard trough layering: sedimentation in a convecting magma chamber, *Contributions to Mineralogy and Petrology*, **173**, 43
- Wager, L.R., Brown, G.M., Wadsworth, W.J. (1960), Types of igneous cumulates, *Journal of Petrology*, **1**, 73-85
- Walker, D., Stolper, E.M., Hays, J.F. (1978), A numerical treatment of melt/solid segregation: size of the eucrite parent body and stability of the terrestrial low-velocity zone, *Journal of Geophysical Research*, **83**, 6005-6013
- Warren, J.M., Hirth, G. (2006), Grain size sensitive deformation mechanisms in naturally deformed peridotites, *Earth and Planetary Science Letters*, **248**, 438-450
- Warren, J.M., Hirth, G., Kelemen, P.B. (2008), Evolution of olivine lattice preferred orientation during simple shear in the mantle, *Earth and Planetary Science Letters*, **272**, 501-512
- Warren, P.H., Claeys, P., Cedillo-Pardo, E. (1996), Mega-impact melt petrology (Chicxulub, Sudbury, and the Moon): effects of scale and other factors on potential for fractional

- crystallization and development of cumulates, *Geological Society of America Special Paper*, **307**, 105-124
- Weisbery, M.K., Smith, C., Benedix, G., Folco, L., Richter, K., Zipfel, J., Yamaguchi, A., Chennaoui Aoudjehane, H. (2009), The Meteoritical Bulletin, No.95, *Meteoritics & Planetary Science*, **44**, 1-33
- Wenk, H.-R., Lonardelli, I., Pehl, J., Devine, J., Prakapenka, V., Shen, G., Mao, H.-K. (2004), In situ observation of texture development in olivine, ringwoodite, magnesiowüstite and silicate perovskite at high pressure, *Earth and Planetary Science Letters*, **226**, 507-519
- Wilson, L., Keil, K. (1996), Volcanic eruptions and intrusions on the asteroid 4 Vesta, *Journal of Geophysical Research*, **101**, 18,927-18,940
- Wilson, L., Keil, K. (2012), Volcanic activity on differentiated asteroids: a review and analysis, *Chemie der Erde*, **72**, 289-321
- Yamaguchi, A., Barrat, A.-J., Ito, M., Bohn, M. (2011), Post-impact magmatism on Vesta: evidence from the petrology and thermal history of diogenites, *Journal of Geophysical Research*, **116**, E08009
- Yamaguchi, A., Barrat, A.-J., Shirai, N., Ebihara, M. (2015), Petrology and geochemistry of Northwest Africa 5480 diogenite and evidence for a basin-forming event on Vesta, *Meteoritics & Planetary Science*, **50**, 1260-1270
- Yang, H., Ghose, S. (1995), A transitional structural state and anomalous Fe-Mg order-disorder in Mg-rich orthopyroxene, $(\text{Mg}_{0.75}\text{Fe}_{0.25})_2\text{Si}_2\text{O}_6$, *American Mineralogist*, **80**, 9-20

- Yang, J., Goldstein, J.I., Scott, E.R.D. (2010), Main-group pallasites: thermal history, relationship to IIIAB irons, and origin, *Geochimica et Cosmochimica Acta*, **74**, 4471-4492
- Yao, Z., Qin, K., Wang, Q., Xue, S. (2017), Weak B-type olivine fabric induced by fast compaction of crystal mush in a crustal magma reservoir, *Journal of Geophysical Research: Solid Earth*, **124**, 3530-3556
- Yilmaz, E., Baltas, H., Kiris, E., Usabas, I., Cevik, U., El-Khayatt, A.M. (2011), Gamma ray and neutron shielding properties of some concrete materials, *Annals of Nuclear Energy*, **38**, 2201-2212
- Žák, J., Schulmann, K., Hrouda, F. (2005), Multiple magmatic fabrics in the Sázava pluton (Bohemian Massif, Czech Republic): a result of superposition of wrench-dominated regional transpression on final emplacement, *Journal of Structural Geology*, **27**, 805-822
- Žák, J., Verner, K., Týcová, P. (2008), Multiple magmatic fabrics in plutons: an overlooked tool for exploring interactions between magmatic processes and regional deformation? *Geological Magazine*, **145**, 537-551
- Zhang, S., Karato, S., Fitz Gerald, J., Faul, U.H., Zhou, Y. (2000), Simple shear deformation of olivine aggregates, *Tectonophysics*, **316**, 133-152

"The cosmos is all that is or ever was or ever will be. Our feeblest contemplations of the Cosmos stir us—there is a tingling in the spine, a catch in the voice, a faint sensation, as if a distant memory, or falling from a height. We know we are approaching the greatest of mysteries."

Carl Sagan



Chapter 5

The Complex Magmatic Evolution and Crustal Processes of Asteroid 4 Vesta, A Summary

Jennifer T. Mitchell¹

¹School of Earth, Atmosphere and Environment, Monash University, Australia

Asteroid 4 Vesta is a surprisingly complex body, recording a vast range of processes and lithologies with many more likely unsampled by the global meteorite collection. Through multiple modelling and experimental techniques, I have explored Vesta's magmatic evolution and crustal processes with reference to observations from NASA's Dawn mission and the HED meteorite suite in order to answer longstanding questions regarding the petrogenesis of diogenites and their relationship to eucrites, as well as suggesting what would be expected of the unsampled Vestan mantle.

5.1. TIMING OF ACCRETION FOR VESTA

The behaviour of magmatism in the early Solar System is a key factor in our understanding of planetary evolution. The heating of planetary bodies was caused by the decay of short-lived radioisotopes, predominantly ^{26}Al , resulting in widespread silicate melting within 3 Myr after CAI formation (Bizzarro et al., 2005) because these short-lived nuclides effectively disappeared within seven half-lives. The time of accretion was vitally important in controlling the extent of heat production and development of magmatism. Bodies that accreted early had a higher abundance of ^{26}Al , higher temperatures, and more extensive melting whereas those that accreted late had limited ^{26}Al and associated heat production.

The thermal modelling presented in *Chapter 3* finds that in order to satisfy the temperature requirements for the formation of eucrite and diogenite lithologies, Vesta must have accreted between 1.5-1.75 Myr after CAI formation (Fig. 5.1). Models in which Vesta accreted prior to $T_0 + 1.25$ Myr achieve temperatures high enough to produce an anorthositic crust (Arai & Maruyama, 2017) and komatiite-like lithologies, neither of which are observed on Vesta. Models of accretion after $T_0 + 1.75$ Myr are unable to generate enough heat to promote significant silicate melting nor complete differentiation.

The $T_0 + 1.5\text{-}1.75$ Myr accretion age proposed in this project is at odds with previous thermal models of Vesta's evolution. Ghosh & McSween (1998) determined an accretion age of $T_0 + 2.85$ Myr – significantly later than our model suggests that Vesta would be able to differentiate – and Formisano et al., (2013) suggested an earlier accretion age than the one presented in *Chapter 3* of $<T_0 + 1.4$ Myr. This discrepancy is the result of differences in the model parameters used in each study. For example, the Ghosh & McSween (1998) model has a higher ^{26}Al abundance, meaning that heating could continue for significantly longer and delaying the onset of accretion in accordance with the model. The Formisano et al., (2013) model requires substantially higher melting than determined by the THERMOCALC modelling in *Chapter 3*, thus early accretion when the ^{26}Al abundance is high is necessary. However, as shown in *Chapter 2* and *Chapter 3*, high degrees of partial melting are not required to produce HED lithologies even at high temperatures. Our model therefore necessitates a lower ^{26}Al budget for Vesta than that of the Formisano et al., (2013) model, and results in a slightly later accretion age.

The modelling presented in this project can be considered an update to these earlier thermal models, giving an accretion age ($T_0 + 1.5\text{-}1.75$ Myr) better constrained by HED petrology and provenance. The accretion age proposed here is consistent with ages for ancient eucrites (Hublet et al., 2017) and is also contemporaneous with the accretion of the ureilite parent body (Budde et al., 2015), the angrite parent body (Kleine et al., 2012), and the eucrite-like NWA 011 ungrouped basaltic achondrite parent body (Sugiura & Fujiya, 2014). This suggests that this time was a period of widespread asteroid growth in the inner Solar System.

5.2. VESTA'S MAGMATIC EVOLUTION & CRUSTAL PROCESSES

As well as the abundance of ^{26}Al , it is also important to consider the location of ^{26}Al in the asteroidal body. ^{26}Al would have been heterogeneously distributed across Vesta's mineralogy,

where Al-rich minerals such as plagioclase and clinopyroxene would have higher proportions of ^{26}Al than olivine and orthopyroxene. As established in *Chapter 3*, the initial extraction of a eucrite-like melt rich in Al and Ca at approximately 3-5 Myr after CAI formation would transport the majority ^{26}Al to the upper regions of the asteroid, forming a lid and leaving an Al- and Ca-poor residue (Fig. 5.1). The concentration of ^{26}Al into the crust means that it acts as a hot lid that insulates Vesta's interior, allowing enhanced mantle heating to continue until diogenite magmatism could begin once temperatures were sufficiently high. Additionally, the decay of ^{26}Al in the crust and serial eucrite magmatism may have driven the thermal metamorphism observed in the majority of eucrite samples (cf. Yamaguchi et al., 1996, 1997).

Diogenite magmatism must have, therefore, occurred after the onset of eucrite magmatism through the remelting of residual material as proposed by Barrat et al., (2008) and Mittlefehldt et al., (2012), at low degrees of partial melt as revealed by THERMOCALC modelling. The thermal models in *Chapter 3* suggests a delay of >1 Myr after the initial eucrite extraction, dependent on accretion time. If Vesta accreted closer to $T_0 + 1.75$ Myr, diogenite magmatism is triggered after a greater delay due to slower internal heating as a result of weaker ^{26}Al decay. Similarly, the dominant mineralogy of diogenites is also dependent on the ^{26}Al abundance where higher temperatures/earlier accretion produces a higher proportion of dunitic diogenite material, and cooler temperatures/later accretion is dominated by orthopyroxenitic diogenites as established through the THERMOCALC models. The pMELTS models in *Chapter 2* show that olivine would have crystallised over a short temperature interval in contrast to orthopyroxene. This is reflected in both the global meteorites collection, where olivine-bearing diogenites make up less than 3 % of the diogenite class and olivine-poor surface of Vesta. These uncommon harzburgitic and dunitic diogenite lithologies may be exposed in crater walls

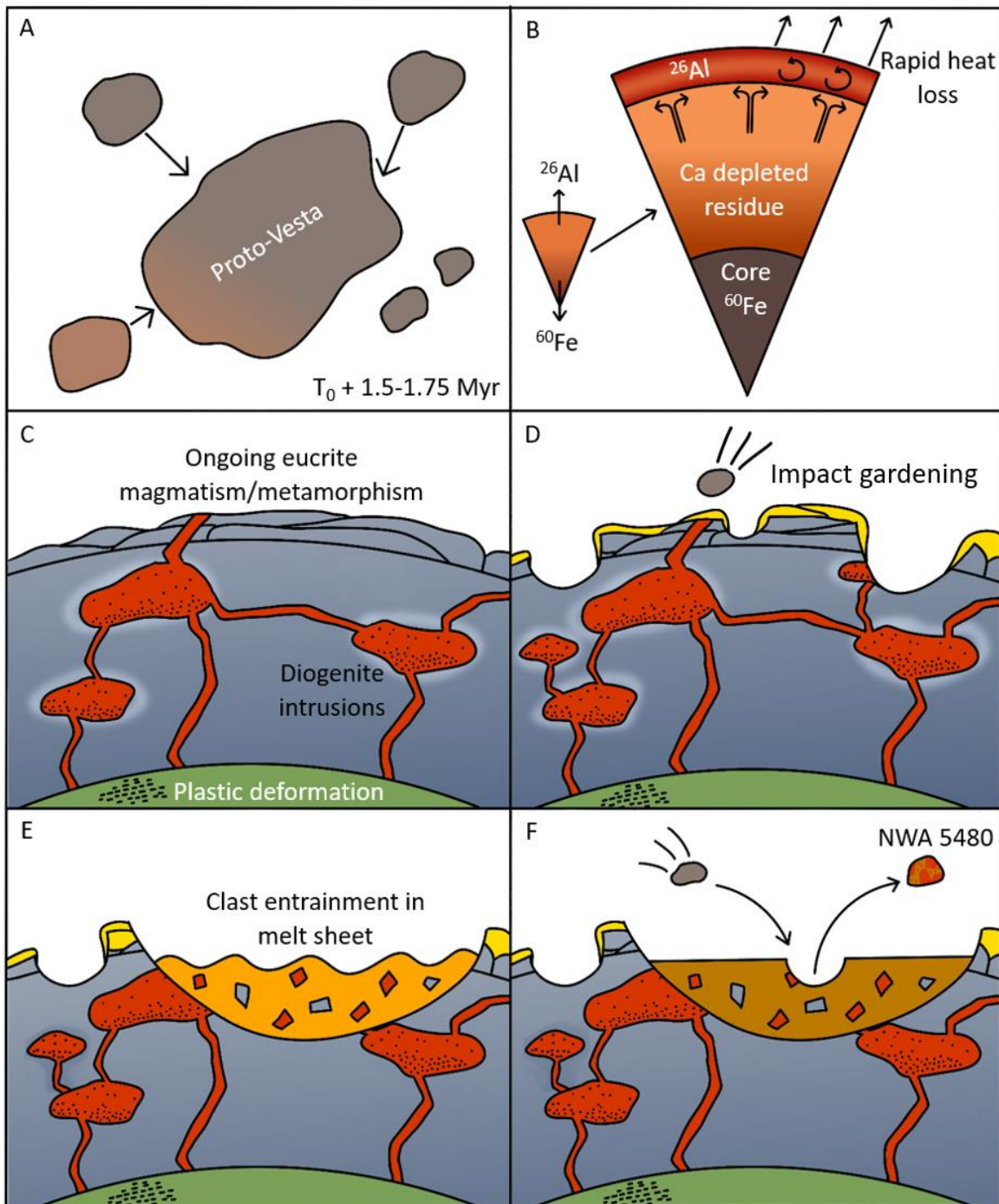


Figure 5.1. A simplified schematic of Vesta's evolution. Euclite = blue, diogenite = red, howardite = yellow, mantle = green. A) Accretion occurs at 1.5-1.75 Myr after CAI formation as established by the combined thermal and compositional modelling presented in Chapter 3; B) Partial melting allows for the migration of ^{60}Fe to the core and ^{26}Al to the crust. ^{26}Al is extracted in an initial euclite-like melt to form a hot stagnant lid, insulating the asteroid interior and depleting the residue in Ca; C) Diogenite magmatism begins once internal temperatures reach $>1340\text{ }^\circ\text{C}$, and melt is transported through a network of dykes to create crustal intrusion and reservoirs, thickening the crust. The euclite crust undergoes localised partial melting and global metamorphism in response to serial magmatism. Gravitational settling generates magmatic foliation in diogenites and shearing during melt transport can form a magmatic lineation as discussed in Chapter 4. Sulfidation occurs, resulting in small changes in $f\text{O}_2$ that drive compositional diversity within the crystallising melt as shown in Chapter 2. Plastic deformation occurs in the dunite mantle, producing textures similar to ureilites; D) Impact gardening causes brecciation. Vestan olivine is exposed in crater walls and associated ejecta; E) Impact causes brecciation of dunite-harzburgite diogenite lithologies; F) Solidified impact melt sheet is further impacted, liberating NWA 5480.

(Ammannito et al., 2013; Thangjam et al., 2014), as clasts in howardites, and as fragments entrained in impact melt sheet samples such as NWA 5480 (Fig. 5.1).

During diogenite magmatism, hot magma is emplaced into the eucrite crust through a complex network of dykes and fractures (Fig. 5.1, Wilson & Keil, 1996, 2012) to form multiple crustal intrusions that underwent fractional crystallisation. Sulfidation reactions within the diogenite source may have driven variations in fO_2 conditions, diversifying the range of pyroxene compositions of natural diogenite samples as discussed in *Chapter 2* (Mitchell & Tomkins, 2019). Interactions between the diogenite melt and the eucritic crust is thought to explain the deep negative Eu anomalies found in some diogenites (Barrat et al., 2008).

Diogenites likely record multiple of petrofabrics across a single intrusion (Žák et al., 2008), ranging from magmatic foliation produced during mineral settling to lineations developing as a result of shearing during magma migration and the re-intrusion of magma into a crystallising melt reservoir. We can also infer that basaltic eucrites would display petrofabrics similar to those of Martian nakhlites, recording the flow of magma as either surface lavas or sills as well as quiescent regimes within the lava body (Daly et al., 2019).

Although NASA's Dawn mission did not provide any conclusive evidence as to the nature of diogenites, the research presented in this project therefore finds that diogenites represent complex crustal intrusions and not magma ocean cumulates. The timing of Vesta's accretion – thus the relative abundance of ^{26}Al – combined with the distribution of ^{26}Al within Vesta's structure dictates the behaviour of magmatism and shows that a magma ocean is not necessary in Vesta's evolution. Magmatism on Vesta seems to be closer to that of terrestrial planets than to smaller asteroids, providing a unique insight into the evolution of early planetary bodies transitional between asteroids and dwarf planets.

5.3. EXPECTATIONS OF VESTA'S HIDDEN MANTLE

NASA's Dawn mission revealed that Vesta's mantle is not exposed not at the surface as initially expected (Ammannito et al., 2013). Instead it is suggested that long-lasting serial eucrite magmatism and the later intrusion of diogenite material substantially thickened the crust (cf. Clenet et al., 2014). The research presented in this study allows us to make the following three key inferences about the nature of Vesta's hidden mantle.

Firstly, the mantle should be composed of a coarse-grained olivine-rich residue that is significantly more magnesian than olivine compositions observed in diogenites. The high-Mg olivine fragments identified in howardites by Lunning et al., (2015) and Hahn et al., (2019) have Mg# >80 and may represent fragmented mantle xenoliths. These fragments are compositionally distinct from olivine-bearing diogenites and dunite clasts in the NWA 5480 impact melt sheet. Secondly, the major element composition of Vestan mantle olivine should be somewhat consistent as is seen in terrestrial mantle samples. In addition, mantle minerals should be depleted in Ca as a result of early eucrite extraction (*Chapter 3*). Lastly, a mantle sample would likely contain olivine with a shape- and lattice-preferred orientation as seen in ureilites (*Chapter 4*) developed through high-temperature/high-pressure deformation and shearing. Upper mantle shearing and deformation caused by grazing impacts is expected (Asphaug et al., 2006; Consolmagno et al., 2015), particularly with reference to Rheasilvia.

5.4. FUTURE RESEARCH

The study of petrofabrics provides a wealth of information about the dynamic environment of crystallising magmatic meteorites but is underutilised in meteoritics as highlighted in *Chapter 4*. As such, continued research of HED petrofabrics will surely result in key insights that cannot otherwise be achieved. Neutron scattering techniques allow for the study of whole-stone samples, collecting vital data about the internal structure of the meteorite as well as crystal

orientation. These data can then be used to best orient the sample for cutting, preserving grain orientation and other key features.

The work presented in *Chapter 4* will be continued when facilities are fully available. Diogenites Dhofar 700, NWA 7977 and 8265 will be analysed using the Kowari strain scanner for comparison with data of ureilite samples, as well as EBSD analysis of various diogenite and ureilite thin sections. In addition, further EBSD analysis of NWA 5480 will create a clearer picture of impact melt sheet processes and the entrained pre-existing lithologies.

5.5. CONCLUDING REMARKS

In the introduction to this project, the following questions were laid out: What is the genetic and chronological relationship between diogenites and eucrites? Why is olivine so uncommon in HED meteorites? Do olivine-bearing diogenites represent samples of the Vestan mantle as many have suggested? What should be expected of Vesta's mantle in terms of composition and evolution? Did Vesta evolve through a magma ocean or through a more complex magmatic differentiation history?

All of these questions have been answered by the research presented in this project.

Vesta is a complex protoplanetary body that has a long magmatic history dictated by initial the abundance and distribution of ^{26}Al , providing a unique insight into the onset and behaviour of magmatism in the early Solar System. The HED meteorite suite records a wealth of information about the early Solar System and warrant continued study in order to better our understanding of planet-building processes.

Future orbital and sample-return missions to various bodies will only further our knowledge of our little corner of space, filling in the details of Solar System chronology, the birth of planets, and how the Earth came to be so markedly different from our neighbours.

5.6. CHAPTER REFERENCES

- Ammannito, E., De Sanctis, M.C., Palomba, E., Longobardo, A., Mittlefehldt, D.W., McSween, H.Y., Marchi, S., Capria, M.Y., Capaccioni, F., Frigeri, A., Pieters, C.M., Ruesch, O., Tosi, F., Zambon, F., Carraro, F., Fonte, S., Hiesinger, H., Magni, G., McFadden, L.A., Raymond, C.A., Russell, C.T., Sunshine, J.M. (2013), Olivine in an unexpected location on Vesta's surface, *Nature*, **504**, 122-125
- Arai, T., Maruyama, S. (2017), Formation of anorthosite on the Moon through magma ocean fractional crystallization, *Geoscience Frontiers*, **8**, 299-308
- Asphaug, E., Agnor, C.B., Williams, Q. (2006), Hit-and-run planetary collisions, *Nature*, **439**, 155-160
- Barrat, J.-A., Yamaguchi, A., Greenwood, R.C., Benoit, M., Cotten, J., Bohn, M., Franchi, I.A. (2008), Geochemistry of diogenites: Still more diversity in their parental melts, *Meteoritics & Planetary Science*, **43**, 1759-1775
- Bizzarro, M., Baker, J.A., Haack, H., Lundgaard, L. (2005), Rapid timescales for accretion and melting of differentiated planetesimals inferred from ^{26}Al - ^{26}Mg chronometry, *The Astrophysical Journal*, **632**, L41-L44
- Budde, G., Kruijer, T.S., Fischer-Gödde, M., Irving, A.J., Kleine, T. (2015), Planetesimal differentiation revealed by the Hf-W systematics of ureilites, *Earth and Planetary Science Letters*, **430**, 316-325
- Clenet, H., Barrat, J.-A., Asphaug, E.I., Benz, W.I., Gillet, P. (2014), A deep crust-mantle boundary in the asteroid 4 Vesta, *Nature*, **511**, 303-306
- Consolmagno, G.J., Golabek, G.J., Turrini, D., Jutzi, M., Sirono, S., Svetsov, V., Tsiganis, K. (2015), Is Vesta intact and pristine protoplanet? *Icarus*, **254**, 190-201

- Daly, L., Piazzolo, S., Lee, M.R., Griffin, S., Chung, P., Campanale, F., Cohen, B.E., Hallis, L.J., Trimby, P.W., Baumgartner, R., Forman, L.V., Benedix, G.K. (2019), Understanding the emplacement of Martian volcanic rocks using petrofabrics of the nakhlite meteorites, *Earth and Planetary Science Letters*, **520**, 220-230
- Formisano, M., Federico, C., Turrini, D., Coradini, A., Capaccioni, F., De Sanctis, M.C., Pauselli, C. (2013), The heating history of Vesta and the onset of differentiation, *Meteoritics & Planetary Science*, **48**, 2316-2332
- Ghosh, A., McSween, H.Y. (1998), A thermal model for the differentiation of asteroid 4 Vesta, based on radiogenic heating, *Icarus*, **134**, 187-206
- Hahn, T.M., Lunning, N.G., McSween, H.Y., Bodnar, R.J., Taylor, L.A. (2018), Mg-rich harzburgites from Vesta: mantle residua or cumulates from planetary differentiation, *Meteoritics & Planetary Science*, **53**, 514-546
- Hublet, G., Debaille, V., Wimpenny, J., Yin, Q.-Z. (2017), Differentiation and magmatic activity in Vesta evidenced by ²⁶Al-²⁶Mg dating in eucrites and diogenites, *Geochimica et Cosmochimica Acta*, **218**, 73-97
- Kleine, T., Hans, U., Irving, A., Bourdon, B. (2012), Chronology of the angrite parent body and implications for core formation in protoplanets, *Geochimica et Cosmochimica Acta*, **84**, 186-203
- Lunning, N.G., McSween, H.Y., Tenner, T.J., Kita, N.T., Bodnar, R.J. (2015), Olivine and pyroxene from the mantle of asteroid 4 Vesta, *Earth and Planetary Science Letters*, **418**, 126-135

- Mitchell, J.T., Tomkins, A.G. (2019), On the source of diogenites and olivine diogenites: compositional diversity from variable fO_2 , *Geochimica et Cosmochimica Acta*, **258**, 37-49
- Mittlefehldt, D.W. (1994), The genesis of diogenites and HED parent body petrogenesis, *Geochimica et Cosmochimica Acta*, **58**, 1537-1552
- Mittlefehldt, D.W., Beck, A.W., Lee, C.A., McSween, H.Y., Buchanan, P.C. (2012), Compositional constraints on the genesis of diogenites, *Meteoritics & Planetary Science*, **47**, 72-98
- Sugiura, N., Fujiya, W. (2014), Correlated accretion ages and $\epsilon^{54}Cr$ of meteorite parent bodies and the evolution of the solar nebula, *Meteoritics & Planetary Science*, **49**, 772-787
- Thangjam, G., Nathues, A., Mengel, K., Hoffmann, M., Schäfer, M., Reddy, V., Cloutis, E.A., Christensen, U., Sierks, H., Le Corre, L., Vincent, J.-B., Russell, C.T. (2014), Olivine-rich exposures at Bellicia and Arruntia craters on (4) Vesta from Dawn FC, *Meteoritics & Planetary Science*, **49**, 1831-1850
- Wilson, L., Keil, K. (1996), Volcanic eruptions and intrusions on the asteroid 4 Vesta, *Journal of Geophysical Research*, **101**, 18,927-18,940
- Wilson, L., Keil, K. (2012), Volcanic activity on differentiated asteroids: a review and analysis, *Chemie der Erde*, **72**, 289-321
- Yamaguchi, A., Barrat, J.-A., Ito, M., Bohn, M. (2011), Posteuclitic magmatism on Vesta: evidence from the petrology and thermal history of diogenites, *Journal of Geophysical Research*, **116**, E08009
- Yamaguchi, A., Taylor, G.J., Keil, K. (1996), Global crustal metamorphism of the eucrite parent body, *Icarus*, **124**, 97-112

Yamaguchi, A., Taylor, G.J., Keil, K. (1997), Metamorphic history of the eucritic crust of 4 Vesta, *Journal of Geophysical Research*, **102**, 13,381-13,386

Žák, J., Verner, K., Týcová, P. (2008), Multiple magmatic fabrics in plutons: an overlooked tool for exploring interactions between magmatic processes and regional deformation? *Geological Magazine*, **145**, 537-551

*“The Earth is the cradle of humanity, but mankind
cannot stay in the cradle forever.”*

Konstantin Tsiolkovsky



APPENDIX

Table A1. Pyroxene compositions of olivine diogenites, diogenites, cumulate eucrites, and basaltic eucrites (Meteoritical Society Bulletin Database)

Name	Ens	Fs	Wo	Name	Ens	Fs	Wo
OLIVINE DIOGENITES				MET 00424	72.00	27.00	1.00
Bir Moghrein	76.60	21.00	2.40	MET 00425	84.00	15.00	1.00
MIL 07001	75.00	23.00	2.00	MET 00855	72.50	26.00	1.50
NWA 5603	74.10	24.40	1.50	MET 001060	71.00	27.00	2.00
NWA 5652	71.70	23.90	4.40	MET 01084	80.00	19.00	1.00
NWA 6149	75.20	23.40	1.40	MIL 03368	72.00	26.00	2.00
NWA 6157	72.90	24.30	2.80	MIL 07003	70.00	27.00	3.00
NWA 6232	74.90	23.50	1.60	MIL 07613	67.00	30.50	2.50
NWA 6351	33.30	64.00	2.70	MIL 090106	53.00	41.00	6.00
NWA 6819	73.50	23.30	3.00	MIL 090112	62.00	36.00	2.00
NWA 7370	72.20	24.60	3.20	MIL 090220	63.00	34.00	3.00
NWA 8404	71.70	25.00	3.30	MIL 090291	53.00	23.00	24.00
DIOGENITES				MIL 090995	75.00	23.00	2.00
ALH A77256	75.00	23.00	2.00	MIL 11099	58.50	39.00	25.00
AP 001	76.40	21.60	2.00	MIL 11197	67.50	28.50	4.00
AP 003	74.20	23.50	2.30	MIL 11201	36.50	39.00	2.50
AP 004	72.00	24.30	3.70	MIL 15309	73.00	25.00	2.00
A-880652	73.55	25.44	1.95	NWA 1459	65.40	29.00	5.60
A-880785	75.15	22.60	2.25	NWA 1461	85.40	13.60	0.80
A-880963	71.15	26.25	2.60	NWA 1821	69.85	27.35	2.80
A-881114	72.15	25.65	2.20	NWA 1880	70.80	26.00	3.20
A-881210	24.05	73.75	2.20	NWA 2048	73.00	25.00	2.00
A-881239	74.05	24.00	1.95	NWA 2081	74.60	23.30	2.10
A-881526	74.80	22.60	2.60	NWA 2115	76.00	22.90	1.10
A-881839	67.05	26.65	6.30	NWA 2219	70.95	25.45	3.60
A-881944	68.00	28.75	3.25	NWA 2286	76.60	21.90	1.50
A-12015	70.05	27.05	2.65	NWA 2434	74.50	24.20	1.30
Dhofar 700	66.50	28.75	4.75	NWA 2515	70.20	26.50	3.30
DOM 10350	72.00	25.00	3.00	NWA 2629	75.10	23.40	1.50
EET A79002	76.00	22.00	2.00	NWA 2753	75.00	24.00	1.00
EET 83247	72.00	25.50	2.50	NWA 2795	71.30	26.20	2.50
EET 87530	71.00	26.00	3.00	NWA 2824	64.05	32.50	3.45
GRA 98108	76.00	22.00	2.00	NWA 2923	72.30	24.80	2.90
JaH 395	74.05	24.35	1.60	NWA 2997	74.90	22.10	3.00
JaH 868	67.10	30.40	2.50	NWA 3106	66.00	30.35	3.65
LAP 91900	75.00	23.00	2.00	NWA 3143	71.80	24.90	3.30
LAP 03569	76.00	22.00	2.00	NWA 3329	68.30	29.30	2.40
LAP 03630	74.00	24.00	2.00	NWA 4034	71.50	25.20	3.30
LAP 03781	75.00	23.00	2.00	NWA 4215	72.40	24.30	3.30
LAP 031381	72.00	25.00	3.00	NWA 4223	72.80	24.20	3.00
LAP 04844	75.00	23.00	2.00	NWA 4255	73.20	25.30	1.50
LAP 12010	72.50	25.00	2.50	NWA 4283	75.85	21.90	2.25
LEW 88008	66.00	30.00	4.00	NWA 4285	71.80	24.50	3.70
LEW 88011	73.00	24.00	3.00	NWA 4302	39.20	25.30	35.50
LEW 88679	71.00	26.00	3.00	NWA 4380	75.60	22.90	1.50
MET 00422	76.50	22.00	1.50	NWA 4395	66.80	30.50	2.70
NWA 4473 A	81.80	17.20	1.00	NWA 7947	75.40	23.40	1.20
NWA 4473 B	76.30	21.60	2.10	NWA 7950 A	74.00	24.50	1.50
NWA 4473 C	59.30	37.20	3.50	NWA 7590 B	72.60	25.90	1.50

NWA 4550	70.40	27.40	2.20	NWA 7977	68.10	28.40	3.50
NWA 4654	76.00	22.10	1.90	NWA 7991	71.40	25.20	3.40
NWA 4678	67.00	29.20	3.80	NWA 7994	76.05	22.60	1.35
NWA 4807	74.80	23.90	1.30	NWA 7997	74.60	23.80	1.60
NWA 4808	75.40	22.00	2.60	NWA 8000	63.40	34.10	2.50
NWA 4965	70.25	27.85	1.90	NWA 8043	68.20	28.20	3.60
NWA 5314	73.70	23.50	2.80	NWA 8057	78.70	19.60	1.70
NWA 5315	63.40	33.00	3.60	NWA 8087	70.30	26.90	2.80
NWA 5405	74.10	23.80	2.10	NWA 8093	82.80	15.90	1.30
NWA 5480	73.40	24.80	1.80	NWA 8107	52.15	34.65	13.20
NWA 5484	76.20	22.60	1.20	NWA 8115	68.20	30.00	1.80
NWA 5600	69.90	28.60	1.50	NWA 8119	74.50	23.60	1.90
NWA 5742	68.45	28.85	2.70	NWA 8178	74.30	23.40	2.30
NWA 5999	70.00	26.50	3.50	NWA 8265	71.60	25.40	3.00
NWA 6050	65.70	30.40	3.90	NWA 8313	71.90	25.30	2.80
NWA 6074	36.00	24.00	40.00	NWA 8316	74.00	23.20	2.80
NWA 6133	59.77	16.12	24.11	NWA 8321	75.50	21.30	3.20
NWA 6267	57.00	39.10	3.90	NWA 8326	62.00	35.50	2.50
NWA 6290	75.10	23.90	1.00	NWA 8367	64.00	33.60	2.40
NWA 6315	73.40	23.40	3.20	NWA 8379	72.20	24.40	3.40
NWA 6340	74.50	23.20	2.30	NWA 8446	71.20	25.80	3.00
NWA 6421	70.50	26.20	3.30	NWA 8476	68.50	28.50	3.00
NWA 6489	20.55	78.75	0.70	NWA 8502	77.20	20.70	2.10
NWA 6575	76.80	21.80	1.40	NWA 8546	80.60	18.40	1.00
NWA 6690	63.00	34.50	2.50	NWA 8633	68.10	28.40	3.50
NWA 6911	76.60	22.30	1.10	NWA 8703	68.00	28.40	3.60
NWA 6927	71.60	25.00	3.40	NWA 8744	63.40	31.20	5.40
NWA 7039	72.10	25.30	2.60	NWA 10159	76.20	21.70	2.10
NWA 7230	71.20	25.15	3.65	NWA 10182	76.20	22.50	1.30
NWA 7280	65.75	31.70	2.55	NWA 10242	69.40	27.90	2.70
NWA 7464	71.35	25.10	3.55	NWA 10268	62.50	34.90	2.60
NWA 7490	70.95	25.05	4.00	NWA 10277	76.00	22.40	1.60
NWA 7599	71.95	24.80	3.25	NWA 10300	71.20	25.90	2.90
NWA 7608	71.40	25.30	3.30	NWA 10362	69.00	28.20	2.80
NWA 7639	74.10	24.10	1.80	NWA 10388	75.90	22.30	1.80
NWA 7672	63.60	33.50	2.90	NWA 10410	77.90	20.80	1.30
NWA 7677	70.40	24.80	4.80	NWA 10446	71.60	25.90	2.50
NWA 7825	72.80	25.10	2.10	NWA 10451	71.80	25.20	3.00
NWA 7831	68.90	28.10	3.00	NWA 10491	72.10	23.60	4.30
NWA 7894	74.10	23.50	2.40	NWA 10505	71.60	24.70	3.70
NWA 7896	69.60	27.85	2.55	NWA 10560	69.20	27.60	3.20
NWA 7908	73.30	25.10	1.60	NWA 10666	62.70	35.10	2.20
NWA 7912	67.70	30.70	1.60	NWA 10706	73.00	24.30	2.70
NWA 7919	70.70	25.90	3.40	NWA 10752	75.30	23.30	1.40
NWA 10763	69.70	27.40	2.90	NWA 8690	60.80	37.30	1.90
NWA 10779	74.40	23.30	2.30	NWA 8730	47.60	49.70	2.70
NWA 10855	70.50	26.40	3.10	NWA 10062	46.40	51.20	2.40
NWA 10921	68.80	28.00	3.20	NWA 10062	34.70	21.70	43.60
NWA 10929	71.90	26.40	1.70	NWA 10163	49.10	46.40	4.50
NWA 10975	69.00	27.40	3.60	NWA 10163	37.50	19.20	43.30
NWA 11049	70.80	25.90	3.30	NWA 10319	36.70	59.50	3.80
NWA 11171	70.30	26.20	3.50	NWA 10319	33.80	47.10	19.10

NWA 11235	73.70	24.00	2.30	NWA 10320	43.30	54.30	2.40
NWA 11342	77.00	20.60	2.40	NWA 10320	40.00	51.20	8.80
PCA 91077	72.00	25.00	3.00	NWA 10320	38.10	40.60	21.30
PCA 02017	76.00	21.50	2.50	NWA 10423	35.50	61.90	2.60
QUE 93009	69.00	28.00	3.00	NWA 10423	30.30	27.50	42.20
QUE 97991	73.00	25.00	2.00	NWA 10423	34.80	52.10	13.10
QUE 99050	77.00	21.00	2.00	NWA 10424	34.40	63.70	1.90
QUE 99231	78.50	20.00	1.50	NWA 10424	34.10	59.00	6.90
QUE 02158	76.00	22.00	2.00	NWA 10424	30.40	34.40	35.20
RaS 287	70.20	27.60	2.20	NWA 10476	62.20	35.20	2.60
Sahara 98111	70.30	28.30	1.40	NWA 10476	41.70	15.20	43.10
SAN 03473	75.00	23.00	2.00	NWA 10642	48.90	48.30	2.80
Taoudenni	69.00	26.00	4.00	NWA 10642	35.70	22.80	41.50
TIL 82410	74.00	24.00	2.00	NWA 10642	40.20	53.10	6.70
CUMULATE EUCRITES				NWA 10894	54.50	37.30	8.20
Abadla	58.00	39.10	2.90	Talampaya	58.60	40.20	1.20
Abadla	45.80	22.10	32.10	UaS 024	32.00	62.50	5.50
Lake Carnegie	31.55	45.25	23.20	UaS 024	26.30	32.20	41.50
NWA 1240	76.00	22.10	1.90	Y-980318	50.00	48.00	2.00
NWA 1240	0.30	83.40	16.30	Y-980318	37.00	18.00	45.00
NWA 1908	28.00	28.00	44.00	BASALTIC EUCRITES			
NWA 1908	33.00	65.00	2.00	Al Haggounia 003	36.40	60.40	3.20
NWA 2064	48.70	49.50	1.80	Al Haggounia 003	29.80	25.90	44.30
NWA 2064	45.70	41.50	12.80	Al Haggounia 005	34.30	63.9	1.8
NWA 2064	46.90	9.10	44.00	Al Haggounia 005	26.10	29.6	44.3
NWA 6731	44.10	52.70	3.20	Alby Sur Cheran	36.00	61	3
NWA 7330	57.00	39.30	3.70	ALH A81001	39.40	59	1.6
NWA 7330	38.00	20.70	41.30	Aoufous	35.60	61.9	2.5
NWA 7367	52.80	43.30	3.90	Aoufous	27.40	27.6	45
NWA 7367	37.70	17.00	45.30	Aouinet Legraa	36.70	57.1	6.2
NWA 7651	34.60	45.20	20.20	Aouinet Legraa	29.70	28	42.3
NWA 7913	51.60	41.40	7.00	AP 005	38.80	52.5	8.7
NWA 7913	38.90	19.40	41.70	AP 005	30.00	42.8	27.2
NWA 8339	63.30	34.50	2.20	AP 006	41.20	56.6	2.2
NWA 8339	48.70	20.30	31.00	AP 006	27.60	28.8	43.6
NWA 8383	61.60	35.30	3.10	Arivaca	42.10	55.3	2.6
NWA 8475	43.90	47.80	8.30	Berthoud	42.82	54.03	3.15
NWA 8475	36.50	29.50	34.00	Berthoud	35.79	31.21	33
NWA 8564	51.60	39.90	8.50	Bluewing 001	67.50	27.7	4.8
Bluewing 001	3.00	82	15	MAC 041169	41.00	57	2
Bou Kra	35.60	58.8	5.6	MET 01081	41.00	55	4
Bou Kra	29.70	28.3	42	MIL 13019	38.00	60	2
BTN 00300	37.00	28	35	MWA 10438	27.40	32.2	40.4
BTN 00300	44.00	49	7	NWA 10069	33.80	63.4	2.8
Caldera	37.00	58	5	NWA 10069	29.30	28.5	42.2
Caldera	30.00	30	40	NWA 10069	7.30	68.7	24
CMS 04049	45.00	50	5	NWA 10070	55.00	42	3
CMS 04049	31.00	28	41	NWA 10072	41.90	56.5	1.6
DaG 1046	37.70	55.5	6.8	NWA 10148	38.80	58.4	2.8
DaG 567	34.70	62.5	2.8	NWA 10148	31.60	27	41.4
Dag 647	28.00	31	41	NWA 10166	38.80	59	2.2
Deakin 010	74.60	24.1	1.3	NWA 10166	30.90	28.5	40.6

Deakin 010	19.70	64.2	16.1	NWA 10179	37.10	59.6	3.3
Dhofar 1429	37.50	60.3	2.2	NWA 10179	30.50	26.8	42.7
Dhofar 1429	36.50	51.2	12.3	NWA 10233	34.60	58.8	6.6
Dhofar 1429	29.70	25	45.3	NWA 10233	29.00	29.7	41.3
Dhofar 1439	61.30	34.7	4	NWA 10302	35.90	60.4	3.7
Dhofar 2036	37.20	60	2.8	NWA 10307	38.10	55.3	6.6
EET 90020	40.00	55	5	NWA 10307	30.80	29.2	40
EET 90020	37.00	40	23	NWA 10307	36.70	55.9	7.4
EET 90029	39.00	57	4	NWA 10307	28.80	33.6	37.6
EET 92004	41.00	57	2	NWA 10364	41.70	56.6	1.7
EET 92004	39.00	43	18	NWA 10364	33.20	23.4	43.4
EET 920223	45.00	45	10	NWA 10390	36.10	59.8	4.1
EET 99029	38.00	50	12	NWA 10390	30.60	33.5	35.9
GRA 06189	38.00	60	2	NWA 10406	48.10	49.4	2.5
GRA 06189	31.00	26	43	NWA 10406	48.60	46.4	5
GRA 98098	36.00	59	5	NWA 10408	38.50	59.8	1.7
GRV 051523	34.00	22	44	NWA 10422	32.40	65.5	2.1
Igdi	29.60	63.5	6.9	NWA 10422	27.70	29.6	42.7
LAP 03782	33.00	30	37	NWA 10438	32.30	61.1	6.6
LAP 03782	38.00	58	4	NWA 10464	37.70	55.9	6.4
LEW 85305	37.00	57	6	NWA 10464	32.80	31.6	35.6
LEW 85305	32.00	31	37	NWA 10466	34.50	63.5	2
LEW 85353	38.00	60	2	NWA 10466	28.50	28.3	43.2
LEW 85353	30.00	22	48	NWA 10468	36.20	61.9	1.9
LEW 87010	41.00	54	5	NWA 10468	31.10	35.8	33.1
LEW 87010	29.00	28	43	NWA 10469	39.00	59.4	1.6
LEW 88009	40.00	58	2	NWA 10469	35.70	38.8	25.5
LEW 88009	33.00	25	42	NWA 10470	38.30	60	1.7
LEW 88010	44.00	55	1	NWA 10470	32.60	30.9	36.5
LEW 88010	37.00	33	30	NWA 10471	35.50	59.8	4.7
Los Vientos 054	40.00	57.9	2.1	NWA 10471	22.20	51.2	26.6
Los Vientos 054	26.90	46.6	26.5	NWA 10514	34.40	57.3	8.3
MAC 02522	32.00	38	30	NWA 10515	35.70	57.1	7.2
MAC 02522	37.00	51	12	NWA 10515	29.50	29.8	40.7
NWA 10540	49.80	46.8	3.4	NWA 11020	36.90	59.2	3.9
NWA 10548	36.20	56.6	7.2	NWA 11020	28.80	29.1	42.1
NWA 10564	34.80	62.6	2.6	NWA 11040	66.00	29	5
NWA 10639	42.40	55.2	2.4	NWA 11040	50.00	49	1
NWA 10639	30.60	29.7	39.7	NWA 11040	17.00	39	44
NWA 10639	37.60	59.2	3.2	NWA 11040	47.00	37	16
NWA 10640	32.40	64.1	3.5	NWA 11050	39.80	57.3	2.9
NWA 10640	29.90	59.4	10.7	NWA 11058	37.30	60	2.7
NWA 10640	27.90	39.2	32.9	NWA 11063	36.00	59.4	4.6
NWA 10647	37.10	56.8	6.1	NWA 11068	53.70	43.6	2.7
NWA 10661	36.30	59.9	3.8	NWA 11068	60.50	35	4.5
NWA 10667	36.20	58.9	4.9	NWA 11068	40.00	17.2	42.8
NWA 10667	29.70	26.9	43.4	NWA 11081	35.00	63.1	1.9
NWA 10681	34.80	59.6	5.6	NWA 11081	31.80	48.8	19.4
NWA 10681	29.90	26.2	43.9	NWA 11084	34.60	62.8	2.6
NWA 10684	39.30	59.1	1.6	NWA 11116	33.30	64.4	2.3
NWA 10684	31.10	24	44.9	NWA 11116	28.20	28.7	43.1
NWA 10710	38.20	58.4	3.4	NWA 11156	37.10	60.9	2

NWA 10710	33.60	37.6	28.8	NWA 11156	29.80	27	43.2
NWA 10711	37.80	59	3.2	NWA 11158	35.00	60.7	4.3
NWA 10711	31.00	28.4	40.6	NWA 11158	28.50	32.3	39.2
NWA 10716	35.60	59.4	5	NWA 11183	57.90	39.2	2.9
NWA 10716	30.30	30.8	38.9	NWA 11209	38.10	60.2	1.7
NWA 10800	36.10	58.9	5	NWA 11242	52.60	44.7	2.7
NWA 10802	36.80	59.3	3.9	NWA 11242	39.50	20.1	40.4
NWA 10866	37.10	60.8	2.1	NWA 11245	36.10	62.1	1.8
NWA 10866	29.60	26.4	44	NWA 11247	38.10	60	1.9
NWA 10886	36.30	60.1	3.6	NWA 11267	39.20	58.9	1.9
NWA 10886	30.10	27.4	42.5	NWA 11302	37.50	60.4	2.1
NWA 10887	36.30	60.3	3.4	NWA 11321	35.70	60.6	3.7
NWA 10887	30.10	28.1	41.8	NWA 1654	44.10	50.3	5.6
NWA 10905	35.50	61.7	2.8	NWA 1654	24.20	60.6	15.2
NWA 10905	30.10	33.5	36.4	NWA 1654	50.10	29.7	20.2
NWA 10909	40.40	57.4	2.2	NWA 1654	11.10	47.4	41.5
NWA 10915	36.70	60.7	2.6	NWA 1771	35.40	60.4	4.2
NWA 10915	30.40	26.4	43.2	NWA 1771	31.40	31.2	37.4
NWA 10919	32.70	55.8	11.5	NWA 1789	38.00	56.5	5.5
NWA 10919	28.20	33.9	37.9	NWA 1789	30.80	27.4	41.8
NWA 10962	37.80	58.6	3.6	NWA 1909	56.00	37	7
NWA 10962	30.80	29.3	39.9	NWA 1909	33.00	47	20
NWA 10966	36.20	61.9	1.9	NWA 1980	49.50	48	2.5
NWA 10971	37.10	57.8	5.1	NWA 1980	39.00	15	46
NWA 10971	29.90	26.1	44	NWA 2063	39.50	58.5	2
NWA 10979	41.60	56.6	1.8	NWA 2063	31.60	24.8	43.6
NWA 11001	37.20	56.2	6.6	NWA 2065	39.70	58.2	2.1
NWA 11001	30.40	30	39.6	NWA 2065	32.70	62.3	5
NWA 11015	37.30	56.5	6.2	NWA 2066	36.00	61.8	2.2
NWA 2079	43.50	55	1.5	NWA 7035	51.90	39.9	8.2
NWA 2079	36.90	61	2.1	NWA 7035	23.10	52.6	24.3
NWA 2422	38.00	60	2	NWA 7035	5.30	80.6	14.1
NWA 2422	31.00	27	42	NWA 7062	39.50	56	4.5
NWA 3056	61.10	36.1	2.8	NWA 7062	34.00	27	39
NWA 3056	42.50	16.1	41.4	NWA 7159	41.40	56.6	2
NWA 3082	40.20	50.1	9.7	NWA 7159	33.30	24.1	42.6
NWA 3082	31.90	53.3	14.8	NWA 7269	36.60	60.3	3.1
NWA 4269	40.00	26	34	NWA 7326	35.90	48.5	15.6
NWA 4269	32.00	27	41	NWA 7326	41.80	55.7	2.5
NWA 4269	29.00	65	6	NWA 7400	31.60	66.9	1.5
NWA 4541	40.90	54.7	4.4	NWA 7465	36.30	58.6	5.1
NWA 4541	15.50	38	46.5	NWA 7465	30.70	25.3	44
NWA 4677	51.80	41.2	7	NWA 7466	37.20	61.1	1.7
NWA 4824	37.70	56.6	5.7	NWA 7466	29.90	26.9	43.2
NWA 4830	37.40	60.5	2.1	NWA 7470	35.70	62.3	2
NWA 4830	27.10	37.4	35.5	NWA 7485	33.40	47.5	19.1
NWA 4831	51.10	46.7	2.2	NWA 7501	33.50	61.7	4.8
NWA 4831	18.90	36.4	44.7	NWA 7501	27.30	31.7	41
NWA 5234	36.60	61.4	2	NWA 7547	34.70	53.2	12.1
NWA 5351	34.90	62.6	2.5	NWA 7549	40.30	55.2	4.5
NWA 5961	36.30	59.1	4.6	NWA 7549	27.90	30.1	42
NWA 5961	30.60	29.1	40.3	NWA 7551	32.30	54.5	13.2

NWA 6262	45.90	50.8	3.3	NWA 7551	24.30	34.3	41.4
NWA 6262	35.10	39.8	25.1	NWA 7552	45.00	50.5	4.5
NWA 6270	36.00	62.3	1.7	NWA 7552	22.60	34.4	43
NWA 6270	29.30	26.3	44.4	NWA 7642	53.20	45.1	1.7
NWA 6273	35.50	62.4	2.1	NWA 7642	33.00	27.7	39.3
NWA 6273	65.40	26.6	8	NWA 7644	37.40	57.2	5.4
NWA 6288	62.50	30.2	7.3	NWA 7903	33.40	62.2	4.4
NWA 6288	30.50	26.7	42.8	NWA 7914	51.70	45.7	2.6
NWA 6477	34.20	59.8	6	NWA 7914	38.40	19.1	42.5
NWA 6477	31.50	45.3	23.2	NWA 7954	40.80	57.4	1.8
NWA 6477	28.70	28.4	42.9	NWA 7960	44.40	47.7	7.9
NWA 6502	36.90	56.5	6.6	NWA 7960	36.50	29.3	34.2
NWA 6502	29.10	30.4	40.5	NWA 7971	36.00	51.5	12.5
NWA 6568	55.20	42	2.8	NWA 8082	37.90	40.9	21.2
NWA 6573	34.60	62.7	2.7	NWA 8162	36.00	61	3
NWA 6573	29.00	29.7	41.3	NWA 8162	30.90	34.8	34.3
NWA 6967	40.90	53.8	5.3	NWA 8177	35.80	62	2.2
NWA 6967	35.50	32	32.5	NWA 8187	35.60	59.4	5
NWA 6969	37.80	59.7	2.5	NWA 8187	30.30	30	39.7
NWA 6969	30.40	26.6	43	NWA 8235	66.80	28.6	4.6
NWA 6984	39.10	57.7	3.2	NWA 8235	41.70	31.3	27
NWA 6984	32.60	23.7	43.7	NWA 8266	37.50	59.5	3
NWA 7013	38.20	60.1	1.7	NWA 8318	40.10	57.8	2.1
NWA 7014	40.30	57.5	2.2	NWA 8336	35.80	59.3	4.9
NWA 8336	30.00	27.2	42.8	PCA 91081	33.00	40	27
NWA 8344	36.00	60.6	3.4	PCA 91245	38.00	58	4
NWA 8344	30.40	31.4	38.2	PCA 91245	33.00	25	42
NWA 8365	37.90	58.7	3.4	Piplia Kalan	34.00	64	2
NWA 8365	31.10	26.6	42.3	Piplia Kalan	33.00	62	5
NWA 8426	29.90	27.5	42.6	QUE 94484	67.00	28	5
NWA 8426	36.00	59.4	4.6	QUE 94484	41.00	49	10
NWA 8436	35.80	61.2	3	QUE 94484	32.00	25	43
NWA 8436	29.50	24.9	45.6	QUE 94484	33.00	65	2
NWA 8439	36.80	58.2	5	QUE 94484	29.00	30	41
NWA 8439	35.70	61.2	3.1	QUE 97053	52.30	41.2	6.5
NWA 8454	36.10	59.6	4.3	QUE 97053	26.50	49	24.5
NWA 8473	34.20	58.2	7.6	QUE 99658	39.00	59	2
NWA 8479	36.30	59.4	4.3	RKP A80224	36.00	54	10
NWA 8549	35.30	59	5.7	SaU 562	29.90	47.6	22.5
NWA 8549	29.90	32.3	37.8	SaU 562	32.70	62.7	4.6
NWA 8550	35.20	62.7	2.1	SaU 562	32.20	35.5	32.3
NWA 8550	30.20	31.2	38.6	SaU 562	34.10	51.3	14.6
NWA 8554	36.40	50.6	13	Tirhert	37.10	53.6	9.3
NWA 8555	34.80	60.7	4.5	Tirhert	30.50	30.3	39.2
NWA 8555	29.60	29.3	41.1	Y 791438	50.00	42	8
NWA 8557	39.50	56.6	3.9				
NWA 8557	31.10	26.6	42.3				
NWA 8558	35.40	62.1	2.5				
NWA 8562	50.00	41.6	8.4				
NWA 8562	16.00	61.4	22.6				
NWA 8563	36.50	60.9	2.6				
NWA 8563	29.90	26.6	43.5				

NWA 8591	40.90	54.1	5	
NWA 8594	59.00	33.9	7.1	
NWA 8594	27.50	46.9	25.6	
NWA 8606	34.00	60	6	
NWA 8606	28.50	30.2	41.3	
NWA 8675	56.68	34.22	9.1	
NWA 8675	30.30	66.3	3.4	
NWA 8675	45.80	8.9	45.3	
NWA 8729	42.50	55.4	2.1	
NWA8558	29.70	28.1	42.2	
PCA 01021	35.80	61.7	2.5	
PCA 82501	39.00	57	4	
PCA 82501	38.00	41	21	
PCA 82502	34.00	61	5	
PCA 82502	30.00	36	34	
PCA 91078	40.00	55	5	
PCA 91078	34.00	33	33	
PCA 91078	34.00	26	40	
PCA 91081	35.00	62	3	

Table A2. Pyroxene compositions generated through pMELTS modelling when the degree of initial partial melt is changed (fO_2 IW -2.05)

	50%			40%			30%			20%		
	Ens	Fs	Wo	Ens	Fs	Wo	Ens	Fs	Wo	Ens	Fs	Wo
Toplis et al., 2013	90.8	7.15	2.1	90.6	7.74	2.1	90.5	7.23	2.3	89.8	7.58	2.6
	90.1	7.7	2.3	90	7.79	2.3	89.7	7.89	2.5	89.1	8.14	2.8
	89.4	8.25	2.4	89.2	8.35	2.4	89	8.42	2.6	88.3	8.74	2.9
	88.5	8.98	2.5	88.3	9.1	2.6	88.1	9.1	2.8	87.8	9.17	3.1
	87.9	9.46	2.7	87.7	9.58	2.7	87.5	9.59	2.9	86.9	9.88	3.2
	87	10.18	2.8	86.8	10.32	2.9	86.7	10.27	3.1	86.2	10.43	3.4
	86.1	10.92	3	85.9	11.07	3	85.8	10.98	3.2	85.3	11.14	3.6
	85.2	11.67	3.2	85	11.85	3.2	84.9	11.71	3.4			
	84.2	12.46	3.3	84	12.65	3.4	83.9	12.46	3.6			
	83.2	13.26	3.5	83	13.47	3.6	82.9	13.25	3.8			
	82.2	14.08	3.7	81.9	14.31	3.8	81.9	14.05	4.1			
	81.1	14.93	4	80.8	15.19	4	80.8	14.89	4.3			
	80	15.82	4.2	79.7	16.08	4.3						
Righter & Drake (1997) CV-H	88.5	8.16	3.3	88.5	8.14	3.3	87.7	8.61	3.7			
	87.8	8.52	3.7	87.8	8.5	3.7	86.6	9.24	4.1			
	86.8	9.15	4.1	86.8	9.12	4.1	85.5	9.89	4.6			
	85.7	9.79	4.5	85.7	9.76	4.5						
Righter & Drake (1997) CV-L	89.4	7.75	2.9	88.4	8.41	3.2	88.4	8.18	3.5			
	88.4	8.42	3.2	87.7	8.8	3.5	87.2	8.9	3.9			
	87.7	8.8	3.5	86.8	9.43	3.8	86.2	9.52	4.3			
	86.7	9.44	3.8	85.7	10.1	4.2	85	10.16	4.8			
	85.7	10.1	4.2	84.6	10.75	4.7						
84.6	10.77	4.7										
Righter & Drake (1997) CM-H	88.4	8.3	3.3	88.6	8.11	3.3	88.5	8.09	3.4			
	87.8	8.66	3.6	87.6	8.76	3.6	86.9	9.08	4			
	86.8	9.3	4	86.6	9.4	4	85.8	9.72	4.5			
	85.7	9.95	4.9	85.5	10.06	4.4						
	84.5	10.61	4.9	84.3	10.73	4.9						
Righter & Drake (1997) CM-L	89.4	7.8	2.9	89.2	7.9	2.9	88.3	8.23	3.5			
	88.4	8.46	3.1	88.6	8.3	3.1	87.3	8.83	3.8			
	87.7	8.86	3.4	87.6	8.96	3.4	86.3	9.43	4.3			
	86.8	9.5	3.7	86.6	9.62	3.8	85.2	10.06	4.7			
	85.8	10.2	4.1	85.5	10.29	4.2						
	84.6	10.84	4.6	84.4	11	4.6						
				83.3	11.74	5						
	89.5	7.83	2.7	89.5	7.8	2.7	89.7	7.49	2.8	88.6	8.02	3.4
	88.8	8.36	2.9	88.8	8.33	2.9	89.1	7.94	2.9	87.8	8.66	3.6
Ruzicka et al., (1997) R-HED-CI	87.9	9.06	3.1	87.9	9.01	3.1	88.3	8.6	3.1	87.2	9.05	3.8
	87.2	9.54	3.2	87.3	9.47	3.2	87.7	8.99	3.3			
	86.3	10.22	3.4	86.4	10.16	3.5	86.8	9.64	3.5			

	85.4	10.94	3.7	85.5	10.88	3.7	85.9	10.32	3.8			
	84.4	11.67	3.9	84.5	11.61	4	85	11.01	4			
	83.4	12.42	4.2	83.4	12.37	4.2	84	11.73	4.3			
	82.3	13.21	4.5	82.3	13.15	4.5	82.9	12.49	4.6			
Ruzicka et al., (1997) R-HED-CM	90.2	7.37	2.5	89.5	7.89	2.7	89.6	7.63	2.8	88.5	8.21	3.3
	89.5	7.89	2.7	88.8	8.43	2.8	88.9	8.17	2.9	87.7	8.77	3.5
	88.8	8.42	2.8	87.9	9.13	3	88.4	8.55	3.1	86.9	9.38	3.8
	87.9	9.13	3	87.2	9.61	3.2	87.5	9.21	3.3	86.3	9.77	4
	87.2	9.6	3.2	86.3	10.31	3.4	86.6	9.89	3.5			
	86.3	10.31	3.4	85.4	11.04	3.6	86	10.33	3.7			
	85.4	11.04	3.6	84.4	11.78	3.9	85.1	11.02	3.9			
	84.4	11.77	3.8	83.3	12.54	4.1	84.1	11.74	4.2			
	83.4	12.53	4.1	82.3	13.33	4.4	83	12.48	4.5			
	82.3	13.32	4.4	81.1	14.15	4.7						
	81.1	14.15	4.7									
Ruzicka et al., (1997) R-HED-L	89.3	8.05	2.7	89.9	7.53	2.6	89.2	7.88	3	87.8	8.6	3.7
	88.6	8.6	2.8	89.2	7.96	2.8	88.4	8.42	3.1	87.2	8.99	3.8
	87.6	9.32	3	88.8	8.32	2.9	87.9	8.82	3.3			
	87	9.82	3.2	87.9	9.01	3.1	87	9.47	3.5			
	86.1	10.55	3.4	87.3	9.47	3.2	86.1	10.12	3.8			
	85.1	11.29	3.7	86.4	10.16	3.5	85.2	10.81	4			
	84.1	12.05	3.9	85.4	10.88	3.7	84.2	11.51	4.3			
	83	12.84	4.2	84.5	11.61	3.9						
	81.9	13.65	4.5	83.4	12.36	4.2						
80.7	14.49	4.8	82.3	13.15	4.5							
Ruzicka et al., (1997) R-HED-EH	89.6	7.68	2.7	89	8.04	3	87.8	8.77	3.5			
	88.8	8.34	2.9	88.2	8.63	3.1	86.6	9.63	3.8			
	87.9	9.03	3.1	87.6	9.05	3.3	85.7	10.28	4			
	87.2	9.5	3.3	86.8	9.7	3.6						
	86.3	10.19	3.5	85.8	10.38	3.8						
	85.4	10.91	3.7	84.9	11.08	4						
	84.4	11.64	4	83.9	11.8	4.3						
	83.3	12.4	4.3									
	82.2	13.19	4.6									
Dreibus & Wanke (1980)	90.3	7.45	2.2	90.2	7.45	2.3	89.8	7.62	2.6	88.9	8.13	3
	89.7	7.97	2.4	89.6	7.97	2.5	89.2	8.08	2.7	87.8	8.94	3.2
	89	8.52	2.5	88.8	8.53	2.6	88.4	8.74	2.9	87.3	9.34	3.4
	88.1	9.22	2.7	88	9.23	2.8	87.8	9.16	3	86.5	9.96	3.6
	87.5	9.71	2.8	87.3	9.73	2.9	87	9.83	3.2			
	86.6	10.42	3	86.5	10.44	3.1	86.1	10.51	3.4			
	85.7	11.15	3.1	81.4	14.29	4.4	85.2	11.21	3.6			
	84.8	11.88	3.3				84.3	11.95	3.8			
	83.9	12.65	3.5				83.3	12.7	4			
	82.9	13.43	3.7				82.2	13.48	4.3			

	81.8	14.25	4									
	80.7	15.08	4.2									
	79.5	15.93	4.6									
Bosenberg & Delaney (1997)	89.3	8	2.7	89.3	7.97	2.7	89.2	7.91	2.9	87.2	8.86	4
	88.4	8.67	3	88.4	8.64	3	87.9	8.76	3.3			
	87.7	9.09	3.2	87.7	9.06	3.2	87	9.41	3.6			
	86.7	9.77	3.5	86.8	9.73	3.5	86.4	9.75	3.9			
	85.7	10.45	3.8	85.8	10.41	3.8	85.3	10.4	4.3			
	84.7	11.15	4.2	84.7	11.11	4.2	84.2	11.06	4.8			
	83.4	11.86	4.6	83.6	11.81	4.6						

Table A3. Pyroxene compositions generated from each starting composition under varying oxygen fugacity conditions.

	fO_2	Ens	Fs	Wo		fO_2	Ens	Fs	Wo		
Toplis et al., 2013	-2.05	90.64	7.24	2.12	Righter & Drake (1997) CV-H	-2.05	88.52	8.14	3.34		
		89.96	7.79	2.25			87.82	8.50	3.68		
		89.24	8.35	2.41			86.82	9.12	4.06		
		88.34	9.10	2.56			85.70	9.76	4.54		
		87.72	9.58	2.70			84.58	10.44	4.98		
		86.83	10.32	2.85			-1.80	84.64	8.14	3.34	
		85.92	11.07	3.01				87.82	8.50	3.68	
		84.97	11.85	3.19				86.82	9.12	4.06	
		83.99	12.65	3.36				85.70	9.76	4.54	
		82.97	13.47	3.56				84.58	10.44	4.98	
		81.91	14.31	3.78				-1.60	80.19	15.22	4.59
		80.79	15.19	4.02			78.30		16.55	5.15	
	79.66	16.08	4.26	77.03	17.19	5.78					
	-1.80	87.44	10.19	2.37	-1.40	74.95	19.87		5.18		
		86.50	10.96	2.54		72.65	21.61		5.74		
		85.52	11.77	2.72		71.25	22.31		6.44		
		84.52	12.61	2.87		Righter & Drake (1997) CV-L	-2.05	88.40	8.41	3.19	
		83.20	13.73	3.07				87.73	8.80	3.47	
		82.28	14.47	3.25				86.75	9.43	3.82	
	80.92	15.62	3.45	85.69	10.10			4.22			
	79.54	16.80	3.66	84.55	10.75			4.70			
	78.08	18.04	3.88	-1.80	85.65			10.97	3.38		
	76.58	19.31	4.11		84.25			11.99	3.75		
	75.03	20.63	4.34		83.40			12.46	4.14		
73.42	22.00	4.57	81.91		13.46			4.62			
71.77	23.42	4.81	80.33		14.50			5.17			
-1.60	83.58	13.80	2.62		-1.60			81.45	14.65	3.90	
	82.32	14.85	2.85	80.06				15.61	4.33		
	81.03	15.97	3.00	78.18		16.99	4.83				
	79.65	17.15	3.20	76.98		17.68	5.36				
	78.21	18.40	3.39	74.97		19.04	5.98				
	76.41	19.99	3.60	-1.40		74.51	20.62	4.86			
	75.03	21.16	3.80			72.20	22.45	5.34			
	73.17	22.83	4.00			70.78	23.27	5.94			
	17.26	24.56	4.18			-1.20	65.61	28.90	5.49		
	69.27	26.37	4.36				Righter & Drake (1997) CM-H	-2.05	88.63	8.11	3.26
	67.23	28.25	4.52						87.64	8.76	3.60
	65.12	30.23	4.65	86.61					9.40	3.98	
-1.40	78.86	18.27	2.87	85.52	10.06				4.43		
	77.23	19.70	3.07	84.33	10.73				4.94		
	75.53	21.19	3.28	-1.80	85.23	10.90			3.87		
	73.76	22.77	3.47		83.11	12.60			4.29		
	71.90	24.43	3.67		82.06	13.16			4.77		
	69.93	26.22	3.85		80.46	14.16			5.38		
97.58	28.43	3.99	-1.60		80.06	15.46			4.48		
65.63	30.23	4.13			78.17	16.83			5.00		
63.16	32.61	4.22		76.90	17.49	5.61					
60.57	35.14	4.30		74.88	18.83	6.29					

		57.87	37.79	4.33		-1.40	74.76	20.18	5.05
	-1.20	70.99	25.76	3.25			72.46	21.97	5.57
		75.54	21.77	2.69			71.05	22.72	6.23
		66.59	29.82	3.59					
		64.23	32.05	3.72					
Richter & Drake CM-L	-2.05	89.23	7.90	2.87			74.82	20.40	4.78
		88.56	8.30	3.13			73.00	21.93	5.07
		87.60	8.96	3.44			71.11	23.53	5.36
		86.59	9.62	3.78		-1.40	78.11	18.38	3.51
		85.54	10.29	4.17			76.64	19.59	3.77
		84.36	11.00	4.64			75.04	20.94	4.02
		83.26	11.74	5.00			73.35	22.37	4.28
	-1.80	85.58	11.08	3.35			71.60	23.88	4.52
		84.19	12.12	3.70			69.37	25.88	4.74
		82.06	13.43	4.51			67.76	27.25	4.98
		80.51	14.15	5.04			65.45	29.39	5.16
		78.86	15.49	5.65		-1.20	78.11	18.35	3.51
	-1.60	81.36	14.77	3.86			75.89	20.35	3.76
		79.98	15.75	4.28			73.59	22.41	4.00
		78.11	17.14	4.75			71.23	24.54	4.23
		76.86	17.85	5.29			68.80	26.77	4.44
		74.90	19.23	5.87			66.29	29.10	4.61
	-1.40	80.08	16.06	3.86			63.70	31.55	4.75
		78.07	17.65	4.28	Ruzicka et al., (1997) R-HED-CM	-2.05	89.46	7.89	2.65
		75.98	19.28	4.75			88.75	8.43	2.82
		73.81	20.96	5.24			87.85	9.13	3.01
		71.60	22.66	5.74			87.20	9.61	3.19
		69.31	24.43	6.26			86.29	10.31	3.40
	-1.20	80.08	16.06	3.86			85.35	11.04	3.61
		78.05	17.65	4.30			84.37	11.78	3.85
		75.97	19.28	4.75			83.34	12.54	4.12
		73.81	20.96	5.24			82.25	13.33	4.42
		71.58	22.68	5.74			81.12	14.15	4.73
		69.29	24.43	6.28		-1.80	86.75	10.43	2.82
Ruzicka et al., (1997) R-HED-CI	-2.05	89.50	7.80	2.70			85.82	11.16	3.01
		88.80	8.33	2.88			84.84	11.93	3.23
		87.92	9.01	3.07			83.81	12.74	3.45
		87.29	9.47	3.24			82.47	13.82	3.70
		86.38	10.16	3.46			81.52	14.54	3.94
		85.45	10.88	3.67			80.13	15.65	4.22
		84.47	11.61	3.93			78.69	16.80	4.51
		83.43	12.37	4.20			77.19	17.98	4.83
		82.34	13.15	4.51			75.65	19.21	5.16
	-1.80	86.85	10.30	2.86		-1.60	82.90	13.94	3.15
		85.92	11.01	3.07			81.68	14.93	3.39
		84.95	11.77	3.29			80.40	15.96	3.63
		83.95	12.55	3.50			79.05	17.07	3.88
		82.64	13.60	3.76			77.32	18.84	4.15
		81.70	14.30	4.00			76.11	19.54	4.41
		80.32	15.38	4.30			74.29	21.00	4.70
		78.88	16.52	4.60			72.44	22.58	4.98

		77.39	17.68	4.93			70.23	24.13	5.63
		75.83	18.88	5.30			68.55	25.96	5.49
	-1.60	83.06	13.75	3.49		-1.40	78.06	18.49	3.45
		81.87	14.70	3.43			76.42	19.87	3.72
		80.60	15.71	3.69			74.48	21.25	3.97
		79.28	16.77	3.95			73.08	22.72	4.20
		77.88	17.90	4.22			71.83	23.82	4.35
		69.01	26.32	4.67			84.88	11.08	4.04
		76.15	19.36	4.49			67.35	27.77	4.89
		65.00	29.94	5.06			83.86	11.80	4.33
	-1.20	78.11	18.44	3.45		-1.80	85.53	11.20	3.27
		75.86	20.43	3.70			84.26	12.16	3.58
		73.57	22.49	3.94			82.98	13.18	3.84
		71.21	24.62	4.17			82.12	13.83	4.06
		68.79	26.86	4.38			80.76	14.87	4.37
		66.27	29.19	4.55			79.35	15.96	4.70
		63.68	31.64	4.68			77.87	17.09	5.04
Ruzicka et al., (1997) R- HED-L	-2.05	89.86	7.53	2.61		-1.60	81.91	14.56	3.53
		88.75	8.43	2.82			80.94	15.33	3.73
		88.80	8.32	2.87			79.65	16.36	3.99
		87.92	9.01	3.07			78.31	17.42	4.27
		87.29	9.47	3.24			76.58	18.85	4.57
		86.38	10.16	3.46			75.32	19.83	4.85
		85.43	10.88	3.69			73.58	21.31	5.17
		84.47	11.61	3.93		-1.40	76.39	19.74	3.87
		83.42	12.36	4.22			75.39	20.53	4.08
		82.34	13.15	4.51			73.75	21.90	4.35
	-1.80	86.68	10.46	2.86			72.05	23.36	4.59
		85.80	11.15	3.05			69.86	25.31	4.84
		84.81	11.93	3.27			68.31	26.61	5.08
		83.77	12.76	3.50	Dreibus & Wanke (1980)	-2.05	90.22	7.45	2.33
		82.45	13.81	3.74			89.55	7.97	2.48
		81.47	14.53	4.00			88.84	8.53	2.63
		80.08	15.64	4.28			87.98	9.23	2.79
		78.64	16.78	4.59			87.33	9.73	2.94
		77.11	17.93	4.93			86.46	10.44	3.10
		75.56	19.18	5.26			81.36	14.29	4.35
	-1.60	83.10	13.78	3.11		-1.80	86.75	10.64	2.61
		81.57	15.02	3.41			85.92	11.27	2.91
		80.27	16.05	3.67			84.82	12.19	2.99
		78.90	17.16	3.94			83.78	13.04	3.18
		77.15	18.65	4.21			82.48	14.14	3.38
		75.93	19.60	4.47			81.50	14.92	3.58
		74.11	21.13	4.76			80.12	16.05	3.82
		72.24	22.71	5.04			87.70	17.23	4.07
		70.31	24.39	5.31			77.23	18.45	4.32
		68.32	26.11	5.57			75.70	19.71	4.59
	-1.40	79.17	17.36	3.47			74.11	21.02	4.88
		77.09	19.16	3.75			72.20	22.29	5.52
		74.96	21.04	4.00		-1.60	82.81	14.26	2.93
		72.77	22.90	4.24			81.58	15.29	3.13
		70.52	25.01	4.47			80.28	16.37	3.35

		68.91	26.39	4.70		78.93	17.52	3.56
		66.59	28.52	4.89		77.17	19.05	3.79
		64.18	30.75	5.07		75.93	20.06	4.01
Ruzicka et al., (1997) R- HED-EH	-2.05	88.99	8.04	2.97		74.09	21.66	4.23
		88.23	8.63	3.14		72.26	23.28	4.46
		87.62	9.05	3.34		70.31	25.00	4.68
		86.75	9.70	3.55		68.32	26.79	4.89
		85.84	10.38	3.78		69.16	25.57	5.27
	-1.40	78.10	18.70	3.20		70.86	25.09	4.05
		76.16	20.40	3.43		68.57	27.21	4.22
		74.49	21.87	3.64		66.81	28.79	4.40
		72.72	23.43	3.86		64.40	31.07	4.53
		61.90	33.48	4.63				
Bosenberg & Delaney (1997)	-2.05	89.29	7.97	2.74				
		88.37	8.64	2.99				
		87.72	9.06	3.21				
		86.77	9.73	3.52				
		85.76	10.41	3.83				
		84.70	11.11	4.19				
		83.57	11.81	4.62				
		82.54	12.51	5.05				
	-1.80	86.47	10.63	2.89				
		85.49	11.35	3.16				
		84.14	12.39	3.48				
		83.29	12.93	3.79				
		81.86	13.97	4.18				
		80.36	15.04	4.59				
		87.77	16.14	5.09				
		77.10	17.27	5.62				
	-1.60	82.54	14.18	3.29				
		81.25	15.13	3.62				
		79.87	16.15	3.98				
		78.05	17.57	4.38				
		76.83	18.37	4.79				
		74.93	19.81	5.26				
		72.96	21.29	5.75				
		71.00	22.80	6.24				
	-1.40	75.84	20.12	4.04				
		74.13	21.45	4.41				
		72.31	22.87	4.82				
		70.00	24.80	5.20				
68.39		25.70	5.64					
66.00		27.97	6.03					

Table A4. Compositions adapted from literature through the removal of eucrite used to generate pMELTS models. % reflects the amount of a mean eucrite component removed from the initial starting composition.

Toplis et al., (2013)						Righter & Drake (1997) CV-H				
	0%	5%	10%	15%	20%	0%	5%	10%	15%	20%
SiO₂	42.59	42.21	41.8	41.33	43.93	40.3	39.2	38.63	38.04	37.33
TiO₂	0.1	0.07	0.04	0.01		0.13	0.1	0.07	0.04	
Al₂O₃	2.7	2.16	1.54	0.87	0.09	2.75	2.17	1.57	0.91	0.16
Cr₂O₃						0.61	0.61	0.62	0.64	0.65
FeO	24.42	24.76	25.14	25.56	24.65	27.4	27.48	28.01	28.61	29.28
MnO						0.36	0.35	0.34	0.32	0.31
MgO	27.92	28.98	30.15	31.46	31.16	26.6	27.17	28.24	29.43	30.77
CaO	2.2	1.78	1.3	0.77	0.17	2.24	1.79	1.32	0.8	0.22
Na₂O	0.07	0.05	0.03			1.01	1.02	1.05	1.09	1.13
K₂O						0.11	0.11	0.12	0.12	0.13
P₂O₅										
Righter & Drake (1997) CV-L						Righter & Drake (1997) CM-H				
	0%	5%	10%	15%	20%	0%	5%	10%	15%	20%
SiO₂	46.1	38.33	44.94	44.69	44.41	43.5	42.5	42.12	41.71	41.24
TiO₂	0.15	0.07	0.09	0.06	0.03	0.13	0.1	0.07	0.04	
Al₂O₃	3.12	1.56	1.98	1.33	0.61	2.89	2.31	1.73	1.07	0.33
Cr₂O₃	0.67	0.62	0.69	0.7	0.72	0.66	0.66	0.68	0.69	0.71
FeO	18.21	27.78	17.95	17.97	17.99	21.73	21.59	21.8	22.04	22.31
MnO	0.38	0.33	0.36	0.35	0.34	0.37	0.36	0.35	0.34	0.32
MgO	29.31	28.01	31.37	32.53	34.06	28.8	29.43	30.63	31.96	33.45
CaO	2.49	2.14	1.59	1.09	0.53	2.34	1.89	1.43	0.92	0.34
Na₂O	1.06	1.05	1.11	1.15	1.19	1.03	1.04	1.08	1.11	1.15
K₂O	0.11	0.11	0.12	0.12	0.12	0.11	0.11	0.12	0.12	0.12
P₂O₅										
Righter & Drake (1997) CM-L						Ruzicka et al., (1997) R HED-CI				
	0%	5%	10%	15%	20%	0%	5%	10%	15%	20%
SiO₂	49.4	48.58	48.54	48.5	48.44	45.34	45.13	44.9	44.64	44.35
TiO₂	0.15	0.12	0.09	0.06	0.03	0.18	0.16	0.13	0.1	0.07
Al₂O₃	3.25	2.69	2.12	1.48	0.77	3.29	2.77	2.2	1.56	0.84
Cr₂O₃	0.73	0.73	0.75	0.77	0.81	0.85	0.87	0.9	0.93	0.96
FeO	12.2	11.72	11.39	11.03	10.63	14.34	14.17	13.97	13.76	13.52
MnO	0.39	0.38	0.37	0.36	0.35	0.4	0.39	0.39	0.38	0.37
MgO	31.72	32.44	33.8	35.31	37.01	32.67	33.99	35.46	37.1	38.94
CaO	2.59	2.15	1.7	1.21	0.65	2.78	2.38	1.94	1.45	0.9
Na₂O	1.07	1.08	1.12	1.16	1.2	0.12	0.1	0.08	0.06	0.04
K₂O	0.11	0.11	0.12	0.12	0.12	0.01	0.01	0.01		
P₂O₅						0.02	0.02	0.02	0.02	0.02

Ruzicka et al., (1997) R HED-CM						Ruzicka et al., (1997) R HED-L				
	0%	5%	10%	15%	20%	0%	5%	10%	15%	20%
SiO₂	45.74	45.55	45.34	45.11	44.84	46.96	46.84	46.7	46.55	46.37
TiO₂	0.18	0.16	0.13	0.1	0.07	0.21	0.19	0.16	0.14	0.1
Al₂O₃	3.25	2.73	2.15	1.51	0.79	3.71	3.22	2.67	2.05	1.36
Cr₂O₃	0.88	0.91	0.93	0.96	1	0.92	0.95	0.98	1.01	1.05
FeO	14.48	14.31	14.13	13.92	13.69	15.11	14.98	14.83	14.66	14.48
MnO	0.41	0.4	0.4	0.39	0.38	0.44	0.44	0.43	0.42	0.42
MgO	32.16	33.45	34.89	36.49	38.3	29.3	30.44	31.71	33.13	34.73
CaO	2.76	2.36	1.92	1.43	0.87	3.17	2.79	2.38	1.91	1.39
Na₂O	0.12	0.1	0.08	0.06	0.04	0.14	0.12	0.11	0.09	0.06
K₂O	0.01	0.01	0.01			0.01	0.01	0.01		
P₂O₅	0.02	0.02	0.02	0.02	0.02	0.03	0.03	0.03	0.03	0.03
Ruzicka et al., (1997) R HED-EH						Dreibus & Wänke (1980)				
	0%	5%	10%	15%	20%	0%	5%	10%	15%	20%
SiO₂	49.06	49.04	49.03	49.01	48.99	46.2	46.08	45.9	45.7	45.47
TiO₂	0.26	0.24	0.22	0.19	0.17	0.16	0.14	0.11	0.08	0.04
Al₂O₃	4.63	4.18	3.69	3.13	2.51	3.27	2.75	2.18	1.54	0.81
Cr₂O₃	0.98	1.01	1.04	1.08	1.12	0.87	0.9	0.92	0.95	0.99
FeO	16.25	16.18	16.09	16	15.9	14.8	14.66	14.5	14.31	14.11
MnO	0.49	0.49	0.49	0.48	0.48	0.42	0.41	0.41	0.4	0.39
MgO	24.15	25.02	25.99	27.07	28.29	31.5	32.79	34.19	35.76	37.52
CaO	3.97	3.64	3.27	2.85	2.39	2.57	2.16	1.71	1.21	0.64
Na₂O	0.17	0.16	0.14	0.12	0.1	0.11	0.09	0.07	0.05	0.03
K₂O	0.01	0.01	0.01			0.01	0.01	0.01		
P₂O₅	0.04	0.04	0.04	0.04	0.04					
Bosenberg & Delaney (1997)										
	0%	5%	10%	15%	20%					
SiO₂	44.64	44.42	44.15	43.84	43.5					
TiO₂	0.16	0.14	0.11	0.08	0.04					
Al₂O₃	2.81	2.27	1.67	0.99	0.24					
Cr₂O₃	0.67	0.68	0.7	0.72	0.74					
FeO	19.1	19.19	19.27	19.37	19.48					
MnO	0.35	0.34	0.33	0.32	0.31					
MgO	29.06	30.21	31.47	32.87	34.45					
CaO	2.31	1.89	1.42	0.9	0.31					
Na₂O	0.84	0.86	0.88	0.91	0.94					
K₂O										
P₂O₅										

Table A5. Pyroxene compositions generated through pMELTS modelling of each starting composition at various degrees of eucrite removal.

	fO_2 ΔIW	% Euc. Removed	Ens	Fs	Wo	fO_2 ΔIW	% Euc. Removed	Ens	Fs	Wo		
Toplis et al., 2013	-1.20	5	72.35	24.81	2.85	-1.60	5	84.57	13.16	2.27		
			70	26.86	3.04			83.3	14.25	2.45		
			67.79	29	3.2			81.98	15.39	2.63		
			65.38	31.3	3.32			80.6	16.59	2.81		
			62.84	33.73	3.43			79.17	17.85	2.98		
			70.97	26.5	2.52			77.64	19.2	3.16		
		10	68.44	28.88	2.68			75.81	20.86	3.33		
			65.82	31.39	2.8			74.31	22.19	3.5		
			63.05	34.07	2.88			72.4	23.93	3.67		
			72.1	26.03	1.87			68.38	27.64	3.97		
			69.24	28.76	2			66.29	29.62	4.1		
			66.31	31.61	2.08			10	84.16	13.81	2.01	
		63.21	34.63	2.16	82.78				15.05	2.17		
		74.29	25.01	0.7	81.37				16.32	2.31		
		71.15	28.12	0.72	76.63				20.63	2.74		
		67.85	31.4	0.75	74.69				22.43	2.88		
		64.36	34.89	0.76	72.71				24.28	3.01		
		20	60.59	38.66	0.74			70.67	26.21	3.12		
			15	85.22	13.8			1.48	15	85.22	13.8	1.48
				83.77	14.63			1.6		83.77	14.63	1.6
				80.75	17.44			1.8		80.75	17.44	1.8
				79.12	18.98			1.91		79.12	18.98	1.91
				77.14	20.85			2.01		77.14	20.85	2.01
				75.51	22.39			2.1		75.51	22.39	2.1
20	73.48		24.33	2.19	73.48	24.33	2.19					
	85.22		13.3	1.48	20	85.22	13.3	1.48				
	83.77		14.63	1.6		83.77	14.63	1.6				
	82.3		16.1	1.7		82.3	16.1	1.7				
	80.74		17.45	1.8		80.74	17.45	1.8				
	79.11	18.98	1.91	79.11		18.98	1.91					
77.14	20.85	2.01	77.14	20.85		2.01						
Righter & Drake (1997) CV-H	-1.20	5	-	-	-	-1.60	5	80.11	15.49	4.4		
		10	-	-	-		78.2	16.86	4.94			
		15	66.54	28.87	4.59		76.91	17.54	5.55			
			63.6	31.45	4.95		74.88	18.88	6.25			
			61.75	32.8	5.45		10	81.74	14.67	3.59		

		20	65.76	32.05	2.2			79.88	16.09	4.02
			62.68	35	2.31			78.81	16.68	4.51
			59.45	38.15	2.4			76.87	18.06	5.07
			55.99	41.53	2.48			74.85	19.46	5.69
			52.31	45.17	2.53			72.25	20.88	6.38
			48.29	49.13	2.57		15	82.15	14.96	2.89
			43.9	53.49	2.6			80.33	16.43	3.24
								79.34	17.05	3.59
								77.49	18.51	3.99
								75.56	20	4.43
								73.56	21.52	4.92
								71.49	23.08	5.43
								69.36	24.67	5.97
							20	83.13	15.56	1.32
								82.5	16.06	1.43
								80.9	17.54	1.55
								79.23	19.1	1.67
								77.46	20.72	1.82
								76.93	21.12	1.95
								75.13	22.77	2.1
								73.24	24.52	2.25
								71.22	26.37	2.41
								69.3	28.15	2.55
								66.87	30.43	2.7
								64.51	32.65	2.84
								62.01	35.06	2.94
Righter & Drake (1997) CV-L	-1.20	5	-	-	-	-1.60	5	81.74	14.67	3.59
		10	67.24	28.33	4.53			79.88	16.09	4.02
			64.93	30.12	4.96			78.81	16.68	4.51
			61.91	32.79	5.3			76.07	18.06	5.07
		15	66.9	29.18	3.92			74.85	19.46	5.69
			63.81	31.97	4.22			72.75	20.88	6.38
			61.99	33.4	4.62		10	82.79	14.14	3.07
			58.79	36.33	4.88			81.46	15.12	3.42
		20	69.6	27.97	2.43			79.59	16.59	3.82
			67.29	30.05	2.66			78.53	17.22	4.25
			64.14	33.01	2.84			76.6	18.67	4.73
			62.29	34.66	3.06			74.61	20.13	5.26
			59	37.78	3.23			72.54	21.63	5.83
			55.55	41.12	3.34		15	82.93	14.45	2.62
			51.83	44.72	3.46			81.61	15.48	2.91
								79.76	16.99	3.25

								78.71	17.7	3.58
								76.82	19.21	3.96
								74.86	20.75	4.39
								72.85	22.33	4.82
								70.75	23.96	5.29
								68.59	25.63	5.77
							20	83.5	14.74	1.77
								82.24	15.82	1.94
								80.46	17.39	2.14
								79.64	18.04	2.32
								77.68	19.76	2.56
								75.82	21.4	2.79
								73.86	23.11	3.03
								71.85	24.88	3.26
								69.74	26.75	3.52
								67.55	28.7	3.75
								65.24	30.76	3.99
								62.84	32.96	4.2
Richter & Drake (1997) CM-H	-1.20	5	-	-	-	-1.60	5	81.52	14.64	3.84
		10	66.05	28.54	5.41			80.11	15.6	4.29
			63.13	31.04	5.84			78.2	16.99	4.81
		15	65.9	29.53	4.56			76.94	17.68	5.38
			62.91	32.19	4.9			74.92	19.04	6.04
			61	33.62	5.38		10	81.54	14.94	3.52
		20	66.78	30.65	2.56			79.67	16.4	3.93
			63.75	33.55	2.71			78.58	17.02	4.4
			60.54	36.61	2.85			76.65	18.43	4.92
			59.03	37.91	3.06			74.64	19.88	5.8
			55.62	41.2	3.17			72.55	21.34	6.11
			51.97	44.79	3.25		15	83.25	14.14	2.61
			47.97	48.7	3.32			81.96	15.13	2.91
								80.14	16.62	3.24
								79.11	17.28	3.61
								77.23	18.75	4.01
								75.32	20.24	4.44
								73.31	21.78	4.91
								71.23	23.26	5.42
								69.08	24.98	5.94
							20	84.49	14.33	1.48
								83.04	15.34	1.62
								81.36	16.86	1.78
								80.48	17.58	1.93

								78.77	19.11	2.12
								77	20.7	2.3
								75.13	22.37	2.5
								73.19	24.12	2.69
								71.14	25.95	2.9
								69.01	27.9	3.09
								66.77	29.94	3.29
								64.39	32.14	3.47
								61.9	34.47	3.64
Righter & Drake (1997) CM-L	-1.20	5	79.53	16.78	3.69	-1.60	5	81.23	15.1	3.67
			77.43	18.47	4.09			79.81	16.1	4.08
			75.25	20.22	4.52			77.93	17.55	4.53
			73.01	22.01	4.98			76.65	18.31	5.04
			70.73	23.84	5.44			74.67	19.75	5.58
			68.34	25.73	5.92			72.62	21.18	6.19
		10	81.1	15.85	3.05		10	82.63	14.32	3.05
			78.99	17.62	3.39			81.3	15.31	3.39
			76.79	19.43	3.78			79.41	16.8	3.78
			74.52	21.31	4.17			78.35	17.47	4.18
			72.2	23.24	4.56			76.42	18.94	4.64
			69.79	25.22	4.98			74.29	20.4	5.31
			67.33	27.28	5.39			72.36	21.96	5.67
			64.77	29.43	5.8		15	82.69	14.69	2.62
		15	80.75	16.62	2.64			81.33	15.75	2.91
			78.56	18.52	2.92			79.47	17.3	3.23
			76.26	20.5	3.24			78.39	18.05	3.56
			73.9	22.53	3.57			76.48	19.59	3.93
			71.48	24.63	3.89			74.51	21.16	4.64
			68.97	26.8	4.23			72.47	22.78	4.75
			66.37	29.07	4.56			70.36	24.44	5.2
			63.7	31.43	4.87			68.2	26.16	5.64
			60.9	33.94	5.17		20	84.19	14.33	1.48
			57.94	36.63	5.43			83.04	15.34	1.62
		20	80.81	17.31	1.88			81.36	16.86	1.78
			78.55	19.37	2.08			80.48	17.58	1.93
			76.21	21.5	2.29			78.77	19.11	2.12
			73.28	23.71	2.51			77	20.7	2.3
			71.27	26.01	2.73			75.13	22.37	2.5
			68.68	28.4	2.92			73.19	24.12	2.69
			65.98	30.9	3.12			71.14	25.95	2.9
			63.19	33.5	3.31			69.01	27.9	3.09
			60.25	36.27	3.47			66.77	29.94	3.29

			57.17	39.23	3.6			64.39	32.14	3.47
			53.4	42.84	3.76			61.9	34.47	3.64
			50.33	45.85	3.82					
Ruzicka	-1.20	5	77.03	19.61	3.36	-1.60	5	82.72	14.2	3.08
et al.,			74.62	21.77	3.6			81.47	15.21	3.32
(1997)			72.16	24.02	3.82			80.16	16.3	3.54
HED-CI			69.01	26.12	4.87			78.78	17.43	3.78
			67.01	28.79	4.2			77	18.95	4.05
			64.32	31.35	4.33			75.77	19.93	4.3
		10	78.12	18.93	2.95			73.92	21.5	4.57
			75.58	21.24	3.18			72.05	23.12	4.83
			72.93	23.67	3.4		10	83.78	13.51	2.71
			70.23	26.19	3.59			82.39	14.68	2.93
			67.45	28.81	3.76			81.08	15.77	3.15
			64.57	31.55	3.89			79.7	16.93	3.37
			61.6	34.32	3.98			78.25	18.15	3.6
		15	76.61	20.71	2.67			76.87	19.3	3.82
			73.75	23.28	2.87			75.46	20.49	4
			70.8	26.15	3.05			74.03	21.69	4.28
			67.76	29.05	3.2			72.6	22.89	4.51
			64.63	32.07	3.3			71.15	24.11	4.74
			61.4	35.21	3.4			69.69	25.34	4.98
		20	77.55	20.43	2.01			68.21	26.57	5.21
			74.33	23.47	2.18			66.73	27.82	5.45
			70.98	26.69	2.32		15	84.57	13.14	2.29
			67.49	30.08	2.43			83.25	14.26	2.49
			64.04	33.37	2.59			81.89	15.42	2.69
			60.48	36.78	2.73			80.47	16.64	2.89
								79.01	17.92	3.07
								77.46	19.29	3.26
								75.56	20.98	3.47
								74.03	22.32	3.65
								72	24.09	3.83
								70.06	25.93	4.01
								67.99	27.84	4.73
							20	84.04	14.1	1.86
								82.57	15.41	2.02
								81.06	16.78	2.16
								79.48	18.22	2.3
								77.78	19.77	2.45
								75.8	21.62	2.58
								73.75	23.54	2.71

								71.64	25.33	2.82
Ruzicka et al., (1997) R HED-CM	-1.20	5	77.02	19.66	3.32	-1.60	5	82.51	14.45	3.04
			74.62	21.82	3.56			81.23	15.51	3.26
			72.16	24.07	3.76			79.87	16.63	3.5
			69.63	26.41	3.97			78.46	17.82	3.73
			67.02	28.84	4.14			76.66	19.36	3.98
			64.33	31.4	4.27			75.35	20.42	4.22
	61.54	34.08	4.39	73.49	22.03	4.48				
		10	78.12	18.97	2.91			71.59	23.69	4.72
			75.58	21.29	3.12			69.61	25.43	4.96
			72.95	23.73	3.34			67.57	27.24	5.18
			70.24	26.23	3.53			65.47	29.16	5.37
			67.47	28.86	3.67		10	83.47	13.88	2.66
			64.61	31.59	3.8			82.17	14.96	2.87
		61.65	34.45	3.9		80.81		16.1	3.09	
		15	79.23	18.34	2.42			79.41	17.3	3.3
			76.48	20.9	2.61			77.9	18.58	3.52
			73.6	23.58	2.81			76.06	20.21	3.73
			70.63	26.4	2.97		74.64	21.4	3.96	
			67.55	29.33	3.12		72.73	23.09	4.17	
			64.39	32.39	3.23		70.77	24.84	4.39	
		20	61.13	35.56	3.32		78.76	26.66	4.57	
			80.73	17.51	1.76		66.76	28.58	4.76	
			77.74	20.33	1.93		64.52	30.58	4.91	
			74.59	23.32	2.09		15	84.44	13.35	2.22
			71.3	26.48	2.22			83.07	14.52	2.41
			67.87	29.8	2.32			81.68	15.71	2.61
		64.34	33.25	2.41		80.23		16.98	2.79	
		60.7	36.82	2.47		78.71		18.31	2.98	
						76.81		20.03	3.16	
						75.4	21.27	3.33		
					73.45	23.03	3.52			
					71.44	24.88	3.68			
					69.38	26.78	3.84			
					67.27	28.75	3.98			
					20	85.48	12.88	1.65		
						84.02	14.18	1.8		
						82.55	15.5	1.94		
						81.03	16.88	2.08		
						79.43	18.34	2.23		
						77.74	19.91	2.35		
					75.74	21.78	2.48			

								73.68	23.71	2.61
								71.57	25.7	2.72
Ruzicka et al., (1997) R HED-L	-1.20	5	80.44	16.44	3.12	-1.60	5	82.45	14.47	3.08
			78.29	18.33	3.39			81.15	15.53	3.32
			76.1	20.28	3.62			79.8	16.64	3.56
			73.84	22.3	3.86			78.37	17.83	3.8
			71.5	24.41	4.08			76.56	19.38	4.06
			69.13	26.59	4.29			75.49	20.25	4.26
			66.66	28.86	4.48			73.38	22.05	4.58
			64.13	31.26	4.61			71.48	23.71	4.82
			61.49	33.78	4.73			69.5	25.44	5.06
		10	79.46	17.55	2.99			67.47	27.25	5.28
			77.16	19.62	3.22			95.37	29.16	5.47
			74.78	21.76	3.46		10	83.59	13.71	2.73
			72.36	23.98	3.66			82.28	14.77	2.95
			69.85	26.28	3.86			80.94	15.87	3.19
			67.28	28.29	4.03			79.54	17.05	3.41
			64.65	31.19	4.16			78.08	18.29	3.63
			61.9	33.83	4.27			76.25	19.88	3.86
		15	80.68	16.76	2.56			74.86	21.03	4.11
			78.24	18.97	2.79			72.97	22.68	4.35
			75.72	21.27	3.01			71.03	24.4	4.56
			73.12	23.67	3.2			69.02	26.19	4.79
			70.45	26.16	3.38			66.97	28.06	4.97
			67.71	28.76	3.53			64.84	30.02	5.14
			64.88	31.46	3.66		15	84.51	13.17	2.33
			62	34.26	3.75			83.16	14.29	2.54
			58.99	37.19	3.82			81.79	15.47	2.74
		20	82.09	15.85	2.06			80.37	16.69	2.94
			79.5	18.25	2.25			78.87	17.98	3.15
			76.81	20.75	2.44			76.99	19.66	3.35
			74.02	23.37	2.61			75.62	20.82	3.56
			71.14	26.09	2.77			73.7	22.55	3.75
			68.16	28.94	2.87			71.7	24.34	3.95
			65.11	31.59	3			69.68	26.19	4.13
			61.99	34.93	3.08			67.59	28.12	4.29
			58.79	38.08	3.13		20	84.13	13.8	2.07
								82.72	15.06	2.23
								81.23	16.36	2.4
								79.7	17.74	2.59
								78.08	19.19	2.73
								76.11	20.99	2.9

								74.53	22.42	3.05
								72.49	24.31	3.2
								70.43	26.24	3.34
Ruzicka	-1.20	5	77.35	19.04	3.61	-1.60	5	82.45	14.26	3.29
et al.,			74.03	21.97	4			81.82	14.75	3.43
(1997) R			71.74	24.04	4.22			80.56	15.77	3.67
HED-EH			69.37	26.2	4.43			79.24	16.83	3.93
			66.92	28.47	4.63			77.51	18.29	4.2
			64.38	30.84	4.77			76.34	19.19	4.47
		10	78.39	18.3	3.31			74.56	20.68	4.76
			75.46	20.91	3.63			72.72	22.25	5.04
			73.1	23.03	3.87			70.81	23.87	5.32
			70.68	25.23	4.09		10	82.96	13.98	3.06
			68.2	27.52	4.28			81.47	15.2	3.34
			65.65	29.92	4.43			80.16	16.26	3.58
			63	32.43	4.57			78.77	17.41	3.82
		15	79.47	17.54	2.99			76.99	18.92	4.09
			76.9	19.83	3.27			75.75	19.91	4.34
			74.51	22.01	3.48			73.92	21.47	4.61
			72.02	24.27	3.7			72.04	23.09	4.87
			67.45	26.59	3.96			70.1	24.77	5.13
			66.86	28.93	4.2			68.1	26.53	5.38
			64.24	31.31	4.45		15	83.55	13.68	2.77
			61.57	33.72	4.7			82.33	14.69	2.99
		20	80.68	16.7	2.62			81.01	15.78	3.21
			78.39	18.76	2.85			79.62	16.95	3.43
			75.91	21.03	3.06			78.16	18.17	3.67
			73.35	23.39	3.26			76.35	19.75	3.9
			70.72	25.84	3.44			74.98	20.87	4.15
			68.01	28.38	3.61			73.1	22.51	4.38
			65.24	31.03	3.73			71.16	24.22	4.62
			62.37	33.78	3.84			69.17	25.99	4.84
			59.42	36.67	3.92			67.12	27.83	5.05
								65.02	29.76	5.22
								62.82	31.79	5.39
							20	84.11	13.43	2.46
								82.26	14.14	2.6
								81.9	15.29	2.82
								80.5	16.48	3.02
								79.04	17.74	3.22
								77.47	19.08	3.45
								75.59	20.75	3.66

								74.1	22.04	3.87
								72.15	23.78	4.06
								70.15	25.59	4.26
								68.1	27.47	4.42
								65.99	29.42	4.59
Dreibus & Wanke (1980)	-1.20	5	79.28	17.9	2.83	-1.60	5	83.83	13.6	2.58
			76.94	20.02	3.04			82.6	14.62	2.78
			74.51	22.23	3.25			81.31	15.71	2.98
			72.02	24.55	3.43			79.97	16.85	3.18
			69.46	26.94	3.6			78.57	18.06	3.37
			66.82	29.45	3.73			76.78	19.64	3.58
			64.1	32.07	3.84			75.47	20.75	3.78
			61.28	34.81	3.91			73.63	22.4	3.98
		10	80.56	17.03	2.41			71.73	24.1	4.17
			78.1	19.29	2.6			69.75	25.88	4.37
			75.54	21.67	2.8			67.72	27.74	4.54
		15	79.35	18.56	2.1			65.63	26.69	4.68
			76.6	21.15	2.25			63.44	31.77	4.79
			70.95	26.51	2.54		10	83.43	14.19	2.37
			67.92	29.43	2.64			82.11	15.34	2.55
			64.81	32.47	2.73			80.33	16.95	2.72
			61.61	35.62	2.77			79.3	17.8	2.9
			58.33	38.87	2.8			77.79	19.13	3.08
		20	80.8	17.79	1.4			75.92	20.83	3.25
			77.82	20.67	1.51			74.45	22.13	3.42
			74.67	23.71	1.62			72.53	23.89	3.58
			71.35	26.94	1.72			70.56	25.71	3.79
			67.92	30.31	1.77			68.51	27.62	3.87
			64.36	33.81	1.83			66.41	29.59	4
			60.73	37.42	1.85		15	84.44	13.64	1.92
								83.07	14.86	2.07
								81.67	16.12	2.21
								80.21	17.43	2.36
								78.67	18.85	2.48
								76.76	20.61	2.63
								75.28	21.96	2.76
								73.31	23.8	2.89
								71.3	25.7	3
								69.23	27.67	3.1
							20	85.6	13.11	1.29
								84.15	14.44	1.41
								82.69	15.82	1.49

								81.16	17.25	1.59
								79.56	18.77	1.68
								77.84	20.4	1.76
								74.54	22.33	1.83
								73.78	24.3	1.92
Bosenberg	-1.20	5	66.45	29.14	4.41	-1.60	5	82.87	14.59	3.13
&			64.1	31.14	4.76			80.93	15.6	3.47
Delaney		10	68.35	27.93	3.72			79.5	16.69	3.81
(1997)			66.05	29.91	4.04			77.62	18.19	4.19
			63.61	32.04	4.34			76.35	19.05	4.6
			60.48	34.94	4.58			74.39	20.55	5.05
		15	70.44	26.77	2.79			72.37	22.1	5.52
			68.12	28.81	3.07			70.31	23.69	6
			65.71	30.97	3.33		10	83.61	13.81	2.58
			62.47	33.99	3.54			82.33	14.82	2.85
			60.46	35.74	3.8			80.96	15.89	3.14
			57.08	38.95	3.97			79.09	17.45	3.47
		20	70.59	27.9	1.5			77.99	18.21	3.8
			68.19	30.2	1.61			76.07	19.76	4.17
			65.63	32.65	1.72			74.09	21.36	4.55
			62.19	35.99	1.82			72.03	23	4.97
			59.97	38.12	1.91			70.76	23.81	5.43
			56.4	41.61	1.99			68.65	25.48	5.87
			62.66	45.31	2.03		15	83.7	14.22	2.09
			48.7	49.24	2.06			82.4	15.3	2.3
			44.77	53.43	2.1			81.03	16.45	2.52
								79.14	18.08	2.78
								78.01	18.96	3.04
								76.08	20.62	3.3
								74.09	22.31	3.61
								72.03	24.07	3.9
								69.9	25.9	4.2
								67.7	27.81	4.5
								65.41	29.79	4.8
								63.04	31.88	5.07
							20	84.33	14.54	1.13
								83.1	15.7	1.21
								81.78	16.91	1.3
								79.92	18.66	1.43
								78.85	19.63	1.53
								76.94	21.41	1.65
								74.97	23.26	1.77

	72.92	25.2	1.88
	70.79	27.2	2.01
	68.56	29.32	2.12